

Wake Dynamics of Cylinders Encountering Free Surface ~~Gravity~~ Waves

by

Richard H Arkell

A thesis submitted for the degree of
Doctor of Philosophy of the University of London
and for the
Diploma of Membership of Imperial College

Department of Aeronautics
Imperial College of Science, Technology and Medicine
London SW7 2BY

1995

LONDON UNIV.

Abstract

A study is carried out of the effects of an in-line free surface wave field on the vortex shedding and subsequent development of the wake of a vertical cylinder. The cylinder moves steadily through the fluid at low to moderate Reynolds numbers, and the forward speed of the cylinder always exceeds the particle orbital velocity of the wave. The investigation of the wake behaviour is carried out numerically, at various levels of idealisation to the physical problem. At the simplest level, an inviscid study of the wake dynamics of an infinite von Kármán point vortex street is made. The response of the street to an in-line progressive wave train is recorded. A two-dimensional Finite Volume viscous particle-mesh method is presented, which models the presence of the cylinder and the development of the wake including viscous effects; a regular Cartesian mesh is employed in the mid- to far-wake to ensure minimal distortion to the flow field, which might otherwise arise through inadequate mesh resolution. The viscous method affords a more realistic representation of the physical problem, but is more limited than the point vortex idealisation in the effective length of wake which is modelled. A three-dimensional Finite Element viscous particle-mesh method employing vortons as the Lagrangian vortex object is presented. This method uses fully unstructured tetrahedral element meshes. The method is used to study the three-dimensional vortex dynamics of a tapered cylinder in uniform flow, and subsequently, to model the interaction of free surface gravity waves with a vertical cylinder in steady translation. The wave field is modelled using linear wave theory. Experiments are carried out in the Department of Aeronautics $20m$ wave flume and water channel. Surface flow visualisations, in which a dye is introduced at the cylinder surface, are presented, and comparisons are made with the present numerical data and other flow visualisation experiments in the literature. The flow past a tapered cylinder is also examined, and the flow visualisation is carried out using an electrolytic precipitation technique.

Acknowledgements

I should like to thank Professor J.M.R. Graham for his supervision over the last few years. The friendly and approachable manner in which he has offered his insight and guidance has been much appreciated, and I thank him for it.

The work presented here was supported by the Office of Naval Research, Washington, under contract number N00014-90-J-4122. I should like to thank the directors of this part of the "Accelerated Research Initiative" on wake dynamics: Dr. Steve Ramberg and Dr. Tom Swean.

Within the department, there have been a great many people who have assisted and whom I should like to thank. From the workshop: Joe Meggyesi, Ernie Turner and Ron Adams; computer support technical staff: Clive Mott, John Wye, and Dr. Letty Allen; design: Peter Gasson; electrical services: Roger Serpell and Russell Carter; photographic: John O'Leary M.B.E. Thanks also to Silvana Kuhtz for her assistance in the wave flume. I should like to thank Dr. Kim Peiro for his assistance with the FELISA package and the demands I made on his time.

Over the last few years, I have had the pleasure to be a part of the research 'workforce' of this department. I have had an opportunity to share an office with many of the above, and I should like to thank in particular: Stelios Pesmajoglou, Mehdi Vadahti (Backgammon champion '90/'91), Mike Savvides, and Paul Mackwood.

For Mum and Dad

Contents

1 Introduction **7**

1.1 Motivation for Research 7

1.2 Layout of Thesis 17

1.3 Vorticity, Vortex Dynamics and Vortex Objects 19

1.4 Creation of Vorticity 24

1.4.1 Introduction 24

1.4.2 Vortex Shedding and the Near Wake 26

1.4.3 The Far Wake 41

1.4.4 Oscillatory Flows 49

2 Vortex Methods **52**

2.1 Introduction 52

2.2 Governing Equations of Motion for a Fluid 54

2.3 Inviscid Methods 57

2.4 Viscous Methods 73

3 Point Vortex Analysis **77**

3.1 Introduction 77

3.2 Case(A) (Concertina Effect) 81

3.2.1 Linearised Stability Analysis 81

3.2.2 Numerical Analysis 102

3.3 Case(B) 118
3.3.1 Model for variation in vortex strengths 118
3.3.2 Linearised Stability Analysis 122
3.3.3 Numerical Analysis 130

4 Two-Dimensional Viscous Analysis **133**
4.1 Introduction 133
4.2 Methodology 135
4.2.1 Discretization 135
4.2.2 Flux evaluation 140
4.2.3 Gradient evaluation 142
4.2.4 Boundary conditions 144
4.2.5 Interpolation from particles to mesh 149
4.2.6 Particle Tracking 154
4.2.7 Accuracy and Stability 156
4.3 Code Validation 161
4.3.1 Introduction 161
4.3.2 Patch test on the Poisson solver 162
4.3.3 Single point vortex in free space 164
4.3.4 Steady incident flow past a circular cylinder 166
4.4 Wave Flows 168
4.4.1 Introduction 168
4.4.2 Results 172

5 Three-dimensional Viscous Analysis **238**
5.1 Introduction 238
5.2 Numerical Method 240
5.2.1 Introduction 240

5.2.2 Velocity Equation 244
5.2.3 Diffusion and stretching equation 249
5.2.4 Vortons 252
5.2.5 Interpolation between Vortons and Mesh Nodes 257
5.2.6 Vorton Convection and Tracking 260
5.2.7 Summary of Code 261
5.2.8 Validation of Code 262
5.3 Results 266
5.3.1 Tapered Cylinder 266
5.3.2 Wave Flows 274

6 Experimental Work **282**
6.1 Tapered Cylinder 282
6.2 Wave Flows 288
6.2.1 Experimental Facility 288
6.2.2 Surface Flow Visualisation 292

7 Conclusions **304**

A Fourier Series **309**

B Conjugate Gradient Algorithm **311**

C Pressure calculation **313**

D Error in continuity of wave velocity field **315**

Chapter 1

Introduction

1.1 Motivation for Research

Bluff body flows have been subject to intensive study for many years, most notably in the field of marine technology since the exploration for oil and gas began in the hostile environment of the open seas. Since the late 1960's the United Kingdom has been engaged in the large scale exploration of offshore gas and oil fields which lie in the North Sea. It is anticipated that the vast reserves that lie in these fields will represent an economically viable source of hydrocarbons until at least twenty years into the next century. Currently, many of the more readily accessible fields (i.e. fields under shallower, calmer bodies of water, which require simpler engineering solutions to extract the oil and are therefore cheaper to exploit) have matured, and much work is now being carried out on deep water sites, where hydrodynamic loading problems caused by large swell, wave loading and high winds are generally present. Motivation for study into bluff body flows ensues from the fact that for most land and sea structures, the primary and leading design criteria are the structural qualities of the body, whereas the hydrodynamic performance generally represents a subordinate, but nevertheless important factor. The perils of not carefully accounting for the effects of fluid dynamic loading on structures can be severe:

perhaps one of the most oft-cited and certainly most graphic cases was the collapse of the Tacoma Narrows suspension bridge on November 7, 1940; strong vortices, fed from high cross-winds, caused ever increasing torsional oscillations of the bridge at its natural frequency, until very large scale rotational movements inevitably led to collapse. It was only discovered in the 1980's through wind tunnel testing that the strong rotational movements of the bridge were caused by the effects of 'lock-in' between a certain structural mode of rotation of the bridge, and the frequency of the vortex street being shed from the bridge. Experimental investigations of fluid loading have been paramount in securing the long-term dynamic structural integrity of offshore structures which experience currents and waves, particularly in the area of fatigue stress evaluation of oil-platform legs. The alternate shedding of vortices in the classical "vortex street" in the wake of a circular cylinder leads to large fluctuating pressure forces in a transverse flow sense, and may cause vibration, resonance and noise. Dynamic vortex loading or flow induced vibration (FIV) is generally an unwanted, destructive phenomenon in engineering, and is enhanced with vortex lock-in, when the natural (i.e. structural) frequency and the vortex shedding frequency are approximately the same. Much effort has been expended in assessing the effects of FIV with a view to minimising its manifestation through both active and passive measures. The harnessing of the phenomenon of vortex shedding for constructive uses is made in the area of flow measurement in channels and ducts by vortex flowmeters, which exploit the fact that flow speed is linearly proportional to the frequency of vortex shedding. A review of current day flowmeters is to be found in Young (1989).

Recently, renewed interest has focused on the problem of open wake flows found behind marine vehicles and towed bodies, for which, in general, the forward speed of the vehicle is greater than the local velocity fields induced by wave motion, and thus

the latter represent a perturbation to the undisturbed wake. Interest is motivated by the present lack of knowledge of the fundamental physics of three-dimensional wake dynamics in general, and the possible gains to be had in terms of say, improved hydrodynamic efficiency (e.g. drag reduction through control of the wake) or reduction in vibration and noise, that are perhaps concomitant with a better physical understanding.

Insofar as a general delineation of an incompressible wake of long cylindrical bodies in cross-flow is possible, and at the risk of over-simplifying matters, there are basically two distinct regions of physical interest downstream: (a) the near-wake, (b) the far-wake. The near-wake is the formation region just behind the body in which the two oppositely signed shear layers detach and roll up in periodic equilibrium; this is the most 'active' region of the wake and is characterised by large fluctuations in velocity and cancellation of vorticity as fluid elements having vorticity of one sign are drawn across the wake mid-line. In fact the formation length has been defined (for example in Bearman (1965); Griffin and Ramburg (1974)) as the distance from the body to the point downstream of the body where the velocity fluctuation level has grown to a maximum. The state of the separating shear layers is of crucial importance in determining the characteristics of the near wake, and thus the microscopic features of the boundary layers, the separation lines and the free shear layers are able to cause macroscopic changes in the fluid over very short distances, typically of the order of the body scale. Downstream of the formation region, the wake is established and consists of compact regions of vorticity, which interact with each other and are free from the direct influence of the body. The processes of molecular diffusion and turbulence, if present, act so as to diminish the kinetic energy of the fluid in favour of the fluid thermal energy, and in so doing cause the wake to spread in a lateral sense and dispossess it of vortical structure. As such, the question must

arise whether the wakes of all bluff bodies asymptote to the same form in the very far-wake (Bearman (1992)) and become indistinguishable from one another. If this is indeed the case, then apparently nothing may be deduced of the near-wake by examining the far-wake; any information of the separated flow around the body is eventually lost through stretching and folding of vortex lines and viscous dissipation.

The fundamental problem of the longevity or persistence of the wake of a moving body is an interesting one: the trailing tip-vortices of an aircraft, revealed via the condensation of moisture, are on occasion seen to exist as undisturbed structures across large arcs of the sky; many body lengths from the aircraft the vortex cores may slowly recede and draw together to form a train of vortex rings. The wake then quickly disintegrates under this process known as the Crow instability. An observer stationed at the stern of a large ship might see ruffled water stretch for many miles behind, apparently undiminished in its turbulent intensity and loath to return to the equilibrium of the surrounding sea. Frictional forces within a fluid tend to make velocities in the wake uniform, and the diffusion of vorticity causes the wake to spread in a lateral sense (where gradients of vorticity are largest), but the effects on the nature and rate of the wake decay of parameters which include body shape, local Reynolds number, vortical structure, free surface conditions, three-dimensional effects and turbulence have not yet been fully appreciated.

The physics of the decaying wake are by themselves complex, and the requirement for studying the behaviour of wakes in engineering problems is both real and important: the operation of mobile Naval systems that are used for coastal and fleet defence, underwater environmental tests, sea bed mapping, acoustic detection and surveillance, together with the possible remote detection of towed and towing platforms are crucially dependent on an understanding of the physics of the near-wake

and its relation to the far-wake. Conversely, the objective of minimising body signatures which exist (though may not persist) in the wake is an integral part of stealth, and as such, is in the forefront of current day military thinking. At a more mundane level, examples of the effects of wakes may be observed all around. For instance, although trailing vortex wakes are quite different from quasi two-dimensional bluff body wakes, trailing vortices from large commercial aircraft can contain a large amount of energy and their persistence in the vicinity of airports can create severe buffeting problems for smaller aircraft attempting to take-off or land. Some studies have been made into the decay rates of trailing tip vortices (Moore (1972)). Indeed, although strong vortices from large aircraft are normally broken up and dissipated by atmospheric turbulence and shear, under certain circumstances trailing vortices can actually strike domestic dwellings near to runways and cause damage, and studies of this slightly bizarre but menacing phenomenon have been carried out (e.g. Blackmore (1994)).

The wakes behind vertically mounted circular cylinders which are translating through a still fluid have been studied by many researchers, and a brief survey of this work is presented in this chapter. There have also been studies of circular cylinders moving through a fluid at a constant speed whilst undergoing in-line oscillations; this situation has much in common with the present study, although it is generally the forces on the body rather than the wake which is of interest to the engineer, and as a result there exist fewer examples of experiments in which the study of the dynamics of the wake itself have been of primary concern. In studying the decaying wake of a circular cylinder from a practical point of view, the effects of wave induced velocity components are an important part of the problem since, on most water masses, waves are pervasive. It is rare for the surface of the water to be quiescent. The physics of wind generated gravity waves is not dealt with in the work presented here, but the

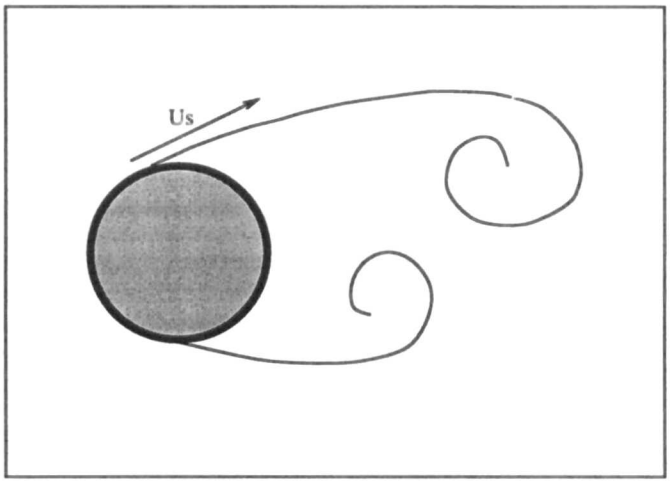
fascinating text of Kinsman (1965) which includes many photographs of sea waves and lucid explanations of the physical processes was found to be of great value by the author.

The current study is concerned with the effect of free surface waves on the vortex shedding and subsequent development of the wake of a vertical cylinder at low to moderate Reynolds numbers, whose forward speed exceeds that of the particle orbital speed of the wave-induced local velocity field. A reversed incident flow is therefore not usually present. In this work the free surface wave is modelled as a sinusoidal wave, and although there exists no such thing as a pure sinusoidal wave on the sea, in many cases a sinusoidal wave represents a reasonable approximation to a 'typical' sea wave. In addition, sinusoidal waveforms are amenable to relatively straightforward mathematical analysis.

The vast majority of wave/bluff body studies have focused on the effects of oscillatory flow on circular cylinders, and some of these have included the effects of a (relatively) weak current. The predilection for oscillatory flow problems is due to the fact that most marine structures are fixed or at most undergo limited motions, and are thus subject only to the oscillatory velocity component induced by passing waves together with at most a very weak steady current. These are not the considerations of the work presented here, although some common ground is to be found when the current, or forward speed, and the wave are of near equal strengths.

The investigation is carried out at various levels of idealisation of the physical problem, which differs from the wake problem for a body in steady incident flow by the appearance of essentially two new mechanisms: (a) the local velocity at the cylinder surface is a combination of a mean component and a component varying in time

(albeit weak by comparison with the mean component), and thus the *strengths* of the shed vortices vary with time, and this results in a (weak) spatial variation of vortex strengths away from the body (see figure 1.1); (b) the vortices in the far-wake are subject to a 'concertina-like' effect in which the wave-induced velocities cause a periodic dilation and extension of the inter-vortex spacing in a sense parallel to the wave number vector (see figure 1.2).

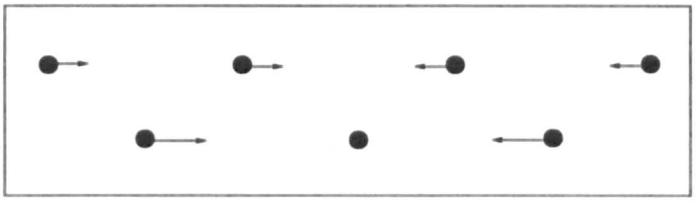


Vortex strength variation due to time-varying local flow

Figure 1.1

(Since this work deals with in-line longitudinal waves only, that direction is the mean flow direction). The former mechanism (a) is dependent on the wave frequency and only weakly dependent on the wavelength of the wave, where this is much larger than the body diameter, whilst the reverse is true for the latter condition (b). It should be stated that the waves considered in this work have wavelengths many times that of the body size (as is generally the case of towed bodies on the open seas), and thus the waves do not diffract around the body; the body is assumed to be insensitive to any spatial variation in the velocity field and only senses a time variation in velocity. In addition, the cylinder speed is generally less than the group

velocity of the wave in the scenarios under consideration. Accordingly, the only deformation of the free surface is due to the imposed incident waves, the localised negative pressure field of the shed vortices, and the cylinder itself, although none of the models presented in this work take account of deformations on the free surface.



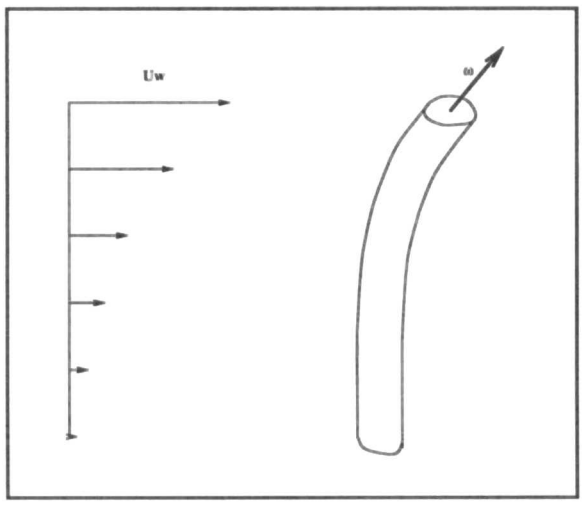
'Concertina-like' effect of wave on shed vortices

Figure 1.2

It is a classical and well known result that the idealisation of a vortex street to an infinite system of point vortices represents a system, which under a linearised stability analysis, may be shown to be neutrally stable (Lamb (1932)). That is to say, an infinitesimal disturbance introduced into the system will grow infinitely slowly and the street therefore evolves as a disturbed street *ad infinitum*. Moreover, there is only a single configuration of streamwise to transverse inter-vortex spacing for which this neutral stability condition holds; all other spacing ratios are unstable. It is manifestly true that real vortex streets persist for reasonably long distances, and it has been suggested that anomalies between the ideal von Kármán result and observed reality may in fact be due to a damping of the process of instability by wavelike motions on the finite area vortices (Zabusky (1977)); Saffman and Schatzman (1982) demonstrated using a linear stability analysis that finite-core vortex streets are stable. It was conjectured by Christiansen and Zabusky (1973) that if finite cores of vortex tubes are taken into account, there appears to be a stable region of spacing ratio around the point vortex value of 0.281 (see also Kida (1982)). For the point vortex representation, the imposition of an additional convective wave

motion as described in (b) is expected to lead to a modification and breaking-up of the wake structure, since it is reasonable to assume that the von Kármán point vortex street configuration which is only neutrally stable, will become unstable to a finite periodic disturbance [1] . The variation of vortex strengths in a staggered von Kármán vortex street is also expected to represent an unstable configuration. The linearised stability analysis of both configurations (termed hereafter Case(A) and Case(B) respectively) is presented in chapter 3 of this thesis.

A surface gravity wave induces orbital velocities which decay exponentially with depth, but are in phase at common lengths in the direction of the wave number vector. Therefore a three dimensional shed vortex experiences a strong spanwise variation in velocity (see figure 1.3). This deformation of the vortices leads to the generation of local helicity ($\int \vec{\omega}.\vec{u}\ d\vec{x}$) and a much more complicated velocity field.



Effect of spanwise velocity decay on vortex

Figure 1.3

[1] Christiansen and Zabusky (1973) remark that any *finite* disturbance of the street immediately implies that the inter-vortex spacing is no longer exactly: $\cosh(\pi b/a) = 1$, and the street therefore becomes susceptible to the growth of infinitesimal disturbances.

The objective of this investigation is to identify characteristics of the perturbed wake and provide insight into the fundamental questions:

- How does the wake differ qualitatively from the unperturbed result (i.e. the von Kármán vortex street)?

- What wave and flow parameters determine the rate of degeneration of the wake?

- Is there a re-organisation of scales?

- How weak can a wave be to have a significant effect - given that the von Kármán street is only neutrally stable in the inviscid limit? i.e. is there an amplification process through non-linear effects in the wake?

- What is the rôle of three-dimensionality?

1.2 Layout of Thesis

The work presented in this investigation is mainly numerical, although some surface visualisation data from experiments have been carried out in the Department's 20m wave tank, and are presented in conjunction with the numerical data. The numerical work is carried out at various levels of idealisation: at the simplest level, an infinite Von-Karman point vortex street is subjected to an in-line progressive wave train and the dependence of wake modification on certain parameters is recorded. Data from two-dimensional and three-dimensional viscous computations are also obtained.

The thesis is divided into seven chapters, the general theme and order of the division being physics, numerical experiments, and flow visualisation. In terms of experimentation, the emphasis here is on numerical work, and the bulk of the thesis is accordingly given over to that.

- Chapter 1 is concerned with the physics of vortex shedding from circular cylinders. A survey of the changing physics of vortex shedding as a function of Reynolds number is presented. Three-dimensional effects, the physics of the far wake, and the effects of in-line oscillations of a vertical cylinder in a steady flow are reviewed.
- Chapter 2 is a survey on the use of vortex methods in the computation of bluff body flows.
- Chapter 3 introduces the point vortex idealisation of the von Kármán wake. In this chapter both a linearised stability analysis and a numerical integration of the idealised wake of a circular cylinder subject to an in-line progressive wave train are presented.
- Chapter 4 is concerned with the development and application of a two-dimensional Finite Volume viscous particle-mesh method, which models the presence of the cylinder and the development of the wake including viscous effects; this method affords

a more realistic representation of the physical problem, but is more limited (due to computer hardware) than the point vortex idealisation in the effective length of wake which is modelled.

• Chapter 5 extends the work presented in chapter 4 to three-dimensions, and the development and application of a three-dimensional Finite Element viscous particle-mesh method employing the vorton concept is presented which includes the effect of the free surface wave. Flow past a tapered cylinder is also included as a prototypical three-dimensional flow problem. This data is compared both with flow visualisation experiments carried out by the author on a tapered cylinder, and with the data from the literature.

• Chapter 6 presents the results of surface flow visualisation experiments conducted in the Department's 20m wave flume on a circular cylinder translating into waves. The results of a flow visualisation experiment for steady flow past a linearly tapered cylinder are also presented. This data is compared with the numerical data reported on in earlier chapters.

• Finally, the conclusions are presented in Chapter 7.

1.3 Vorticity, Vortex Dynamics and Vortex Objects

Vorticity, defined as the curl of the velocity field $\vec{\omega} = \nabla \wedge \vec{u}$, is of fundamental importance in the study of incompressible fluid flows. Its importance derives from the fact that it forms the most compact mathematical representation of the flow evolution, and more often than not the patterns of vortex motion reveal the underlying physics clearly, and thus lead to a better comprehension of the physical processes.

It may be shown (Sommerfeld (1950)) that any finite continuous vector field $\vec{a}$ which vanishes at infinity together with its first derivative, may be decomposed uniquely into two vector fields $\vec{a}_1$ and $\vec{a}_2$ such that:

$$\vec{a} = \vec{a}_1 + \vec{a}_2 \tag{1.1}$$

$$\nabla \wedge \vec{a}_1 = 0 \; ; \; \nabla \cdot \vec{a}_2 = 0 \tag{1.2}$$

$$\nabla \cdot \vec{a}_1 = \nabla \cdot \vec{a} \; ; \; \nabla \wedge \vec{a}_2 = \nabla \wedge \vec{a} \tag{1.3}$$

Thus, any incompressible velocity field (for which the divergence is zero) may be decomposed into the gradient of a potential function and a rotational or vortical term (called the solenoidal term in vector field classification - in fact both $\vec{a}_1$ and $\vec{a}_2$ are solenoidal in an incompressible fluid). The motion of an incompressible fluid can therefore be represented by the creation and subsequent evolution of a self-interacting vorticity field plus the solution to a potential problem (ϕ). For incompressible flow problems the velocity field may be expressed as:

$$\vec{u}(\vec{x},t) \;=\; \nabla\phi(\vec{x}) \;+\; \vec{u}_r(\vec{x},t) \tag{1.4}$$

where $\vec{u}_r(\vec{x},t)$ is related to the vorticity field by $\nabla \wedge \vec{u}_r(\vec{x},t) = \vec{\omega}(\vec{x},t)$. Hence the evolution of the entire flow field is given by the solution $\vec{\omega}(\vec{x},t)$, which has, in general, a compact spatial support. Indeed, even if ϕ is a function of t, it does not represent the 'convective evolution' part, just an instantaneous response to the changing boundary conditions, i.e. the whole of the true time dependence is in $\vec{u}_r$.

In his paper of 1858 (translated into English by P.G. Tait and appearing in the Philosophical Magazine in 1868) Helmholtz delivers the fundamental concepts of vortex dynamics for an inviscid fluid. This work is remarkable if one considers that at the time there existed no mathematical formulation of the effects of friction in the fluid, although this was acknowledged at the time as being highly significant and representing the difference between theory and observed fact. Helmholtz alludes to this, but pursues it no further. Instead, he seeks solutions to the Euler equations for which no velocity potential exists (i.e. for which $\nabla \wedge \vec{u} \neq 0$). Euler (1755) had pointed out that there existed cases of fluid motion in which no velocity potential exists - for instance the rotation of a fluid about an axis when every fluid element has the same angular velocity. Helmholtz's theoretical investigation shows that:

- *No element of the fluid which was not originally in rotation is made to rotate*

- *Each vortex line (a line whose direction coincides everywhere with the instantaneous axis of rotation of the element of fluid) remains continually composed of the same elements of fluid, and swims forward with them in the fluid*

- *The product of the section and the angular velocity of an infinitely thin vortex filament is constant throughout the whole length, and retains the same value during all displacements of the filament. Hence vortex filaments can never end within a fluid and must either be closed curves, or must have their ends in the bounding surface of the fluid*

It follows that a vortex tube (comprised of vortex lines) and defined such that $(\nabla \wedge \vec{u}).\vec{n} = 0$ everywhere on its surface (where $\vec{n}$ is a normal vector to the surface which separates the irrotational and rotational fluid), must move with the fluid velocity and maintain its intensity or circulation. Stretching (elongation) of the tube therefore results in an increase in the vorticity through any plane normal to the vortex lines which comprise the vortex tube; by Stokes theorem the increase in vorticity is kinematically equivalent to an increase in the local circumferential velocity on this plane, and stretching of the vortex tube thereby provokes a modal shift in the spectrum of the fluid kinetic energy towards higher frequencies. Vortex stretching presents itself as one of the possible structural mechanisms for the energy cascade process evident in three-dimensional turbulent flows.

For an inviscid fluid, vorticity is a kinematic property of a given fluid particle; it cannot be created or destroyed. Vortex-lines are thus fluid material lines and can only undergo convection and deformation. Consequentially, for an inviscid flow, the tracking of vorticity leads naturally to a Lagrangian description of the flow field. The use of interacting Lagrangian vortex objects embedded in the the potential field to model the behaviour of incompressible flows has a rich history, from the early work of von Kármán (1911) on point vortices to the current day three-dimensional Navier-Stokes problems, and reviews of vortex methods are made by Saffman and Baker

(1979), Leonard (1980,1985), Aref (1983), Sarpkaya (1989). The application of the vortex dynamics concept requires the solution of two correlated problems, namely: (1) ascription of some object representation to the vorticity field, (2) derivation of a (finite) set of ODE's to describe the evolution of each of the vortex objects. In a three-dimensional analysis, further equations are required to represent the stretching of vortex tubes. Vortex methods are considered in greater detail in chapter 2 of this thesis, which briefly reviews the use of these methods in the numerical modelling of separated flows.

Unfortunately, vorticity diffusion and vorticity production at solid boundaries violate the Helmholtz theorem, and thus the principal basis of the vortex dynamics concept becomes untenable in a viscous medium. Vortex lines are no longer material lines, and the idea of 'rigid' Lagrangian vortex objects completely describing the fluid motion by their self-evolution becomes strictly invalid. A vortex arising in a viscous fluid diffuses instantaneously (if the problem is being looked at in a continuum mechanics sense), and introduces vorticity everywhere in the field. Therefore, the very concept of what actually constitutes a vortex in a viscous medium is a moot one. The idea of a vortex having compact spatial support defers to one in which the 'effective' vortex has compact spatial support, i.e. most of the vorticity resides locally and spatially decays to a small 'cutoff' value rapidly. The diffusion of a vortex is thus represented by an increasing number of vortex objects.

In a viscous incompressible flow there are now three correlated processes in evidence: convection, molecular diffusion and the generation of vorticity at solid surfaces from the viscous-adhesion or no-slip condition. In the literature there are a host of different numerical approaches to the problem of viscous vortex dynamics and, in principle, all of these are extensions of the inviscid vortex dynamics method

with the diffusion and generation processes 'tacked-on'; the elegance of the inviscid method is somewhat lost, but this has in itself given rise to new and novel numerical techniques to accommodate the viscous processes.

1.4 Creation of Vorticity

1.4.1 Introduction

A body immersed in a fluid and undergoing relative motion disturbs the fluid and creates within it a spatially varying pressure field. Near to the surface of the body, fluid elements are subject to shear forces as a result of the no-slip condition at the surface of the body; a flux of vorticity is generated at the surface and diffuses into the fluid, forming the boundary layer. For an isothermal, incompressible and viscous fluid, the Reynolds number *Re* (which may be thought of as the ratio of inertia to shear forces in the fluid, or the ratio of typical convective to diffusive time scales) is the single parameter determining the stability of the flow subsequent to a disturbance. This may be illustrated by considering the Navier-Stokes equations:

$$\frac{\partial \vec{u}}{\partial t} + (\vec{u}.\nabla)\vec{u} = -\frac{1}{\rho}\nabla p + \nu\nabla^2\vec{u} \tag{1.5}$$

Under a transformation to dimensionless variables:

$$[\vec{x}, \vec{u}, t, p] \mapsto [\vec{x}^*, \vec{u}^*, t^*, p^*] = [\vec{x}/L, \vec{u}/U, tU/L, p/\rho U^2] \tag{1.6}$$

where L is a typical length scale (e.g. the body size) and U a typical velocity (e.g. the free stream velocity). When (1.6) is inserted into (1.5), the non-dimensional Navier-Stokes equations result:

$$\frac{\partial \vec{u}^*}{\partial t^*} + (\vec{u}^*.\nabla^*)\vec{u}^* = -\nabla^* p^* + \frac{1}{Re}\nabla^{*2}\vec{u}^* \tag{1.7}$$

$$Re = \frac{UD}{\nu} \tag{1.8}$$

Equations (1.7) and (1.8) indicate that for a given geometric shape, the equation of evolution, and thus the flow behaviour, is identical for a family of flows of differing viscosities, length and velocity scales, provided there exists a common value of Reynolds number.

If the (relatively) thin layer of vortical flow which envelops the body becomes detached locally from the surface (due to the presence of an adverse pressure gradient), the flow is deemed to have separated there. Bluff bodies are characterised by the presence of large regions of separated flow over their surfaces. The significance of large-scale flow separation lies in the fact that for the vast majority of cases (that is to say at everyday engineering Re, which might be typically $10^3 \rightarrow 10^7$), the resulting flow adjacent to a body is unsteady, leading to substantial dynamic loading; in addition, the vortical structures which form are no longer confined to the vicinity of the body surface and once shed, are free to interact and perturb the flow far from the body. Bodies with surface slope discontinuities, such as a flat plate placed normal to a fluid stream, experience separation at the salient edges. In the case of a circular cylinder however, the interplay over the smooth surface between the separated flow region and the attached boundary layers leads to a Reynolds number dependence. A survey of this dependence is presented in section 1.4.2.

The study of separated flows around bluff bodies, particularly with regard to the phenomenon of vortex shedding and dynamic loading, has represented a major focus in the field of unsteady hydrodynamics over the last century. However, there are many areas of bluff body flow problems which are still poorly understood; as remarked recently by Roshko (1992): "the problem of bluff body flows remains almost entirely in the empirical, descriptive realm of knowledge". From a fundamental fluid

dynamics viewpoint, the predilection for experimental and numerical surveys of the circular cylinder in particular is prompted by the somewhat surprising fact that a myriad of flow phenomena present themselves from this simplest of geometric shapes (Morkovin (1964)). From a practical viewpoint, the circular cylinder is a common engineering 'shape', and many structural components of marine vehicles and platforms are, or approximate to, circular cylinders (e.g. oil platform legs). With all these factors in mind, it is perhaps inevitable that the circular cylinder has been the subject of a great deal of experimental, theoretical and more recently, numerical analysis. Many scientific papers have been published over the years, which include Rosenhead (1953), Wille (1960), Morkovin (1964), Bearman and Graham (1980), Bearman (1984), Coutanceau and Defaye (1991), and Roshko (1992). The advancement and application of non-linear dynamics theory (low dimensional chaos theory) to explain bifurcations in the Navier-Stokes equations which give rise to periodic solutions, and the onset of turbulence, and the recent use of stability theory in an attempt to interpret vortex shedding as a manifestation of absolute instability in the near-wake (for a review see Huerre and Monkewitz (1992)), have all added new impetus and vigour to the field of bluff body flows research.

1.4.2 Vortex Shedding and the Near Wake

The observation and recording of vortex shedding is by no means a modern-day preserve, and the phenomenon was first alluded to by the Ancient Greeks. However, it was not until 1878 that the first formal investigation was conducted by the Czech scientist Cenek Strouhal in Liepzig, in which the frequency of sound generated by the translation of cylindrical rods through air was measured. Strouhal showed that the frequency f from a rod of diameter D placed in a stream of velocity U was:

$$f = \frac{U}{6D} \tag{1.9}$$

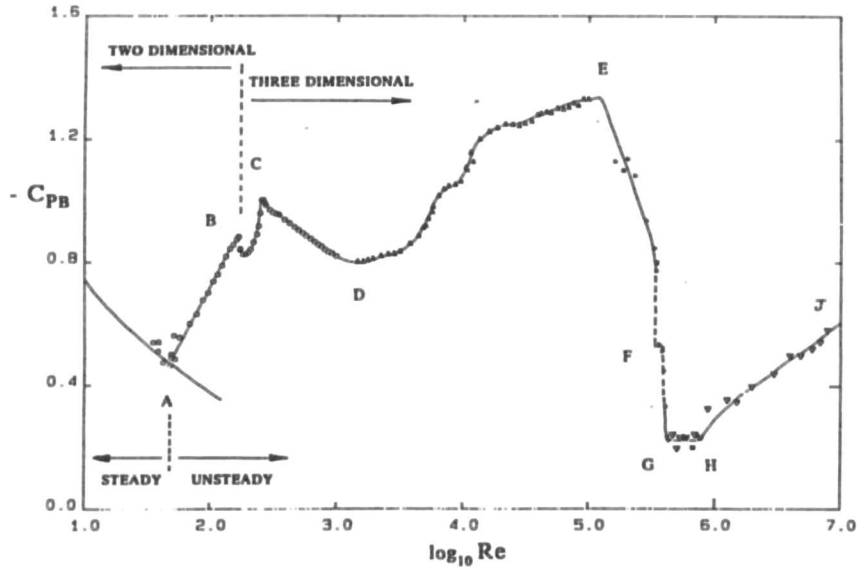
Lord Rayleigh later non-dimensionalised this frequency to the so-called "Strouhal number" S. The first pictures showing the alternating arrangement of vortices in the wake were published by Ahlborn in 1902, but the dynamics of the vortex street and the stability characteristics of the alternating configuration were first analysed by von Kármán in his pioneering work of 1911; by representing the wake as two parallel rows of point vortices, he was able to show that no such configuration was stable except for the particular case of vortex spacing ratio $b/a = 0.281$, (where a=inter-vortex spacing in one row, b=inter-row spacing), which was neutrally stable. It would seem that the limitations of this highly idealised analysis precludes it from bearing much resemblance to the actual behaviour of a viscous wake in the presence of a body, so it is remarkable that experimental data for finite-length vortex streets behind circular cylinders display spacing ratios of a similar magnitude.

This section of the thesis includes a brief synopsis of the physics of the flow past a circular cylinder at low to moderate Reynolds numbers, encompassing the regimes of interest here; its purpose is to serve as a general introduction to the physics and thus, indirectly, as a precursory indicator of the problems that are encountered in the numerical modelling of such flows.

Much is known of the behaviour of global quantities such as Strouhal number, drag coefficient and base pressure coefficient over a wide range of Reynolds numbers for a cylinder in uniform incident flow. Figure 1.4 is a plot of the coefficient of base pressure against Reynolds number (Williamson (1995)) and demonstrates the multitude of regimes and changing physics in the shedding process. Plots of variations in drag coefficient versus Reynolds number show similar trends, but are not as sensitive and therefore enlightening as the variations in base pressure coefficient, particularly in

the lower Reynolds number regimes.

At very low Reynolds numbers (<5) the flow around a cylinder is attached everywhere and steady; for Reynolds numbers smaller than about 1 the upstream and downstream sides are symmetrical (figure 1.5), but for increased Reynolds numbers the rear stagnation region is stretched out in the streamwise direction, whilst the forward region is compressed. At $Re > 5$, the flow separates at the rear stagnation point, and the size of the separation region increases with increasing Reynolds numbers.

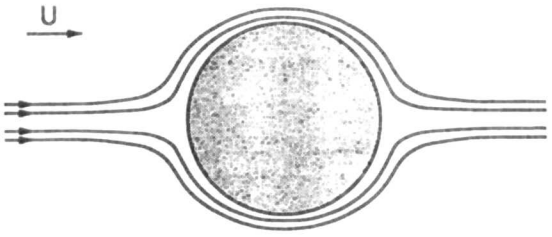


Plot of base suction coefficients over a large range of Reynolds numbers.

○	Williamson & Roshko (1990)	✱	Flaschbart (1929)
△	Norberg (1988)	▽	Shih, Wang, Coles & Roshko (1992)
+	Bearman (1969)	——	Dennis & Chang (1970) - steady computations.

Base pressure coefficient versus Reynolds number

Figure 1.4

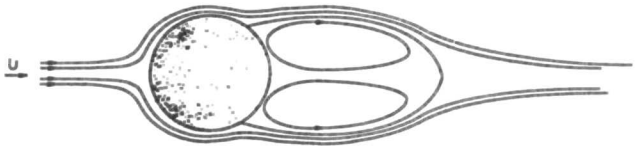


Creeping flow past a circular cylinder. $Re < 5$. (Streamlines)

From Szepessy (1991)

Figure 1.5

It is paradoxical that the flow at these Reynolds numbers, where viscous forces predominate, should closely resemble the potential solution to flow around a cylinder. At Reynolds numbers larger than about 5 separation occurs at the base of the cylinder and a symmetric pair of opposite-signed standing eddies are formed. The streamlines around the body envelop the eddies, and a rear stagnation region is found at the rear end of the separation bubble (figure 1.6).



Flow past a circular cylinder. $5<Re<45$. (Streamlines)

From Szepessy (1991).

Figure 1.6

The separation streamline is not tangential to the surface and the separation points move forward with increasing Reynolds number. The wake vortices meanwhile grow linearly with Reynolds number in the streamwise direction; transverse growth is weaker. It is a well recognised experimental fact that periodic shedding begins at a Reynolds number of about 45 (a two-dimensional instability occurs in which the flow undergoes a Hopf bifurcation - see Noack and Eckelmann (1993)), and the symmetric configuration of two standing eddies is no longer stable; the symmetry is broken in the wake just downstream of the saddle point, leading to a sinusoidal oscillation of the wake and rolling up of the shear layers there (figure 1.7). The Reynolds number at which symmetry is broken is sensitive to free stream turbulence, acoustic disturbances and cylinder end effects.



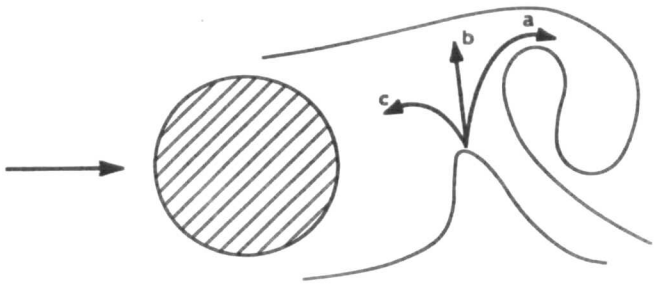
Flow past a circular cylinder. $45 < Re < 100$. (Streamlines)

From Szepessy (1991).

Figure 1.7

Initially, the twin vortices immediately behind the cylinder are resilient to fluctuations in the wake, but as the Reynolds number increases and the effective damping is reduced, perturbations cause one of the vortices to become slightly larger than

its twin; once a certain level of imbalance in vortex strengths has been reached this configuration is untenable; the larger vortex grows until it is shed and the sequence of alternate vortex shedding is realised. A very useful descriptive physical model of the mechanics of the vortex formation region immediately behind the cylinder was postulated by Gerrard (1966). In it, the key factor is the interplay between the two separating shear layers. Figure 1.8 illustrates the formation region by means of filament lines within the rolling-up shear layers. It is shown at the instant when irrotational flow is beginning to cross the wake axis.



Filament-line sketch of the formation region.
Arrows showing reverse flow (c) and entrainment (a) and (b). Gerrard (1966)
Figure 1.8

The upper shear layer is feeding its vortex with circulation, which grows in strength accordingly. The induced velocity field of this relatively strong vortex causes the shear layer from the opposite side to be drawn across the wake, and circulation

of opposite sign is entrained into the vortex (a) and into the feeding shear layer (b). There is also a component of reversed flow (c). Due to the character of the induced velocity field and the presence of the body, the entrainment is strongest in the direction (a). The effect of this entrained opposite-signed vorticity is to diminish the overall strength of the upper vortex and cut off the supply of circulation from its shear layer. At this point the vortex ceases to grow, is cut off, and convects downstream. The lower shear layer, now deformed from being drawn across in the above process, begins to roll-up rapidly, and the cyclic shedding process begins anew.

The existence of concentrated vortices in the wake is a result of the inherent instability of thin parallel shear layers which are generated at the surface of a body in the form of the separated boundary layer. The presence of the body itself is not very important in the development of the wake (save for the initial free shear layer generation). Abernathy and Kronauer (1961) performed numerical simulations of the non-linear interaction of two parallel infinite vortex sheets (represented by a periodic array of point vortices) and found that provided the transition from sheet to street was not too abrupt, the development of concentrated vortex clouds, i.e. the vortex street, could be simulated by the growth in time of periodic disturbances in the two initially parallel vortex sheets. The development of the clouds emulates the entrainment process and strength diminution (vorticity cancellation) of Gerrard's model by the sweeping of some vortices from one row into the clouds which form in the opposite row.

Organised, two-dimensional periodic shedding continues up to a Reynolds number of about 150 (figure 1.9). Up to this point the flow everywhere is laminar, and the vortex street persists far from the body. The fluctuating energy of the flow has a discrete spectrum and simply decays downstream without transfer to other frequen-

cies. The only agent of destruction of structure is the process of molecular diffusion, which broadens the spatial support of vorticity with distance downstream.



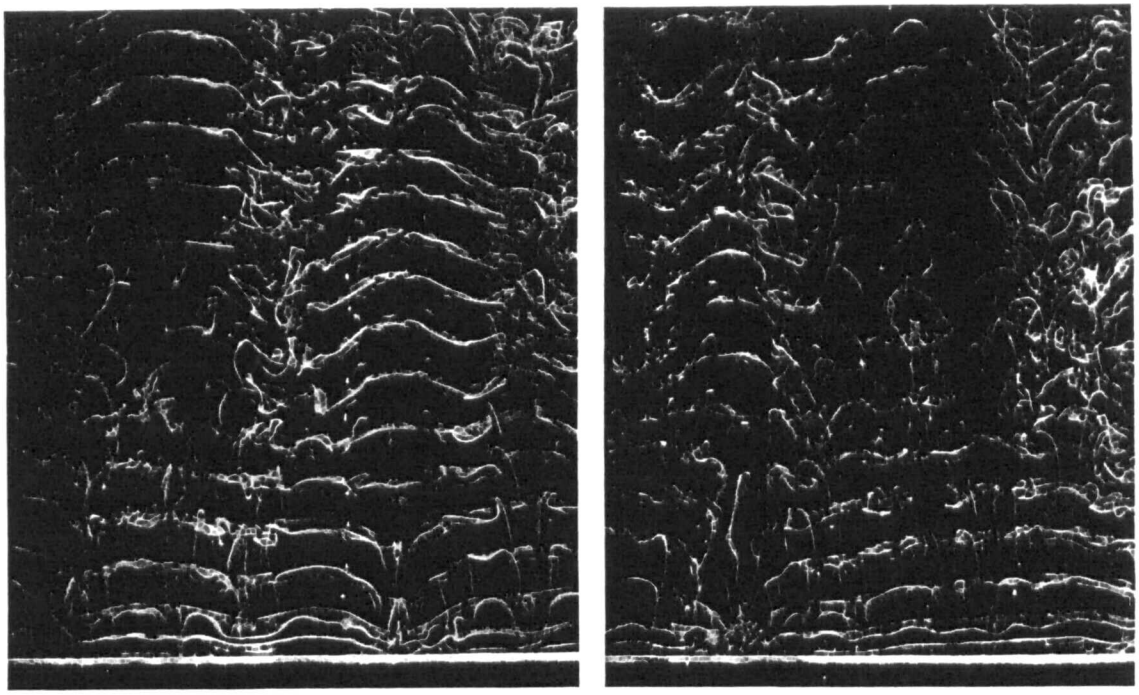
Flow in the laminar vortex shedding range ($100 < Re < 150$)

From Szepessy (1991).

Figure 1.9

Beyond a Reynolds number of about 180 (though this is an approximate figure and to a certain extent depends on the prevailing conditions of the experimental set-up), transition to turbulence is seen to occur downstream. Roshko (1954) reports the existence of a regime of $150 < Re < 300$ which he calls the 'transition range'. In this range there are irregular bursts of velocity in the wake, and both laminar and turbulent vortices are observed. In the wake there still exists a major component of the shedding frequency, but this is now accompanied by by a broad-band contribution. Roshko reports that in this transitional region: "downstream, the discrete energy, at the shedding frequency, is quickly dissipated or transfered to other frequencies, so that by 50 diameters the wake is completely turbulent, and the energy of the velocity fluctuations approaches that of isotropic turbulence". Bloor (1964) confirms the existence of such a range, albeit at a slightly higher value of Reynolds number of 200-400. (There is an inference that this small upward shift

in the Reynolds number region is due to the low turbulence levels of the 20" wind tunnel at Manchester, although the turbulence intensity figures quoted by both authors are the same). Bloor reports that below a Reynolds number of about 400 the transition to turbulence occurs by means of low-frequency irregular fluctuations which are basically three-dimensional. These low-frequency fluctuations have been shown to be the result of large-scale vortex dislocations (Williamson (1992)) caused by local shedding-phase dislocations along the span (figure 1.10).



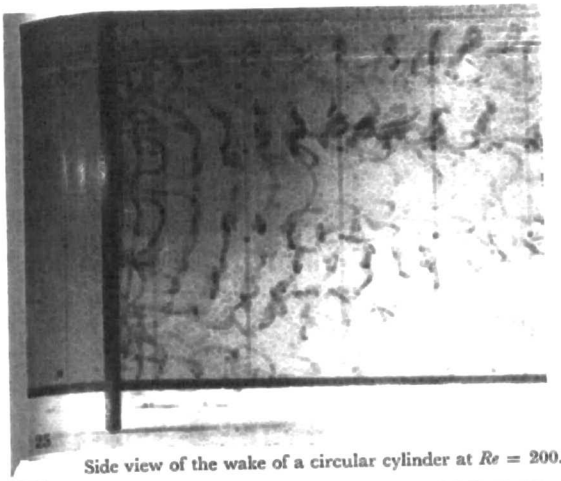
Large scale vortex dislocations

Figure 1.10

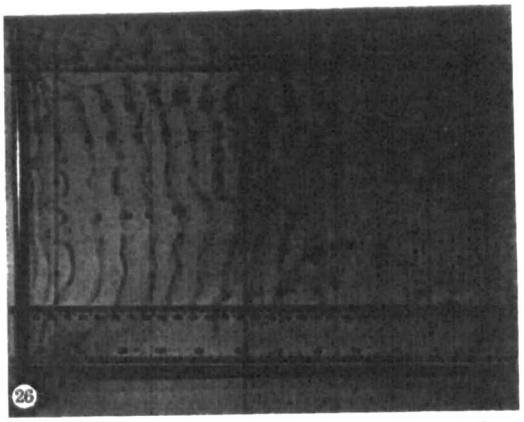
Williamson also notes the appearance of small-scale three-dimensionalities at $Re = 180$ in which streamwise vortex pairs are formed due to the deformation of the primary vortices as they are shed. At a slightly higher Reynolds number of 230-250, the flow changes again, and the three-dimensional shedding comprises finer-scale streamwise vortices and a more uniform deformation of the primary vortices as they are shed. Figure 1.11 is a photographic plate from Gerrard's (1978) work on the wakes of cylindrical bluff bodies at low Reynolds number. It shows most clearly the three-dimensional character of the nominally two-dimensional flow past a circular cylinder. The vortex loops reported by Williamson can be observed, and the change of these loops to finer and finer scales as the Reynolds number increases over the transition range is evident.

At higher Reynolds numbers (> 400) the physics of the generation of turbulence is somewhat different, and transition occurs in the separated shear layers; the primary vortices which roll up are always turbulent. Bloor (1964) studied the appearance of two-dimensional transition waves in the free shear layers and found that the frequency of these waves varies as $Re^{\frac{3}{2}}$, implying that the ratio of the transition wave frequency to the fundamental (shedding) frequency is proportional to $Re^{\frac{1}{2}}$. Bloor identifies these waves with the Tollmien-Shlichting waves observed by Sato (1960) for a separated shear layer in a rectangular jet. The conclusions of these findings are that transition in the shear layers at these Reynolds numbers occurs through amplification of essentially a two-dimensional instability producing Tollmien-Shlichting waves. The Kelvin-Helmholtz type instability observed in the shear layers is principally two-dimensional at its inception (figure 1.12), and the tight rolling up of the shear layer to form Bloor or Gerrard vortices results in fluctuations of velocity at fine scales and a modal transfer towards higher frequencies in the energy spectrum.

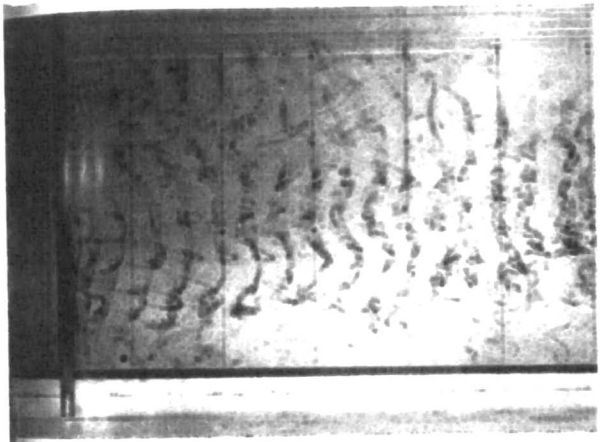
At higher Reynolds numbers three-dimensional instabilities develop.



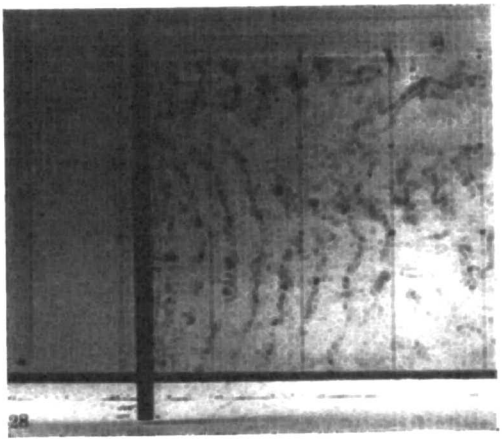
Side view of the wake of a circular cylinder at $Re = 200$.



Side view of the wake of a circular cylinder at $Re = 217$.



Side view of the wake of a circular cylinder at $Re = 232$.

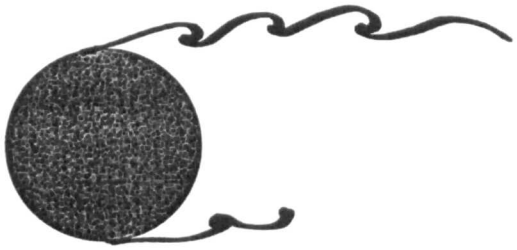


Side view of the wake of a circular cylinder at $Re = 344$.

Formation of spanwise vortex loops

From Gerrard (1978).

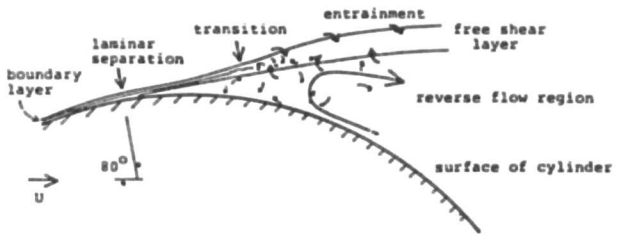
Figure 1.11



Kelvin-Helmholtz type instability of separated shear layers

Figure 1.12

For $Re < 10^3$, the transition point in the shear layer moves towards the cylinder, causing strong variations in base pressure coefficient with Reynolds number (see figure 1.4). At a $Re > 4 \times 10^4$ transition to turbulence (see figure 1.13) occurs very soon after the shear layer has separated and the transition waves evident at lower Reynolds numbers disappear (Szepessy (1991)).



Early transition in the shear layer.

From Basu (1985).

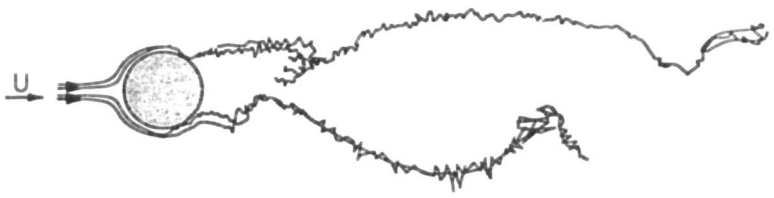
Figure 1.13

Data from experiments conducted by Cantwell and Coles (1983) on the processes of entrainment and transport in the near wake of a circular cylinder at a Reynolds number of 1.4×10^5 (i.e. just subcritical) seem to indicate that the mechanism responsible for a substantial part of the turbulence production in the wake arises from the stretching of small-scale vorticity near to saddles in the flow patterns. The turbulent kinetic energy is then transported to the centres of the primary von Kármán vortices where it accumulates. The large-scale coherent structures are thus fed turbulent energy from the small scales; this concept is somewhat at odds with the conventionally received idea of modal energy transfer from large to small scales, i.e. one in which larger vortex structures act as energy sources for intermediate and small scale vortices, following the famous energy cascade law of $k^{-\frac{5}{3}}$ predicted by Kolmagorov (1942). Cantwell and Coles note that: "...(the) larger scale may be deceptively conspicuous in measured spectra or correlations", and point out that although much experimental evidence supports the energy cascade law of fully developed turbulence, little is known of the physical mechanisms by which energy production and dissipation are actually carried out.

At a $Re = 2 \times 10^5$, the boundary layer separates, undergoes transition immediately, and reattaches as a turbulent boundary layer. A separation bubble is formed (Tani (1964)). The boundary layer is now more robust and stays attached till about $120° - 140°$ from the front of the cylinder. The flow is now in the critical Reynolds number regime and drastic changes to the flow patterns (figure 1.14), base pressure coefficient, drag coefficient and Strouhal number are observed.

From what precedes in the discussion of the physics of the vortex formation and shedding process behind the circular cylinder, it is clear that great challenges are

presented to any numerical simulation. It is evident that up to a Reynolds number of about 150 a two-dimensional simulation is capable of capturing the full range of scales and of simulating the separated boundary layers and formation process correctly, and confirmation of this is provided by the excellent agreement between experimental and numerical data at these Reynolds numbers (see Graham (1992)).



Flow in the critical Reynolds number range ($2 \times 10^5 < Re < 7 \times 10^5$)

From Szepessy (1991)

Figure 1.14

Beyond these Reynolds numbers the appearance of three-dimensional secondary instabilites manifested in the form of streamwise vortex loops must preclude any two-dimensional analysis. The transition region noted by Roshko of $150 < Re < 300$ is characterised by vortex loops of finer and finer scale; beyond the upper limit of this region, transition waves appear in the separating shear layers and produce what are principally two-dimensional instabilities; the modelling of these instabilities is amenable to 2-D simulations with appropriate spatio-temporal resolution. There remain, however, three-dimensionalities in the shedding process and in the wake. The mechanism of turbulence production reported by Cantwell and Coles can only be

captured in a full three-dimensional simulation, but this in itself remains largely an academic point since the Reynolds number limit on state-of-the-art direct numerical simulations is approximately $O(10^3)$. The apparently insurmountable problem with simulating flows around bluff bodies in general is that there exist at high and even moderate Reynolds numbers such a broad range of scale of structure: the primary von Kármán vortices, the interconnecting braid vortices in the wake, the Bloor vortices in the separating shear layers and the boundary layer itself; in addition, and somewhat unusually, the difficulty in simulation is compounded by the fact that it is the smallest scales in the shear layers which to a certain extent dictate the nature of formation of the large coherent structures found in the wake, and faithful reproduction of the physics therefore implies proper resolution of these scales. This seemingly pessimistic viewpoint on the limitations of numerical simulations is at odds with the fact that a number of high Reynolds number simulations have been carried out (e.g. Kawamura and Kuwahara (1984), Kuwahara and Ishii (1986)), well beyond the current direct simulation limit. Clearly, the physics are not fully modelled, and any apparent capability in capturing very high Reynolds number effects such as the drag crisis at the critical Reynolds number must be considered dubious. It may be that numerical diffusion in the very small elements near to the surface fortuitously but quite arbitrarily impersonates the effects of the very small scale turbulence that exists in the separated shear layers.

In two-dimensional vortical flows, there is a tendency for coherence, i.e. vortices tend to coalesce to form large structures. Perhaps the most startling examples of this phenomenon are to be found in atmospheric physics: the formation of tornados on Earth, and Jupiter's giant Red spot. Novikov (1975) shows there to be a statistically irreversible tendency to transfer energy from small to large scale lengths for a system of point vortices, and the formation of structure in hydrodynamic flows with

regard to forwarding a physical interpretation of the phenomenon of turbulence is currently undergoing much research (see Fieldler (1988)) - though this is quite outside the scope of the work presented here. The point to be made in context with simulation of flows around bluff bodies is that for a quasi two-dimensional flow there is a tendency in the wake for the coalescence of vortices; the use of point vortices in the simulation of wakes and flows behind bluff bodies in the inviscid limit has a long history, and these calculations, with due regard to all caveats mentioned above, have been remarkably successful given that often, only a single scale is present (the primary von Kármán vortex).

1.4.3 The Far Wake

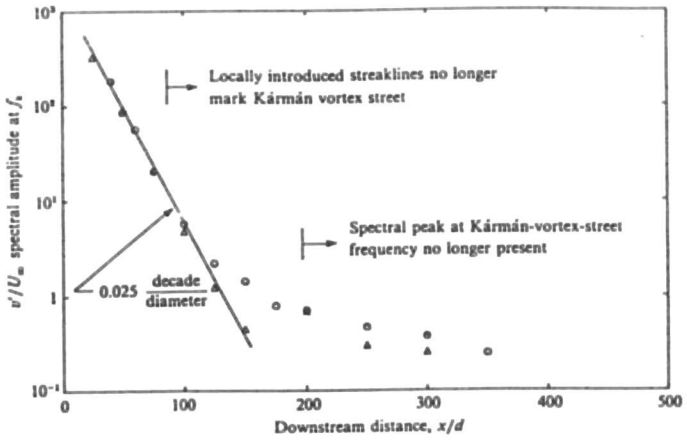
The vast majority of experiments of flow past bluff bodies have been concerned with the evaluation of global quantities such as force coefficients, and measurements of velocity values and spectra in the near wake. The far wake, which is generally regarded as ranging from tens to hundreds of body lengths downstream, has traditionally been of secondary interest to designers and engineers, principally, it may be argued, because it has little or no direct influence on the body itself. The physics of the decaying wake are poorly understood. The wakes of high Reynolds number flows past bluff bodies are three-dimensional and turbulent, and little is known of the mechanisms of decay of vortical structure, turbulent kinetic energy, etc... Even the much simpler case of two-dimensional wakes of circular cylinders at very low Reynolds numbers ($O(10^2)$) is cause for some disagreement among researchers, specifically with regard to the mechanisms responsible for the large scale structures observed in the far wake.

The study of the long-term behaviour of wakes subject to a wave field is an intrinsically difficult problem, and presents many challenges to both experimental

surveys and numerical analyses, not least of which is the vast tract of flow field that must be observed or calculated. In terms of flow visualisation, the tracking of dye or seed particles far from the body becomes rapidly futile as the effects of surface deformation, three-dimensionality, diffusion, and in most cases, turbulence conspire to confuse the picture somewhat. The velocity field far from the body is a complicated one, and is generally not susceptible to practical visualisation; however, the objective of performing visualisation of the flow is to elucidate, as far downstream as possible, the *patterns* of the flow so that some understanding might be had of the physics of the wake/wave interaction.

Flow visualisation experiments of the far wake of cylinders in steady incident flow have been carried out mainly at very low Reynolds numbers (see Taneda (1959), Morkovin (1964), Coutanceau and Defaye (1991)). Photographs of flow visualisations of vortex streets indicate that the street persists for very long distances downstream (e.g. Zdravkovich (1969)). However, as noted by Cimbala, Nagib and Roshko (1988), great care must be exercised in the interpretation of any flow visualisation image of substantial length. Most flow visualisation experiments for incompressible flows elucidate the flow patterns by introducing a passive marker (e.g. dye) at a fixed point in the flow, which is usually at the body. Streaklines are generated, and in unsteady flows, streaklines are not the same as streamlines; streaklines far downstream of their origin convey 'integrated' information of the local velocity field at every point in space through which the marker has passed. The marker therefore has a 'memory' associated with it. If the diffusion rate of vorticity is different from that of the marker, as is normally the case, it is possible that vortex structures in the wake will have decayed long before the marker indicates that they have. The marker will be convected downstream in an unchanging pattern until the marker itself is completely diffused. Cimbala *et al.* (1988) demonstrate the effect of introducing

smoke marker at different distances downstream. They show that the apparent existence of the very long wake from injection of the marker solely at the cylinder conveys a false picture; the vortex street in reality decays much more rapidly than indicated. At a Reynolds number of 90, they could not discern the vortices by about 125-150 diameters downstream: at a Reynolds number of 155 (near the limit of the laminar regime) the distance is about 75-100 diameters. For transitional and turbulent wakes they quote an $\frac{x}{D} = 50$. If the longitudinal vortex spacing is roughly $5D$, one may infer that only 30 vortices in each row are present in the laminar regime, at best, and 10 in the transitional regime. The exponential decay in the vortex induced velocity field downstream made apparent by flow visualisation recordings and velocity spectra from hot-wire measurements is sufficiently rapid to cause Cimbala *et al.* hesitation in terming the wake patterns a vortex street at all (see figure 1.15).



Exponential decay of Kármán vortex street; circular-cylinder wake at $Re = 140$ (○) and 150 (△).

From Cimbala, Nagib and Roshko (1988)

Figure 1.15

Their technique for flow visualisation (described by Corke *et al.* (1977)) of introducing smoke tracer at different streamwise locations and thereby reducing the integration effect of streaklines, shows the existence of a secondary vortex street (also

noted by Taneda (1959)), far downstream of the body, and appearing after the primary von Kármán vortex street has decayed. It was postulated by Taneda (1959) that the evolution of this secondary vortex street structure in the far wake is due to the changing hydrodynamic stability of the mean wake velocity profile. Gerrard (1966) studied the development of a circular cylinder wake at Re=113. At $\frac{x}{D} = 450$ he found that the fundamental shedding frequency was lost in the background noise, but a lower frequency fluctuation was apparent. The possibility of a secondary vortex street was suggested, but the scale change noted by Gerrard was approximately 30:1 - very different from any other data. Later, Matsui and Okude (1983) proposed the hypothesis that the subharmonic process of vortex pairing was responsible for the observed large structures in the wake. Their conclusions were partly based on flow visualisation data in which the marker emanated solely from the body and was thus susceptible to the streakline integration effect mentioned earlier. Indeed, it would seem that the diverse range of vortex spacing ratios (between secondary and primary streets) from various sets of data (e.g. Taneda: $1.5 \rightarrow 3.5$) lends little credence to this hypothesis, since vortex pairing or amalgamation would require a nearly exact doubling of the longitudinal vortex spacing. In addition, experiments conducted by Cimbala, Nagib and Roshko (1981) show that the von Kármán vortex street decays exponentially fast, and the complete absence of the primary vortex structure prior to the formation of the secondary street in the far wake perhaps confirms that vortex pairing cannot be the structural mechanism for the observed increase in scale of structure there.

An example of the formation of a vortex street as a consequence of a growing wake instability far from the body may be seen for flows past aerofoils at low incidence. Figure 1.16 is a two-dimensional numerical simulation of flow past a symmetric aerofoil at $\alpha = 5°$, $Re = 1000$.

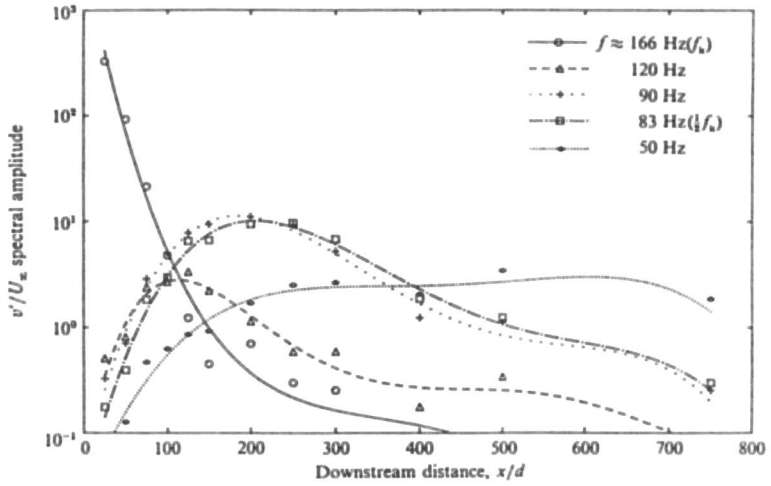


Development of a vortex street from an aerofoil at low incidence

From Giannakidis (1994)

Figure 1.16

Hot-wire velocity measurements in the wake performed by Cimbala *et al.* (1988) show that frequencies in the wake undergo a distinct growth-decay cycle in the laminar regime. Frequencies lower than the fundamental shedding frequency are selectively amplified in the wake, the growth of lower frequencies appearing at greater streamwise distances (figure 1.17).



Growth and decay of selected discrete frequencies: circular-cylinder wake at $Re = 150$.

From Cimbala et al (1988).

Figure 1.17

It is postulated therein that the local growth rates of the frequencies selected for amplification are determined by the local wake profile. The reason for such a rapid decay of the von Kármán vortex street is attributed mainly to viscous diffusion and de-amplification in the sense of hydrodynamic instability. In the context of flow past a cylinder with an imposed in-line progressive wave-train, this begs the question: given that the mean wake velocity profile is in this case no different from that of steady uniform incident flow past a cylinder, what will be the effect of having a finite amplitude forcing function at a certain frequency in the wake? i.e. will the wave cause resonance in the wake at or near its own frequency, and encourage the evolution of structures consistent with the frequency of the wave?

Rearrangement of the wake at higher Reynolds numbers is more difficult to observe due to the presence of three-dimensionality and turbulence in the wake. Cimbala *et al.* (1988) report the existence of a much larger structure (scale change of about a factor of 5) beyond $\frac{x}{D} \approx 200$ for a circular cylinder wake at Re=2200, and 'groups' or 'bursts' of large vortical structures are occasionally evident. Townsend (1966) proposed a growth-decay mechanism of large scale vortices in a high Reynolds number turbulent wake. Essential to this model is the interplay between coherent structures, the small scale turbulence and the mean flow. Large eddies are formed due to the hydrodynamic instability of the mean wake velocity profile; as the eddies grow and entrain irrotational fluid from outside the wake, the level of turbulent intensity at all scales rises; turbulent motions of small scales tend to resist the growth of the large eddies by extracting some of their energy. The large eddies then decay, entrainment is reduced and a period of quiescence is realised. The cycle is then repeated, but over time the wake broadens and the mean wake velocity profile becomes flatter. Hydrodynamic instability of the broadened profile favours amplification of lower

frequencies, and the structures which form at every new cycle are thus increasingly larger.

Townsend (1979) conducted experiments at a Re=8000 using multiple hot-wire arrays and found large structure in the wake at $\frac{x}{D} = 170$; groups of three to five vortical structures were observed, and the time between groups passing a fixed point in space was found to vary considerably. Regions of random fluctuations seemed to lie in between the groups of vortical structure. The formation of large scale eddies in the turbulent wake (also noted by Grant (1958)) spaced between regions of small scale random fluctuations would not register a definite peak in a long time-averaged spectral analysis of the flow - though evidently structure does form from time to time.

Crucial to Townsend's model is the formation of large eddies as a result of the hydrodynamic instability of the mean wake velocity profile *whilst* the small scale random fluctuations are in a state of relative quiescence. Also important is the fact that in a long term (large flow scale period) statistical sense there is generally a one-way energy exchange from large to small scale. The model may be thought of in terms of a modal shift in the fluctuating components of energy; the hydrodynamic instability of the mean wake velocity profile provides the mechanism for the creation of coherent structures (small wavenumber) which cause, via some mechanism, the smaller scales to intensify (for one possible mechanism see section 1.4.2 Vortex Shedding and the Near Wake); energy is now transferred across the wavenumber spectrum to the finer scales. If Townsend's model is correct, it may be possible that the combination of a steady uniform free stream and an in-line progressive wavetrain will result in a preferred amplification or resonance of frequencies at or close to the forcing wave frequency. This may interrupt the large eddy annihilation process and manifest greater periods of large structure realization and shorter periods of

quiescence than in the steady flow case.

A discussion on the physics of the far wake must include the rôle of three-dimensionality. Much work has recently been carried out on the dynamics of three-dimensional vortex dynamics in the far wake, and for a fairly recent review see Williamson (1995). Even for flow past cylinders at low Reynolds numbers (i.e. below the transition region), the importance of three-dimensional structures in the far wake has been appreciated for some time. Gerrard (1966) performed flow visualisation the length of the cylinder and observed slantwise shedding of the spanwise vortices. Cimbala *et al.* (1988) also observed slantwise shedding and noticed it to be quasi-stable, i.e. sometimes the vortices were shed parallel to the cylinder and at other times the vortices were slanted relative to the cylinder. Williamson (1988) reports the existence of 'Chevron' patterns (termed 'an elbow' by Cimbala *et al.*) in which slantwise shedding occurs from the two ends of the cylinder at opposing angles. Cimbala *et al.* (1988) notice a honeycomb type structure in the far wake at a Re=140, $\frac{x}{D} \approx 250$. Williamson (1992) using a special end control technique shows that the formation of the honeycomb structure requires there to be slantwise shedding upstream; he found no such structure for a maintained parallel shedding mode, and concludes that the honeycomb structure is not therefore a manifestation of a parametric subharmonic instability, but is formed through the interaction of the decaying oblique shedding waves from upstream and the large scale two-dimensional waves which grow in the wake. The scale of the honeycomb structure is found to be influenced by the angle of obliqueness of the vortices.

The effects of a combination of a (weak) three-dimensional wave flow and a steady incident flow on the long term development of the wake has not, it is believed, been studied to date. Three-dimensionalities of geometry (e.g. a stepped cylinder: Lewis

and Gharib (1992); tapered cylinder: Gaster (1969), Piccirillo and Van Atta (1993), Papangelou (1992); wavy trailing edge: Tombasis (1993)) have displayed complex wake patterns which include oblique shedding, cellular shedding, and vortex dislocations.

1.4.4 Oscillatory Flows

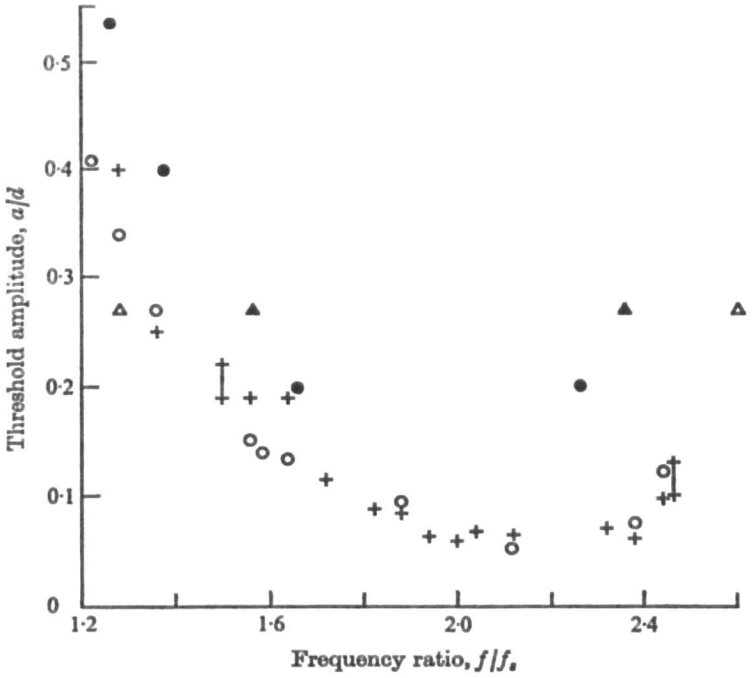
The problem of a cylinder translating into surface gravity waves has much in common, certainly over the near-wake region, with the case of a cylinder translating into a quiescent fluid whilst undergoing in-line oscillations. In the former case of course the incident flow is three-dimensional since the magnitude of the wave induced velocity field decays exponentially with depth. In addition, the former has a spatial phase term for the velocity field which relates to the wavelength of the wave, which is typically many times the scale of the cylinder diameter; the wavelength in the latter case is infinite.

It is principally transverse oscillations that have concerned engineers, since the fluctuating component of the drag term due to vortex shedding is typically an order of magnitude smaller. Bishop and Hassan (1964) investigated the forces on a circular cylinder which was made to oscillate transversely. They found that a range of frequencies exists near to the Strouhal frequency for which the forced transverse oscillations of the body cause the vortex shedding frequency to become synchronised with the body's oscillation frequency. This phenomenon of synchronisation is usually termed "lock-in", and is of great importance in terms of fluid/structure interactions.

For a cylinder in a steady uniform flow the fluctuating component of the drag forces oscillates at twice the Strouhal frequency. As a result of this, the boundary for lock-in is centred around $2f_n$. Griffin and Ramberg (1976) report on the lock-in

BIBL. LONDIN. UNIV.

boundary for an in-line oscillation of a cylinder for a flow at $Re = 190$. Figure 1.18 is a plot of "threshhold amplitude a/d" versus "frequency ratio f/f_s". In their notation d is the cylinder diameter, a the peak-to-peak amplitude of vibration, f the frequency of vibration, and f_s the Strouhal frequency.



Amplitude and frequency regions over which the vibrations of a cylinder control the vortex shedding. Measurements of in-line oscillations near twice the Strouhal frequency ($f \approx 2f_s$). Present study, $Re = 190$: +, oscilloscope comparison; ○, spectral measurements, Tanida *et al.* (1973): ▲, $Re = 80$; △, $Re = 4000$. Tatsuno (1972): ●, $Re = 100$.

From Griffin and Ramberg (1976).

Figure 1.18

The threshold amplitude was determined at a given frequency as the minimum amplitude of motion of the cylinder for which the vortex shedding frequency became synchronised with the cylinder motion.

They also report on the modifications to the wake structure which take place for oscillation parameters within the lock-in boundary. These are of great interest in connection with the work presented here, and some of the photographic plates from Griffin and Ramberg depicting the near-wake structure are presented in conjunction with the present data later in this thesis.

Chapter 2

Vortex Methods

2.1 Introduction

The very rapid advancement of computer hardware technology over the last few decades has led to an inexorable rise in the development, diversity and application of numerical solution techniques in the field of fluid mechanics. In spite of this, solutions to flow problems at high and even moderate engineering Reynolds numbers remain practically impossible to compute due to the phenomenally broad range of spatial and temporal scales evident in these flows. Consider the case of a turbulent flow which is bounded, in a scale sense, by the dimensions of the flow field and the dissipative action of the molecular viscosity. The ratio of the largest length scale L to the smallest length scale l (the Kolmogorov scale) is:

$$\frac{L}{l} = R_t^{3/4} \tag{2.1}$$

where $R_t = uL/\nu$; $u = (\frac{1}{3}\overline{u'^2})^{1/2}$ and u' is the fluctuating velocity. The number of mesh points in one coordinate direction required to resolve all scales is $O(L/l)$, and therefore for a three-dimensional homogeneous turbulence computation the number

of mesh points becomes $O(R_t^{9/4})$. Typically, a Finite Element code (say) might require a total storage of 50 real numbers per node (including mesh overheads), and therefore the total storage for the computation becomes $O(10^2.R_t^{9/4})$. The storage requirements are thus large and rise rapidly with (turbulent) Reynolds number. In fact, it is Spectral methods which are generally used to study low Reynolds number homogeneous turbulence directly, due to the fact that storage requirements are less severe and for smooth functions these methods attain exponential accuracy - i.e. to achieve a given level of accuracy, far fewer degrees of freedom are required than say in a Finite Difference algorithm. Studies of turbulent free shear layers have been carried out by Orszag and Pao (1974); Metcalfe *et al* (1987) have used Spectral methods to study a prototype of three-dimensional instability leading to transition. In many ways the continual gap between requirement and availability of computer resources has been beneficial inasmuch as it has actually reinforced the need for ***physical understanding and insight*** where the problems of complex fluid flow phenomena, such as transition, separation and turbulence are addressed, and has led to the development of new and novel numerical techniques.

The categorisation of the many different methods used in CFD is increasingly difficult, whilst they are essentially application-specific. It is certainly not within the scope of this thesis to present a survey of all numerical methods, and indeed this chapter is only concerned with the methodology of vortex based numerical schemes, particularly with regard to the simulation of flows past bluff bodies. Roach (1972) gives a review of Finite Difference methods and numerical fundamentals; an introduction to the use of Finite Elements in engineering is given by Morgan and Zienkiewicz (1983); the theory and application of Spectral methods are presented by Gottlieb and Orszag (1977), and a later review is given by Canuto, Hussaini, Quarteroni, and Zang (1988); for a review of current algorithmic trends see Hus-

saini, Kumar and Salas (eds.) (1993). Since both Finite Volume and Finite Element techniques are used in conjunction with vortex methods in work presented in this thesis, they are briefly discussed in chapters 4 and 5 respectively.

Vortex methods are fundamentally different from Eulerian methods, such as the Finite Difference, Finite Element, Finite Volume, and Spectral methods [1] mentioned above. Vortex methods are particle methods in which properties of the flow are transported by (topologically) undeformable vortex objects in a Lagrangian frame. Thus, crudely speaking, in Eulerian methods it is the space through which the fluid flows that is discretised, whereas in Lagrangian vortex methods it is the flow structures themselves which are discretised; the former pays no regard to the flow structures which occupy that space (except recently with the use of Adaptive Meshing techniques), whilst the latter pays no regard to the space in between the flow structures.

2.2 Governing Equations of Motion for a Fluid

The momentum equation for an incompressible fluid (omitting body force terms) is given by:

$$\frac{D\vec{u}}{Dt} = \frac{\partial \vec{u}}{\partial t} + (\vec{u} \cdot \nabla)\vec{u} \ = -\frac{1}{\rho}\nabla p + \nu \nabla^2 \vec{u} \tag{2.2}$$

where $\frac{D}{Dt}$ is a total derivative and ν is the fluid kinematic viscosity. The equation system is closed by an equation for the conservation of mass, which in incompressible flows is often termed the incompressibility constraint:

$$\nabla \cdot \vec{u} = 0. \tag{2.3}$$

[1] There are numerical schemes which combine both methods to give a hybrid formulation - these are discussed later in this chapter

The vorticity is defined as:

$$\vec{\omega} = \nabla \wedge \vec{u} \tag{2.4}$$

Taking the curl of equation (2.2) yields an equation for the transport of vorticity:

$$\frac{D\vec{\omega}}{Dt} = \frac{\partial \vec{\omega}}{\partial t} + (\vec{u} \cdot \nabla)\vec{\omega} \quad = \quad (\vec{\omega} \cdot \nabla)\vec{u} + \nu \nabla^2 \vec{\omega}$$

$$\nabla \cdot \vec{u} \quad = \quad 0 \tag{2.5}$$

The term $(\vec{u} \cdot \nabla)\vec{\omega}$ represents the convection of vorticity by the velocity field; the term $(\vec{\omega} \cdot \nabla)\vec{u}$ is known as the vortex stretching or tilting term and represents the deformation of vortex tubes; it is identically zero in two-dimensional flows. The pressure term has disappeared from the equation of motion since the curl of the gradient of any scalar field is zero; it is found, in general, that in primitive variable (i.e. velocity/pressure) formulations, the removal of the pressure term from the vorticity equation is seen as a distinct disadvantage since the computation of the pressure field and subsequent evaluation of body forces requires additional post-processing. Conversely, in vorticity based methods the removal of the pressure term is seen as a clear advantage since the sometimes awkward problem of the stipulation of the pressure boundary condition is automatically circumvented. Additionally, the problem of decoupling between the velocity and pressure fields present in incompressible flows is avoided. However, one might justifiably argue that the stipulation of boundary conditions for vorticity represents at least as formidable an encumbrance to vortex methods, and this particular problem is specifically addressed at a later stage. The purpose of this chapter is not to list the advantages and disadvantages of vorticity based methods next to those of a primitive variable formulation, but, as a final

note, it should be recalled that for incompressible flows the principal quantity of interest is the vorticity; vorticity methods deal directly with this quantity, whereas primitive variable methods must perform a post-analysis reconstruction from the velocity field, whilst incurring an inevitable loss of accuracy due to the relationship between velocity and vorticity which involves spatial gradients. It *is* certain that the vorticity formulation is particularly succinct in two-dimensions. The vorticity vector reduces to a scalar, since only one component of the vorticity is non-zero, i.e. $\vec{\omega} = (0, 0, \omega_z)$. There is therefore only one transport equation to be solved. In addition, if the streamfunction is employed, defined by $u = \frac{\partial \psi}{\partial y}$; $v = -\frac{\partial \psi}{\partial x}$, continuity of mass is guaranteed, and the equations of motion become:

$$\frac{\partial \omega}{\partial t} + \frac{\partial \psi}{\partial y}\frac{\partial \omega}{\partial x} - \frac{\partial \psi}{\partial x}\frac{\partial \omega}{\partial y} = \nu \nabla^2 \omega \tag{2.6}$$

With the streamfunction/vorticity relationship being:

$$\nabla^2 \psi = -\omega \tag{2.7}$$

In three-dimensions the vortex method loses its compactness somewhat as there are now, in general, three components of vorticity to be solved. In addition, the streamfunction cannot be used and there are three kinematic velocity relations to be determined, making six field equations in all. If the curl of equation (2.4) is taken, the following equation is obtained:

$$-\nabla \wedge \nabla \wedge \vec{u} = \nabla^2 \vec{u} - \nabla(\nabla \cdot \vec{u}) = -\nabla \wedge \vec{\omega}. \tag{2.8}$$

Since $\nabla \cdot \vec{u} = 0$, this implies:

$$\nabla^2 \vec{u} = -\nabla \wedge \vec{\omega} \tag{2.9}$$

This Poisson equation for velocity may be integrated to give:

$$\vec{u}(\vec{x},t) = \frac{1}{4\pi} \int\int\int \frac{\vec{\omega}(\vec{x'},t) \wedge (\vec{x} - \vec{x'})}{|(\vec{x} - \vec{x'})|^3} d\vec{x'} \ . \tag{2.10}$$

The potential solution is not included in the above equation. In two-dimensions, equation (2.10) reduces to:

$$u_\theta = \frac{\Gamma}{2\pi|\vec{x} - \vec{x'}|} \quad ; \quad u_r = 0 \tag{2.11}$$

where Γ is the circulation of the vortex at $\vec{x'}$, u_θ is the induced tangential velocity, and u_r the radial velocity. It is a property of the induced velocity field of a point vortex that an integral of the velocity field along any closed contour that includes the vortex is equal to the circulation Γ. Equation (2.10) is analogous to the formula in electromagnetic field theory for the magnetic field intensity induced by an element of electric current, which was found experimentally by Biot and Savart in 1820 and established analytically by Ampère in 1826.

2.3 Inviscid Methods

Helmholtz (1858) was the first to show that in an inviscid fluid vorticity may be represented by vortices of finite circulation and "infinitesimal cross section", i.e. by embedded singularities. Accordingly, in two-dimensional flow, the vorticity field may be modelled as the sum of a set of straight vortex lines, which intersect the analysis plane normally and exist there as a set of points.

$$\omega_z = \sum_{\alpha=1}^{N} \Gamma_\alpha \delta(x - x_\alpha(t))\delta(y - y_\alpha(t)) \tag{2.12}$$

where ω_z is the component of $\vec{\omega}$ in the direction normal to the plane (in this case the x-y plane), Γ_α is the circulation of the point vortex located at $x = x_\alpha$, $y = y_\alpha$ and δ is the Dirac delta function. Employing the complex plane for convenience, the point vortices evolve according to:

$$\dot{z}_\alpha^* = (u - iv)_\alpha = \frac{1}{2\pi i} {\sum_{\beta=1}^{N}}' \Gamma_\beta (z_\alpha - z_\beta)^{-1} \tag{2.13}$$

where the prime denotes $\beta \neq \alpha$, the asterisk denotes complex conjugation, and $z_\alpha = x_\alpha + iy_\alpha$. Following the theorem of Helmholtz, there are no mechanisms whereby the circulations of the point vortices may change and thus $\frac{d\Gamma}{dt} = 0$. Consequently, the flow evolution is determined solely by the *relative* positions of the vortices.

It is known that the equations of point vortices in an unbounded domain define a Hamiltonian system (Kirchoff (1876)). The equations of motion for the point vortices may be cast in the form:

$$\Gamma_\alpha \dot{x}_\alpha = \frac{\partial H}{\partial y_\alpha} \; ; \; \Gamma_\alpha \dot{y}_\alpha = -\frac{\partial H}{\partial x_\alpha} \tag{2.14}$$

$$H = -\frac{1}{4\pi} {\sum_{\alpha,\beta=1}^{N}}' \Gamma_\alpha \Gamma_\beta \, log_e \mid z_\alpha - z_\beta \mid \tag{2.15}$$

H has been termed the "kinetic energy of interaction" by Kraichnan, and is the Hamiltonian. Continuing the particle analogy, there are other integrals of motion which relate to the conservation of linear and angular momenta, and these arise through the invariance of the system to translation and rotation. These results are examples of a more general result known as Noether's theorem which states that for every group of transformations that leave the Lagrangian function invariant, there is an associated conserved quantity.

In general, the three linear invariants for an unbounded fluid are:

$$\begin{aligned} \vec{\Omega} &= \int \vec{\omega} dV \\ \vec{I} &= \frac{1}{2}\int \vec{x} \wedge \vec{\omega} dV \\ \vec{A} &= \frac{1}{2}\int \vec{x} \wedge (\vec{x} \wedge \vec{\omega}) dV \ . \end{aligned} \tag{2.16}$$

There are also two quadratic invariants associated with the conservation of kinetic energy and helicity:

$$\begin{aligned} E &= \frac{1}{2}\int \vec{u}^2 dV \quad = \int (\vec{u} \wedge \vec{x}) \cdot \omega dV \\ He &= \int \vec{u} \cdot \vec{\omega} dV \ . \end{aligned} \tag{2.17}$$

In two-dimensional flows $He = 0$ identically. Enstrophy, defined as $\int \vec{\omega} \cdot \vec{\omega}\ dV$ is a quadratic invariant in two-dimensions, but is not conserved in three-dimensions due

to stretching of vortex lines. In a viscous flow the kinetic energy E is not constant in time, but decays in proportion to the enstrophy (see Batchelor (1967)); linear and angular impulse are conserved.

The classical decomposition of the vorticity field into the sum of a set of embedded singularities (equation (2.12)) represents an exact solution to the two-dimensional Euler equations. Aref (1983) notes that "the point vortices are singularities which are embedded in the flow field itself and solutions produced by the point vortices constitute a 'weak' or 'generalised' solution to the two-dimensional Euler equations. There is apparently no reason that schemes providing a non-singular decomposition should not exist, but so far none has been advanced". Part of the scepticism concerning the use of vortex methods in the simulation of fluid flows is to do with the singular nature of the induced velocity fields and how these singularities are removed or 'smoothed', i.e. although the representation of the vorticity field by a finite set of point vortices is mathematically correct, the numerical implementation is often made unstable by the singular nature of the velocity field in the neighbourhood of the point vortex. Since, for an inviscid flow, there are no physical mechanisms by which the energy of the flow is removed at the small length scales (i.e. there is no viscosity), and whilst for particle/particle calculations there is no artificial diffusion arising from the numerical scheme, inviscid vortex based methods are inherently unstable. An example of this is the calculation of a vortex sheet. A planar vortex sheet is an unstable fluid flow, and infinitesimal disturbances applied to it grow rapidly due to the Kelvin-Helmholtz instability; the growth rate of the disturbances is proportional to the wavenumber (k) of the disturbance and can therefore be arbitrarily large as $k \to \infty$. Asymptotic analyses of Moore (1979) show that singularities form on the vortex sheet at a finite critical time t_c, at which the curvature of the sheet becomes infinite. Immediately after t_c the sheet rolls up into a spiral with an

infinite number of windings and with the diameter of the spiral being zero at t_c. The stability of unsteady two-dimensional vortex sheets is discussed by Moore and Griffith-Jones (1974). Moore shows that a discrete approximation of the sheet using point vortices is also unstable and that the fastest growth rates of the disturbances are associated with the smallest wavelengths (the smallest wavelength in this case is twice the inter-vortex spacing - see chapter 3). It is shown by Moore that increasing the number of vortices (i.e. making a better discrete approximation to the thin shear layer) results in an increase in the growth rate of the disturbances. The problem of vortices approaching closely to one another in simulations and causing numerical instabilities may be made apparent by considering the evolution of a like-signed vortex pair, in which the circulation of each vortex is Γ, and the inter-vortex spacing is a. In an unbounded fluid the pair undergoes a steady rotation about the centroid of circulation. The path of each vortex is a circle of circumference πa, and the time to complete one orbit is $2\pi^2 a^2/\Gamma$. The same pair with inter-vortex spacing λa ($0 < \lambda < 1$ for example) completes an orbit of length $\lambda \pi a$ in time $\lambda^2 2\pi^2 a^2/\Gamma$, i.e. for a system of vortices of the same circulation, a reduction in the inter-vortex spacing leads to a reduction squared in the time scale. The more general result follows from examining the Euler equations:

$$\frac{\partial \vec{u}}{\partial t} + (\vec{u} \cdot \nabla)\vec{u} = -\frac{1}{\rho}\nabla p \tag{2.18}$$

which are invariant under the transformation:

$$x^* \to \lambda x \; ; \; t^* \to \lambda^{1-h} t \; ; \; u^* \to \lambda^h u \quad (\lambda > 0) \tag{2.19}$$

with h arbitrary. Thus in the above example of a vortex pair: $\Gamma^* \to \Gamma \;\Rightarrow \lambda^{h+1} = 1 \; \forall \; \lambda \;\Rightarrow h = -1$, and the variables behave as:

$$x^* \;\; \to \;\; \lambda x$$

$$t^* \rightarrow \lambda^2 t$$
$$u^* \rightarrow \lambda^{-1} u$$

The first instances in the use of vortex methods occurred in the early part of this century; von Kármán (1911) modelled the wake of a circular cylinder by a staggered array of point vortices, and was concerned with the stability of such a configuration. Later, Rosenhead (1931) was actually the first to integrate the paths of point vortices, and his work concerned the instability and roll-up of a discretised vortex sheet. Abernathy and Kronauer (1962) examined the development of two parallel discrete shear layers of opposite sign; it was found that applied disturbances resulted in the formation of opposite signed vortex clouds (i.e. concentrated groups of point vortices). This computation was an example of the Direct Summation method in which the influence of each vortex on every other is computed (see equation (2.10)). One of the problems of this method is that it represents a computational effort that scales as $O(n_v^2)$, where n_v is the number of particles in the computation. If n_v is $O(10^3)$ this is quite manageable on current day Workstation computer architectures, but much beyond this the effort becomes infeasible [2] . An additional problem of the direct summation method, perhaps in terms of the future, is that on parallel architectures it does not numerically scale.

One approach to help alleviate this computational problem of scaling was first employed by Ham (1968), and involves the merging of two or more vortices. By altering the discrete vorticity field in replacing many vortices by few and discarding spatial information, one is clearly rendering an approximation; it is difficult to quantify the effects of such an operation, and numerical experimentation, though arduous, is per-

[2] It should also be remarked that in the summation of a very large number of vortices, the accumulation of machine round off error may come to bear on the solution

haps the only sound way to evaluate the effects. In performing the amalgamation it is normal (see Young (1989)) to preserve as many integrals of motion as is possible, so that the pre- and post-operative vortex systems are, at least in an integral sense, as closely equal as possible. It is customary to replace a group of vortices by a single vortex whose position and strength are given as follows:

$$\Gamma = \sum_{j=1}^{n_v} \Gamma_j \quad ; \quad z = \sum_{j=1}^{n_v} \Gamma_j z_j \; (\sum_{j=1}^{n_v} \Gamma_j)^{-1} \tag{2.20}$$

The position of the resultant vortex is the circulation-weighted centroid of the group of vortices; this ensures preservation of linear momentum [3] , as the above 'interpolation' scheme is itself linear. Also, the pre- and post-operative total circulation is the same. Under this scheme, the post-operative local velocity field may, in general, be very different, but far from the point of amalgamation the velocity field closely approximates that of the original vortex system. This merging or amalgamation technique has been used by a number of authors, including Spalart (1982), who uses it to reduce the computational effort in the simulation of separated flows. The amalgamation of two vortices of opposite sign leads to some noise in the solution.

One of the other inherent numerical problems associated with vortex methods, namely the presence of a singularity in the velocity induction kernel (equation (2.10)), is also ameliorated by this amalgamation technique; by increasing the local inter-vortex spacings, the technique effectively smoothes the local convection velocities. Also, although it is perhaps unwise to promote too far the benefits of what is in essence an ad hoc scheme, the technique may go some way in mimicking the natural process of vortex merging, or vorticity cancellation. In computations involving vortex sheets, it has been recognised that in the roll-up of the tip vortex (say),

[3] compare this with the Cloud-in-Cell interpolation practices presented later in this section

instabilities may develop if the radial distance between arms became similar to the arc lengths between vortices on the same local part of a spiral. A spiral with an infinite number of turns may be better modelled by a single vortex rather than a finite number of vortices.

In addressing this problem of the singularity in the velocity field many other techniques have been developed. All these methods rely on 'spreading' the singularity by de-singularizing either the vortex itself (**blob methods**) or the kernel inside the induction integral (**smoothing schemes**); de-singularization is born of numerical expediency in an attempt to remove instabilities, and the resultant solutions do not strictly represent exact solutions of the hydrodynamic equations.

Moore (1972) uses a smoothing scheme for the calculation of finite amplitude waves on aircraft trailing vortices. For an in-depth review of smoothing schemes see Sarpkaya (1988). A second de-singularization scheme introduced by Chorin and Bernard (1973) replaces the line vortex by a vortex 'blob'. The vortex blob has an invariant core which contains all the vorticity; a finite jump in velocity gradient is imposed, and there is a discontinuity in the gradient of vorticity at the edge of the blob radius, i.e. at $r = \sigma$. The Chorin and Bernard blob is a Rankine vortex, so that:

$$u_\theta = \begin{cases} \frac{\Gamma}{2\pi r} & r > \sigma \\ \frac{\Gamma r}{2\pi\sigma^2} & r \leq \sigma \end{cases} \tag{2.21}$$

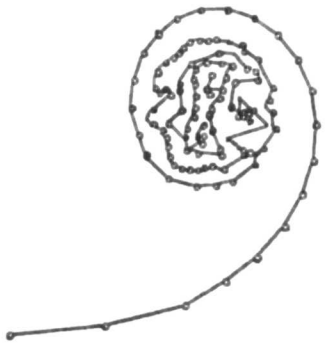
Therefore for $r \leq \sigma$ the velocity induced by this vortex is that of a rigidly rotating fluid core and for $r > \sigma$ the induced velocity is identical to that of a line vortex. The use of vortex blobs to assist in the computation of smooth solutions in (say) the evolution of a vortex sheet is a numerical artifice; Moore (1984) shows that the effects of introducing finite core vortices is to damp the development of short

wavelength waves. Saffman (1992) notes: "The accuracy with which a vorticity field is approximated by a set of in general overlapping, non-deforming circular vortex patches is not a problem of vortex dynamics, since they do not constitute an Euler flow, but is a question of numerical analysis." . The overlapping of vortex patches (necessary to attain smooth distributions of the velocity and vorticity fields) violates Helmholtz's theorem and the laws of the conservation of energy.

Another method which has been employed to reduce numerical instability in computations involving vortex sheets is due to Fink and Soh (1974,1978). It involves the complete rediscretization of the vortex sheet at every time step by a system of point vortices such that the inter-vortex spacing is constant throughout. The vortex strengths are adjusted so that a good representation of the original vorticity density is achieved. This and other methods of the same ilk, such as regridding or redistribution techniques (e.g. Siddiqi (1987)) can retard the effects of the discrete form of the Kelvin-Helmholtz instability (Moore (1984)), but not suppress them altogether. The rediscretization technique still leads to chaotic solutions manifested by unphysical sheet crossings in the vortex sheet problem (see figure 2.1).

As mentioned above, one of the main drawbacks of the Direct Simulation methods is that their computational effort scales as $O(n_v^2)$. Now that both accurate simulations of flows past complex geometries and also three-dimensional simulations are required in order that vortex methods may compete with other solution methods, the number of vortex particles in the computation has begun to rise rapidly, and many researchers have investigated ways to reduce the operation count of such schemes. There are basically two ways in which this has been approached: through the use of a hybrid method, in which interactions between vortex elements are performed on a fixed mesh and the need to solve the Biot-Savart equation is circumvented or

through some decomposition of the induction field into near and far components. The former is discussed in detail later on.



Unphysical sheet crossings

From Baker (1980).

Figure 2.1

The latter approximates the far field from a cluster of vortices, and the **fast multipole method** introduced by Greengard and Rokhlin (1987) uses multipole and Taylor series expansions together with a hierarchical level of computational domain; this method has a computational effort which scales optimally as $O(n_v)$. Sarpkaya (1989) has called this 'pseudomerging', in that the merging of vortices is temporary and fictitious. Anderson's (1986) **method of local corrections** approximates the far-field interactions by solving a Poisson equation over a regular finite difference mesh, whilst calculating the near-field interactions directly.

In two-dimensional computations, the Cloud-in-Cell (CIC) or Vortex-in-Cell (VIC) method is a hybrid scheme in which a Lagrangian description of the vorticity field in the form of point vortices progresses across a fixed Eulerian mesh. The CIC

method has its origins in the particle-in-cell (PIC) methods, which were developed in the 1950's at Los Alamos (Harlow (1964)). The CIC method was used in the study of plasma physics (Eastwood and Hockney (1974)); Christiansen (1973) used the method to study the interaction of vortices, and many authors have since used a viscous version of the method to study the flow past bluff bodies (e.g. Graham (1988), Smith and Stansby (1987)). The CIC method is outlined in some detail here since it is used extensively in work presented in this thesis. The basic idea of the inviscid method is that information is interpolated from a population of particles to mesh points, and *vice versa*. Specifically, the circulation of any particular vortex lying in a computational cell is interpolated onto the mesh nodes that define that cell; once this process has been completed for every vortex, the original point vortex population ($1 \rightarrow n_v$) is effectively replaced by a distribution of point vortices which are coincident with the mesh node locations. The circulation at each node may now be made equivalent to a vorticity value at the node by dividing through by an area pertinent to the node. Once the vorticity field is known, the streamfunction may be evaluated everywhere via a field solution of equation 2.7. The velocity field may then be calculated from the streamfunction, and thus the velocity at each node is known. Velocity information is re-interpolated back to each vortex in the original population, whereupon each is convected over the time step. This interpolation step from particle to mesh node has much in common with the pseudomerging schemes mentioned earlier, in that the transfer of information is temporary and fictitious; the original point vortex population is always retained. The order of the interpolation scheme used in the transfer of information to and fro between particle and mesh determines the 'integral of motion' equivalence between the point vortices and the mesh node vortices. E.g. if the circulation of a point vortex is loaded equally on to the cell nodes whatever its position within that cell, this would be termed a zeroth order interpolation, and the only equivalent integral property is the conservation of

total circulation (e.g. for a four-noded cell $\sum_{j=1}^{4} \Gamma_j = \Gamma_v$); if a linear interpolation method is used the value of the total circulation and the linear momentum of the two vortex systems is identical. It should be noted that point vortices carry the integral quantity of circulation, not vorticity (which is infinite on each point vortex); thus, in the transfer between particle and mesh node it is this quantity which is interpolated. One common type of interpolation of circulation from point vortex to mesh node is shown in figure 2.2; the vorticity deduced from the node circulation in this case is given by:

$$\omega_i = \Gamma_v A_i / (A.A^{(i)}) \qquad i = 1, 2, 3, 4 \tag{2.22}$$

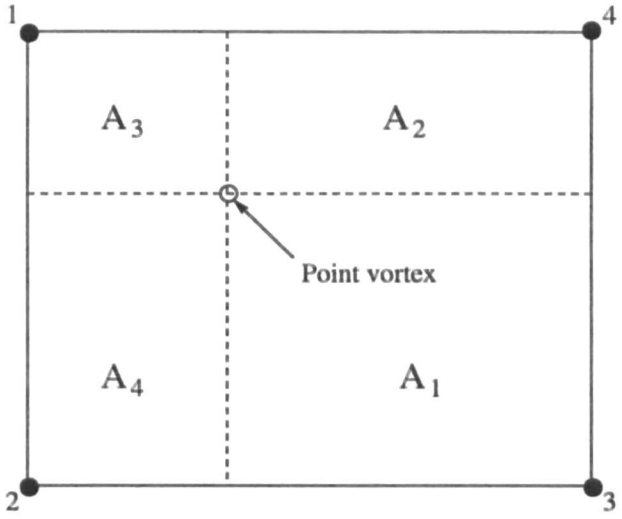
where Γ_v is the circulation of the point vortex, $A^{(i)}$ is an area associated exclusively with node i, and A is the area of the cell. For the special case where all the computational cells or elements are regular and orthogonal $A^{(i)} = A$. (It will be shown later that in the case of integral solution techniques such as Finite Volume and Finite Elements, $A^{(i)}$ is the 'control volume' for node i - the more general case of non-orthogonal, irregular elements is looked at in chapters 4 and 5).

The velocity field for the vortex is calculated from the known velocities at the nodes of the mesh, i.e. :

$$\vec{u}_v = \sum_{i=1}^{4} \vec{u}_i A_i / A \ . \tag{2.23}$$

A single infinite straight line vortex in free space exerts no velocity on itself, therefore the above numerical scheme should yield $\vec{u}_v = 0$ for $n_v = 1$. It may be shown that provided the same weights are applied to the evaluation of the node circulation as are applied in reverse to the node velocities, this condition remains true. The

weights in the above case are A_i/A. From the basic algorithm shown above, it is clear that the CIC method has much in common with other vortex method.



Area weighting scheme

Figure 2.2

Since it may be assumed that the spatial distributions of the nodes in the Eulerian mesh are reasonably smooth, the problem of vortices approaching too close is guaranteed to be avoided. As a point vortex approaches a computational node, the velocity at that node tends to zero rather than infinity. This is because in the mesh solution method the interpolation of the point vortex to surrounding nodes will result in a decreasing amount of circulation at the neighbouring nodes. The conversion from 'nodal' point vortices to a spatial variation of vorticity across the element for the solution to the field equation (Poisson equation for streamfunction) smears the vortex structures, and is reminiscent of the vortex blob method.

The basic advantage of the CIC method is the reduced computational cost: convection of the vortices scales as $O(n_v)$, whilst the velocity solution scales roughly as $O(n \ln n)$, where n are the number of mesh nodes. The Poisson equation is either

solved using a Fast Poisson solver (e.g. Fast Fourier Transform) where this is possible, or by some fast iterative solver such as the Preconditioned Conjugate Gradient Method. The Laplacian operator in the streamfunction equation leads to a symmetric matrix, which is numerically convenient. In practice, it is the mesh solution that dominates the overall computing costs.

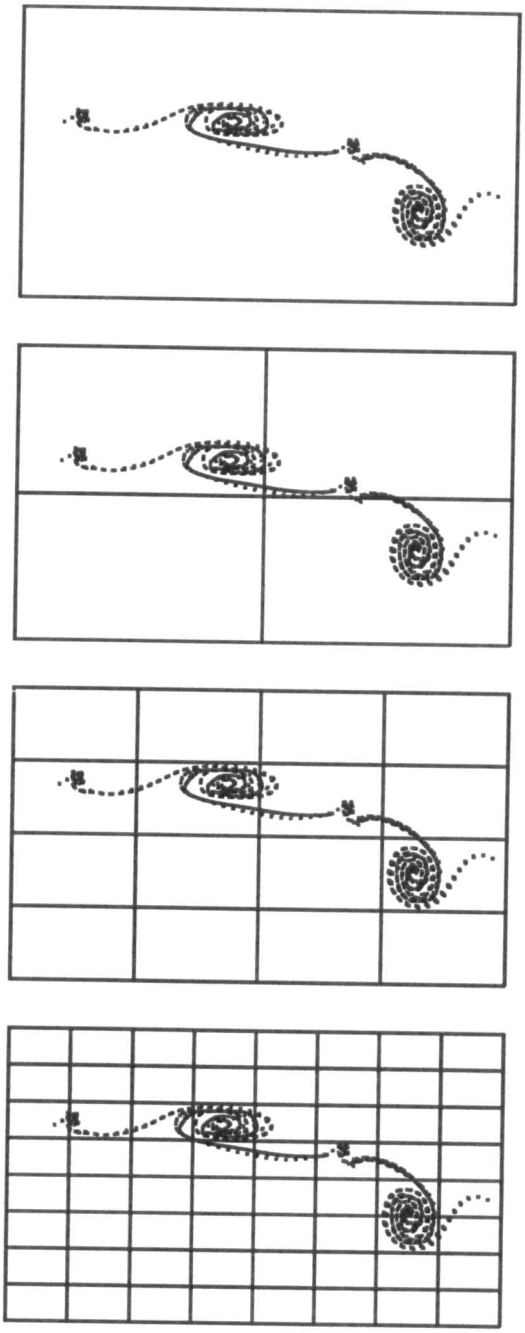
The introduction of a fixed mesh into the overall solution makes the CIC method dependent on the qualities of the mesh. In reality the dependence on the mesh in this case is no different in form to the dependence of other 'grid-free' vortex methods on smoothing parameters, cut-off functions, vortex core sizes, etc... The latter carry the 'mesh' with the particles, and therefore are efficient in that only vortical regions of the flow are considered; the CIC method requires a field solution over all space in determining the velocity field, even though computations relating to the particles themselves are localised. This inherent drawback of the CIC method may be greatly ameliorated by increasing element densities in regions of the mesh where the particles are expected to go, and having a commensurate reduction in the number of elements over purely potential regions, assuming of course, that the potential solution has a weak spatial variation in these regions.

The fusion of Euler and Lagrangian methods in the CIC method was made so that the best characteristics of both methods could be used, namely, the relative computational efficiency of Eulerian methods and the lack of numerical diffusion present in the convection step of Lagrangian methods. The flow past bluff bodies is characterised by the presence of very fine complex vortical structures at a multitude of scales which wander across the spatial domain, and a Lagrangian simulation is very effective in capturing these structures. The calculation of the velocity field at the scale of the element size has the effect of acquiring the same scale of vortical

structure present in the population of vortices within that element, but the important thing is that all other scales are left intact over the convection step. In pure Eulerian methods there is only ever one local scale in the flow, and that is dictated by the element size. Figure 2.3 shows a population of vortices, comprised of many scales, interpolated onto a range of different size elements.

The effect of increasing the element size is to remove from the convection stage more and more of the small scale distortions and local velocity contributions which arise from the small scale vortical structures; since the scale of the effective velocity field applied to them is so much greater than their structure, they move approximately under translation. Thus the effect of interpolating information to the scale of the element is to filter out all incommensurate scales of the flow, whilst the Lagrangian convection step operates on all particles at the scale of the calculated velocity field and therefore preserves all scales of the flow.

Structures smaller than the element size are effectively switched off; if the population of vortices re-enters a region of smaller elements, the smaller vortical structures become active once more. An example where this is useful is the case of oscillating flow past a cylinder in which the fine vortical structures are generated in regions of high element density but are then swept out in to regions of low element density before being drawn back across the cylinder into a dense region of elements.



Interpolation of vortex structure on to differing element sizes

Figure 2.3

In the simulation of three-dimensional inviscid flows, there are basically three types

of vorticity 'object' used: the vortex lattice, the line vortex, and the vortex particle or **vorton** [4] . The first of these has mainly been used in the case of rotating blades, such as the wake of a wind turbine; (e.g. see Simoes (1991), Gould and Fiddes (1992)). Other workers use a set of vortex filaments which emanate from the trailing edge for the simulation of a rotor wake. Some researchers have used three-dimensional vortex particle methods for the simulation of flows past thin aerofoils (Rehbach (1978)) and turbine wakes (Zervos et al (1988)). Vortex ring computations using vortons have also been carried out (e.g. see Sommer (1990)).

2.4 Viscous Methods

In a viscous medium the concept of tracking undeformable Lagrangian vortex objects (e.g. point vortices) becomes strictly invalid, since the creation of vorticity at solid boundaries, and the process of molecular diffusion both violate Helmholtz's theorem of vortex dynamics. Attempts have been made to extend the concept of vortex dynamics to viscous fluid flows, and Ostrikov and Zhmulin (1994) construct a theory of analytic vortex dynamics of an incompressible viscous fluid in two-dimensions on the basis of the product-integral method. Vortex methods were conceived as inviscid methods (i.e. methods which work well as $Re \rightarrow \infty$), and much of their simplicity and elegance is lost in extending them to viscous flows. As noted by Sarpkaya (1994): "The basic idea of every deterministic vortex method is that diffusion is treated as a perturbation: as the viscosity vanishes, the method becomes a vortex method for the Euler equations...".

In viscous vortex methods the transport equation for vorticity may be split into a convection part and a diffusion part; this numerical technique was proposed by Chorin (1973) in connection with his work on 'slightly' viscous flows. The method

[4] Vortons are discussed in depth in chapter 5

is also known as the fractional-step or time-splitting method and is detailed by Marchuk (1971). The transport equation for vorticity (2.5) is split and becomes:

$$\frac{\partial \vec{\omega}}{\partial t} + (\vec{u} \cdot \nabla)\vec{\omega} = 0$$

$$\frac{\partial \vec{\omega}}{\partial t} = (\vec{\omega} \cdot \nabla)\vec{u} + \nu \nabla^2 \vec{\omega} \tag{2.24}$$

The convection is done by particle as detailed in the section on Inviscid Methods. In equation 2.24 the stretching term has been included in the 'diffusion' equation; for three-dimensional flows most authors apply an equation for stretching which modifies the particle's strength, e.g. see Winckelmans (1989).

In two-dimensions the vorticity becomes a scalar and the diffusion equation is equivalent to the classical heat conduction equation. Chorin (1973) introduced the idea of simulating the molecular process of Brownian motion by applying a random walk to the vortices. The random walks of the vortices were random variables from a Gaussian distribution of zero mean and standard deviation equal to $\sqrt{2\nu\Delta t}$. In order to accurately represent the ∇^2 term in the diffusion equation, the number of vortices must be very large, and Stansby et al. (1987) quote the error scaling as $O(\sqrt{\frac{Re}{n_v}})$. Peters (1975) shows that a very large number of particles are required to solve even the one-dimensional heat conduction problem. The extension of random walk methods to three-dimensional computations was carried out by Chorin (1980) and Fishelov (1990). In order to limit the effect of tracking a vast number of particles, Stansby and Dixon (1983) have used the method in conjunction with the CIC method. Smith and Stansby (1988) have studied the impulsively started flow around a circular cylinder over the Reynolds number range of $250 \rightarrow 10000$.

By using the incompressibility constraint, the transport equation for vorticity may be rewritten as:

$$\frac{\partial \omega}{\partial t} + \frac{\partial (u\omega - \nu \frac{\partial \omega}{\partial x})}{\partial x} + \frac{\partial (v\omega - \nu \frac{\partial \omega}{\partial y})}{\partial y} = 0 \tag{2.25}$$

i.e. the convection velocities may have an additional term added to them. This approach, called the "diffusion velocity method" was introduced by Ogami and Akamatsu (1991).

A more common approach to introducing diffusion, and one that perhaps relates more closely to the vortex particle 'ideology', is to assume that the vortices themselves expand in time, and may be represented by for instance a Lamb vortex. A single Lamb vortex in unbounded flow represents an exact analytic solution to the Navier-Stokes equations; Kuwahara and Takami (1973) used this method and studied the rotation of vortex tubes of elliptic and circular section. They noted that the velocity field from a multitude of Lamb vortices does not constitute an exact solution to the Navier-Stokes equations, since the equations are non-linear. Greengard (1985) showed that the idea of an expanding core does not converge to the correct equation of motion. Benson et al (1989) modified the spreading core idea by redistributing the change in vorticity at a certain point in space either to an existing set of particles, and if none existed, by creating new ones, i.e. as each vortex diffused and became spread, the vortex was split into a collection of new vortices, or redistributed to existing ones. The particles were then convected according to the velocity field that existed there.

Graham (1988) introduced a method in which the diffusion equation is solved by finite differences on a fixed mesh. This method was used in conjunction with the CIC

method detailed earlier. Changes to the value of vorticity introduced by diffusion are re-interpolated back to the vortices, so that the method preserves the original vortex population. If a mesh node received no circulation contributions from any vortex, but subsequently a finite value of vorticity exists as a result of diffusion, a new vortex is released from this node. This differs substantially in effect from a method developed by Chang and Chern (1991) in which the original vortex population is entirely replaced by vortices which emanate from the mesh nodes - thus making this method much more akin to a pure finite difference method. Graham's method has been successfully applied by Cozens (1987), Meneghini (1993), and Zhou (1994) in the study of incompressible flow past bluff bodies.

Three-dimensional viscous flow simulations using vortex methods have been relatively scarce. Meiburg and Lasheras (1988) used a continuous vortex filament method to investigate the three-dimensional transition in plane wakes behind flat plates. Doorly and Liu (1995) have studied the interaction of a vortex ring with a solid wall using an extension of the CIC method to three-dimensions; in this case representation of the vorticity field is made by three-dimensional vortex singularities - vortons , and the diffusion of vorticity follows the model developed by Graham. Winckelmans (1989) uses a grid free method also employing vortons to calculate the evolution of vortex rings; the diffusion method used by him is the Particle Strength Exchange (PSE) introduced by Mas-Gallic (1987) (see also Choquin and Huberson (1988)).

Chapter 3

Point Vortex Analysis

3.1 Introduction

As an introduction to understanding the effects of waves on the wake of a circular cylinder, the highly idealised case of an in-line periodic progressive wave-train perturbing an infinite von Kármán point vortex street is modelled.

In this analysis there are three parameters associated with the wave, which are: (a) the wavelength λ_w, (b) the wave angular frequency ω_w, (c) the wave amplitude u_w. The street itself has the parameters U_s - the street self-induced velocity, and a - the inter-vortex spacing. The induced x-velocity field for a sinusoidal wave of frequency f_w travelling in the positive x-direction is given by:

$$\begin{aligned} u(\vec{x},t) &= u_w \cos(\omega_w t - k_w x) \\ \omega_w &= 2\pi f_w \\ k_w &= \frac{2\pi}{\lambda_w} \end{aligned} \tag{3.1}$$

Integration of this equation gives the displacement in the x-direction of a fluid particle, which undergoes oscillations up to $h = u_w/\omega_w = u_w\tau_w/2\pi$ from its mean po-

sition. For the case of planar oscillatory flow (i.e. $k_w = 0$), the parameter $u_w\tau_w/L$, where L is some length scale of a body in the flow, and τ_w the period of the flow, is the Keulegan-Carpenter number (denoted by KC) and it is a measure of the magnitude of displacement of a fluid particle relative to the body scale. In the case of pure planar oscillatory motions, the importance of this non-dimensional quantity [1] in relation to the physics of the vortex formation process and hydrodynamic loading on the body may be easily inferred: at sufficiently low KC the boundary layer is everywhere attached, laminar and stable; as KC is increased the separated shear layers form vortices roughly the size of the body, and some or all of the vorticity may be swept back across the cylinder (wake re-encounter) during the period of the oscillation, leading to a highly complex flow field - for a review of flows around oscillating cylinders see Bearman (1984).

The work presented in this thesis is concerned with the combination of a mean flow and an oscillatory flow, for which the mean component is the larger. Thus the complication of concentrated vorticity sweeping back past the cylinder and interacting with the formation process does not arise. Since the work presented here is concerned with a body scale of D travelling at a speed of U_c through typical deep sea waves of wavelength of $O(10 \rightarrow 100D)$ and height $O(D)$, it is implied that:

$$\begin{aligned} &\frac{u_w}{U_c} < 1 \\ &f_s\tau_w \sim O(1) \quad ; \quad f_s = \frac{U_c}{a} \\ &\frac{u_w\tau_w}{a} < 1 \end{aligned} \tag{3.2}$$

The last non-dimensional term is a 'street' KC, and is a measure of the magnitude of motion of a fluid particle relative to the wake inter-vortex spacing a. The wave amplitudes under consideration here are small.

[1] Flows around an oscillating cylinder are also a function of the Reynolds number $Re = \frac{KCD^2}{\nu\tau}$, where D is the cylinder diameter, ν the kinematic viscosity, and τ the period of oscillation

The analysis presented in this chapter does not include many of the mechanisms that are present in the real flow, for example: (a) the presence of the body and the vortex formation process, (b) finite core vortices and effects of diffusion of vorticity, (c) three-dimensionality of the wave induced velocity field and the vorticity field. However, this basic inviscid model of the wake behind a circular cylinder allows for a parametric study of the effects of the wave field on the vortex dynamics, in that the breaking up of the von Kármán vortex street may be determined as a function of the wave parameters.

In the Introduction (chapter 1), it was postulated that, as far as a two-dimensional analysis goes, there are two mechanisms likely to cause degeneration of the wake in the presence of waves. The first of these is the concertina-like effect of the wave-induced velocity field on the vortex street which forces, over a wave period, a small shifting of the vortices away from their neutrally stable configuration of $\frac{b}{a} = 0.281$. The second mechanism is the variation in vortex strengths in the wake, which it is assumed, represents in general an unstable configuration, even with $\frac{b}{a} = 0.281$. The analysis presented in this chapter begins with an in-line progressive periodic wave-train perturbing a von Kármán vortex street in which the vortex strengths are all equal and differ only by sign in the upper and lower rows. In effect, the variations in shed vortex strength are ignored, and this analysis therefore isolates the 'concertina' effect of the wave on the vortex street. This scenario may be interpreted as the case of a cylinder moving through a quiescent fluid upon which waves subsequently develop downstream of the cylinder.

A theoretical analysis of the departure of the vortices from their initial positions and the subsequent breakup of the vortex street poses particularly difficult prob-

lems. Although equations of motion may be written down for each vortex over a periodic part of the street as a finite sum of the contributions from all other vortices plus an imposed wave term (see the later section on Numerical Analysis), it is not possible to derive (say) a Floquet analysis of this nearly time-periodic system since the coefficients in the equations are not constant, i.e. by writing $\vec{x}(n\tau) = \vec{x}(0)e^{\vec{\sigma}t}$, where n is a positive integer, and substituting into the equations of motion, it is not possible to derive a set of linear equations for $\vec{\sigma}$. However, in the following section a linearised stability analysis (LSA) is presented which examines the growth of infinitesimal disturbances [2] on an infinite vortex street which has undergone a perturbation by a finite (weak) strength wave, and the effects of the wave parameters of wavelength and wave height [3] are recorded. For the purposes of this LSA, it is assumed that the growth terms which are sought are characterised by much smaller time scales than those displayed by the self-induced motions of the diverging wake. Thus we seek the development of short wavelength disturbances on any given wake configuration reached as a result of perturbations quasi-statically imposed by a 'long' wave.

In addition, the equations of motion of the vortex street assuming spatial periodicity are integrated numerically, and the evolution of the street under various wave conditions is presented. The results of this analysis are compared with the predictions of the LSA.

Finally, account of vortex *strength* variation is made via a simple analytic model, and both the linearised stability and numerical analyses of a periodic part of the

[2] In this chapter it should be noted that the word *perturbation* refers to a finite strength wave which is applied to the wake, and the word *disturbance* refers to an infinitesimal wave.

[3] Although this is a two-dimensional analysis in which vertical motions are ignored, the term 'height' is retained here but refers of course to an horizontal amplitude of motion alone.

wake are repeated. In this case the staggered von Kármán vortex street has no spatial perturbation applied, so that the longitudinal inter-vortex spacing is constant throughout the wake. Physically, this case may therefore be interpreted as that of a cylinder translating through a fluid at constant velocity whilst undergoing (weak) in-line oscillations, the assumption of equal longitudinal inter-vortex spacing of course being implied.

The former scenario is referred to as case(A), and the latter as case(B). The part of the analysis which is common to both cases is dealt with in case(A), and therefore this section is somewhat larger than that dealing with case(B).

3.2 Case(A) (Concertina Effect)

3.2.1 Linearised Stability Analysis

Linearised Equations

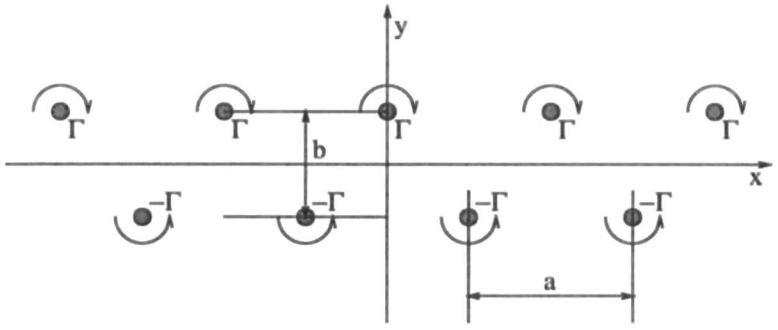
The linearised stability analysis (LSA) of a regular von Kármán vortex street and a double row of vortices symmetric about the x-axis is detailed in Lamb (1932), and later, Kochin *et al* (1964) carried out a higher order analysis of the von Kármán point vortex street.

For the case of a von Kármán vortex street undergoing in-line progressive wave motions, it is expected that the vortices interact non-linearly with each other and that over a certain period of time the structure of the street is lost, the wake going on to degenerate rapidly. In the following analysis, the case of a von Kármán vortex street which has been perturbed [4] by a finite (weak) wave is considered, and the sus-

[4]The perturbation is considered to apply instantaneously such that there exists no history of interaction between the vortices.

ceptibility of the resulting street to infinitesimal disturbances is examined. It should be stressed at this stage that there are essentially three mechanisms of motion associated with the vortices in the street: (a) the self-induced velocity field, (b) the 'external' velocity field of the imposed perturbing wave, (c) the movement of vortices due to amplification of infinitesimal disturbances. The first of these may be decomposed into a steady and unsteady component; the steady term is the translational self-induced velocity of the street, whilst the unsteady term comes about through the action of (b) displacing the vortices in the street; these terms are discussed later on in this analysis. Although mechanism (b) may be thought of as the forcing term which drives the wake, the relative importance of mechanism (c) is linked to (a), inasmuch as the growth rates of the disturbances are likely to be a function of the vortex positions and associated induced velocity fields.

Consider the unperturbed infinite von Kármán vortex street:



The von Kármán vortex street

Figure 3.1

At the instant shown, the coordinates of the vortices in the top row are:

$$(ma, \frac{b}{2}) \quad m = 0, \pm 1, \pm 2, ... \tag{3.3}$$

and in the lower row are:

$$(pa, -\frac{b}{2}) \quad p = \pm\frac{1}{2}, \pm\frac{3}{2}, ... \tag{3.4}$$

If this system of vortices has an in-line wave-like perturbation applied to it instantaneously, the coordinates become:

$$(ma - h\sin(mk_w + \varepsilon), \frac{b}{2}) \quad m = 0, \pm 1, \pm 2, ... \tag{3.5}$$

$$(pa - h\sin(pk_w + \varepsilon), -\frac{b}{2}) \quad p = \pm\frac{1}{2}, \pm\frac{3}{2}, ... \tag{3.6}$$

This perturbation away from the von Kármán vortex street results from considering the integration over a given time of the type of velocity equation for a fluid particle given by (3.1), i.e. $h \equiv u_w/\omega_w$ (amplitude term), $\varepsilon \equiv -\omega_w t$ (phase term), and $k_w \equiv 2\pi a/\lambda_w$ is the non-dimensional wavenumber of the wave. Although the following analysis will, for the sake of simplicity, examine the behaviour of the zeroth vortex (i.e. top row $m = 0$), it will be shown that the rate of growth or decay of a disturbance of a particular vortex will depend on its position relative to the perturbing wave, i.e. the rate of growth or decay of disturbances varies spatially and is periodic over the imposed periodicity of the applied wave. Thus the rôle of the phase term ε is to accommodate analysis for *all* vortices at any position in the wave, or indeed, to consider the instantaneous stability of any one vortex during all instants of time over the wave period.

If an infinitesimal disturbance is added, the nature of which is to be prescribed at a later stage, the coordinates of each vortex become, finally:

$$(\delta x_m + ma - h\sin(mk_w + \varepsilon), \delta y_m + \frac{b}{2}) \quad m = 0, \pm 1, \pm 2, ...$$

$$(\delta x_p + pa - h\sin(pk_w + \varepsilon), \delta y_p - \frac{b}{2}) \quad p = \pm\frac{1}{2}, \pm\frac{3}{2}, ... \tag{3.7}$$

It may be seen that for the case $k_w = 0$ (i.e. pure planar oscillatory perturbations) all vortices are shifted by a constant $h\sin\varepsilon$ from their integer positions. Since for the general case the equations of motion are to be written for the zeroth vortex at which the origin of the axes is based, all vortices are translated by a constant amount $h\sin\varepsilon \ll \lambda_w$.

After displacement by a wave the contributions from vortices in the m-row to the velocity of the zeroth vortex are:

$$\frac{d(\delta x_0)}{dt} = \frac{\Gamma}{2\pi}\sum_m \frac{\delta y_0 - \delta y_m}{r_m^2}$$

$$\frac{d(\delta y_0)}{dt} = -\frac{\Gamma}{2\pi}\sum_m \frac{\delta x_0 - \delta x_m - ma + h\sin(mk_w + \varepsilon) - h\sin(\varepsilon)}{r_m^2}$$

$$m = \pm 1, \pm 2, ... \tag{3.8}$$

Where,

$$r_m^2 = (\delta x_0 - \delta x_m - ma + h\sin(mk_w + \varepsilon) - h\sin\varepsilon)^2 + (\delta y_0 - \delta y_m)^2 \tag{3.9}$$

Neglecting products of the disturbances gives:

$$r_m^2 = (ma - h\sin(mk_w + \varepsilon) + h\sin\varepsilon)^2 - 2(\delta x_0 - \delta x_m)(ma - h\sin(mk_w + \varepsilon) + h\sin\varepsilon) \tag{3.10}$$

Upon substitution, the contributions from the m-row to the equations of motion for the zeroth vortex are:

$$\frac{d(\delta x_0)}{dt} = \frac{\Gamma}{2\pi a^2}\sum_m \frac{\delta y_0 - \delta y_m}{m^2} + \frac{\Gamma h}{\pi a^3}\sum_m \frac{(\delta y_0 - \delta y_m)(\sin(mk_w+\varepsilon) - \sin\varepsilon)}{m^3}$$

$$\frac{d(\delta y_0)}{dt} = \frac{\Gamma}{2\pi a^2}\sum_m \frac{\delta x_0 - \delta x_m}{m^2} + \frac{\Gamma h}{\pi a^3}\sum_m \frac{(\delta x_0 - \delta x_m)(\sin(mk_w+\varepsilon) - \sin\varepsilon)}{m^3}$$

$$+\frac{\Gamma h}{2\pi a^2}\sum_m \frac{\sin(mk_w+\varepsilon) - \sin\varepsilon}{m^2} -$$

$$\frac{\Gamma h^2}{2\pi a^3}\sum_m \frac{(\sin(mk_w+\varepsilon) - \sin\varepsilon)^2}{m^3} +$$

$$m = \pm 1, \pm 2, ... \qquad (3.11)$$

There are terms in the y-component equation independent of the disturbance which are anti-symmetric about the origin, and thus if the sum is taken over pairs equidistant from the zeroth vortex, these terms tend to zero; the only disturbance-independent term remaining (to these orders of magnitude) is the third term on the RHS of the equation for δy_0. The x-component equation has no terms independent of the disturbance. Terms of $O(\delta x_m h^2)$ or $O(\delta y_m \frac{h}{a}^2)$ are neglected, as are terms of $O(\frac{h}{a}^3)$ - implying that the applied perturbation is weak. The leading terms in the expansions which involve the wave and are dependent on the disturbance are of $O(\delta x_m h)$ or $O(\delta y_m h)$, and are retained. The equations thus have a formal error of $O(\delta x_m^2, \delta y_m^2, \delta x_m \frac{h}{a}^2, \delta y_m \frac{h}{a}^2, \frac{h}{a}^3)$.

The contributions from the p-row to the velocity of the zeroth vortex are:

$$\frac{d(\delta x_0)}{dt} = -\frac{\Gamma}{2\pi}\sum_p \frac{\delta y_0 - \delta y_p + b}{r_p^2}$$

$$\frac{d(\delta y_0)}{dt} = \frac{\Gamma}{2\pi}\sum_m \frac{\delta x_0 - \delta x_p - pa + h\sin(pk_w + \varepsilon) - h\sin\varepsilon}{r_p^2}$$

$$p = \pm\frac{1}{2}, \pm\frac{3}{2}, \ldots \tag{3.12}$$

where,

$$r_p^2 = (\delta x_0 - \delta x_p - pa + h\sin(pk_w + \varepsilon) - h\sin\varepsilon)^2 + (\delta y_0 - \delta y_p + b)^2 \tag{3.13}$$

Neglecting products of the disturbances gives:

$$\begin{aligned} r_p^2 \;=\; & (pa - h\sin(pk_w + \varepsilon) + h\sin\varepsilon)^2 + b^2 - \\ & 2(\delta x_0 - \delta x_p)(pa - h\sin(pk_w + \varepsilon) + h\sin\varepsilon) + \\ & +2(\delta y_0 - \delta y_p)b \end{aligned} \tag{3.14}$$

Substituting $d = \frac{b}{a}$, and after some reduction, the complete equations of motion for the zeroth vortex including the displacement-independent terms are:

$$\begin{aligned} \frac{d(\delta x_0)}{dt} \;=\; & \frac{\Gamma}{2\pi a^2}\sum_m \frac{\delta y_0 - \delta y_m}{m^2} + \frac{\Gamma h}{\pi a^3}\sum_m \frac{(\delta y_0 - \delta y_m)(\sin(mk_w + \varepsilon) - \sin(\varepsilon))}{m^3} \\ & -\frac{\Gamma}{2\pi a^2}\sum_p \frac{(p^2 - d^2)(\delta y_0 - \delta y_p)}{(p^2 + d^2)^2} - \frac{\Gamma}{\pi a^2}\sum_p \frac{pd(\delta x_0 - \delta x_p)}{(p^2 + d^2)^2} - \\ & \frac{\Gamma h}{\pi a^3}\sum_p \frac{p(\delta y_0 - \delta y_p)(\sin(pk_w + \varepsilon) - \sin\varepsilon)}{(p^2 + d^2)^2} + \end{aligned}$$

$$\frac{4\Gamma h}{\pi a^3}\sum_p \frac{pd^2(\delta y_0-\delta y_p)(\sin(pk_w+\varepsilon)-\sin\varepsilon)}{(p^2+d^2)^3}+$$

$$\frac{\Gamma h}{\pi a^3}\sum_p \frac{d(\delta x_0-\delta x_p)(\sin(pk_w+\varepsilon)-\sin\varepsilon)}{(p^2+d^2)^2}-$$

$$\frac{4\Gamma h}{\pi a^3}\sum_p \frac{p^2d(\delta x_0-\delta x_p)(\sin(pk_w+\varepsilon)-\sin\varepsilon)}{(p^2+d^2)^3}-$$

$$\frac{\Gamma}{2\pi a}\sum_p \frac{d}{p^2+d^2}-\frac{\Gamma h}{\pi a^2}\sum_p \frac{pd(\sin(pk_w+\varepsilon)-\sin\varepsilon)}{(p^2+d^2)^2}+$$

$$\frac{\Gamma h^2}{2\pi a^3}\sum_p \frac{d(\sin(pk_w+\varepsilon)-\sin\varepsilon)^2}{(p^2+d^2)^2}-$$

$$\frac{2\Gamma h^2}{\pi a^3}\sum_p \frac{p^2d(\sin(pk_w+\varepsilon)-\sin\varepsilon)^2}{(p^2+d^2)^3}$$

$$\frac{d(\delta y_0)}{dt} = \frac{\Gamma}{2\pi a^2}\sum_m \frac{\delta x_0-\delta x_m}{m^2}+\frac{\Gamma h}{\pi a^3}\sum_m \frac{(\delta x_0-\delta x_m)(\sin(mk_w+\varepsilon)-\sin\varepsilon)}{m^3}+$$

$$\frac{\Gamma}{\pi a^2}\sum_p \frac{pd(\delta y_0-\delta y_p)}{(p^2+d^2)^2}-\frac{\Gamma}{2\pi a^2}\sum_p \frac{(p^2-d^2)(\delta x_0-\delta x_p)}{(p^2+d^2)^2}+$$

$$\frac{3\Gamma h}{\pi a^3}\sum_p \frac{pd(\delta x_0-\delta x_p)(\sin(pk_w+\varepsilon)-\sin\varepsilon)}{(p^2+d^2)^2}-$$

$$\frac{4\Gamma h}{\pi a^3}\sum_p \frac{p^3(\delta x_0-\delta x_p)(\sin(pk_w+\varepsilon)-\sin\varepsilon)}{(p^2+d^2)^3}-$$

$$\frac{\Gamma h}{\pi a^3}\sum_p \frac{d(\delta y_0-\delta y_p)(\sin(pk_w+\varepsilon)-\sin\varepsilon)}{(p^2+d^2)^2}+$$

$$\frac{4\Gamma h}{\pi a^3}\sum_p \frac{p^2 d(\delta y_0 - \delta y_p)(\sin(pk_w+\varepsilon)-\sin\varepsilon)}{(p^2+d^2)^3} +$$

$$\frac{\Gamma h}{2\pi a^2}\sum_m \frac{\sin(mk_w+\varepsilon)-\sin\varepsilon}{m^2} -$$

$$\frac{\Gamma h^2}{2\pi a^3}\sum_m \frac{(\sin(mk_w+\varepsilon)-\sin\varepsilon)^2}{m^3} -$$

$$\frac{\Gamma h}{\pi a^2}\sum_p \frac{(p^2-d^2)(\sin(pk_w+\varepsilon)-\sin\varepsilon)}{(p^2+d^2)^2} +$$

$$\frac{3\Gamma h^2}{2\pi a^3}\sum_p \frac{p(\sin(pk_w+\varepsilon)-\sin\varepsilon)^2}{(p^2+d^2)^2} -$$

$$\frac{4\Gamma h^2}{2\pi a^3}\sum_p \frac{p^3(\sin(pk_w+\varepsilon)-\sin\varepsilon)^2}{(p^2+d^2)^3}$$

$$m = \pm 1, \pm 2, \ldots \quad p = \pm\frac{1}{2}, \pm\frac{3}{2}, \ldots \tag{3.15}$$

The 9^{th} term on the RHS of the x-component equation is independent of both the disturbance and the wave; it represents the steady translational component of the vortex street on itself. Without loss of generality this term may be removed by adopting an axis system that translates to the left at this self-induced speed. If this is done, the only point of note is that the applied wave undergoes a Doppler shift, with the wave celerity changing to: $c = c_0 + U_s$, where c_0 is the celerity of the wave in the original system, and U_s is the self- induced velocity of the street. Note that $U_s \ll c_0$. This change may be incorporated into the phase term ε, which is a measure of (angular encounter frequency)$\times$(time). However, for the rest of this analysis, the nomenclature remains the same. Note that for $h = 0$ or $k_w = 0$, the equations for a regular von Kármán vortex street are recovered (see Lamb (1932)).

Consider now an infinitesimal disturbance of the type:

$$\begin{aligned} \delta x_m &= \alpha_u(t)e^{imk_d} \\ \delta y_m &= \beta_u(t)e^{imk_d} \\ \delta x_p &= \alpha_l(t)e^{ipk_d} \\ \delta y_p &= \beta_l(t)e^{ipk_d} \end{aligned} \tag{3.16}$$

where k_d is the non-dimensional wavenumber of the disturbance, i.e. $k_d = \frac{2\pi a}{\lambda_d}$. which is applied to the street. This disturbance may arise from any noise or deviation from the exact conditions in the flow. Substitution of equation (3.16) into (3.15) leads to a set of coupled first order ordinary differential equations for α_u and β_u:

$$\begin{aligned} \frac{2\pi a^2}{\Gamma}\frac{d\alpha_u}{dt} &= A\alpha_u + B\beta_u + C\alpha_l + D\beta_l + I_1 \\ \frac{2\pi a^2}{\Gamma}\frac{d\beta_u}{dt} &= B\alpha_u - A\beta_u + D\alpha_l - C\beta_l + I_2 \end{aligned} \tag{3.17}$$

Where the I_1 and I_2 are the independent terms and the coefficients A B C and D are:

$$\begin{aligned} A = {} & \frac{2h}{a}\sin\varepsilon\sum_p \frac{d\cos pk_w}{(p^2+d^2)^2} - \frac{2h}{a}\sin\varepsilon\sum_p \frac{d}{(p^2+d^2)^2} - \\ & \frac{8h}{a}\sin\varepsilon\sum_p \frac{p^2 d\cos pk_w}{(p^2+d^2)^3} + \frac{8h}{a}\sin\varepsilon\sum_p \frac{p^2 d}{(p^2+d^2)^3} \end{aligned}$$

$$B = \sum_m \frac{1}{m^2} - \sum_m \frac{\cos mk_d}{m^2} + \frac{2h}{a}\cos\varepsilon\sum_m \frac{\sin mk_w}{m^3} -$$

$$\frac{2h}{a}\cos\varepsilon\sum_m \frac{\sin mk_w \cos mk_d \sin mk_d}{m^3} - \frac{2ih}{a}\sin\varepsilon\sum_m \frac{\cos mk_w \sin mk_d}{m^3} +$$

$$\frac{2ih}{a}\sin\varepsilon\sum_m \frac{\sin mk_d}{m^3} - \sum_p \frac{p^2-d^2}{(p^2+d^2)^2} -$$

$$\frac{2h}{a}\cos\varepsilon\sum_p \frac{p\sin pk_w}{(p^2+d^2)^2} + \frac{8h}{a}\cos\varepsilon\sum_p \frac{pd^2\sin pk_w}{(p^2+d^2)^3}$$

$$C = 2i\sum_p \frac{pd\sin pk_d}{(p^2+d^2)^2} - \frac{2ih}{a}\cos\varepsilon\sum_p \frac{d\sin pk_w \sin pk_d}{(p^2+d^2)^2} -$$

$$\frac{2h}{a}\sin\varepsilon\sum_p \frac{d\cos pk_w \cos pk_d}{(p^2+d^2)^2} + \frac{2h}{a}\sin\varepsilon\sum_p \frac{d\cos pk_d}{(p^2+d^2)^2} +$$

$$\frac{8ih}{a}\cos\varepsilon\sum_p \frac{p^2 d\sin pk_w \sin pk_d}{(p^2+d^2)^3} + \frac{8h}{a}\sin\varepsilon\sum_p \frac{p^2 d\cos pk_w \cos pk_d}{(p^2+d^2)^3} -$$

$$\frac{8h}{a}\sin\varepsilon\sum_p \frac{p^2 d\cos pk_w}{(p^2+d^2)^3}$$

$$D = \sum_p \frac{(p^2-d^2)\cos pk_d}{(p^2+d^2)^2} + \frac{2h}{a}\cos\varepsilon\sum_p \frac{p\sin pk_w \cos pk_d}{(p^2+d^2)^2} +$$

$$\frac{2ih}{a}\sin\varepsilon\sum_p \frac{p\cos pk_w \cos pk_d}{(p^2+d^2)^2} - \frac{2ih}{a}\sin\varepsilon\sum_p \frac{p\sin pk_d}{(p^2+d^2)^2} -$$

$$\frac{8h}{a}\cos\varepsilon\sum_p \frac{pd^2\sin pk_w \cos pk_d}{(p^2+d^2)^3} - \frac{8ih}{a}\sin\varepsilon\sum_p \frac{pd^2\cos pk_w \sin pk_d}{(p^2+d^2)^3} +$$

$$\frac{8ih}{a}\sin\varepsilon\sum_p \frac{pd^2\sin pk_d}{(p^2+d^2)^3}$$

$$m = \pm 1, \pm 2, \ldots \quad p = \pm\frac{1}{2}, \pm\frac{3}{2}, \ldots \tag{3.18}$$

The doubly infinite sums in the coefficients A B C and D may be expressed in terms of hyperbolic sines and cosines (see Appendix A).

Similar equations for the lower row may be derived by reversing the signs of Γ and d, whilst interchanging the indices m and p:

$$\begin{aligned} \frac{2\pi a^2}{\Gamma}\frac{d\alpha_l}{dt} &= A\alpha_l - B\beta_l + C\alpha_u - D\beta_u + I_1 \\ \frac{2\pi a^2}{\Gamma}\frac{d\beta_l}{dt} &= -B\alpha_l - A\beta_l - D\alpha_u - C\beta_u - I_2 \end{aligned} \tag{3.19}$$

In generating these equations from those of the upper row it is necessary that $\lambda_w \gg a/2$. The solution to these 1^{st} order ODE's for $(\alpha_u, \beta_u, \alpha_l, \beta_l)$ have complementary functions (derived from the homogeneous set with $I_1 = I_2 = 0$), and particular integrals. The complementary functions admit solutions of the form:

$$\alpha_u = \alpha_l; \quad \beta_u = -\beta_l \tag{3.20}$$

and:

$$\alpha_u = -\alpha_l; \quad \beta_u = \beta_l \tag{3.21}$$

The first of these represents a symmetric disturbance, and the second an anti-symmetric disturbance to the two vortex rows. For the symmetric disturbance case,

we have:

$$\begin{aligned} \frac{2\pi a^2}{\Gamma}\frac{d\alpha_u}{dt} &= (A+C)\alpha_u + (B-D)\beta_u + I_1 \\ \frac{2\pi a^2}{\Gamma}\frac{d\beta_u}{dt} &= (B+D)\alpha_u + (C-A)\beta_u + I_2 \end{aligned} \tag{3.22}$$

Assuming that the coefficients A B C D are approximately constant over the pertinent time scales, i.e. this analysis is at a given time, and $\frac{\partial(I_1,I_2)}{\partial t} \approx 0$, a second order ODE may be derived from these two coupled equations, and substituting for the complementary function the form $\alpha_u = \hat{\alpha}e^{\hat{\sigma}t}$ etc., the values of $\hat{\sigma}$ are given by:

$$\frac{2\pi a^2}{\Gamma}\hat{\sigma} = C \pm (A^2 + B^2 - D^2)^{\frac{1}{2}} \tag{3.23}$$

for the symmetric disturbance, and:

$$\frac{2\pi a^2}{\Gamma}\hat{\sigma} = -C \pm (A^2 + B^2 - D^2)^{\frac{1}{2}} \tag{3.24}$$

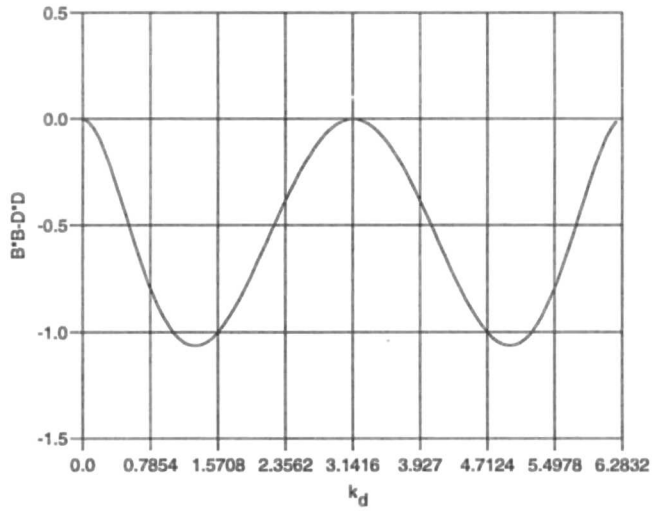
for the anti-symmetric disturbance.

Results

In equations (3.23) and (3.24) of the previous subsection, it is found that there is always a root with $\Re(\hat{\sigma}) > 0$ for all admissible values of k_w, k_d and h, and thus the perturbed street is *unstable* to infinitesimal disturbances. This concurs with the point made in chapter 1, which follows from arguments put forward by Christiansen and Zabusky (1973). The disturbances eventually grow in proportion to $e^{\hat{\sigma}t}$, with the constant of proportionality being a function of the level of disturbance present

at time t.

If $h = 0$ or $k_w = 0$ the case of the unperturbed von Kármán vortex street is recovered, and it may be shown (see Lamb (1932)) that this configuration is neutrally stable to all values of k_d for a street spacing ratio of $d = 0.281$. Figure 3.2 is a plot of $(B^2 - D^2)$ for this configuration ($A^2 = 0$ and C is pure imaginary in this case):



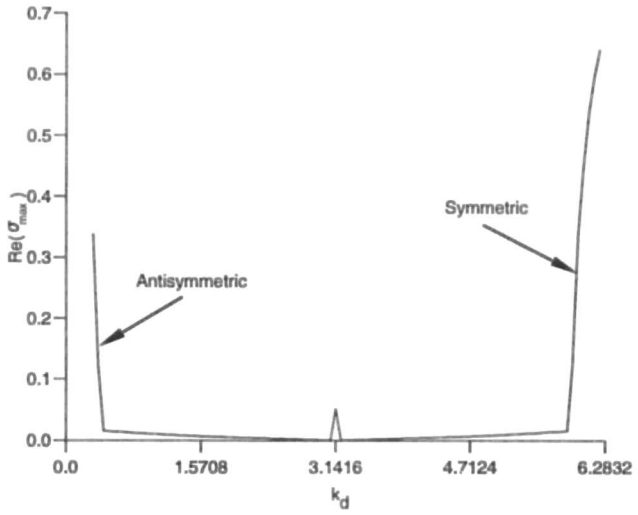
$B^2 - D^2$ for von Kármán vortex street.

Neutral stability points at $k_d = 0, \pi, 2\pi$.

Figure 3.2

Figure 3.3 is a plot of $\Re(\sigma_{max})$, where $\sigma = \frac{2\pi a^2}{\Gamma}\hat{\sigma}$, versus disturbance wavenumber for the case $h/a = 0.05$ and $\lambda_w = 20a$. (Here ε ranges over 0 to 2π, and the maximum σ over this range is selected). The wavelength of the disturbance which is plotted ranges from a - the shortest lengthscale in the domain - to λ_w. The upper bound of λ_d for which the analysis is valid is dictated by the previously stated assumptions concerning the time scales of the disturbance, which should be short by comparison with the period of the imposed wave.

Figure 3.3 shows which of the modes is dominant over the range of disturbance wavenumber, i.e. the antisymmetric mode σ is larger for $k_d < \frac{\pi}{7}$, and the symmetric mode σ is larger for $k_d > 1.85\pi$. In between this range, the antisymmetric and symmetric values of $\Re(\sigma_{max})$ are identical.



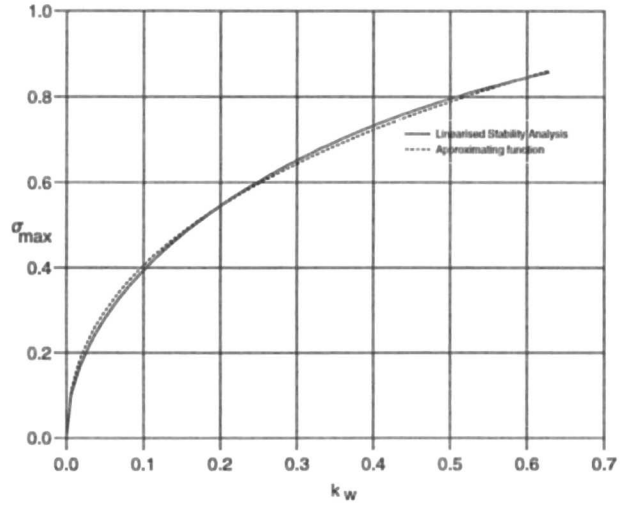
Variation of $\Re(\sigma_{max})$ versus k_d; $h/a = 0.05$ and $\lambda_w = 20a$.

Figure 3.3

The σ_{max} curve is fairly flat over k_d except at three points: (a) $\lambda_d = \lambda_w$; (b) $\lambda_d = 2a$; (c) $\lambda_d = a$, with the fastest growth rate occurring at the shortest wavelength of $\lambda_d = a$. These points coincide with the three neutral points of the unperturbed street result, and pretty much concur with expectations if we consider the induced velocities for a particular vortex in (say) the upper row: for the case of $\lambda_d = a$ all vortices in the upper row move in-phase and the inter-vortex spacing is constant in the x-direction; thus the wave produces no effect here, whilst in the lower row the vortices experience a shift relative to the vortex in the upper row (being a longitudinal distance of $a/2$ from that vortex). For the case of $\lambda_d = 2a$ the

same is true, but in reverse, i.e. the two nearest vortices in the upper row experience maximum displacement, whilst those in the lower row maintain a constant longitudinal inter-vortex spacing. The above argument depends of course on the relative phase between the wave and the vortices. The large value of σ_{max} near to $\lambda_d = \lambda_w$ is probably a result of resonance between the two waves, with the imposed wave helping to amplify the disturbance, but not too much relevance should be placed on this particular result, since, strictly speaking, λ_d is outside the bounds of validity here.

The variation of $\Re(\sigma_{max})$ versus wavenumber of the perturbation wave is shown in figure 3.4. For this case $h = 0.05a$. Note that for $k_w = 0$, $\Re(\sigma_{max}) = 0$. The range of wavenumber gives an equivalent range of wavelength of between $10a$ and ∞.



Variation of $\Re(\sigma_{max})$ versus k_w.

Figure 3.4

Also on this plot, a curve is fitted (f_1) which approximates the result of the LSA.

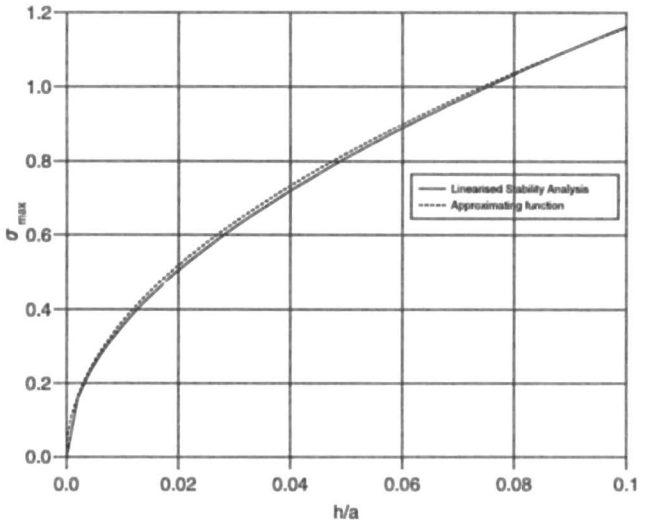
The equation of the curve is:

$$f_1(k_w) \propto \ln(1 + \sqrt{k_w}) \tag{3.25}$$

From the LSA the growth of disturbances is proportional to $e^{\Re(\tilde{\sigma})t}$, and therefore $f_1(k_w)$ implies that the initial growth of disturbances is approximately proportional to $\frac{1}{\sqrt{\lambda_w}}$. The effect of increasing the wavelength of the applied wave produces a smaller change in the inter-vortex spacing; it is therefore consistent that longer wavelength waves result in a weaker growth of disturbances in the wake.

Figure 3.5 is a plot of the variation of $\Re(\sigma_{max})$ versus wave height. Again, a curve is fitted (f_2) to the data, the equation of which is:

$$f_2\left(\frac{h}{a}\right) \propto \sqrt{\frac{h}{a}} \tag{3.26}$$



Variation of $\Re(\sigma_{max})$ versus $\frac{h}{a}$.

Figure 3.5

The agreement between the LSA result and the function $f_2(\frac{h}{a})$ is good. The function

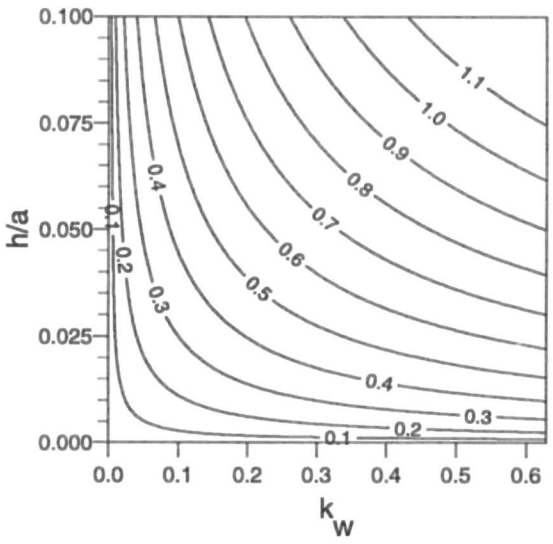
$f_2(\frac{h}{a})$ implies that, for weak waves, the initial growth of disturbances is approximately proportional to $\sqrt{\frac{h}{a}}$. If it is assumed that $\Re(\sigma_{max})$ from the LSA may be approximated by a composite function:

$$f_3(k_w, \frac{h}{a}) = f_1(k_w) f_2(\frac{h}{a}) \tag{3.27}$$

this implies that:

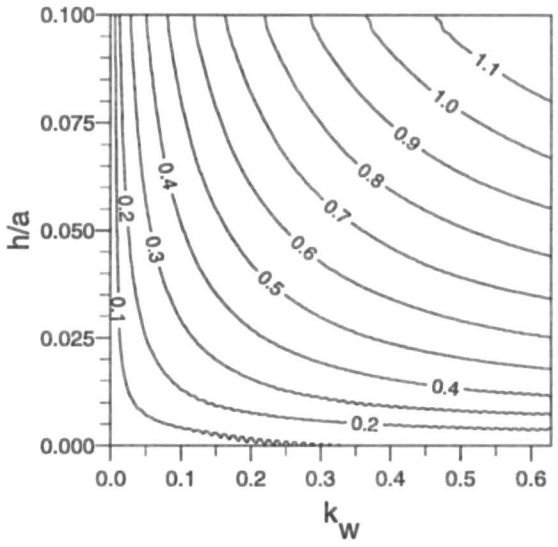
$$Re(\sigma_{max}) \propto \ln(1 + \sqrt{k_w}) \sqrt{\frac{h}{a}} \tag{3.28}$$

Figure 3.6 shows a contour plot of $f_3(k_w, \frac{h}{a})$; figure 3.7 is a contour plot of $\Re(\sigma_{max})$. It may be seen that $f_3(k_w, \frac{h}{a})$ represents a fairly good approximation to $\Re(\sigma_{max})$.



Contour plot of fitted composite function showing variation in $\Re(\sigma_{max})$ versus k_w and $\frac{h}{a}$.

Figure 3.6

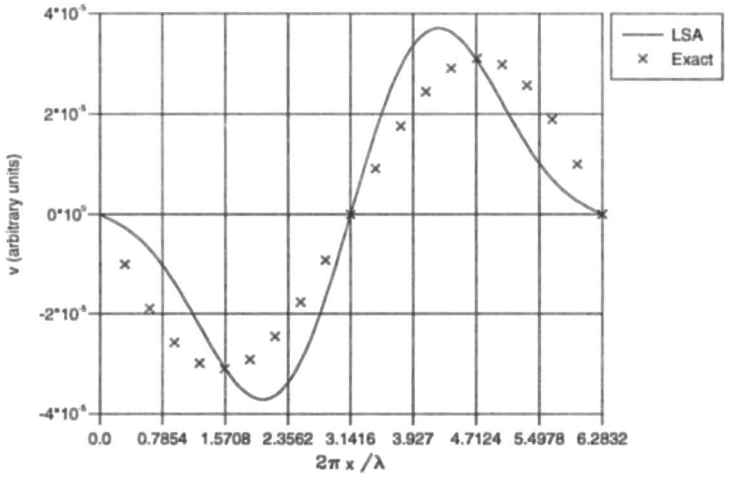


Contour plot of $\Re(\sigma_{max})$ versus k_w and $\frac{h}{a}$ from Linearised Stability Analysis result.

Figure 3.7

Having examined the development of the disturbances, which grow exponentially fast, consider now the disturbance-independent or secular terms in the equations of motion (3.15). The last three terms on the RHS of the x-component equation, and the last five terms on the RHS of the y-component equation (3.15) are the independent terms associated with the perturbing wave. After some reduction, the terms from the x-component equation may be expressed as: $\sin\varepsilon.f_x(\Gamma, h, a, k_w, d)$ and $\sin^2\varepsilon.g_x(\Gamma, h, a, k_w, d)$, where $f_x()$ and $g_x()$ are some functions of the problem parameters. The y-component terms may be reduced to $\sin\varepsilon.f_y(\Gamma, h, a, k_w, d)$ and $\sin 2\varepsilon.g_y(\Gamma, h, a, k_w, d)$, where $f_y()$ and $g_y()$ are some functions of the problem parameters. If these terms are integrated over the space $0 \leq x \leq 2\pi a/\lambda_w$, the net value of the transverse velocity is zero, whilst the net value of the x-component is $\tau_w/2.g(\Gamma, h, a, k_w, d)$. It should be recalled that what the secular terms in equation 3.15 actually represent are the *instantaneous* induced velocities of vortices over the space $0 \leq x \leq 2\pi a/\lambda_w$ for the wide range of wake configurations given by equa-

tions 3.5 and 3.6. As a means of verifying the secular terms in equation 3.15, the streamwise variation of the transverse velocity is evaluated for two wave cases; one of realistic strength, one a very weak perturbation. The *exact* velocity equations for a periodic length of street, which are presented in section 3.2.2, are used to compare with the present results. The wake configuration represented by equations 3.5 and 3.6 is inserted into the computer program developed in section 3.2.2, and the induced velocity at each point vortex is calculated; of course, no time development of the street is evaluated. The cases presented here are of $k_w = \pi/10$ and $\hat{h} = 0.025$ and $\hat{h} = 0.001$. Figure 3.8 shows the former case.

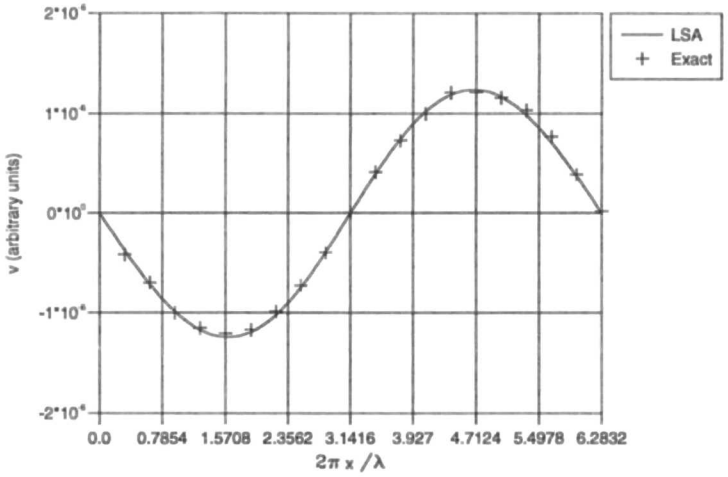


Transverse velocity for typical wave case.
Linearised equations result and 'exact' solution.

Figure 3.8

Figure 3.8 indicates that the wake 'thins' and 'bulges' over the wave period. It should be stated that the values of transverse velocities are of course much smaller than the wave term, or indeed the steady translational term. The transverse deformations that go on in the wake are therefore very weak. The LSA result agrees fairly well with the exact solution. The secular terms have errors which are of order

$\hat{h}^3$ and higher. If the wave strength is reduced, the agreement between the exact and LSA result should become better. Figure 3.9 is a plot of the case $\hat{h} = 0.001$.



Transverse velocity for very weak wave case.

Linearised equations result and 'exact' solution.

Figure 3.9

Recalling that $\varepsilon \equiv -\omega_w t$, and assuming that the non-linear interaction between the vortices over the wave period is weak, the above results indicate that the vortex street undergoes nearly periodic motions until the the growth in the error terms (i.e. until such time that equations 3.5 and 3.6 no longer 'fit' the resultant wake configuration) cause the rapid degeneration of the wake structure. It is postulated here that it is in fact the secular terms which give rise to small deviations away from the initial conditions; these deviations are then amplified exponentially fast by the disturbance dependent terms in equation 3.15, the rate of growth being a function of the wave parameters as discussed above. The amount of deviation from the initial conditions is related to the non-linear interactions of the vortices over the wave orbit, which are themselves related to the *strengths* of the vortices in the street; the evolution equations for the growth terms (3.17) were used to calculate

$\hat{\sigma}$ as functions of the wave parameters, although the actual growth exponent is σ, which is equal to $\frac{2\pi a^2}{\Gamma}\hat{\sigma}$. The premultiplier of $\hat{\sigma}$ is a measure of the natural frequency of the wake itself; the greater this value, the greater the deviation over the wave orbit.

The analysis presented here is for the highly idealised case of an infinite vortex street being perturbed by a finite, but weak wave. In reality, of course, vortex streets are of *finite* size, so the above analysis and its applicability becomes less relevant near to the 'ends' of the street.

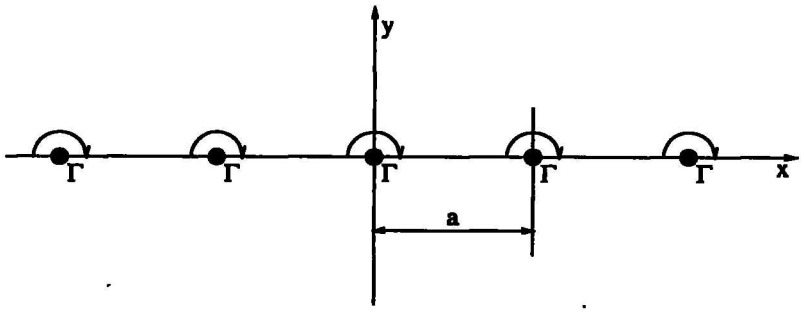
At the beginning of this section it was implied that the wake was assumed *a priori* to be 'frozen' in its perturbed state, meaning that we would expediently ignore the motions arising from the secular terms. However, from the above analysis, it would appear that this proviso is perhaps cautious: in the absence of infinitesimal disturbances, the vortices undergo practically closed orbits, so that divergence from the staggered von Kármán vortex street configuration is attained only very slowly. An applied infinitesimal disturbance grows exponentially fast in time and therefore it seems that it is the growth of these disturbances rather than the secular terms which provide the mechanism for degeneration of structure in the wake.

The following section examines the full non-linear behaviour of the wake over many wave orbits by numerically integrating the full equations of motion of a periodic vortex street.

3.2.2 Numerical Analysis

Equations of Motion

The complex potential for an infinite system of point vortices may be written in terms of trigonometric functions. First, the simple system of point vortices all lying on the real axis of the complex plane is considered, but the analysis is later extended for a vortex street. Consider the system:



Single row of vortices lying on the real-axis

Figure 3.10

For a single vortex at the origin the complex potential is:

$$W = \phi + i\psi = \frac{i\Gamma}{2\pi} \ln z \tag{3.29}$$

where ϕ is the velocity potential, ψ the stream function, Γ the strength of the vortex, $i = \sqrt{-1}$, and $z = x + iy$.

The complex potential of $2n + 1$ vortices nearest to the origin is:

$$W = \frac{i\Gamma}{2\pi} \ln z + \frac{i\Gamma}{2\pi} \ln(z \pm a) \ldots . + \frac{i\Gamma}{2\pi} \ln(z \pm na)$$

$$\Rightarrow W = \frac{i\Gamma}{2\pi}\ln[\frac{\pi z}{a}(1-\frac{z^2}{a^2})(1-\frac{z^2}{4a^2}) \ldots (1-\frac{z^2}{n^2a^2})] +$$

$$\frac{i\Gamma}{2\pi}\ln[\frac{a}{\pi}a^2 2a^2 \ldots n^2a^2] \tag{3.30}$$

As $n \to \infty$:

$$W = \frac{i\Gamma}{2\pi}\ln[\sin(\frac{\pi z}{a})] + const. \tag{3.31}$$

In the following analysis, it is assumed that the flow is periodic with finite period, that is a length L can be chosen over which there exists an integer number of basic street wavelengths (say n) and waves (say m):

$$na = m\lambda_w \tag{3.32}$$

where a is the inter-vortex longitudinal spacing, and λ_w is the wavelength of the wave.

The complex potential of the vortex street considered here as a periodic system of period L containing N vortices over the two rows may now be written down as:

$$W = \sum_{j=1}^{N} \frac{i\Gamma_j}{2\pi}\ln[\sin(\frac{\pi}{L}(z-z_j))] + const. \tag{3.33}$$

In order to calculate the velocity acting on say the j^{th} vortex, the complex potential at z near the j^{th} vortex is examined:

$$W_j = \frac{i\Gamma_j}{2\pi}\ln[\sin(\frac{\pi}{L}(z-z_j))] + \frac{i\Gamma_k}{2\pi}\ln[\sin(\frac{\pi}{L}(z-z_k))] -$$

$$\frac{i\Gamma_j}{2\pi}\ln[z - z_j] + const.$$

$$k = 1, ..., N \quad (k \neq j) \tag{3.34}$$

following the summation convention.

The first term on the right hand side is the contribution from all the periodic images of the j^{th} vortex (including itself); the second term is the contribution from all other vortices in the periodic space plus their periodic images, and the final term is the complex potential of the j^{th} vortex itself. This is subtracted off since the vortex has no effect on itself. Differentiating equation (3.34) with respect to z, and noting that $\frac{d}{dz}(\frac{1}{a}\ln[\sin(az)]) = \cot(az)$, where a is a constant, gives:

$$\frac{dW}{dz} = \frac{i}{2L}[\Gamma_j \cot(\frac{\pi}{L}(z - z_j)) \quad + \quad \Gamma_k \cot(\frac{\pi}{L}(z - z_k)) - \Gamma_j \frac{L}{\pi}\frac{1}{z - z_j}]$$

$$k = 1, ..., N \quad (k \neq j) \tag{3.35}$$

At a point $z = z_j + \varepsilon$, where $\varepsilon \ll L$, the conjugate of the complex velocity is:

$$\frac{dW}{dz} = \frac{i}{2L}[\Gamma_j \cot(\frac{\pi\varepsilon}{L}) \quad + \quad \Gamma_k \cot(\frac{\pi}{L}(z_j + \varepsilon - z_k)) - \Gamma_j \frac{L}{\pi\varepsilon}]$$

$$k = 1, ..., N \quad (k \neq j) \tag{3.36}$$

As $\varepsilon \to 0$:

$$\frac{dW}{dz} = \frac{i\Gamma_k}{2L}\cot(\frac{\pi}{L}(z_j - z_k))$$

$$k = 1, ..., N \quad (k \neq j) \tag{3.37}$$

Thus the velocity induced on the j^{th} point vortex by all others (i.e. from $-\infty \rightarrow +\infty$) is:

$$(u - iv)_j = \frac{i}{2L} \sum_{k \neq j}^{N} \Gamma_k \cot(\frac{\pi}{L}(z_j - z_k)) \tag{3.38}$$

The velocity field of a sinusoidal wave travelling in the positive x-direction is given by:

$$\begin{aligned} u(\vec{x}, t) &= u_w \sin(\omega_w t - k_w x) \\ \omega_w &= 2\pi f_w \\ k_w &= \frac{2\pi}{\lambda_w} \end{aligned} \tag{3.39}$$

This may be added to the equation for the unperturbed system (3.38) to render a set of equations of motion for all vortices within the periodic space ($0 < x < L$). This represents the complete definition of the system to examine case(A).

A first order accurate time marching code was written to integrate the equations of motion over many periods of the wave. The periodic conditions at the boundaries of the domain are effected by allowing vortices which leave the domain to re-enter from the opposite face.

In deciding the value of the time step to be used, reference was made to other vortex computations employing the Biot-Savart law, for example, Abernathy and Kronauer (1962). They used a fixed time step, which was a function of characteris-

tic velocity and length scales. However, it was decided here to make the time step dynamic, according to:

$$\Delta t = \frac{r_{min}(t)}{u_{max}(t) f_t} \tag{3.40}$$

where r_{min} is the smallest inter-vortex spacing over the periodic space, u_{max} is the largest velocity, and $f_t = 100$ is an arbitrary factor. Since the characteristic length is likely to change substantially during the computation and the induced velocity field behaves as $\frac{1}{r}$, a dynamic time step provides greater accuracy and control.

Results

With the assumed periodicity in the x-direction, the change in the wake structure is quantified in relation to changes in the y positions of the vortices. There are a variety of measures one might use, but the degeneration and lateral spreading of the wake is quantified in the present results by the Standard Deviation of the transverse (y) coordinates of the vortices, non-dimensionalised by the original von Kármán value:

$$\Theta(t) = \left(\frac{1}{N-1}\sum_{j}^{N}(y_j(t) - \bar{y}(t))^2\right)^{\frac{1}{2}} \cdot \left(\frac{1}{N-1}\sum_{j}^{N}(y_j(0) - \bar{y}(0))^2\right)^{-\frac{1}{2}} \tag{3.41}$$

where $\bar{y}$ is the mean and $\bar{y}(0) = 0$. Thus the wake starts with a value of $\Theta = 1$, and it is expected that $\Theta(t) > 1$ for $t > 0$. If $\Theta(t) < 1$ for $t > 0$ this would perhaps imply at a practical [5] level that there exist stable states for the wake for which $\frac{b}{a} < 0.281$. The numerical integration of the equations of motion is not necessarily confined to

[5] The inter-vortex spacing value of $b/a = 0.281$ represents the *only* neutrally stable configuration, but it is possible that there exist unstable states of very long time periods for which $\Theta(t) < 1$.

weak wave perturbations of the wake as was the case for the LSA. The two wave parameters λ_w and h are non-dimensionalised, *viz.* $\hat{\lambda} = \lambda/a$ and $\hat{h} = h/a$.

Typical wavelengths in practical scenarios (e.g. sea waves passing a body of 1m in diameter) are of the order of $\hat{\lambda} = 10$ or even greater. This is roughly equivalent to a wavelength of about 50 body diameters. The wave heights included in this study are typical of those encountered in some practical scenarios.

In calculating the evolution of the vortex street, a third parameter comes into consideration: $\hat{u} = u_w/U_c$. There are thus two spatial parameters $\hat{\lambda}$ and $\hat{h}$, and one temporal one. (Equally, $\hat{u}$ might well be replaced by a non-dimensional frequency parameter, say: $\hat{f} = f_w/f_n$, where f_n is the natural shedding frequency, and $f_n = U_c/a$; therefore $\hat{u} = 2\pi\hat{f}\hat{h}$).

In this two-dimensional analysis the frequency of the wave is arbitrarily related to the wavelength of the wave through the wave celerity, i.e. $c_w = f_w\lambda_w$, and the frequency is not a necessarily a function of the wavelength. However, for waves travelling on deep water, the linkage between frequency and wavelength is established through a dispersion type relationship:

$$\omega_w = \sqrt{\frac{2\pi g}{\lambda_w}} \tag{3.42}$$

where g is the gravitational constant, through linearised wave theory. Gravity has no meaning in this two-dimensional analysis and so the explicit calculation of the wave frequency from the dispersion relationship is not necessary. The important term here is $\hat{f}$, which for the scenarios under consideration, lies in the approximate

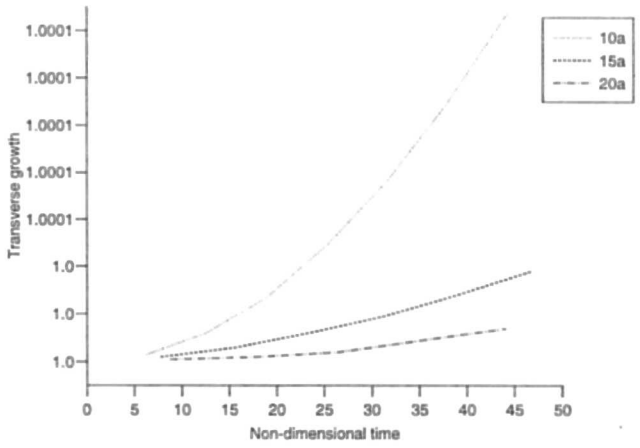
range: 1.0 $\rightarrow$ 2.0. The variables in this problem are: λ_w, f_w, h, D [6] , U_c, g. In real scenarios, the last of these is not truly a variable. These variables have length and time dimensions only. Buckingham's Pi theorem says that the number of independent non-dimensional parameters of a system is equal to the number of independent variables minus the number of dimensions. In this case, f_w and λ_w are related, so the number of independent non-dimensional parameters here is three. Conventionally, these three parameters are a Froude number ($\frac{U_c}{\sqrt{g\lambda_w}}$), a Keulagan Carpenter number ($\frac{h}{a}$), and a Diffraction number ($\frac{\lambda_w}{a}$). (Here the Froude number is equal to $\hat{f}\hat{\lambda}$).

Figure 3.11 is a plot of $\Theta(t)$ for the cases $\hat{\lambda} = 10, 15, 20$ over the first couple of cycles of the wave, i.e. $0 < t < 2\tau_w$. The maximum displacement of the wave in these case is $\hat{h} = 0.05$. It may be seen that the fastest departure from the original von Kármán vortex street occurs for the case $\hat{\lambda} = 10$, i.e. for $k_w = \pi/10$, whilst increasing wavelength results in a reduced growth rate. The non-dimensional time here is t^*, where $t^* = U_c t/D$. Note that although U_c and D do not appear explicitly in this analysis, time is non-dimensionalised in this way so as to be consistent with the viscous data, presented in chapter 4. Here, $U_c \approx 5U_s$, where U_s is the self-induced velocity of the street, and $D \approx 5a$.

If the computations are carried on further through time (say up to a non-dimensional time of 1000), it may be seen that the transverse growth rates are periodic, such that the wake returns very closely to its initial configuration. In figure 3.12 it may just be seen that the case $\hat{\lambda} = 10$ is just beginning to grow away from $\Theta(t) = 1.0$.

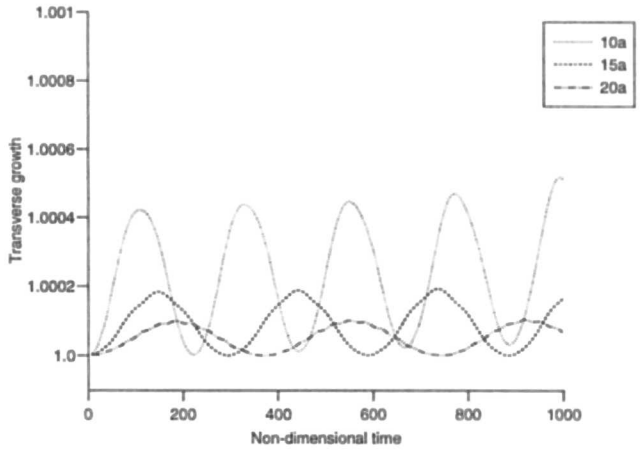
---

[6] D is not present in this analysis, but is implied by a - the inter-vortex spacing.



Initial transverse growth rates $\Theta(t)$ for various $\hat{\lambda}$ cases.

Figure 3.11

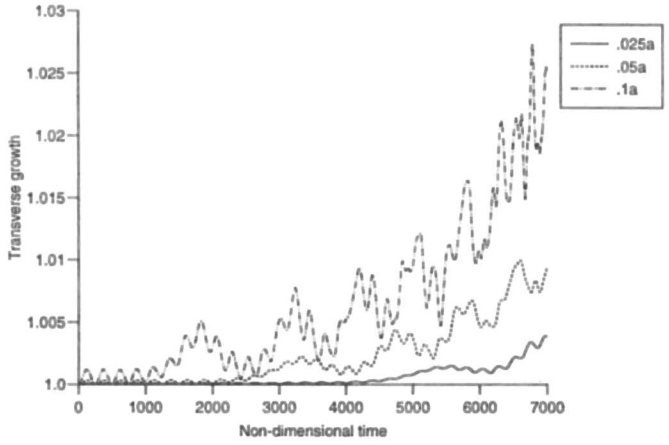


Increase in transverse growth up to a non-dimensional time of 10^3.

Figure 3.12

Figure 3.13 shows the cases $\hat{h} = 0.025, 0.05, 0.1$ up to a non-dimensional time of 7000. It shows that after the periodic fluctuations in $\Theta(t)$ at the early stages, a

much lower frequency fluctuation exists, and the wake starts to degenerate rapidly. The earlier regular frequency region is separated from the lower frequency region by a sudden change in frequency across one period, after which the amplitude of oscillation becomes much greater and more erratic.



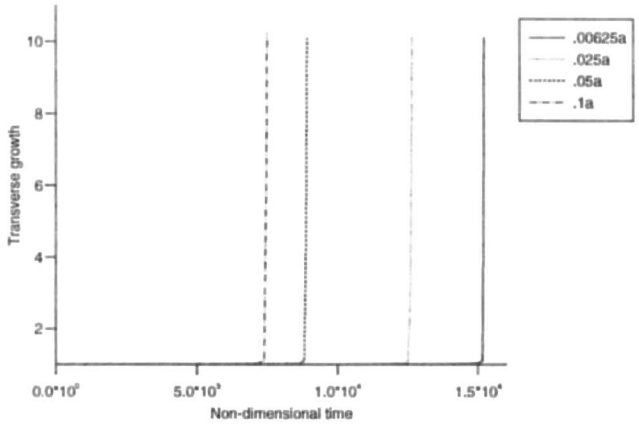
Initial transverse growth rates $\Theta(t)$ for various $\hat{h}$ cases.

Figure 3.13

If the equations of motion are integrated still further through time, definite breakpoints appear in plots of $\Theta(t)$, at which the exponential growth rate exhibited in the earlier stages of degeneration (see figure 3.13) gives way to an essentially linear variation with time. The growth rate in this linear region is much more rapid. Figure 3.14 shows plots of $\Theta(t)$ versus t^* for different height waves, and figure 3.15 shows data for cases of different wavelengths. Figure 3.14 shows that increasing the wave height of the wave, whilst holding the other two parameters constant, produces an earlier degeneration of the wake. Comparisons with the LSA are drawn later in this section.

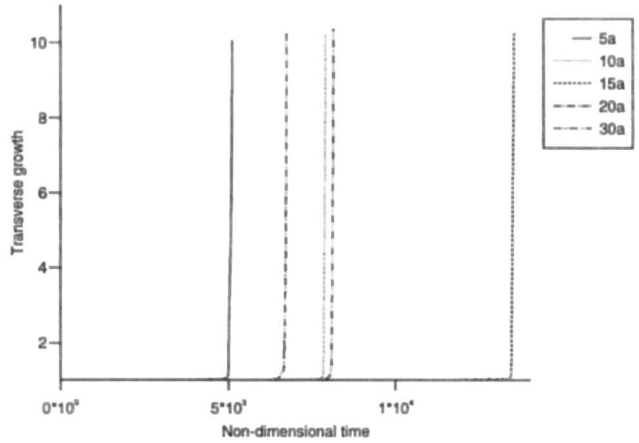
Figure 3.15 is inconclusive as to the relationship between wavelength and the time at which the wake 'breaks'. For $5 \leq \hat{\lambda} \leq 15$, the evolution of the wake is as expected,

i.e. shorter wavelength waves produce a greater effect on the wake. However, the cases of $\hat{\lambda} = 20, 30$ seem to be at odds with the rest of the data.



Final transverse growth rates $\Theta(t)$ for various $\hat{h}$ cases.

Figure 3.14



Final transverse growth rates $\Theta(t)$ for various $\hat{\lambda}$ cases.

Figure 3.15

Inspection of the early part of the transverse growth history shows that the cases

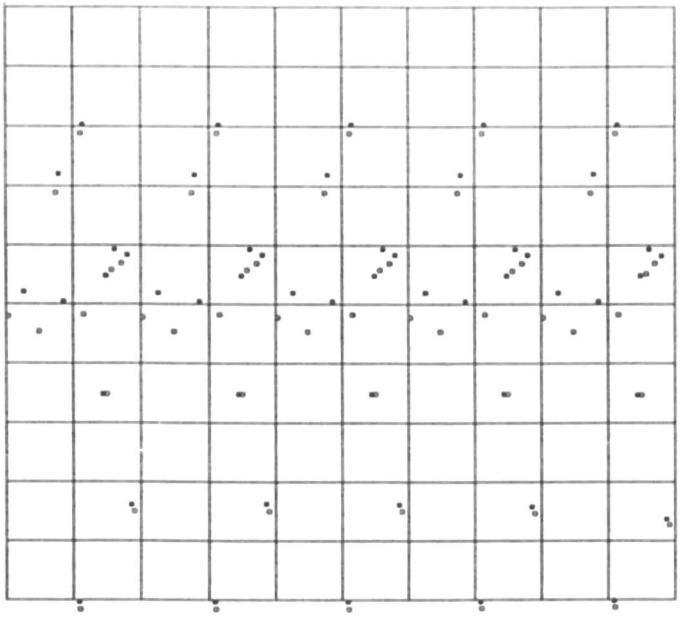
$\hat{\lambda} = 20, 30$ are in fact growing more slowly than $\hat{\lambda} = 15$, but the sudden change in the flow periodicity mentioned earlier takes place much sooner in the former cases. It is not clear to the author why this should be the case.

Variation of the Froude parameter (which here is a relative measure of the 'phantom' cylinder speed and the wave celerity), whilst keeping $\hat{h}$ and $\hat{\lambda}$ fixed, showed there to be very little variation in the time to 'break' data over the range of $0.03 \rightarrow 0.06$.

Examination of the vortex positions reveals the reason for the sudden change in $\Theta(t)$. During the early stages of the process of degeneration the vortices are basically undergoing wave induced orbits about their $t = n\tau_w$ positions; during the orbit the vortices interact with each other weakly and on returning to their $t = n\tau_w$ positions they accumulate a small offset, i.e. the original von Kármán vortex street is not quite recovered. The amount of local vortex interaction depends on the inter-vortex spacing (with Γ fixed), and thus the largest induced velocities are experienced at the extrema of the orbit. When the offset in the vortex position reaches a certain value the local interactions begin to dominate and the possibility of vortex pair formation arises. If the alignment of a vortex pair (i.e. the direction of the mutually induced velocity vector) is not along the x-axis and the vortices are sufficiently close to each other so that the mutually induced velocity is large, the pair leaves the wake and continues ever onwards. The mutually induced velocity remains nearly constant in the presence of the wave field since the inter-vortex spacing of the pair is very much smaller than the wavelength of the wave, i.e. the pair undergoes a temporal oscillation but is insensitive to spatial variations in wave induced velocity field. Hence, the standard deviation of the transverse coordinates of the vortices $\Theta(t)$ becomes predominantly linear. In fact, animated sequences of the pair ejection process show that after a certain time, vortices undergo rapid rotations around

vortices of the same sign and experience sudden linear acceleration in the presence of opposite signed vortices. At this stage the velocity field experienced by vortices is very localised because the inter-vortex spacings are so small in some parts of the periodic space. It is impossible for vortices to collide with each other since the velocity field prevents this, but the rapid accelerations cause a vortex to undergo a flurry of brief interactions with other vortices until such time that it combines with a vortex of opposite sign with sufficiently small inter-vortex spacing and alignment appropriate for ejection. The reasons for this are intuitively clear since, if a pair has temporarily formed but is approximately aligned with the x-axis and is therefore moving along this axis, the probability of a near collision with another vortex is very high, and thus the chances of longevity for this pair are small. A corollary of this is that there exists a minimum angle to the x-axis at which pairs are seen to eject. Once pairs of vortices eject, the main wake 'relaxes', in that the rapid rotations and accelerations of vortices cease, and the remaining vortices are left with a structure similar to the original von Kármán street. What remains represents an unstable configuration, since, in general, $b/a \neq 0.281$ anymore; however, the rate at which such a configuration diverges is (apparently) slow by comparison with the wave induced effects. The vortices remaining in the wake continue to undergo wave induced oscillations. With fewer vortices now occupying the same length of space the inter-vortex spacings are generally larger and the process of degeneration over the wave orbit recommences. After a certain period of time the remaining vortices again undergo rapid localised interactions and a second phase of ejections is realised. Figure 3.16 is a plot of vortices demonstrating this process.

Once strong local interactions begin to take place and inter-vortex spacings become small, characteristic velocities increase rapidly due to the $1/r$ nature of the induced velocity field of a point vortex.



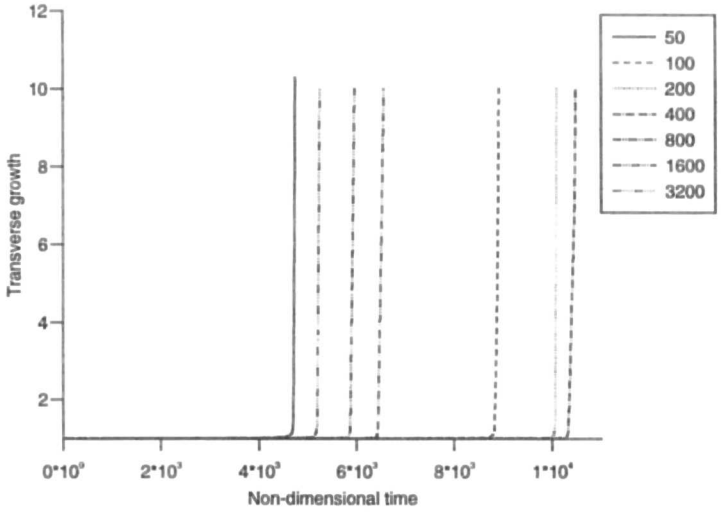
Multiple phases of vortex pair ejections

Figure 3.16

Sources of error in the numerical integration arise from the truncation of a series in the time marching method and round-off errors in the computer. Reduction of errors associated with the former through use of smaller time steps, and with the latter through use of double precision mantissae results in the formation of vortex pairs at different times, i.e. the break-points seen in figures 3.14 and 3.15 appear after different times. In fact, it is found that solutions using smaller and smaller time steps *never* converge to a particular solution for the cases under consideration. Figure 3.17 is a plot of $\Theta(t)$ for $\hat{h} = 0.1$, $\hat{\lambda} = 12$ for different f_t.

The above plot shows that for coarse time steps, e.g. $f_t = 50$, the vortex pairs form relatively early on. As the time step is refined the breakpoints tend, apparently, to asymptote to a limit; however, there is no actual limit for this system because of

the inherent instability, and for still finer time steps the breakpoints begin to move back towards the origin.



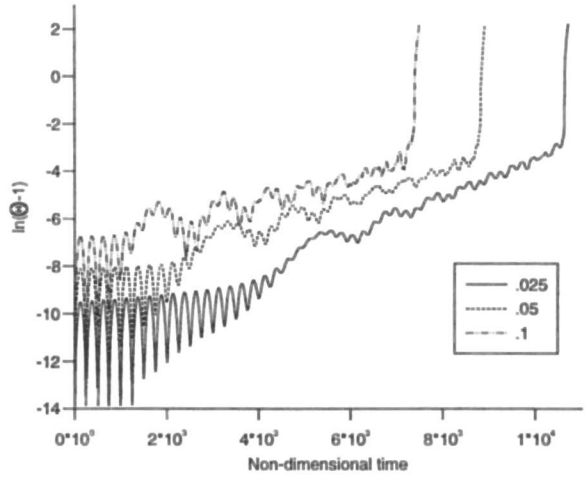
Effect on transverse growth for various values of f_t

Figure 3.17

It is possible that the above plot demonstrates the separate effects of the two sources of error in the solution, namely that associated with the truncation of the time series, and that associated with the round-off errors in the computer. (The accumulated machine error is $\propto n$, where n is the number of time steps, and therefore the smaller the time step, greater the number of time steps used to provide a solution, and the greater value of error from round-off). The dependence of the solution on the value of the time step tends to imply that the long term solution is sensitive to small errors in the numerical integration of the vortex positions, i.e. the *signal-to-noise* ratio of the vortex positions on completion of the wave orbits is not very high. The above result is in agreement with the predictions of the LSA (previous section). Clearly, any computation that does not involve the manipulation of integers alone, or which marches a solution through discrete points in time using approximate representa-

tions of temporal derivatives is susceptible to the generation of noise, and the effects of noise on the evolution of a system of vortices which is undergoing nearly periodic motions will be a function of the magnitude of displacements in vortex positions at the end of each orbit. (The displacements occur throughout the orbit, but the completion of each orbit is a convenient point at which to consider them).

More details of the degeneration process are given in figure 3.18, which is a plot of the logarithm of the percentage difference in $\Theta(t)$ between the wave cases and the von Kármán vortex street. It shows that the initial growth is dependent on the wave height, but at a certain point in time, the growth rates change, and become essentially independent of the wave parameters. In all three cases, a vortex pair ejects at $\Theta(t) \approx 1.05$.



Detail of the degeneration process.

Figure 3.18

The numerical analysis presented in this section has demonstrated that a von Kármán vortex street, when subjected to an in-line periodic progressive wave-train undergoes degeneration and break up in the following manner:

• The initial transverse growth, quantified by the standard deviation of the transverse coordinates of the vortices, is periodic and has a mean exponential growth rate. The deviation from exact conditions in the flow and the subsequent increase in the mean of the transverse growth parameter $\Theta(t)$ is a result of the amplification of infinitesimal disturbances. The rate of amplification depends on the height and wavelength of the perturbing wave.

• The amplitude of the sinusoidal variations grows in time until local vortex interactions become irresistible; rapid vortex accelerations take place resulting in the formation of vortex pairs, which eject from the main wake. Transverse growth is then dominated by the self-advection of the pair and is therefore essentially linear.

Finally, all of the above computations have commenced with the first vortex initially at $x = 0$; therefore the initial phase relationship between the wave and the vortices of the street is confined to $2\pi ja/\lambda_w, j = 0, 1, 2, ...$ In order to assess if the initial phase between the street and the wave is important, and thus whether the above results hold true for a given wave interacting with a given von Kármán vortex street - there being no special conditions between the two - a phase change spanning 0 to 2π is introduced into the wave. Thus the velocity field induced by the wave is given by:

$$u(\vec{x}, t) = u_w \sin(\varepsilon + \omega_w t - k_w x) \tag{3.43}$$

Where ε is an arbitrary phase shift, $0 \leq \varepsilon \leq 2\pi$. Tests for these cases showed there to be no discernible difference in transverse growth between the various values of ε. This is not altogether an unexpected result because $\Theta(t)$ is an integral measure

over the whole of the periodic space, i.e. changes in ε result in vortices initially at different points in the periodic space experiencing the same motions at the the same time, but the net effect on $\Theta(t)$ is the same.

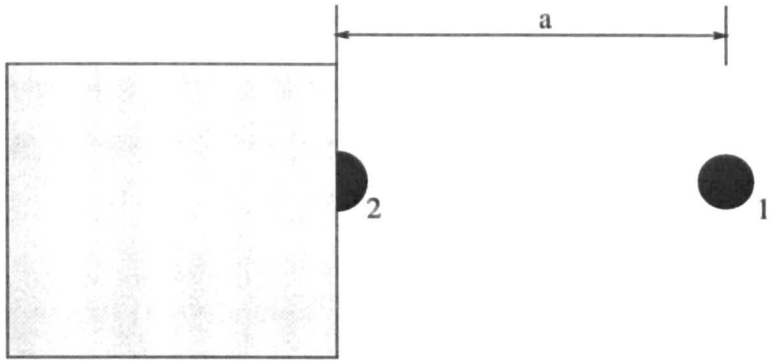
3.3 Case(B)

3.3.1 Model for variation in vortex strengths

It has been found that for oscillatory flow problems with and without mean components, a constant Strouhal number model i.e. $S = \frac{fD}{U} \approx 0.2$, can be used to give reasonable predictions of the transverse force time history (Bearman, Graham, Obasaju (1984)). The implication is that the spacing between vortices in the wake is a function of the body scale only. The imposed oscillatory velocity field is given by:

$$u(t) = U_c + u_w \sin(\omega_w t) \tag{3.44}$$

For the purposes of this analysis, imagine that the region around the cylinder which includes the formation region is represented by a 'black box', which issues fully formed vortices at a certain rate. In figure 3.19 vortex 1 is just about to arrive at $x = a$, and vortex 2 is just about to be released. The formation time for vortex 2 is the time it took vortex 1 to travel a distance a. It is now possible to write down general recurrence relations for the formation time of the vortices, for example consider the general case of the j^{th} vortex with a formation time of τ_j.



Issuing of vortices from 'black box'.

Figure 3.19

$$\int_{t^-}^{t^+} u(t).dt = a \tag{3.45}$$

where,

$$\begin{aligned} t^+ &= \sum_{i=1}^{j} \tau_i \\ t^- &= \sum_{i=1}^{j-1} \tau_i \ . \end{aligned} \tag{3.46}$$

If the equation for velocity (3.45) is put into equation (3.46), the recurrence relations become:

$$U_c \tau_j - \frac{u_w}{\omega_w} \cos \omega_w \sum_{i=1}^{j} \tau_i + \frac{u_w}{\omega_w} \cos \omega_w \sum_{i=1}^{j-1} \tau_i = a \tag{3.47}$$

This may be solved from some arbitrary starting point using an iterative method, e.g. Newton-Raphson to give $\tau_j \quad j = 1, 2, ...$

The rate of convection of circulation into the free shear layers is given by the formula:

$$\frac{d\Gamma}{dt} = \frac{1}{2}u_s^2 \quad ; \quad u_s = ku(t) \quad ; \quad k \approx 1.5 \tag{3.48}$$

To evaluate each Γ, the above equation is integrated over the formation time for each vortex, to give for the j^{th} vortex (say):

$$\Gamma_j = \frac{k^2}{2}(U_c^2\tau_j - 2U_c h\cos\omega_w \sum_{i=1}^{j}\tau_i + 2U_c h\cos\omega_w \sum_{i=1}^{j-1}\tau_i) \tag{3.49}$$

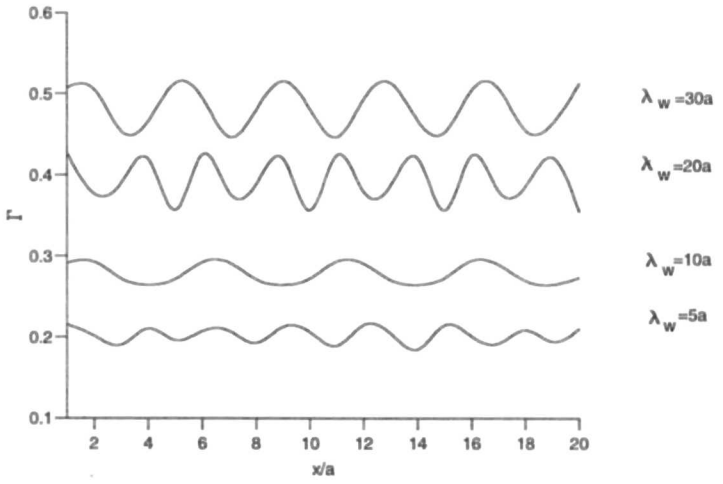
Terms of the order of (u_w^2) have not been included in this equation, as they are small. It should be noted that the above is a simple model for the variation in vortex strengths due to the varying local velocity field at the cylinder, and is not necessarily precisely accurate.

This equation for Γ_j is generated from an equation which is pertinent to the formation process. In the near wake there is cancellation of vorticity, which typically reduces the shed vortex strength by about 50%, i.e. Γ_j(released)= $\frac{1}{2}\Gamma_j$(formed), and so the values of Γ_j are adjusted accordingly. If the values of Γ_j are plotted out for vortices in the wake, a near sinusoidal variation in vortex strength results, for which the wavelength of oscillation is equal to $\tau_w a/\tau_n$ where τ_n is the period of the street and is equal to a/U_c, i.e. $\lambda_\Gamma = \frac{a}{j}$. Figure 3.20 is a plot of this variation for the case $\hat{h} = 0.05$. The vortex strengths are approximately decomposed into a steady ($\bar{\Gamma}$) and an unsteady term ($\Gamma'(x)$), i.e. ,

$$\begin{aligned} \Gamma(x) &= \bar{\Gamma} + \Gamma' \sin(k_\Gamma m) \\ k_\Gamma &= \frac{2\pi}{qa} \end{aligned} \tag{3.50}$$

where $x = ma$, q is the number of vortices per wavelength of vortex strength variation, and k_Γ is a non-dimensional wavenumber.

If the wave height is set to zero, all Γ_j are the same and have the value $\bar{\Gamma} = \frac{k^2 U_c a}{4}$. This may be compared with the equation for the steady velocity term of the von Kármán street which gives: $\Gamma = 2\sqrt{2}aU_s$, where $U_s \approx U_c/5$.



Variation in vortex strength in the wake for cases of different wavelength.

$\hat{h} = 0.05$.

Figure 3.20

Since the fluctuating component of circulation (Γ') also depends on the term $U_c\tau_j$, and τ_j is 180° out of phase with the other part of the fluctuating terms (involving h), the effect of the $U_c\tau_j$ term is to reduce the magnitude of the fluctuating component by an amount $U_c(\tau_j - \bar{\tau})$, where $\bar{\tau}$ is the mean formation period. It is interesting to note that should the rate of circulation fed into the shear layer be related to the velocity rather than the square of the velocity (equation (3.48)), there would be no variation in vortex strength in the wake.

3.3.2 Linearised Stability Analysis

Linearised Equations

The LSA of the vortex strength variation configuration now follows, and is based on that presented in the previous section on the 'concertina' effect of the wave. In the present case, the LSA is much more straightforward because it does not involve expansions of the wave terms which exist in denominators of the latter. There is however an implied limit on the validity of this LSA with respect to h since 2^{nd} order terms involving the wave velocity u_w are ignored in the equations for $\Gamma'(x)$.

Again, consider the case of the induced velocity for the zeroth vortex lying in the m-row from all other vortices in the street. The contributions from the m-row itself are:

$$\frac{d(\delta x_0)}{dt} = \frac{1}{2\pi}\sum_m \Gamma_m \frac{(\delta y_0 - \delta y_m)}{r_m^2}$$

$$\frac{d(\delta y_0)}{dt} = -\frac{1}{2\pi}\sum_m \Gamma_m \frac{(\delta x_0 - \delta x_m - ma)}{r_m^2}$$

$$r_m^2 = m^2a^2 - 2ma(\delta x_0 - \delta x_m) + O(\delta^2)$$

$$m = \pm 1, \pm 2, ... \tag{3.51}$$

This gives:

$$\frac{d(\delta x_0)}{dt} = \frac{1}{2\pi a^2}\sum_m \Gamma_m \frac{(\delta y_0 - \delta y_m)}{m^2}$$

$$\frac{d(\delta y_0)}{dt} = \frac{1}{2\pi a^2}\sum_m \Gamma_m \frac{(\delta x_0 - \delta x_m)}{m^2} + \frac{1}{2\pi a}\sum_m \frac{\Gamma_m}{m}$$

$$\Gamma_m = \bar{\Gamma} + \Gamma' \sin(\varepsilon + k_\Gamma m) - \Gamma' \sin(\varepsilon)$$

$$m = \pm 1, \pm 2, ... \tag{3.52}$$

The p-row contributions are:

$$\frac{d(\delta x_0)}{dt} = -\frac{1}{2\pi}\sum_p \Gamma_p \frac{(\delta y_0 - \delta y_m + b)}{r_p^2}$$

$$\frac{d(\delta y_0)}{dt} = \frac{1}{2\pi}\sum_p \Gamma_p \frac{(\delta x_0 - \delta x_p - pa)}{r_p^2}$$

$$r_p^2 = p^2a^2 + b^2 - 2pa(\delta x_0 - \delta x_p) + 2b(\delta y_0 - \delta y_p) + O(\delta^2)$$

$$p = \pm\frac{1}{2}, \pm\frac{3}{2}, ... \tag{3.53}$$

Substituting $d = b/a$, the complete equations for the zeroth vortex then become:

$$\frac{d(\delta x_0)}{dt} = \frac{\bar{\Gamma}}{2\pi a^2}\sum_m \frac{\delta y_0 - \delta y_m}{m^2} - \frac{\bar{\Gamma}}{2\pi a^2}\sum_p \frac{\delta y_0 - \delta y_p}{p^2 + d^2} -$$

$$\frac{\bar{\Gamma}}{2\pi a^2}\sum_p \frac{2pd(\delta x_0 - \delta x_p)}{(p^2 + d^2)^2} + \frac{\bar{\Gamma}}{2\pi a^2}\sum_p \frac{2d^2(\delta y_0 - \delta y_p)}{(p^2 + d^2)^2} -$$

$$\frac{\Gamma'}{2\pi a^2}\sum_m \frac{(\delta y_0 - \delta y_m)(\sin(\varepsilon + mk_\Gamma) - \sin\varepsilon)}{m^2} -$$

$$\frac{\Gamma'}{2\pi a^2}\sum_p \frac{(\delta y_0 - \delta y_p)(\sin(\varepsilon + pk_\Gamma) - \sin\varepsilon)}{p^2+d^2} -$$

$$\frac{\Gamma'}{2\pi a^2}\sum_p \frac{2pd(\delta x_0 - \delta x_p)(\sin(\varepsilon + pk_\Gamma) - \sin\varepsilon)}{(p^2+d^2)^2} +$$

$$\frac{\Gamma'}{2\pi a^2}\sum_p \frac{2d^2(\delta y_0 - \delta y_p)(\sin(\varepsilon + pk_\Gamma) - \sin\varepsilon)}{(p^2+d^2)^2} -$$

$$\frac{\bar{\Gamma}}{2\pi a}\sum_p \frac{d}{p^2+d^2} - \frac{\Gamma'}{2\pi a}\sum_p \frac{d(\sin(\varepsilon + pk_\Gamma) - \sin\varepsilon)}{p^2+d^2}$$

$$\frac{d(\delta y_0)}{dt} = \frac{\bar{\Gamma}}{2\pi a^2}\sum_m \frac{\delta x_0 - \delta x_m}{m^2} - \frac{\bar{\Gamma}}{2\pi a^2}\sum_p \frac{(p^2-d^2)(\delta x_0 - \delta x_p)}{(p^2+d^2)^2} +$$

$$\frac{\bar{\Gamma}}{2\pi a^2}\sum_p \frac{2pd(\delta y_0 - \delta y_p)}{(p^2+d^2)^2} + \frac{\Gamma'}{2\pi a^2}\sum_m \frac{(\delta x_0 - \delta x_m)(\sin(\varepsilon + pk_\Gamma) - \sin\varepsilon)}{m^2} -$$

$$\frac{\Gamma'}{2\pi a^2}\sum_p \frac{(p^2-d^2)(\delta x_0 - \delta x_p)(\sin(\varepsilon + pk_\Gamma) - \sin\varepsilon)}{(p^2+d^2)^2} +$$

$$\frac{\Gamma'}{2\pi a^2}\sum_p \frac{2pd(\delta y_0 - \delta y_p)(\sin(\varepsilon + pk_\Gamma) - \sin\varepsilon)}{(p^2+d^2)^2} +$$

$$\frac{\Gamma'}{2\pi a}\sum_m \frac{\sin(\varepsilon + pk_\Gamma) - \sin\varepsilon}{m} - \frac{\Gamma'}{2\pi a}\sum_p \frac{p(\sin(\varepsilon + pk_\Gamma) - \sin\varepsilon)}{p^2+d^2}$$

$$m = \pm 1, \pm 2, \ldots \qquad p = \pm\frac{1}{2}, \pm\frac{3}{2}, \ldots \tag{3.54}$$

Again, using the method of normal modes, and introducing an infinitesimal disturbance of the form:

$$\begin{aligned} \delta x_m &= \alpha_u(t)e^{imk_d} \\ \delta y_m &= \beta_u(t)e^{imk_d} \\ \delta x_p &= \alpha_l(t)e^{ipk_d} \\ \delta y_p &= \beta_l(t)e^{ipk_d} \end{aligned} \tag{3.55}$$

where k_d is the non-dimensional wavenumber of the disturbance, i.e. $k_d = \frac{2\pi a}{\lambda_d}$, leads to a set of coupled first order ordinary differential equations for α_u and β_u:

$$\begin{aligned} \frac{2\pi a^2}{\bar{\Gamma}}\frac{d\alpha_u}{dt} &= A\alpha_u + B\beta_u + C\alpha_l + D\beta_l + I_1 \\ \frac{2\pi a^2}{\bar{\Gamma}}\frac{d\beta_u}{dt} &= B\alpha_u - A\beta_u + D\alpha_l - C\beta_l + I_2 \ . \end{aligned} \tag{3.56}$$

Where the I_1 and I_2 are the independent terms. Defining $\hat{\Gamma} = \Gamma'/\bar{\Gamma}$, the coefficients are given by:

$$A = -\hat{\Gamma}\cos\varepsilon \sum_p \frac{2pd\sin pk_\Gamma}{(p^2+d^2)^2}$$

$$\begin{aligned} B = {} & \sum_m \frac{1}{m^2} - \sum_m \frac{\cos mk_d}{m^2} - \sum_p \frac{p^2-d^2}{(p^2+d^2)^2} + \\ & \hat{\Gamma}\sin\varepsilon \sum_m \frac{\cos mk_\Gamma}{m^2} - \frac{\hat{\Gamma}\sin\varepsilon}{2}\sum_m \frac{\cos mk_d}{m^2} - \\ & \hat{\Gamma}\sin\varepsilon \sum_m \frac{\cos mk_\Gamma \cos mk_d}{m^2} - i\hat{\Gamma}\cos\varepsilon \sum_m \frac{\cos mk_\Gamma \cos mk_d}{m^2} - \end{aligned}$$

$$\hat{\Gamma}\cos\varepsilon\sum_p \frac{(p^2-d^2)\cos pk_\Gamma}{(p^2+d^2)^2}$$

$$C = i\sum_p \frac{2pd\sin pk_d}{(p^2+d^2)^2} - i\hat{\Gamma}\sin\varepsilon\sum_p \frac{2pd\sin pk_d\cos pk_\Gamma}{(p^2+d^2)^2} -$$

$$\hat{\Gamma}\sum_p \frac{2pd\sin pk_\Gamma\sin pk_d}{(p^2+d^2)^2}$$

$$D = \sum_p \frac{(p^2-d^2)\cos pk_d}{(p^2+d^2)^2} + \hat{\Gamma}\sin\varepsilon\sum_p \frac{(p^2-d^2)\cos pk_\Gamma\cos pk_d}{(p^2+d^2)^2} +$$

$$i\hat{\Gamma}\cos\varepsilon\sum_p \frac{(p^2-d^2)\sin pk_\Gamma\sin pk_d}{(p^2+d^2)^2}$$

$$I_1 = -a\sum_p \frac{d}{p^2+d^2} - \hat{\Gamma}a\sin\varepsilon\sum_p \frac{d\cos pk_\Gamma}{p^2+d^2}$$

$$I_2 = \hat{\Gamma}a\cos\varepsilon\sum_m \frac{\sin mk_\Gamma}{m} - \hat{\Gamma}a\cos\varepsilon\sum_p \frac{p\sin pk_\Gamma}{p^2+d^2}$$

$$m = \pm1, \pm2, \ldots \qquad p = \pm\frac{1}{2}, \pm\frac{3}{2}, \ldots \tag{3.57}$$

Equations (3.57) may be used to deduce a set of equations for the lower row. Following the analysis as in case(A), we have the same equation for the 'growth' term $\hat{\sigma}$:

$$\frac{2\pi a^2}{\bar{\Gamma}}\hat{\sigma} = C \pm (A^2 + B^2 - D^2)^{\frac{1}{2}} \tag{3.58}$$

for the symmetric disturbance, and

$$\frac{2\pi a^2}{\bar{\Gamma}}\hat{\sigma} = -C \pm (A^2 + B^2 - D^2)^{\frac{1}{2}} \tag{3.59}$$

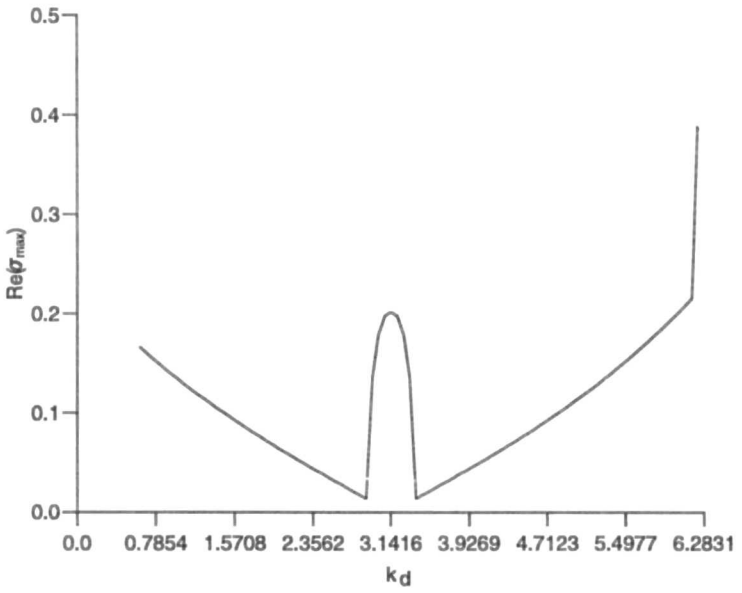
for the anti-symmetric disturbance.

Results

Figure 3.21 is a plot of $\Re(\sigma_{max})$, $\sigma = 2\pi a^2\hat{\sigma}/\bar{\Gamma}$ versus wavenumber of the disturbance for values of $\lambda_\Gamma = 10a$, $\hat{\Gamma} = 0.1$ over the range $0 \leq \varepsilon \leq 2\pi$. The curve is similar in form to that of case(A). Again, there is always a root with $\Re(\hat{\sigma}) > 0$ and thus the configuration is *unstable* to infinitesimal disturbances.

If $\hat{\Gamma} = 0$ or $k_\Gamma = 0$ the von Kármán vortex street stability characteristics are recovered, i.e. the street is neutrally stable to infinitesimal disturbances with $d = 0.281$.

The variation of $\Re(\sigma_{max})$ versus wavenumber of circulation strength wave is shown in figure 3.22. For this case $\hat{\Gamma} = 0.05$. The range of the wavenumber gives an equivalent range of wavelength of between $10a$ and ∞. It may be seen that the relationship between σ and k_Γ is linear - implying that the growth of disturbances in time is proportional to $e^{\lambda_\Gamma^{-1}t}$.

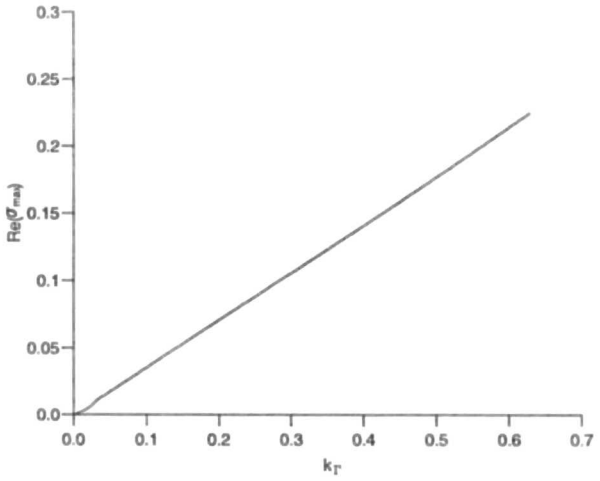


Variation of $\Re(\sigma_{max})$ versus k_d

Figure 3.21

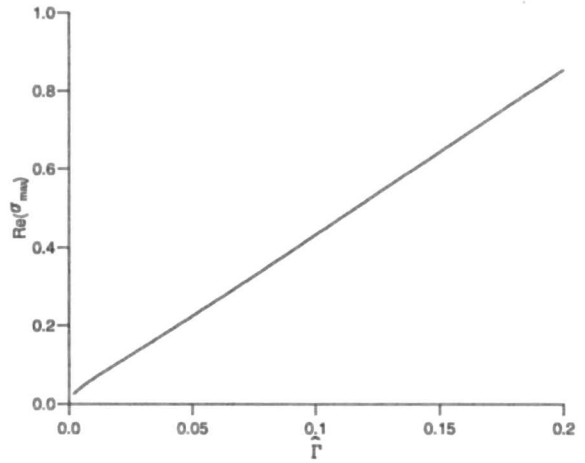
Figure 3.23 is a plot of the variation of $\Re(\sigma_{max})$ versus $\hat{\Gamma}$. Again, the variation is linear - implying that the growth in time of infinitesimal disturbances behaves as $e^{\hat{\Gamma}t}$. These results are slightly different from those of case(A), in which the dependence is approximately of the form $\frac{1}{\sqrt{\hat{\lambda}}}$ and $\sqrt{\hat{h}}$. The implication is that for a given wave, the growth rate of infinitesimal disturbances due to vortex strength variation is greater than that due to the concertina effect of the wave velocity field.

Another important point is the difference between k_w and k_Γ. In section 3.3.1, it was shown that the wavelength of the spatial variation in Γ is equal to $\frac{a}{f}$; for the scenarios under consideration in this work $\hat{f}$ is of the order of 1, implying that $k_\Gamma \gg k_w$ for the most part. Thus the *actual* growth rates due to vortex strength variation in the wake are expected to be much greater than those due to the concertina effect.



Variation of $\Re(\sigma_{max})$ versus k_Γ

Figure 3.22



Variation of $\Re(\sigma_{max})$ versus $\hat{\Gamma}$

Figure 3.23

In terms of the stability of the wake then, the mechanism which provides the vortex strength variation in the wake (i.e. the time varying velocity at the cylinder) is at least an order of magnitude more significant than the mechanism which provides the

concertina effect on the vortices in the wake (i.e. the wavelength phase term of the wave).

One important implication of the equation for the wavelength of vortex strength variation in the wake, i.e. $\lambda_\Gamma = \frac{a}{\hat{f}}$ is that the non-dimensional wavenumber k_Γ equals $2\pi n$, for $\hat{f} = n$, where n is an integer. The result is that there is no difference in vortex strengths in the wake, and the stability characteristics of these configurations are identical to the von Kármán street; i.e. they are *neutrally* stable.

3.3.3 Numerical Analysis

Equations of Motion

The equations of motion for this configuration are given by equation 3.38. The velocity field induced by a wave is not added to this set of equations, and of course the Γ's remain within the summation sign. The periodic space includes an even integer number of vortices and at least one wavelength of the strength variation wave (of wavelength $\tau_w a/\tau_n$), i.e. :

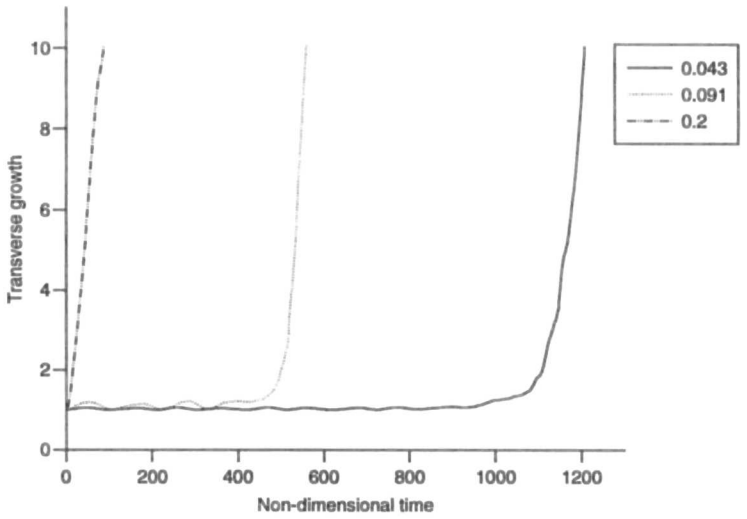
$$m\lambda_\Gamma = na \tag{3.60}$$

Results

In order to assess the degeneration of the wake, the same measure of $\Theta(t)$ is adopted as in case(A). In this particular case the parameters are $\hat{\Gamma}$ - the ratio of the fluctuating to mean component of the vortex strengths, and λ_Γ - the wavelength of this

variation.

The same criterion for the time step is employed in the integration, i.e. $f_t = 100$. Figure 3.24 shows plots of $\Theta(t)$ for three values of the $\hat{\Gamma}$ parameter. These data are at $\lambda_\Gamma = 1.5a$ and $\hat{\Gamma} = [0.043, 0.091, 0.2]$. The wave cases in figure 3.24 are therefore $\lambda_w = 12a$ and $\hat{h} = [0.025, 0.05, 0.1]$; these data are directly comparable with those in figure 3.14 in the section on the concertina effect.



Transverse growth rates $\Theta(t)$ for various $\hat{\Gamma}$ cases.

Figure 3.24

These plots are similar in form to those of case(A), and are characterised by the appearance of definite breakpoints in $\Theta(t)$, i.e. the rapid breakup of the wake is due to the formation and ejection of vortex pairs. However, the non-dimensional time at which the wake starts to degenerate is very much earlier in the cases here. The implication is that for a given set of flow conditions, it is the effect of vortex strength variation rather than the concertina effect of the wave which dominates the

evolution of the wake. This concurs with the general findings of the LSA.

The LSA requires $\lambda_\Gamma \gg a$ to be strictly valid; the range of the parameters presented here give quite short values for λ_Γ because of the scenarios under consideration and therefore comparison between this numerical data and the LSA is not really justified under these conditions. A valid comparison might be made for the case of a cylinder translating in the same direction as the progression of the wave-train. In this particular case the encounter frequency experienced by the cylinder is much lower, and so the wavelength of variation of $\Gamma(x)$ is much greater, and the requirement of $\lambda_\Gamma \gg a$ is upheld. Another possibility is for the case of a cylinder moving very rapidly into waves, so that $\hat{u} \ll 1$, which implies $\hat{f} \ll 1$.

Chapter 4

Two-Dimensional Viscous Analysis

4.1 Introduction

The results from an analysis of an infinitely long idealised wake in chapter 3 showed the effects of an in-line progressive wave on the von Kármán vortex street. This model is limited in its relevance to the physical problem since it does not include, among other factors, the presence of the body and viscous effects. In order to analyse the effects of waves on the wake of a circular cylinder more realistically, a two-dimensional Navier-Stokes solver was developed, based on the viscous CIC method first proposed by Graham (1988). Although this approach admits more realistic solutions to the physical problem, the additional complexity involved over the point vortex model means that the wake development cannot be studied for as long a natural period of time due to limitations of computer hardware. Moreover, it is found that three-dimensional viscous computations (presented in chapter 5) are constrained to an even greater restriction on the length of wake that can be modelled, although the approximation to the physical problem is probably closer still.

The results from the point vortex analysis in chapter 3 demonstrate that the effects of the variation in shed vortex strengths on the development of the wake should be observed at an earlier stage than those of the concertina-effect of the wave velocity field, because the growth of infinitesimal disturbances in the former case is much more rapid. This suggests that the rearrangement of the wake takes place close to the cylinder. All analyses have so far been concerned with the effects of waves on established streets; the circulation strength variation model presented in the latter half of chapter three attempted to account for the effects of a 'phantom' cylinder in the presence of a time varying velocity field, but the actual vortex formation process at the cylinder has as yet not been properly modelled. This problem is addressed in this chapter.

A two-dimensional viscous CIC code employing a conformal transformation to a periodic rectangular region with solution by a Fast Fourier Transform (FFT) method existed in the Department of Aeronautics, and the methodology and implementation of this code have been documented by Graham and his co-workers (e.g. see Zhou (1994)). To avoid too much repetition this thesis does not include a review of the method in its original form. Although this code is relatively fast, its main disadvantage derives from an inability to employ general meshes because of the conformal transformation of the coordinate system, which in itself often leads to numerical difficulties (e.g. Young (1989)). In its basic form the code is restricted to uniform polar meshes, which are ideal for the modelling of oscillatory flow problems in which the vortex structures remain in the vicinity of the body, in general. However, these mesh types are not so effective in the modelling of the far wake of a cylinder for which there is a major component of steady flow, since the elements of the mesh always become coarser away from the cylinder and the simulation of the far wake becomes progressively poorer. In fact, there is no practical way to ensure a near even

element size far from the cylinder, since simply increasing the number of elements over a given space implies that elements near to the cylinder become very small, and the time step limitations associated with such a fine mesh are prohibitively severe. For steady incident flow cases past a circular cylinder, the original code shows fairly strong distortions in the flow structures, which are a function of the rapidly increasing element size far from the body. In the present study of weak waves perturbing the wake of a circular cylinder in translation, it is vital that any artificial distortions which arise due to numerical inadequacy be minimised. In addition, for typical runs over polar meshes for steady incident flow past a circular cylinder approximately 90% of the elements have no vortices in, and this represents a substantial and unnecessary overhead in computer memory allocation.

A new two-dimensional viscous CIC code has been developed in the present work, which uses a Finite Volume solution technique on a block-unstructured mesh; in this case block-unstructured means that the solution domain comprises up to N structured grids, where N is the total number of elements in the computational domain. The elements are arbitrary quadrilaterals. The advantage of this approach is that regions of vortical flow may be targeted with smooth, dense distributions of elements, which implies better resolution of the far field flow structures and greater overall computational efficiency.

4.2 Methodology

4.2.1 Discretization

The Finite Volume method is based upon an integral form of the equations to be solved. The computational domain is discretized into elementary control volumes

over which the integration is carried out. The equations are cast in conservation or divergence form, and this approach ensures conservation of the working variables. In addition, complex geometries may be considered without the need of having the equations written in curvilinear form; only the node coordinates of each element are needed to prescribe the element, and local axis systems, which need not necessarily be orthogonal, can be used to define the set of volumes. Gauss' theorem may be used to relate a volume integral over the element to a surface integral around each element, such that integration over the element reduces to the summation of normal fluxes across the faces of each element. The guarantee of conservation may immediately be seen, since the normal flux leaving the face of one element is the same flux entering the neighbouring element. The Finite Volume approach has proved to be popular since it is straightforward to understand and is physically intuitive. Gauss' theorem for a closed bounded region in space R, whose boundary is a piecewise smooth orientable surface S is given by:

$$\int\int_R \int \nabla \cdot \vec{a}\, dV = \int_S \int \vec{a} \cdot \vec{n}\, dA \tag{4.1}$$

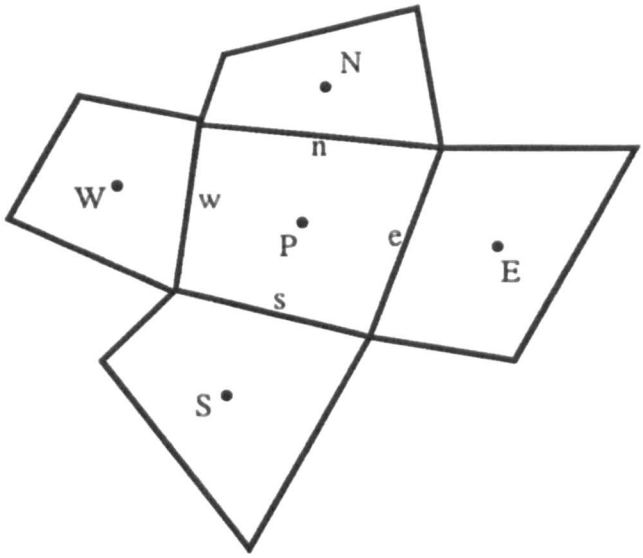
where $\vec{a}$ is a general vector and $\vec{n}$ is the outer unit normal vector from S. If $\vec{a}$ is replaced by the gradient of a general scalar, say ϕ, the equation becomes:

$$\int\int_R \int \nabla^2 \phi\, dV = \int_S \int \nabla\phi \cdot \vec{n}\, dA \tag{4.2}$$

In two-dimensions, a surface integral of the Laplace operator may be expressed in terms of the line integral of the normal gradient of ϕ along a closed contour C:

$$\int_S \int \nabla^2 \phi\, dA = \oint_C \nabla\phi \cdot \vec{n}\, dl \tag{4.3}$$

Figure 4.1 shows a typical arrangement of control volumes or elements in the computational domain, in which values of the working variable are solved for at the centroids of each element; the conventional notation for element connectivity is adopted, i.e. element Ω_P has centroid P with E(ast), N(orth), W(est) and S(outh) centroidal neighbours, and the respective interfaces are identified by lower case letters.



Element notation in Finite Volume code.

Figure 4.1

The local axis system (ξ, η) is defined as straight lines between the mid-points of each element interface, with the point P at the origin of this system. In general, the local axis system need not be orthogonal. The kinematic relationship between streamfunction and vorticity (equation (2.7)) is integrated over the element to give:

$$\int_{\Omega_P} \int \nabla^2 \psi \; dA = - \int_{\Omega_P} \int \omega \; dA \tag{4.4}$$

$$\Rightarrow \oint_{ensw} \nabla \psi \cdot \vec{n} \; dl = - \int_{\Omega_P} \int \omega \; dA \tag{4.5}$$

where $\vec{n}$ is now an outward unit normal vector from the interfaces e, n, w, s.

The different treatments for the evaluation of the normal fluxes gives rise to various types of Finite Volume methods used - see Peyret, Taylor (1983). If equation (4.5) is discretized, we get:

$$(\psi_E - \psi_P).a_e + (\psi_N - \psi_P).a_n + (\psi_W - \psi_P).a_w + (\psi_S - \psi_P).a_s = \Gamma_P \tag{4.6}$$

where the coefficients a_i; $i = e, n, w, s$ are geometric coefficients. For regular orthogonal elements the above equation is equivalent to central differencing at the interfaces. Note that Γ_P has not been defined yet. If the above discretization is carried out for all elements in the domain $(1 \rightarrow N)$, the N equations may be assembled into matrix form:

$$[A]\{\psi\} = \{b\} \tag{4.7}$$

where $[A]$ is a square [1] , symmetric matrix comprising all the geometric coefficients, $\{\psi\}$ are the unknowns, and $\{b\}$ contains the circulations and any source terms. This system is solved by the Preconditioned Conjugate Gradient method (see Appendix

[1] A convention of square brackets denoting a square matrix and braces denoting a vector is adopted in this thesis

B) to give: $\psi_P \; \forall P$. Once the streamfunction has been evaluated, the velocity field at each node is directly calculated by: $u = -\frac{\partial \psi}{\partial y}$ and $v = \frac{\partial \psi}{\partial x}$.

The diffusion equation, integrated over an element Ω_P is:

$$\int_{\Omega_P} \int \frac{\partial \omega}{\partial t} \, dA = \nu \oint_{enws} \nabla \omega \cdot \vec{n} \, dl \tag{4.8}$$

This equation can be solved explicitly (all spatial gradients of ω at time level n), implicitly (all spatial gradients of ω at time level $n+1$), or by a combination of the two. A fully implicit treatment represents a robust, stable algorithm, but is only 1^{st} order accurate in time; an explicit treatment is subject to time step limits for stability and again is 1^{st} order accurate in time. The diffusion treatment in the original FFT code is semi-implicit, i.e. implicit in one direction and explicit in the other, so that the leading term is 1^{st} order. The most commonly adopted method in the solution to a diffusion type equation is the Crank-Nicholson method, which is second order accurate in time, and has no theoretical time step limitations for stability. The Crank-Nicholson method is adopted here. The discretization of equation (4.8) over element Ω_P therefore becomes:

$$\begin{aligned} \frac{\omega_P^{n+1}.A_P}{\nu \Delta t} \; + \; & \frac{1}{2}[(\omega_P^{n+1} - \omega_E^{n+1}).a_e + (\omega_P^{n+1} - \omega_N^{n+1}).a_n + (\omega_P^{n+1} - \omega_W^{n+1}).a_w + \\ & (\omega_P^{n+1} - \omega_S^{n+1}).a_s] = \frac{\omega_P^n.A_P}{\nu \Delta t} - \frac{1}{2}[(\omega_P^n - \omega_E^n).a_e + (\omega_P^n - \omega_N^n).a_n + \\ & (\omega_P^n - \omega_W^n).a_w + (\omega_P^n - \omega_S^n).a_s] \end{aligned} \tag{4.9}$$

The coefficients $a_i; \; i = e, n, w, s$ are identical to those in equation (4.6). Again, after assembly over all the elements in the domain, this equation may be expressed

in matrix form:

$$[A + M]\{\omega\} = \{b\} \tag{4.10}$$

where $[M]$ is termed the 'mass matrix', $[A]$ is the discrete representation of the Laplace operator, and $\{b\}$ contains the RHS terms. The matrix that premultiplies the vector of unknowns is termed the stiffness matrix. The above system is solved using the Conjugate Gradient method to give: $\omega_P^{n+1}\ \forall P$.

4.2.2 Flux evaluation

The Finite Volume method for the Poisson equation requires the evaluation of the gradients of the working variables in a direction normal to the element faces. The scheme is 2^{nd} order accurate in that ϕ and first derivatives of ϕ exist through each element. The normal flux has a linear variation over each element interface, and therefore to calculate the integral of this flux variation, it is necessary to evaluate $\frac{\partial \phi}{\partial n}$ at the mid-point of the element interface. The fluxes of gradients of a general variable ϕ normal to (say) the east face are represented by the discretization $(\phi_P - \phi_E).a_e$. For non-orthogonal cells, evaluation of a_e is not straightforward and requires additional terms. Figure 4.2 shows the calculation of the gradient of ϕ at the east face of an element Ω_P.

Now,

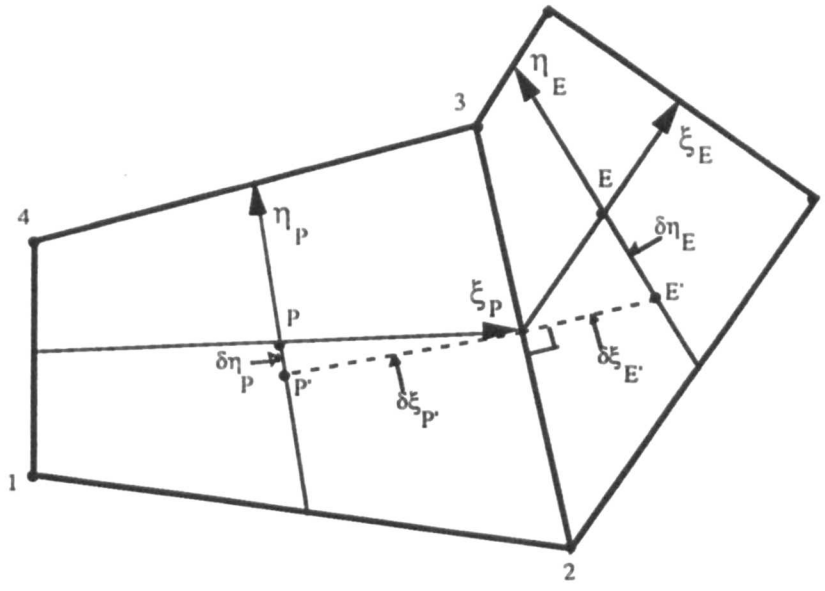
$$\left(\frac{\partial \phi}{\partial n}\right)_e = \frac{\phi_{E'} - \phi_{P'}}{\delta\xi_{P'} + \delta\xi_{E'}} \tag{4.11}$$

$$\phi_{E'} = \phi_E + \left(\frac{\partial \phi}{\partial \eta}\right)_E .(\delta\vec{\eta}_E \cdot \vec{\eta_E}) \tag{4.12}$$

$$\phi_{P'} = \phi_P + \left(\frac{\partial \phi}{\partial \eta}\right)_P .(\delta\vec{\eta}_P \cdot \vec{\eta_P}) \tag{4.13}$$

$$\Rightarrow \left(\frac{\partial \phi}{\partial n}\right)_e = \frac{\phi_E - \phi_P}{\delta\xi_{P'} + \delta\xi_{E'}} + \frac{\left(\frac{\partial \phi}{\partial \eta}\right)_E (\delta\vec{\eta}_E \cdot \vec{\eta_E}) - \left(\frac{\partial \phi}{\partial \eta}\right)_P (\delta\vec{\eta}_P \cdot \vec{\eta_P})}{\delta\xi_{P'} + \delta\xi_{E'}} \tag{4.14}$$

where $\vec{\eta_E}$ and $\vec{\eta_P}$ are unit vectors in the directions η_E and η_P respectively.



East face flux evaluation in Finite Volume method.

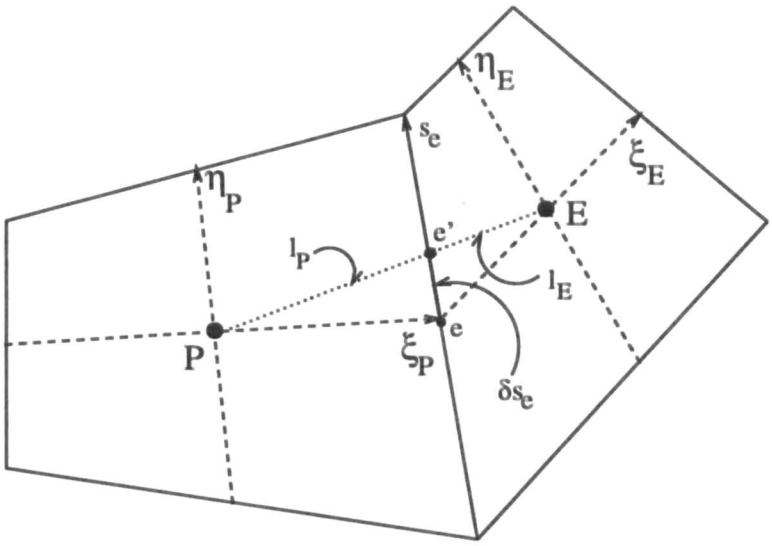
Figure 4.2

The second term on the RHS of (4.14) represents the non-orthogonal contribution to the east face coefficient, and becomes identically zero in the case of Ω_P and Ω_E both being orthogonal. The first term on the RHS is the orthogonal contribution and appears within $[A]$. It is therefore an implicit term, whereas the second term,

which is small in comparison with the first, is treated explicitly as a source term on the RHS of equation (4.10). The explicit term requires the evaluation of local gradients of the variable ϕ through the element, and this process is detailed below. The coefficients for the other faces (n, w, s) are dealt with in a similar fashion.

4.2.3 Gradient evaluation

The gradients of variables in the direction of the local coordinate system (ξ, η) of each element are needed at various times in the computation. Figure 4.3 again shows the detail for the east face of an element Ω_P:



East face geometry in Finite Volume method.

Figure 4.3

$$\phi_{e'} = \phi_P.(1 - f_P) + \phi_E.f_P \quad ; \quad f_P = \frac{l_P}{l_P + l_E} \tag{4.15}$$

$$\phi_e = \phi_{e'} - \frac{\partial \phi}{\partial s_e}.(\vec{\delta s_e} \cdot \vec{s_e}) \tag{4.16}$$

where $\vec{s_e}$ is a unit vector in the direction of face e (anti-clockwise convention), and f_P is a linear weighting factor. The gradient of ϕ in the direction of s_e may be evaluated by weighting the local gradients in the two neighbouring elements:

$$\frac{\partial \phi}{\partial s_e} = \left[\left(\frac{\partial \phi}{\partial \eta}\right)_P .(\vec{\eta_P} \cdot \vec{s_e}) + \left(\frac{\partial \phi}{\partial \xi}\right)_P .(\vec{\xi_P} \cdot \vec{s_e})\right] .(1 - f_P) +$$

$$\left[\left(\frac{\partial \phi}{\partial \eta}\right)_E .(\vec{\eta_E} \cdot \vec{s_e}) + \left(\frac{\partial \phi}{\partial \xi}\right)_E .(\vec{\xi_E} \cdot \vec{s_e})\right] .f_P. \tag{4.17}$$

Therefore the value of ϕ at e may be calculated explicitly. The gradient of ϕ in the ξ_P direction (say) then becomes:

$$\left[\frac{\partial \phi}{\partial \xi}\right]_P = \frac{\phi_e - \phi_w}{\delta \xi_P} \tag{4.18}$$

Since the value of the gradient of ϕ in the direction along the interface between the two elements is a function of the values of the gradients through each element, the calculation of ϕ_e, and therefore that of the gradients along the local systems (η, ξ) in each element, becomes non-linear and requires an iterative solution. The amount of iteration depends on the non-orthogonality of the local mesh.

In generating ϕ_e and ϕ_w from the centroidal values ϕ_E, ϕ_P and gradients through each element, care must be taken to ensure that ϕ_e and ϕ_w are locally bounded so that no new extrema are computed, which may lead to instabilities, i.e. :

$$(\phi_i)_{min} \leq \quad \phi_e \quad \leq (\phi_i)_{max} \quad i = P, E, N, S, NE, SE$$

$$(\phi_i)_{min} \leq \quad \phi_w \quad \leq (\phi_i)_{max} \quad i = P, W, N, S, NW, SW \tag{4.19}$$

4.2.4 Boundary conditions

The proper treatment of boundary conditions is essential in vortex methods. As described in the previous chapter on Vortex Methods, the solution to the Navier-Stokes problem is generally obtained by splitting the convection and diffusion operators in to two separate equations. In vortex methods, the convection stage consists of two sub-stages: (a) evaluation of the velocity field via the kinematic relationship between streamfunction and vorticity, (b) convection over the time step of the vortex particles by the computed velocity field. It may be shown (see Lamb (1932)) that for a given distribution of vorticity in space, the velocity (or streamfunction) field is explicitly calculable by specification of a zero normal component of velocity at a solid surface [2] alone. Stipulation of a tangential component of velocity at the solid surface (i.e. a second boundary condition for velocity) results in an over-specified equation system. This is true also of three-dimensional flows . Thus, evaluation of the streamfunction from a known vorticity field at time $n\Delta t$ results, in general, in the appearance of a tangential (or slip) component of velocity at the solid surface. This result is quite consistent and mathematically correct, since the calculated velocity field is the solution to the inviscid problem of a (compact) spatial distribution of embedded vorticity in an otherwise potential field inducing velocities at all points in the flow to infinity. However, the effect of a no-slip solid surface (i.e. wall) is to force the flow adjacent to the wall to have zero relative velocity; the existence of the finite tangential velocity at the surface of the wall, and specifically its line integral, is then interpreted in vortex methods as being kinematically equivalent to an infinitely thin vortex sheet that lies on the surface of the wall. This vortex sheet is equal and opposite in

[2] The more general case of a porous surface is not considered here.

strength to the local tangential velocity field and therefore exactly cancels it. This model of vorticity creation at solid walls was originally proposed by Lighthill (1963). The coupling between the inviscid solution to the embedded vorticity field and the diffusion of vorticity over a time step is therefore complete, since the vorticity in the exterior domain gives rise to a non-zero velocity field at the no-slip surface, which in turn provides a time-dependent boundary condition for the **creation** of vorticity from the wall. The diffusion of vorticity follows from the solution to equation (4.10).

The coupling between the inviscid solution and viscous solution is established at no-slip surfaces; thus, the boundary condition for vorticity at the wall 'drives' the solution to the vorticity field, and proper treatment of this condition is essential. The manner in which the the surface vortex sheet is introduced into the flow domain through the diffusion equation has been approached in essentially two different ways by researchers: one treats the appearance of the incremental vorticity value at the wall as a quantity which is held fixed over the time step, and is implemented as a Dirichlet type boundary condition; Chorin (1973) divides the strength of the vortex sheet by a length equal to the elementary discretization length on the body surface; Wu (1976) divides it by a distance from the wall to the first mesh point in the domain. The other approach is to regard the vortex sheet as a normal flux of vorticity that is generated over the time step; Koumoutsakos et al (1994) employ this method, which is fashioned as a Neumann type boundary condition for vorticity. The latter approach is used in three-dimensional calculations herein by the author, and the theory and reasons for adopting this method are detailed in chapter 5. The original FFT code developed by Graham and co-workers used a Dirichlet type boundary condition, and this method is adopted here for the Finite Volume CIC code.

The value of vorticity at the wall may be expressed via a Taylor series expansion of

ψ and ω in the vicinity of the wall:

$$\psi_P = \psi_0 + \left[\frac{\partial\psi}{\partial n}\right]_0 .\Delta n + \left[\frac{\partial^2\psi}{\partial n^2}\right]_0 .\frac{(\Delta n)^2}{2} + \left[\frac{\partial^3\psi}{\partial n^3}\right]_0 .\frac{(\Delta n)^3}{6} + ... \tag{4.20}$$

$$\omega_P = \omega_0 + \left[\frac{\partial\omega}{\partial n}\right]_0 .\Delta n + \left[\frac{\partial^2\omega}{\partial n^2}\right]_0 .\frac{(\Delta n)^2}{2} + \left[\frac{\partial^3\omega}{\partial n^3}\right]_0 .\frac{(\Delta n)^3}{6} + ... \tag{4.21}$$

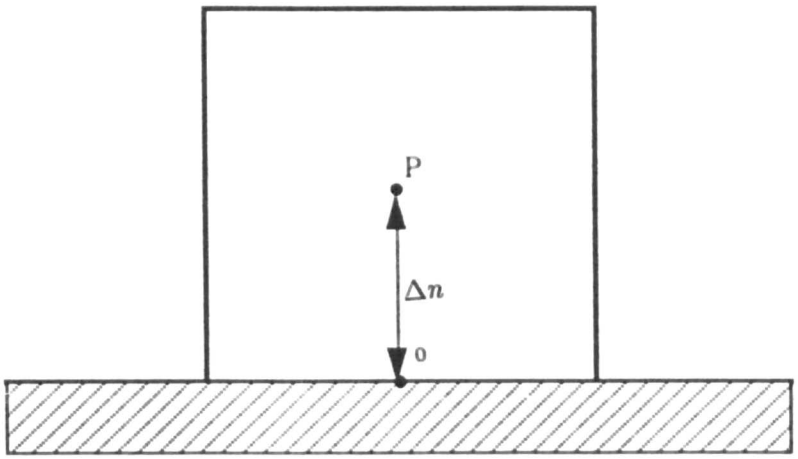
where the subscript $_0$ refers to values at the wall, and Δn is the normal distance from the wall to the point P (see figure 4.4). Noting that $\nabla^2\psi = -\omega$, and $\vec{u} = 0$ is imposed at the wall, we derive an expression for ω_0:

$$\omega_0 = (\psi_0 - \psi_P).\frac{3}{(\Delta n)^2} - \frac{\omega_P}{2}. \tag{4.22}$$

This is 2^{nd} order accurate in that the normal gradient of ω is accounted for using both equations (4.20) and (4.21). A 1^{st} order accurate expression for ω_0 is given by:

$$\omega_0 = (\psi_0 - \psi_P).\frac{2}{(\Delta n)^2} \tag{4.23}$$

Usually, a 1^{st} order treatment is employed as this is most robust; higher order methods have been shown to produce instabilities (Naylor (1982), Cozens (1987)) unless care is taken (see Roache (1972)). Here, it was found that a 2^{nd} order treatment of the boundary condition may be made stable by splitting equation (4.22) into an implicit and an explicit part, the implicit part being incorporated into the matrix $[A]$ for the solution to (4.10). The implicit term always has the same sign as the main diagonal term, and therefore by enhancing the diagonal dominance, the condition number of the stiffness matrix is lowered.



Geometry of boundary element

Figure 4.4

At inlets, and for boundary regions of the flow field far from the wake, the vorticity is zero, and a Dirichlet condition is used. At the outflow boundary, again far from the body and across which the wake may eventually pass, the normal outflow condition is used, *viz.*, $\frac{\partial \omega}{\partial n} = 0$. This condition is an approximation, since it implies that there is no normal variation of vorticity at the outlet, whereas in fact there will be a small amount of variation. Strictly, only at infinity is the above condition valid. Once particles cross this boundary, no attempt at tracking them is made, and they disappear from the computation.

The surface of the body prescribes a streamline, since the normal component of velocity at the surface is always zero. Therefore, the boundary condition for the streamfunction at the wall is $\psi_0 = \bar{\psi}$, where $\bar{\psi}$ is a constant, and by convention takes the value of zero. At the far boundaries the specification of the boundary

condition is a little more involved, and there are a variety of different types of condition that may be applied, each with a progressively greater degree of accuracy. The velocity of a vortex in an unbounded two-dimensional domain decays as $\frac{1}{r}$ and the streamfunction behaves as $\ln r$; since the computational domain is of finite limit, a vortex within the domain induces a finite, but (usually) small velocity at the far field boundaries. If we therefore consider the streamfunction to be comprised of a free stream term and a perturbation term at the far field boundary, we have:

$$\psi_{\infty} = \psi_{free} + \psi' \tag{4.24}$$

where $\psi_{free} = U_{\infty} y$ for the case of steady incident uniform flow parallel to the x-direction. The simplest approximation is to make is $\psi' = 0$, which implies that the far field is modelled as a straight streamline, and that the effects of solid blockage due to the body are negligible. The next level of approximation is to set the streamfunction equal to the potential value, and for the case of flow past a circular cylinder, this is a known analytic expression. This model takes account of the solid blockage of the body, and the far field streamlines are then curved (with the curvature going to zero as $r \rightarrow \infty$). This model takes no account of the vortical contributions to the far field boundary, i.e. the blockage due to the presence of the vortical wake is ignored. If the far field boundary is many body lengths away, and the body periodically sheds vorticity of opposite sign, i.e. is non-lifting in the mean, this model becomes quite a good approximation since the contributions from each of the von Kármán vortices in the wake approximately cancel each other out. The most 'complete' treatment of the boundary conditions evaluates the streamfunction at the far field boundaries from the entire vorticity field, and uses this in the following time step as a Dirichlet condition - i.e. the boundary conditions 'lag' the solution. The major problem associated with this technique is that it is computationally very

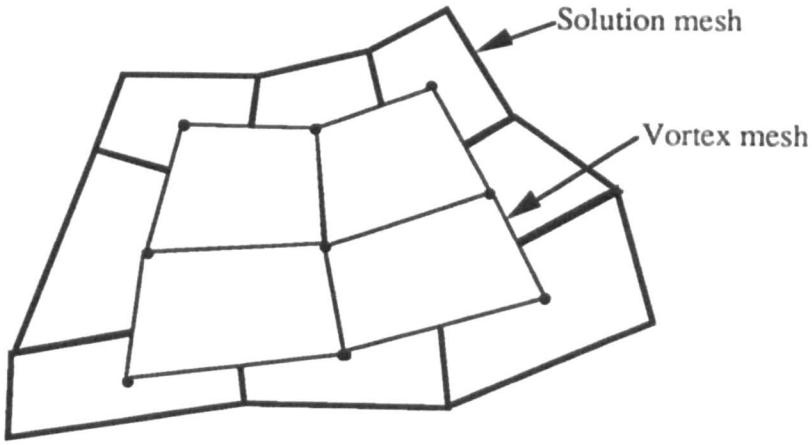
expensive, since it requires the direct evaluation of influences over $N_b \times N$ points, where N are the number of nodes in the domain, and N_b the number of boundary nodes. It has been reported (Graham - private communication) that up to 80% of the entire computational effort for two-dimensional flows may be consumed by calculation of the boundary conditions by this method; an approximation, which involves computing influences at only a few boundary points and applying a linear interpolation to all other boundary points reduces this enormous cost, but still represents a substantial effort. Sa and Chang (1990) present a method for two-dimensional streamfunction/vorticity computations in which the far field streamfunction value is computed from an integral expansion of the vorticity field; this is computationally cheaper than a direct summation method (they quote a factor of 10% of the total computing effort), and their results indicate that using this method allows the far field boundary to be brought in very close to the body (approximately 2D, where D is the cylinder diameter) without compromising the solution for flow past a circular cylinder at a Reynolds number of 20. In their tests on the various types of boundary conditions, they note that for a far field boundary which is about 40D from the body, all models give identical results; it is only as the boundary is brought in that differences become apparent. In the present computations, the potential solution was used as the far field boundary condition, and the mesh extended up to 30D from the body.

4.2.5 Interpolation from particles to mesh

The field equations (4.7) and (4.10) are solved for at the centroids of each element in the computational domain. The first of these equations (the streamfunction/vorticity equation) requires the evaluation of the following integral:

$$\int_{\Omega} \omega . dA \ . \tag{4.25}$$

In order to calculate this integral, vortices need to be interpolated onto the mesh nodes. The simplest way of doing this is to sum all the vortices that lie within a certain element, and assign the combined value of circulation to that centroid. However, this interpolation practice is of low order, since the contributions of any particular vortex to the mesh nodes are discontinuous as the vortex travels from one element to the next. A higher order scheme is to use bi-linear weighting to distribute each point vortex to a surrounding set of element centroids, as was used in the original FFT code. This requires the introduction of a second mesh ('vortex' mesh) whose nodes are coincident with the centroids of the 'solution' mesh (see figure 4.5).

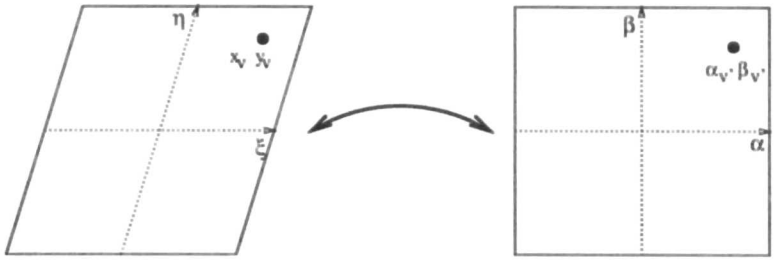


Solution mesh and Vortex mesh

Figure 4.5

If the derivatives of the local coordinate system in an element of the vortex mesh (i.e. $\frac{\partial \xi}{\partial x}, \frac{\partial \xi}{\partial y}, \frac{\partial \eta}{\partial x}, \frac{\partial \eta}{\partial y}$) are constant throughout (e.g. orthogonal and skewed elements see figure 4.6), the transformation between this element and the unit square is exact,

and bi-linear interpolation follows straightforwardly:



Transformation of a skewed element to the unit square.

Figure 4.6

$$\begin{aligned} \alpha_{v'} &= \frac{(x_v - x_P)}{\Delta\xi}.\frac{\partial\xi}{\partial x} + \frac{(y_v - y_P)}{\Delta\xi}.\frac{\partial\xi}{\partial y} \\ \beta_{v'} &= \frac{(x_v - x_P)}{\Delta\eta}.\frac{\partial\eta}{\partial x} + \frac{(y_v - y_P)}{\Delta\eta}.\frac{\partial\eta}{\partial y} \; . \end{aligned} \tag{4.26}$$

If however the above derivatives vary in space across the element, an iterative technique is required to calculate $(\alpha_{v'}, \beta_{v'})$ from the (x_v, y_v) position of vortex v.

The mapping between physical space (x, y) and the unit square is such that:

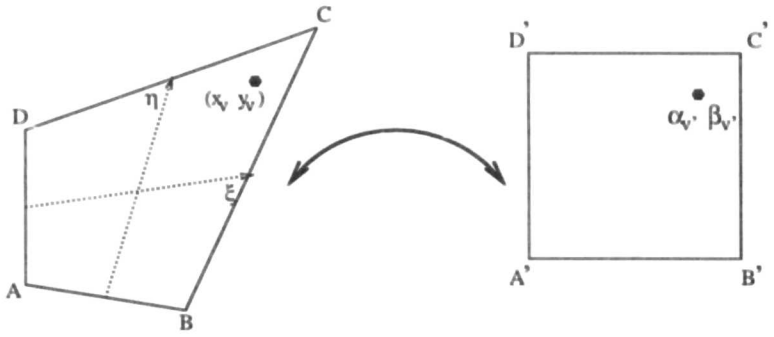
$$A \rightarrow A';\; B \rightarrow B';\; C \rightarrow C';\; \bar{\iota} \rightarrow \bar{\iota}' \; . \tag{4.27}$$

This implies that a general point lying in the $\alpha - \beta$ plane, of coordinates (α_g, β_g) maps to a point in the physical plane with coordinates (x_g, y_g), where:

$$x_g = (0.5 - \alpha)(0.5 - \beta)x_A + (0.5 + \alpha)(0.5 - \beta)x_B +$$

$$(0.5+\alpha)(0.5+\beta)x_C + (0.5-\alpha)(0.5+\beta)x_D$$

$$\begin{aligned} y_g \;=\; & (0.5-\alpha)(0.5-\beta)y_A + (0.5+\alpha)(0.5-\beta)y_B + \\ & (0.5+\alpha)(0.5+\beta)y_C + (0.5-\alpha)(0.5+\beta)y_D \end{aligned} \tag{4.28}$$



Transformation between a non-orthogonal element and the unit square

Figure 4.7

The local derivatives $\left(\frac{\partial x}{\partial \alpha}\right)_g$, $\left(\frac{\partial x}{\partial \beta}\right)_g$,$\left(\frac{\partial y}{\partial \alpha}\right)_g$, $\left(\frac{\partial y}{\partial \beta}\right)_g$ follow from equations (4.28) and (4.29). The method of finding $(\alpha_{v'}, \beta_{v'})$ is then to solve this system:

$$\begin{Bmatrix} x_v^* \\ y_v^* \end{Bmatrix} + [J] . \begin{Bmatrix} \Delta\alpha \\ \Delta\beta \end{Bmatrix} = \begin{Bmatrix} x_v \\ y_v \end{Bmatrix} \tag{4.29}$$

$$[J] = \begin{bmatrix} \frac{\partial x}{\partial \alpha} & \frac{\partial x}{\partial \beta} \\ \frac{\partial y}{\partial \alpha} & \frac{\partial y}{\partial \beta} \end{bmatrix} \tag{4.30}$$

where (x_v^*, y_v^*) are the iterates, $[J]$ is the Jacobian, (x_v, y_v) is the vector of knowns, and $(\Delta\alpha, \Delta\beta)$ are the unknowns, and represent the difference between the current value of the point in the $(\alpha - \beta)$ plane and the exact value. The algorithm is:

- Initialise: guess $\alpha_{v'}, \beta_{v'}$ (e.g. assuming an orthogonal system)
- calculate $[J]$
- calculate (x^*, y^*)
- calculate $((x_v - x^*), (y_v - y^*))$
- calculate $(\Delta\alpha, \Delta\beta)$
- calculate new values of (α, β)
- repeat calculation until convergence criteria are met.

The convergence rate of this equation system depends on the amount of spatial variation of the derivatives of the local system - i.e. on the condition number of $[J]$. The 'worst' elements in typical meshes required fewer than 5 iterations for convergence, though, of course, the vast majority of elements with vortex populations are orthogonal.

Once the mapped point is found, the weighting factors may be readily evaluated, and bi-linear interpolation from the vortex at (x_v, y_v) to A,B,C,D follows straightforwardly. The velocity field which is later calculated at all the nodes is interpolated to each vortex position using these same weighting factors.

Once all point vortices have been loaded on to the mesh points, the diffusion equation (4.10) is solved, and the **changes** in circulation over the time step are distributed back to the point vortices. The redistribution of circulation back to the point vortices is performed using the same weighting factors that were used in the interpolation stage from particle to mesh, i.e. if a node P has a population of vortices $(1 \rightarrow n_P)$ contributing to its value of circulation, each with a weight $0 \leq A_v^{(P)} \leq 1$, and the change in circulation at node P over the time step is $\Delta\Gamma_P$, then the incremental

circulation lumped back on to vortex v is:

$$\Delta\Gamma_v = \Delta\Gamma_P . \frac{A_v^{(P)}}{\sum_{j=1}^{n_P} A_j^{(P)}} \tag{4.31}$$

For the case in which $n_P = 0$ and $\Delta\Gamma_P \neq 0$, a new point vortex, of strength $\Delta\Gamma_P$, is released from the point (x_P, y_P). In Graham's original method (1988), the position of the point vortices are also shifted so that the integral of hydrodynamic linear momentum is the same before and after the redistribution of circulation. In the present code this was not followed, since Meneghini (private communication) reports little if any discernible difference between computed results for which the conservation of impulse is enforced and that for which it is not. In point of fact, since the present code is a Finite Volume code and has a spatial accuracy which is second order in that variables and their first derivatives are evaluated across each element, the solution to the diffusion equation should preserve all properties of the flow to the same order; whilst the re-interpolation from mesh node to particle is bi-linear, both the total circulation and its linear momentum should be conserved throughout. This is not necessarily guaranteed for a Finite Difference algorithm in which spatial accuracy deteriorates for unequal computational stencils.

4.2.6 Particle Tracking

In the original FFT code the integer location of each point vortex follows trivially from its coordinates in the transformed domain. The present code has no global $i - j$ axis system (i.e. is block-unstructured) and the process of tracking particles is a little more involved. The approach adopted here is to tag each particle with an integer identifier, which relates to the global element numbering system, and denotes the current element in which the particle resides. After the convection step, the original element is searched first, and if the particle is no longer resident, the

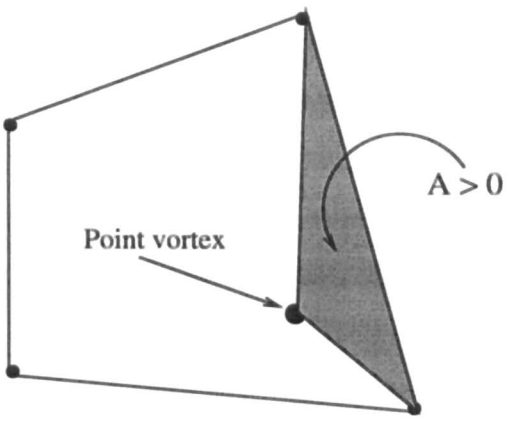
neighbours of this element are searched in preferential order. This *localised* searching method is fast, but of course requires additional memory allocation to store a vector of integers, whose length is equal to the number of particles in the computation - this is in excess of the total number of elements in the domain, typically by a factor of approximately 10 or less.

In order to determine whether or not a particle is resident in an element, the sign of the area formed by a triangle consisting of two nodes of each element interface and the particle is checked; the ordering convention of the nodes of each element is consistent such that the area of all elements are vectors of different magnitudes (in general), but of the same sign.

If the particle lies somewhere outside the original element, the search path goes in the direction of the maximum negative area calculated over all four interfaces of the original element. In calculating these areas, a tolerance is introduced so that if a particle lies on an interface (within say machine accuracy) it is included in the element; this is to make sure that the algorithm is able to determine at least one element of residence for each particle.

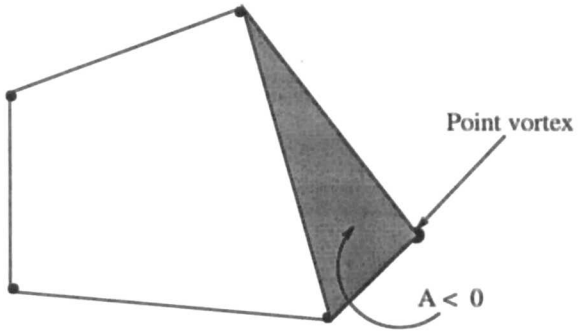
Figure 4.8 shows the case of a particle lying inside an element, and figure 4.9 shows the case of a particle lying outside an element.

In terms of computational cost, the tracking of particles scales as $O(n_v)$. Although the effort increases as more particles are introduced into the solution domain, in the overall computational budget, the computational effort represented by the tracking algorithm is very small.



Point vortex inside an element

Figure 4.8



Point vortex outside an element

Figure 4.9

4.2.7 Accuracy and Stability

There are a number of parameters which determine the quality of solution obtained with the viscous CIC method developed here. Since this is a hybrid method, there are parameters associated with both the mesh solution and the vortex particles. This section details the method of operator splitting, and the accuracy and stability of the convection and diffusion stages within the algorithm.

The equation to be split is the transport equation for vorticity:

$$\frac{\partial \omega}{\partial t} + (\vec{u} \cdot \nabla)\omega = \nu \nabla^2 \omega \tag{4.32}$$

Physically, this equation implies that the vorticity value $\omega(\vec{x}, t)$ at a given point in space is changing in time through a process of convection $((\vec{u} \cdot \nabla)\omega)$ by the velocity field, and by a process of diffusion $(\nu \nabla^2 \omega)$. Denoting these processes by the operators $C\{\}$ and $D\{\}$ respectively, the method of operator splitting attempts to 're-assemble' equation (4.32) from a series of linear substeps constructed from operators $C\{\}$ and $D\{\}$. The simplest such case is to have a single substep of $C\{\}$ and $D\{\}$, i.e. $[D\{\omega\}, C\{\omega\}]$ over the time step Δt. For a known vorticity field at time $n\Delta t$, the velocity field is obtained through solution to the Poisson equation for the streamfunction, i.e. $\nabla^2 \psi = -\omega^n \quad \rightarrow \psi^n \quad \rightarrow u^n$. The values of u^n at the solid surface serve as a boundary condition for the diffusion of vorticity. The changes in vorticity due to diffusion are then evaluated (via $D\{\}$). The new vorticity field, denoted (say) by ω^* is then convected using u^n, so the algorithm over the time step might be represented thus:

$$\omega^n \rightarrow [D\{\omega^n\}, C\{\omega^*\}] \rightarrow \omega^{n+1} \tag{4.33}$$

The convection velocity is based at time $n\Delta t$, and this is mathematically correct, since in a Lagrangian frame of reference, a Taylor series expansion of the position of the v^{th} vortex is given by:

$$x_v^{n+1} = x_v^n + \Delta t u_v^n + O((\Delta t)^2) \tag{4.34}$$

This two-substep scheme is 1^{st} order accurate in time. To increase the accuracy of the scheme more substeps must be added, and the accuracy of each substep must match (at least) the desired accuracy of the overall scheme, e.g.

$$\omega^n \rightarrow [D\{\omega^n\}, C\{\omega^*\}, C\{\omega^{n+\frac{1}{2}}\}, D\{\omega^{**}\}] \rightarrow \omega^{n+1} \tag{4.35}$$

with each operator $D\{\}$ and $C\{\}$ 2^{nd} order accurate in time yields an overall scheme which is 2^{nd} order accurate in time. In the current method, a 1^{st} order accurate scheme is used (see Summary of Algorithm section).

The Reynolds number of the flow dictates the relative importance of the two operators $C\{\}$ and $D\{\}$; for increasing Reynolds numbers, the contributions to the changes in ω over the time step from $D\{\}$ diminishes, and the overall scheme is dictated by the convection operator $C\{\}$. The converse is true for low Reynolds number flows i.e. the importance of $D\{\}$ rises, whilst that of $C\{\}$ diminishes.

The new vorticity field ω^* is convected by a velocity field $u = u^n(\omega^n)$, so, for example, the new particles introduced at the diffusing front are convected by a velocity field which was constructed in their absence. If the Reynolds number is low the changes in the vorticity field are large over a given Δt, so that the inconsistency between the vorticity and velocity fields is large at the end of the time step.

The convection of the vortex particles is done using a Backward Euler scheme; the scheme is stable for all values of Δt, and has an accuracy of $O(\Delta t)$. The stability of the solution to the diffusion equation is given by the following formula on a mesh of spacing Δx and Δy:

$$\nu\Delta t\left[\frac{1}{(\Delta x)^2}+\frac{1}{(\Delta y)^2}\right]\leq\frac{1}{2(1-2\theta)}\quad 0\leq\theta<1/2 \tag{4.36}$$

where θ is the fraction of implicitness in the scheme, i.e. $\theta = 0$ - scheme fully explicit, $\theta = 1$ - scheme fully implicit. For $1/2 \leq \theta \leq 1$ there is no theoretical stability limit. The Crank-Nicholson scheme ($\theta = 1/2$) has the benefit of being 2^{nd} order accurate, whilst for all other values of θ, the method is 1^{st} order accurate. The Crank-Nicholson scheme is employed here. Although the two operators $C\{\}$ and $D\{\}$ are unconditionally stable, it is difficult to quantify the stability of the overall scheme of $[D\{\}, C\{\}]$.

One of the advantages of the splitting method in terms of stability is that it is self-correcting, in that (say) a large vortex near to a wall induces a slip velocity at the wall, which in turn leads to the development of vorticity of opposite sign from the original vortex; diffusion of this vorticity at the wall then tends to cancel the original vortex. If a vortex particle passes through the wall (this is rare, but possible due to the accuracy of the convection step) the loss of vorticity in the field is compensated for at the following time step by the deficit in the slip velocity arising from the absence of the original vortex particle. However, it is possible that if a large number of particles pass through the wall the 'holes' created in the vorticity field near to the wall give rise to very sharp gradients of vorticity in a direction tangential to the surface, which can lead to the development of instabilities. These instabilities are usually manifested in the form of long wavy lines of point vortices which emanate radially from the cylinder.

If no particle has contributed to a node which subsequently has a non-zero value of vorticity after the diffusion step, a new particle materialises at the node. In the

case of $\theta \neq 0$ (in the above stability constraint for the diffusion equation), vorticity reaches all points in space instantaneously, though far away from the wake the value is very small indeed. In order that the mesh not become inundated with particles, a numerical 'cut-off' is introduced to limit the number of particles which exist through the domain. The value of the cut-off prescribed is based on a minimum level of vorticity, in contrast to other workers using the original FFT code (e.g. Cozens (1987), Meneghini (1993)) who used a cut-off based on a minimum value of circulation. It was felt here that a limit on vorticity rather than circulation was more appropriate since vorticity is the working variable, whereas circulation is an integral construct; near to the surface of the body where elements are very small (typical areas might be $O(10^{-3} \rightarrow 10^{-4})$) diffusion of vorticity from the surface leads to vorticity values of $O(1)$ a few nodes from the wall, although the circulation at these nodes might be several orders of magnitude less. Prescribing a circulation cut-off tends to discriminate against survival of vorticity in small elements. The value of the cut-off was fixed at 10^{-5} for the low Reynolds computations carried out here in which the free stream velocity has a value of 1 and the cylinder diameter has a value of 2. This value is close to that used by other workers (e.g. Meneghini 1993) for the mid to far wake where element areas are $O(1)$, but is much finer in the near wake region.

There are essentially three parameters associated with the non-orthogonality of the elements: (a) the number of iterative corrections to normal flux terms, (b) the number of iterative corrections in the calculation of gradients through an element, (c) the number of iterations to map the position of a point vortex to the unit square. Unfortunately, there is no definitive way of prescribing these parameters, but we seek an optimal compromise between computational expense and consistent accuracy through the scheme. In reality, the meshes which were used in the solution to flow past a circular cylinder were made as smooth as possible; a polar mesh sur-

rounds the cylinder, and this is linearly blended in the mesh generator with a regular cartesian mesh for the mid to far wake. The problem of non-orthogonality arises at the 'junction' of these two mesh types, but is most severe at the far (i.e. top and bottom) regions of the junction. The region where vortices pass is relatively smooth and orthogonal. Since the streamfunction is decomposed into a potential component and a vortical component, with the potential component being given by the analytic result for a circular cylinder, it was decided that it would be sufficient if the correction terms to the normal fluxes were treated explicitly - i.e. correction terms were calculated at a given time step, stored, and used as sources at the following time step. The fact that the time steps used are fairly small - the evolution of a large structure von Kármán vortex is discretized by around 1000 time steps - helps to justify this approximation of explicit corrections. In the calculation of gradients through an element, five iterations loops were used as this was found to be sufficient. The vortices in non-orthogonal elements were mapped on to the unit square until the change in position in the unit square was less than 10^{-5} - this represents an error in position of $\frac{1}{1000}\%$.

4.3 Code Validation

4.3.1 Introduction

Although convection is carried out by the incremental displacement of vortex particles, the code developed here resembles a standard Eulerian streamfunction/vorticity method quite closely; the evaluation of the velocity field and changes in the vorticity field through diffusion are both carried out through the solution to field equations over the computational elements. The convection of particles is algorithmically trivial, and the interpolation practices between mesh and particle are also relatively straightforward. Because of its hybrid nature, which entails the selection of a number of operational parameters, a full validation of the code in terms of robustness

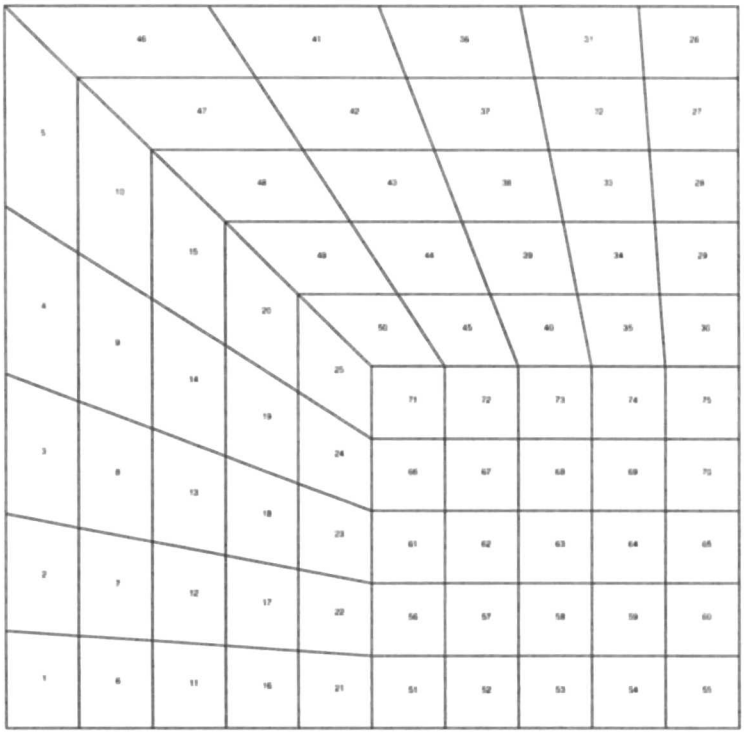
and accuracy is a difficult task. It is probably true that the formal accuracy and stability limits of the Eulerian part of the algorithm are more easily quantifiable, whereas ascertaining those pertaining to the Lagrangian part relies more heavily on experience and testing. There are, however, a number of basic tests that should be carried out on the code before starting to look at the interaction of waves on the wake of a circular cylinder.

4.3.2 Patch test on the Poisson solver

For a general analytic function which is linear over space, e.g. $\phi(x,y) = ax + by + c$, where a, b, c are constants, the algorithm which solves the Poisson equations in the code should give exact solutions at the nodes of the mesh, since the spatial accuracy in this code is 2^{nd} order; if the entire computational domain were discretized by a single element, the representation of the function across this element should be exact. The following system is solved:

$$\begin{aligned} \nabla^2\phi &= 0 \ \ in \ \ \Omega = \sum_{i=1}^{N_e} \Omega_i \\ \phi &= \bar{\phi} \ \ on \ \ \gamma = \sum_{j=1}^{N_b} \gamma_j \\ \bar{\phi} &= ax + by + c \end{aligned} \tag{4.37}$$

If ϕ is the streamfunction, i.e. $\psi = \phi$, this is the case of a steady uniform flow through the domain at an angle $\alpha = \tan^{-1}(a/b)$ to the x-axis. Clearly, one of the basic requirements of any code is that a uniform flow should remain uniform through the mesh, and the algorithm should be sufficiently robust to allow the use of distorted elements.



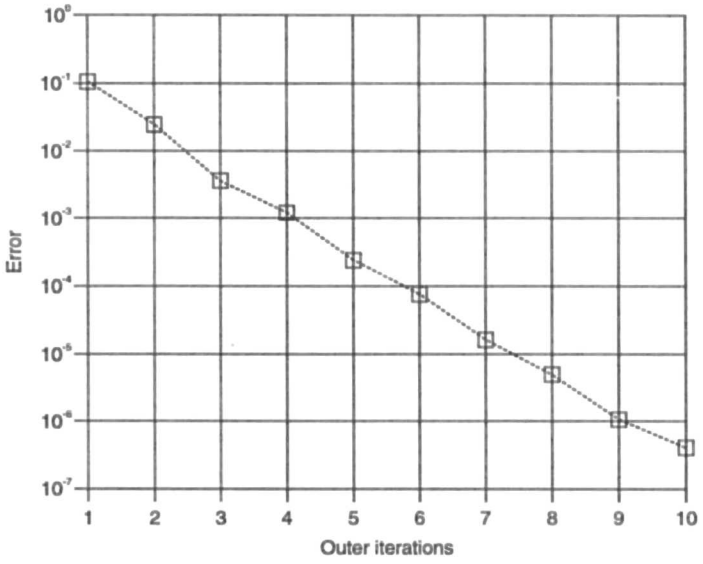
Mesh used in patch test

Figure 4.10

A simple test case is set up to solve equation (4.37) over the unit square. The mesh which is used in shown in figure 4.10, and the element numbering is shown. The elements in this case are much more distorted than those used in the computation of flows past circular cylinders. In this test case, $a = -1$; $b = 1$; $c = 0$, which represents the most 'difficult' function for this particular mesh.

Figure 4.11 is a plot of the maximum error (i.e. difference between analytic and numerical values) in the field as a percentage of the maximum value of the function over the unit square (i.e. 1.0). The horizontal axis is the number of iterations in the outer loop; in the outer loop the RHS source terms which arise due to local

non-uniformity of the elements are updated. These are corrections for the 2^{nd} order terms in the normal gradients of the function across element interfaces, and the amount of work done in solving the Poisson equation (inner iteration) diminishes very rapidly with each outer loop. It may be seen that there is a logarithmic decrease in the maximum error of the function across the domain over the outer loop, which goes to the order of the machine accuracy in about 10 outer iterations.



Maximum error versus outer loop iteration number

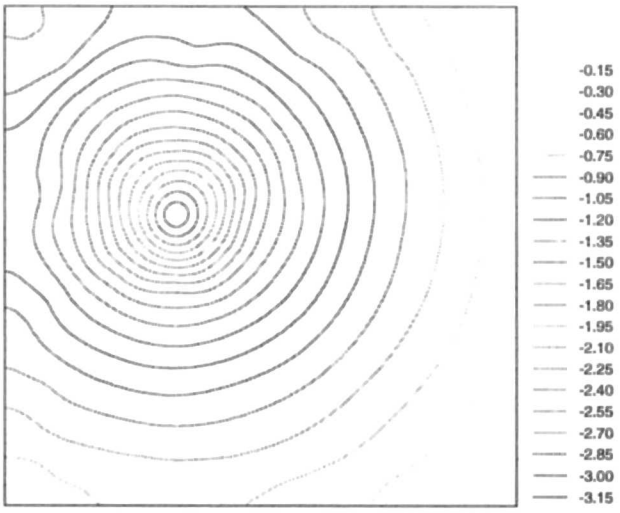
Figure 4.11

The maximum error is centred around $x = 0.5; y = 0.5$, that is in elements 71, 25 and 50.

4.3.3 Single point vortex in free space

Having established that the algorithms for the calculation of gradients normal fluxes are correct, the next step is to compare the numerical and analytic values of stream-function for a point vortex in free space. This test demonstrates the accuracy of

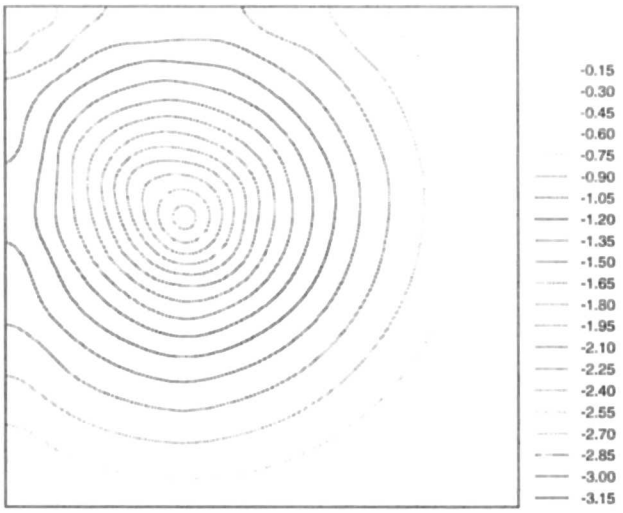
interpolating the circulation of the point vortex on to the mesh nodes to give the RHS source term for the streamfunction equation. Since the streamfunction for a single vortex behaves as $\ln r$, we would not expect an exact representation of the streamfunction over the domain, as was the case for the general linear function above. In this test the same mesh is used; a point vortex of strength 2π is placed in element 20 in the mesh. Figure 4.12 is a plot of the analytic solution at the mesh nodes, and figure 4.13 is a plot of the numerical solution after 5 outer iterations. From the analytic result it may be seen that the contour program apparently has difficulty in rendering what should be smooth concentric circles over this particular mesh.



Analytic solution of streamfunction for a single point vortex

Figure 4.12

The numerical result shows slight mesh dependence: the contours are fractionally pulled along a 45^o line top left of the vortex, in a region in which there is a sudden and large change in the directions of the local coordinate systems, e.g. between elements 15 and 48.



Numerical solution of streamfunction for a single point vortex

Figure 4.13

4.3.4 Steady incident flow past a circular cylinder

The previous results for the solution to the Poisson equation over the unit square have demonstrated the integrity of the algorithms of the code connected with the Finite Volume mesh solution for irregular meshes. There now follows a series of tests on steady incident flows past a circular cylinder at low Reynolds numbers. These cases additionally test the diffusion and vortex tracking algorithms; they include all factors relevant to the present study except the wave terms.

Much work, both experimental and numerical, has been carried out by many researchers in the study of steady flows past circular cylinders at low Reynolds numbers, and data such as forces, Strouhal numbers, base pressure coefficients, and flow visualisation are extensive. These flow cases therefore represent a good basis for

validation of the viscous CIC code developed here.

The tests are carried out on polar meshes, for which the outer diameter is at 60 radii. In each case there are 60 elements in the radial direction, and 100 in the azimuthal direction. Polar meshes are used since the primary concern of these tests is the presentation of force coefficients and Strouhal numbers; the structure of the far wake is of no concern here. Figure 4.14 is a table showing the present results compared with other computations (all 2-D), and some experiments.

Source	Re	S	$\overline{C_D}$
NUMERICAL:			
Present data	100	0.167	1.312
Savvides (1994)	100	0.162	1.296
Braza et al (1986)	100	0.16	1.37
Present data	200	0.196	1.260
Savvides (1994)	200	0.195	1.310
Braza et al (1986)	200	0.2	1.35
EXPERIMENTAL:			
Williamson (1991)	100	0.164	
Norberg (1992)	200	0.186	1.30

Summary of tests for steady incident flow past a circular cylinder.

Figure 4.14

The non-dimensional time step used in the present data is quite small, and is equal to: $\Delta t^* = \frac{\Delta t U_c}{D} = 0.0025$. The agreement between the present data and other computations is fairly good. The Strouhal numbers of the present data also agree well with those of Williamson (1991). The value of $\overline{C_D}$ from Norberg (1992) has

the skin friction empirically calculated and added to the pressure term and agrees reasonably well with the present data.

4.4 Wave Flows

4.4.1 Introduction

A series of numerical experiments are carried out to study the results of adding a progressive wave to the steady incident flow past a circular cylinder. The characteristics of the flow field are examined in the form of instantaneous plots of point vortices and vorticity contours; these demonstrate the dynamics of the vortices in the wake and the overall structure of the wake. In addition, the streamwise time-average structure of the absolute value of the vorticity field is presented, along with time traces of the transverse velocity component at various stations in the streamwise sense. The decay in streamwise flux of the time-average absolute value of vorticity ($\bar{|i|}$) at various streamwise locations is also presented; this gives a global indication to the decrease in the 'activity' of the flow away from the body.

We start by considering the far field free stream velocity to which the cylinder is subjected:

$$\begin{aligned} u(\vec{x},t) &= U_c + u_w \sin(\omega_w t - k_w x) \\ v(\vec{x},t) &= 0 \end{aligned} \tag{4.38}$$

where U_c is the translational velocity of the cylinder, u_w is the particle orbital speed induced by the wave, ω_w is the angular frequency of the wave, and k_w the wavenumber of the wave. Equation (4.38) is the velocity field of a progressive wave of wavelength $\lambda_w = \frac{2\pi}{k_w}$ travelling in the positive x-direction with a celerity

$c = f_w \lambda_w = \frac{\omega_w \lambda_w}{2\pi}$. The three-dimensional free surface wave problem also has components of velocity in the direction normal to the free surface (i.e. spanwise in this case) such that the divergence of this potential velocity field is identically zero. Since the vertical motions are not accounted for in this two-dimensional analysis, we are immediately faced with a problem of mass conservation in the potential field. Indeed, if equation 4.38 is used as the far field boundary condition for the potential solution to flow past a cylinder, it is found that the streamfunction solver yields solutions in which there exist large components of transverse velocity, which are spatially consistent with the wave. The solver is attempting to conserve mass and the resultant velocity field is clearly not representative of a two-dimensional section of the proper three-dimensional free surface wave problem.

The solution adopted herein is to split the temporal and spatial components of the phase of the wave so that the potential velocity field applied at the centroids of the computational elements consists of a steady free stream component plus a planar oscillatory component, whilst the velocity applied to the point vortices also includes the spatial component. The potential velocity field for the cylinder problem is therefore given by:

$$\begin{aligned} u_p(\vec{x},t) &= (U_c + u_w \sin\omega_w t)\left(1 - \frac{x^2-y^2}{(x^2+y^2)^2}\right) \\ v_p(\vec{x},t) &= -(U_c + u_w \sin\omega_w t)\frac{2xy}{(x^2+y^2)^2} \ . \end{aligned} \tag{4.39}$$

This velocity field satisfies continuity, i.e. $\nabla \cdot \vec{u}_p = 0$. The positions of the vortices are updated using the following velocity field:

$$u_v = u_p + u_r + u_w(\sin(\omega_w t - k_w x_v) - \sin\omega_w t)\left(1 - \frac{x^2 - y^2}{(x^2+y^2)^2}\right)$$

$$v_v = v_p + v_r - 2u_w(\sin(\omega_w t - k_w x_v) - \sin\omega_w t)\frac{2xy}{(x^2+y^2)^2} \tag{4.40}$$

where subscript $_p$ refers to the potential solution, $_r$ refers to the rotational or vortical solution, and $_v$ refers to the point vortex with integer identifier v. The vortices in the field have therefore been subjected to a velocity field as in equation 4.38. One problem arising from this approach is that the potential solution forms part of the boundary condition for the diffusion equation for vorticity, and clearly there is a finite but very weak spatial variation in the potential velocity field which is associated with the wavelength term of the wave, but this is not modelled. This anomaly becomes insignificant as the parameter λ_w/D becomes larger. The maximum error in the wave term velocity is approximately $2\pi D/\lambda_w$ for fairly large λ_w/D (say $\lambda_w/D \geq 20$), i.e. the difference in the actual and applied wave velocities in the vicinity of the cylinder has a maximum error of around $2\pi D/\lambda_w$; since u_w is itself small by comparison with U_c, the error becomes a 2^{nd} order one. e.g. consider the case: $\lambda_w = 30D$, $h = D/5$; the maximum error in the velocity field is given by:

$$u_w\frac{2\pi D}{\lambda_w} = \omega_w h\frac{2\pi D}{\lambda_w} = 0.06D^{\frac{1}{2}} \tag{4.41}$$

if the deep water dispersion relationship is used, with the gravitational constant of acceleration, $g = 9.81$ (see below).

The effect of ignoring the spatial variation of the potential field associated with the wavelength of the wave is felt only in the boundary conditions for vorticity creation; whilst vortices at the surface of the cylinder are never convected ($\vec{u} = 0$ there),

all vortices in the field experience both a temporal and spatial phase of oscillation.

There are two spatial parameters associated with the wave, which are:

$$\hat{\lambda} = \frac{\lambda_w}{D} \quad ; \quad \hat{h} = \frac{h}{D} \, . \tag{4.42}$$

Note that the parameter $\hat{h}$ is composed of h and D, rather than h and a (the inter-vortex spacing) as was the case in chapter 3 on the Point Vortex Analysis. Again, the relationship between wavelength and frequency is an arbitrary one in two-dimensions, but the deep water relationship is used here to link the two parameters. It is felt here that the parameter $\hat{f}$ is more important than $\hat{\lambda}$ in connection with the vortex formation and shedding processes, simply because of the scales which are of interest in this particular study. For gravity waves on deep water, a certain frequency implies a certain wavelength, and so the parameter $\hat{\lambda}$ is included in the table of parameters for the reason of consistency between the frequencies of the waves tested and the (approximate) correspondence this implies for wavelength of such waves in real, three-dimensional cases.

Once the cylinder is in motion, with speed U_c, a third parameter may be inferred for the relative time scales. A natural choice for this third parameter in this case is the ratio of the frequency of the wave to the natural vortex shedding frequency in the absence of the wave, i.e. $\hat{f} = \frac{f_w}{f_n}$, where $f_n = SU_c/D$. The deep water dispersion relation is used to link the wave frequency and wavelength,

$$f_w = \sqrt{\frac{g}{2\pi\lambda_w}} \, . \tag{4.43}$$

The parameter $\hat{u} = \frac{U_w}{U_c}$ may now be derived by specifying either the frequency of

the wave or the wavelength and $\hat{h}$, since:

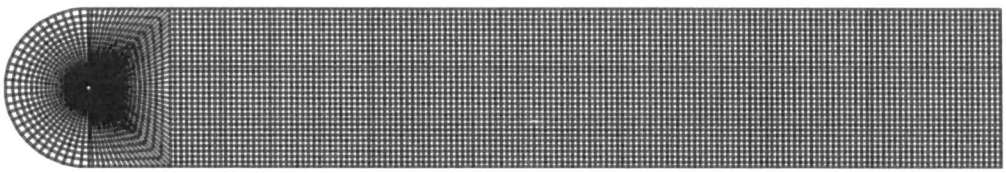
$$\frac{u_w}{U_c} = 2\pi S \left(\frac{f_w}{f_n}\right) \left(\frac{h}{D}\right) \ . \tag{4.44}$$

In all cases presented here, the Reynolds number is 150. This is near the upper limit of the two-dimensional vortex shedding regime for steady incident flow, and within the known 'working range' of the two-dimensional code.

4.4.2 Results

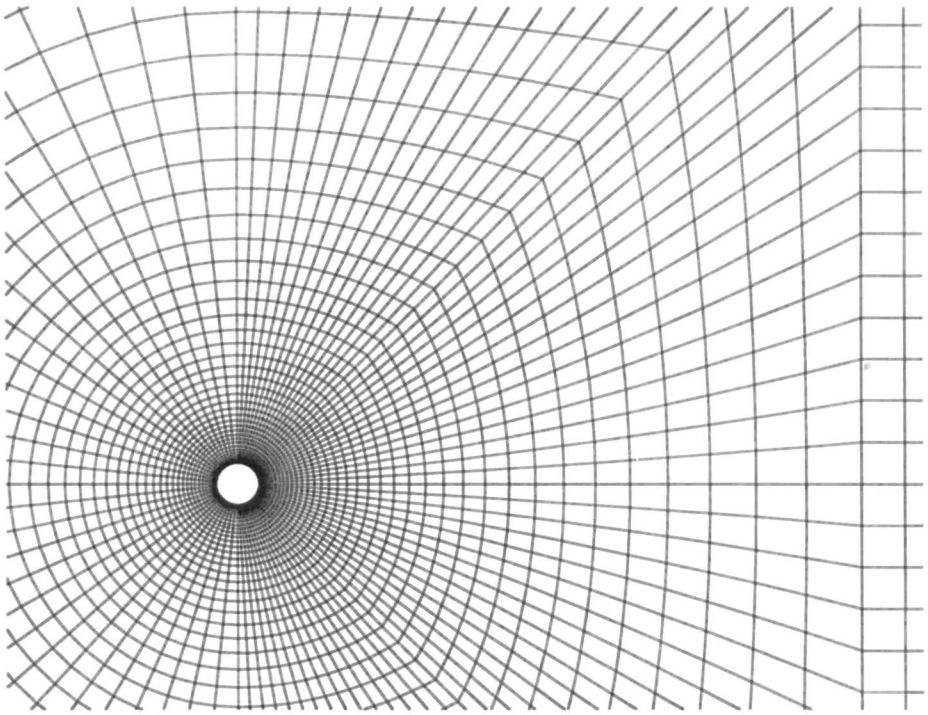
1.4.2.1 No Waves

The particular case of steady incident flow is presented first so that the effects of waves on the wake structure may be compared with a 'standard' result. The mesh used here is shown in figure 4.15, and an enlargement of the region around the cylinder, which shows the linear blending of a polar and square mesh downstream of the cylinder, is shown in figure 4.16.



Computational Mesh (8100 cells).

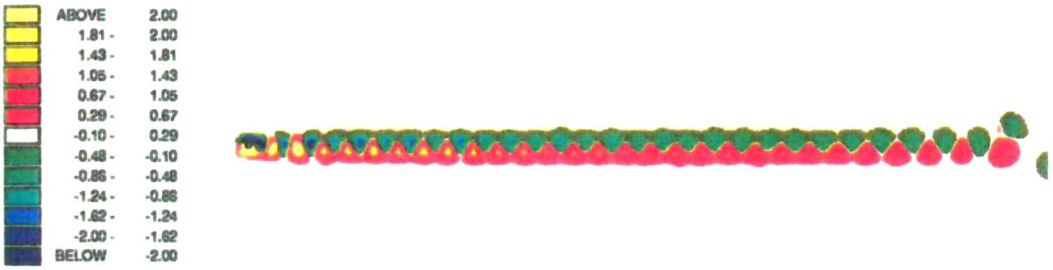
Figure 4.15



Enlargement of Computational Mesh near the Cylinder.

Figure 4.16

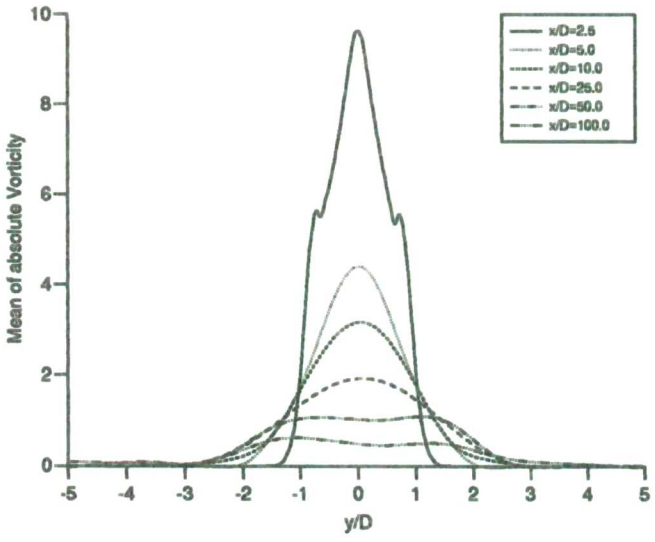
Figure 4.17 is a plot of the contours of vorticity at a non-dimensional time $t^* = U_c t/D = 165$. At the far right of the plot the start-up vortex may just be observed. All results presented here follow the same start-up procedure to encourage early vortex shedding. The start-up procedure consists of rotating the incident flow through an angle of some 6^o over the first few time steps, so that a bias in the vorticity distribution around the cylinder is established early on. All contour plots of the vorticity presented here span the range: $-2.5 < x/D < 150.0$ over the streamwise ordinate. Figure 4.17 shows that the strengths of the vortices downstream decay due to diffusion, and that the wake broadens slightly with distance downstream. Note that large scale distortions due to mesh inadequacies are not present.



Vorticity contours. $Re = 150$. No waves.

Figure 4.17

The change in the structure of the wake is perhaps best seen by examining the changes in the time-average values of absolute vorticity $\overline{|\omega|}$ with distance downstream. Figure 4.18 is a plot of this data at six streamwise stations in the wake. In evaluating the time-average structure of the wake, samples of the absolute values of vorticity are recorded and summed at all transverse points for the six streamwise stations at each time step; the mean is taken at the end of the computation.



Time-average of absolute vorticity. $Re = 150$. No waves.

Figure 4.18

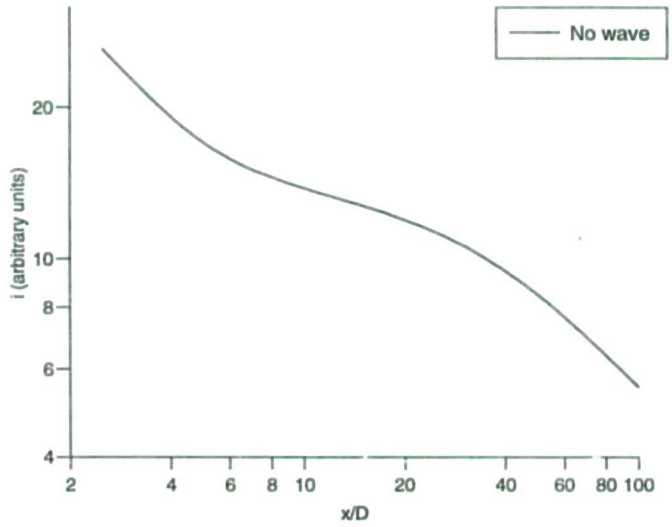
Since all flows computed here begin with the potential solution, the values at the sample stations are not recorded until a substantial portion of the vortical wake structure has passed by; this is to prevent any start-up transient from being included in the results.

Figure 4.18 shows the spatial variation of $\overline{|\omega|}$ in the transverse sense, and the general trend of the decay of $\overline{|\omega|}$ with distance downstream.

The value of the time-average of the absolute vorticity at a streamwise location in the wake is defined here as:

$$\bar{i} = \int \overline{|\omega|} dy \tag{4.45}$$

Assuming that this integral quantity $\bar{i}$ behaves as: $\bar{i} = \alpha(\frac{x}{D})^{-\beta}$, it is instructive to plot the variation of $\bar{i}$ with x/D on log-log axes. Figure 4.19 shows this plot for the steady incident flow case. The slope of this plot shows three separate regions, whose approximate intervals are: (1) $2.5 < x/D < 5$, (2) $5 < x/D < 40$, (3) $40 < x/D < 100$. Regions (1) and (3) have the same slope, and $\beta = 0.35$; the central interval has a slope $\beta = 0.23$. This plot indicates that the activity of the flow decreases quite rapidly behind the cylinder up to about $x/D = 5$, whereafter the decrease levels off substantially until about $x/D = 40$. Beyond $x/D = 40$ the activity of the flow again begins to decrease rapidly. From figure 4.18, it may be seen that up to about $x/D = 25.0$ the curves of $\overline{|\omega|}$ are bell-shaped, and $\overline{|\omega|}_{max}$ is located at $y/D = 0$. The transverse inter-vortex spacing in this region is relatively small, so that vortices from both the upper and lower rows contribute to the mean value of $\overline{|\omega|}$ along the centerline.



Variation of the time-average absolute vorticity with distance downstream.

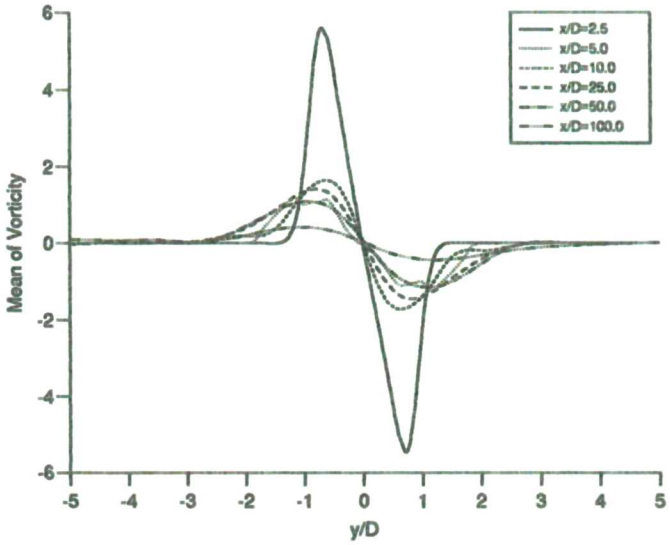
$Re = 150$. No waves.

Figure 4.19

Further from the cylinder (at $x/D > 25.0$), inflexion points appear in the curves. The transverse inter-vortex spacing increases with downstream distance, so that eventually one might expect two flattened peaks in the mean vorticity profiles very far downstream, with virtually zero at $y/D = 0$.

Figure 4.20 is a plot of the time-average of the vorticity field, i.e. $\overline{\omega}$, which is quite different from $\overline{|\omega|}$:

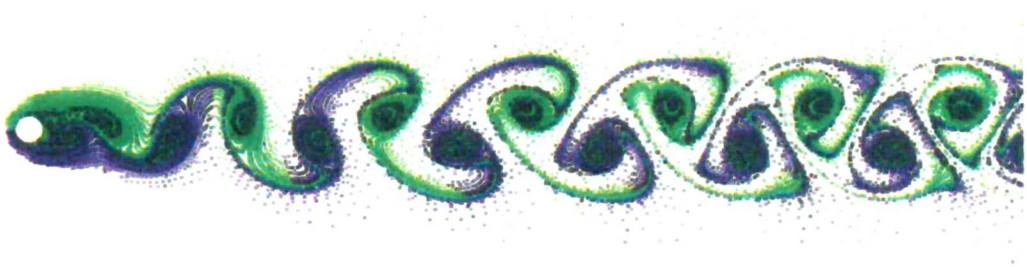
If the absolute of this function were to be taken, it may be seen that the function does not decay monotonically with distance downstream.



Time-average of vorticity. $Re = 150$. No waves.

Figure 4.20

The detail of the vortex structures in the near-wake is shown in the point vortex plot for this no wave case (figure 4.21).



Point vortices. $Re = 150$. No waves.

Figure 4.21

The Strouhal number for the steady incident flow case at this Reynolds number of 150 was found to be 0.182, through measuring the zero-crossings over many peri-

ods in the time trace of the transverse velocity field close to the cylinder.

1.4.2.2 Waves

Figure 4.22 is a table of the various wave cases studied here.

Case #	$\hat{\lambda}$	$\hat{f}$	$\hat{h}$	$\hat{u}$
1	30	2.265	0.077	0.2
2	30	2.265	0.193	0.5
3	30	2.000	0.087	0.2
4	30	2.000	0.219	0.5
5	30	1.825	0.096	0.2
6	30	1.825	0.240	0.5
7	60	1.565	0.112	0.2
8	60	1.565	0.279	0.5
9	60	1.295	0.135	0.2
10	60	1.295	0.338	0.5
11	100	1.200	0.146	0.2
12	100	1.200	0.364	0.5
13	100	1.000	0.175	0.2
14	100	1.000	0.437	0.5
15	200	0.690	0.253	0.2
16	200	0.690	0.634	0.5

Summary of wave cases.

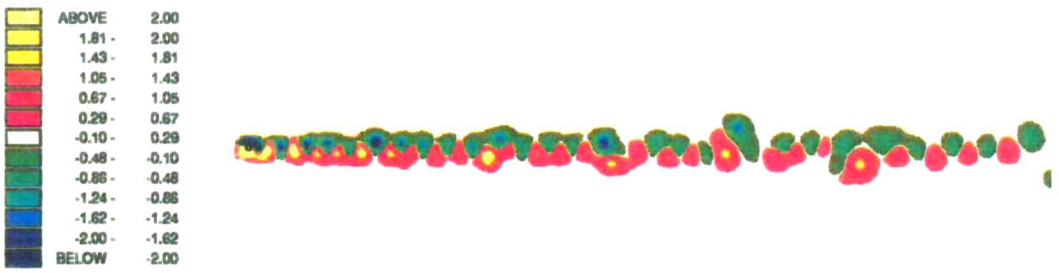
Figure 4.22

The range of $\hat{f}$ is quite large, and spans the two central values at which lock-in occurs for in-line oscillations ($\hat{f} = 2.0$) and transverse oscillations ($\hat{f} = 1.0$). Assuming that, as far as the near wake is concerned, the hydrodynamic effects of in-line oscillations and progressive wave-trains are correlated, the data from Griffin and Ramberg (1976), who conducted experiments on in-line oscillations of a circular cylinder in a steady free stream, indicate that not all the wave cases presented here lie within the lock-in region. Their experiments were carried out at $Re = 190$, which is close to that of the present data; data in the literature indicate that the effect of increasing Reynolds number is generally to broaden slightly the region of lock-in.

The wave cases are basically divided into two categories of weak ($\hat{u} = 0.2$) and strong ($\hat{u} = 0.5$) waves, each being studied over a range of frequencies ($\hat{f}$) and amplitudes ($\hat{h}$). Weak wave case numbers are odd, and strong wave case numbers even.

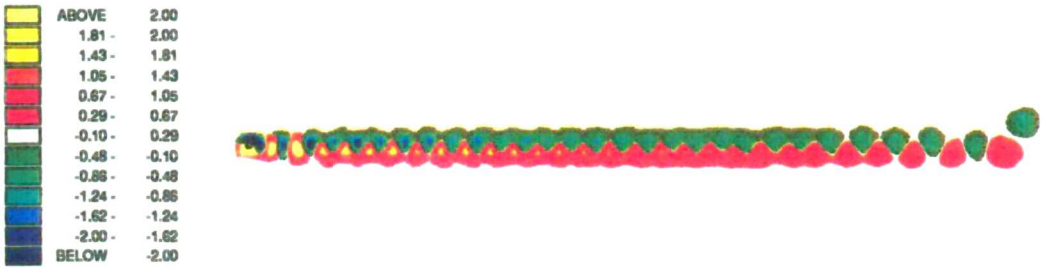
Weak Waves

Figures 4.23 to 4.24 are instantaneous vorticity contour plots of all the weak wave cases. All these data are at $t^* = 165$. The flow is from left to right, and the waves are propagating from left to right.



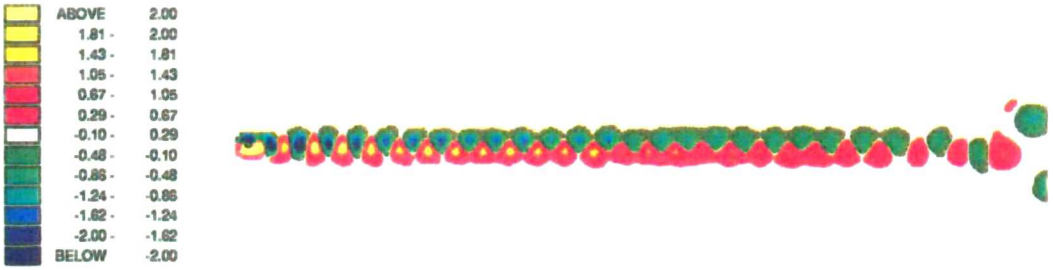
Vorticity contours. $Re = 150$. Case 1.

Figure 4.23



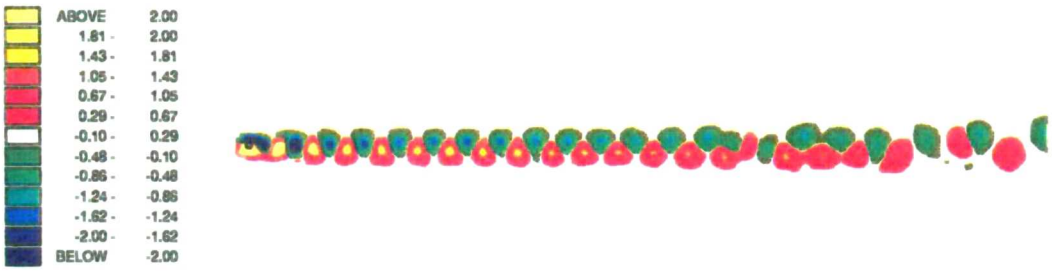
Vorticity contours. $Re = 150$. Case 3.

Figure 4.24



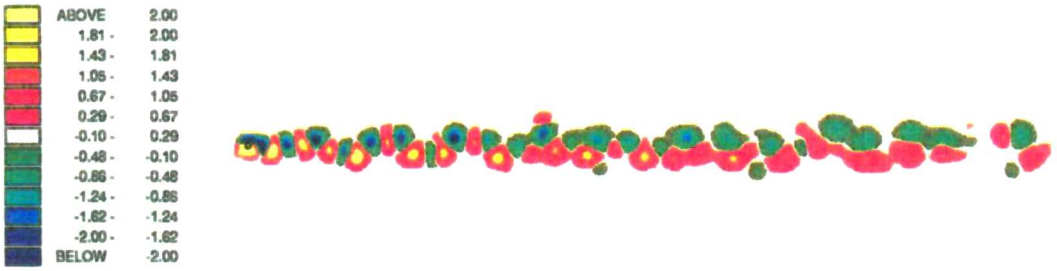
Vorticity contours. $Re = 150$. Case 5.

Figure 4.25



Vorticity contours. $Re = 150$. Case 7.

Figure 4.26



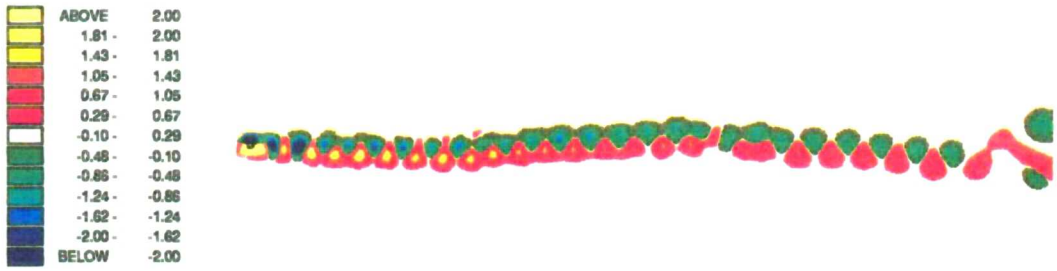
Vorticity contours. $Re = 150$. Case 9.

Figure 4.27



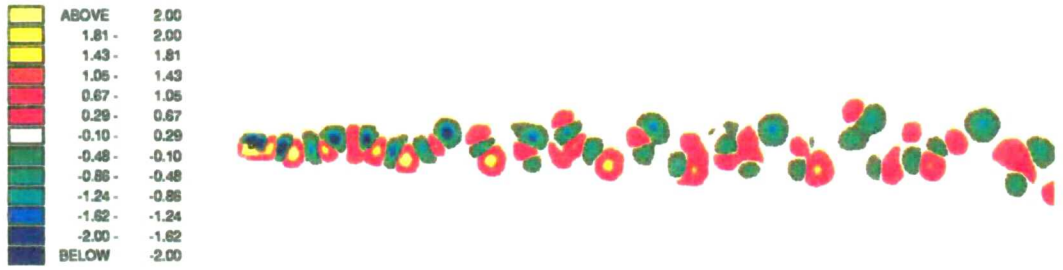
Vorticity contours. $Re = 150$. Case 11.

Figure 4.28



Vorticity contours. $Re = 150$. Case 13.

Figure 4.29



Vorticity contours. $Re = 150$. Case 15.

Figure 4.30

Figures 4.31 to 4.38 are plots of point vortices for all weak wave cases presented here, and show the vortex structures of the near-wake. The wakes are shown up to $x/D = 32.5$.



Point vortices. $Re = 150$. Case 1.

Figure 4.31



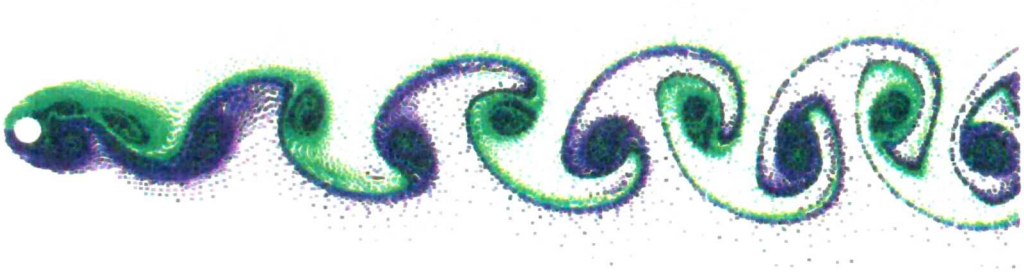
Point vortices. $Re = 150$. Case 3.

Figure 4.32



Point vortices. $Re = 150$. Case 5.

Figure 4.33



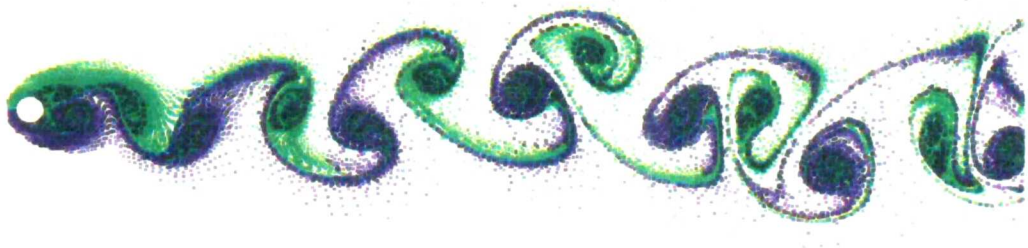
Point vortices. $Re = 150$. Case 7.

Figure 4.34



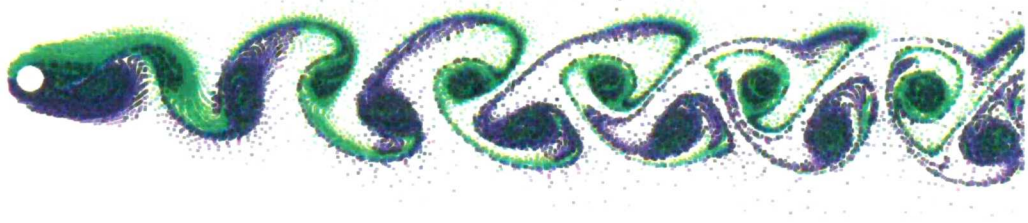
Point vortices. $Re = 150$. Case 9.

Figure 4.35



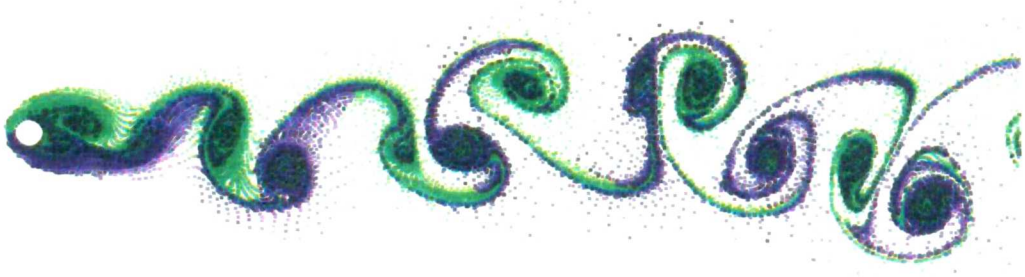
Point vortices. $Re = 150$. Case 11.

Figure 4.36



Point vortices. $Re = 150$. Case 13.

Figure 4.37



Point vortices. $Re = 150$. Case 15.

Figure 4.38

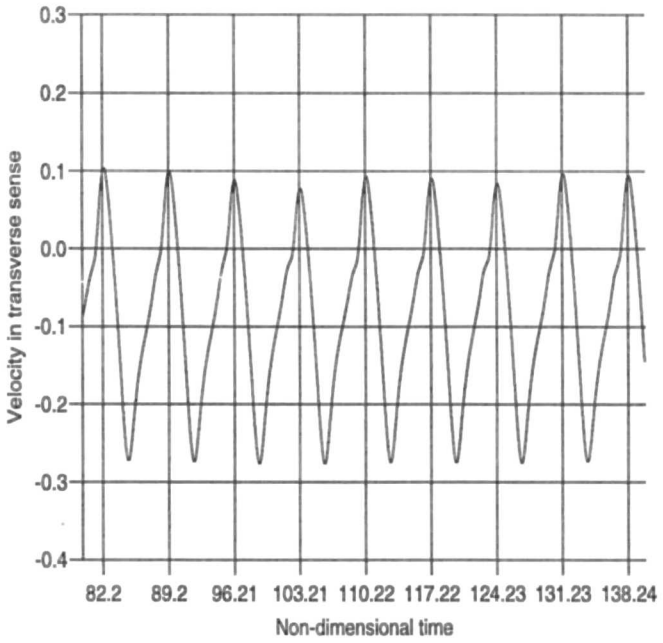
The characteristics of the wakes in the weak and strong wave cases are quite different. For weak wave cases for which $1.565 \leq \hat{f} < 2.267$ (cases 3,5,7), the wake is regular and closely resembles that of the steady incident flow case, in which alternate signed vortices are shed to form a staggered street. This is true even at very large distances downstream. It seems that for waves of this amplitude and within this frequency band, the stability of the resultant street is similar to the steady incident flow case. Case 3 most resembles the steady incident flow case, but as the frequency of the wave decreases, and the amplitude increases, the staggered structure of the wake is lost; in case 5 (figure 4.33) a modification to the wake structure is just beginning to appear at $x/D \approx 140$; in case 7 (figure 4.34) the modification point has moved closer to the cylinder, and the regular wake structure is lost at about $x/D = 100$.

At frequencies outside this range, the alternate pattern is disrupted fairly close to the cylinder. In the near-wake, the inter-vortex spacing is no longer regular, and the formation of vortex pairs is apparent (see figure 4.36). The irregularity of the inter-vortex spacing is generally small; the formation of a definite vortex pair is slow, and takes place several diameters downstream of the cylinder. Often, the vortex pair results from the interaction of three closely spaced vortices; such

a vortex triplet may be seen at $x/D \approx 24$ in figure 4.36. The two vortices with negative circulation vie with each other to form a pair with the central vortex. If the left-hand vortex succeeds, the resultant vortex pair has a self-induced velocity vector which is directed in the positive transverse direction, whilst if the right-hand vortex succeeds, the velocity vector is directed in the negative transverse direction. This competition to form vortex pairs is sensitive to relative vortex strengths and inter-vortex spacings. In weak wave cases the vortex pairs are not able to travel too far in the transverse sense due to the small differences in vortex strengths and inter-vortex spacings. The result is that the shape of the wake is mildly jagged (e.g. see figure 4.27), and not particularly broad far downstream of the cylinder, by which time of course, the vortex strengths have been greatly diminished by diffusion and vorticity cancellation. The far wakes of these cases are sometimes characterised by the presence of large vortex structures (e.g. see figure 4.27), which arise through the coalescence of like-signed vortices. In general, the vortices in these cases are not so compactly arranged, and once the staggered configuration has been interrupted close to the cylinder, the vortices tend to spread out in the longitudinal sense (e.g. see figure 4.28), with the lengthscale of the vortex structures increasing with distance downstream.

If the transverse velocity field is sampled close to the cylinder ($x/D = 2.5$, $y/D = 1.5$), it is observed that in cases (3,5,7) the period of the fluctuation in velocity is equal to *twice* the wave period. The vortex shedding has become synchronised with the wave. This synchronisation phenomenon, in which the wave is of sufficient amplitude and appropriate period to dictate the formation and shedding processes, has been studied for the case of cylinders and cables vibrating in-line (e.g. Griffin and Ramberg (1976)) and transversely (e.g. Meneghini (1993)). If the non-dimensional period of the flow is referred to by τ^*, and the usual subscripts are retained, then

in case 7, $\tau_w^* = 3.5025 \rightarrow \tau_n^* = 7.005$, and figure 4.39 is a plot of the time trace of the transverse velocity component at $x/D = 2.5$, $y/D = 1.5$. The increment on the x-axis has been set to $2\tau_w^*$.

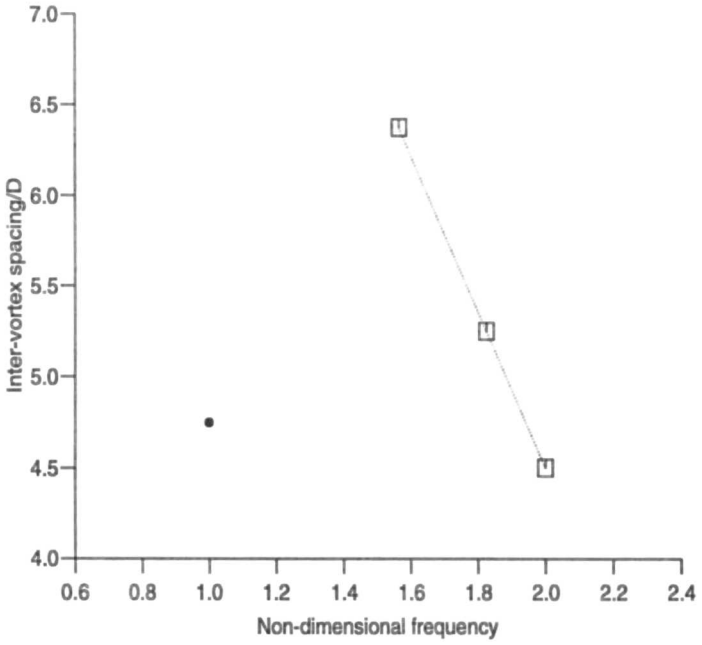


Transverse velocity sampled at $x/D = 2.5$, $y/D = 1.5$. Case 7.

Figure 4.39

From the corresponding point vortex plots of these cases (i.e. figures 4.31 to 4.38), it is possible to measure the longitudinal inter-vortex spacing (a). Care must be taken in doing so since these are instantaneous plots of point vortices and there is a finite wavelength wave imposing a concertina velocity field; providing $\lambda_w \gg a$ (as is the case here), where a is a typical inter-vortex spacing, then the errors will be small. Figure 4.40a is a plot of the values of the non-dimensional longitudinal inter-vortex spacing (a/D) versus non-dimensional frequency ($\hat{f}$). This plot applies to the synchronised cases only (3,5,7), although the special case of the $\hat{f} = 1.0$ (case 13) is also included (filled circle). The longitudinal inter-vortex spacing in this case

is the same as the steady incident flow case, and the vorticity contour plot (figure 4.29) shows that a regular staggered street has formed, although the wake has a weakly undulating nature. There is a very low beat frequency in this case, perhaps indicating that the Strouhal number in the wave case is not identical to the Strouhal number of the steady incident flow case (i.e. that $\hat{f} \neq 1.0$ exactly). Figure 4.40b is a plot from Griffin and Ramberg (1976) which shows the variation in longitudinal inter-vortex spacing over a similar non-dimensional frequency range. Unfortunately, no direct quantitative comparison is possible since the units used in both cases are different. The trend, however, is similar in both cases.

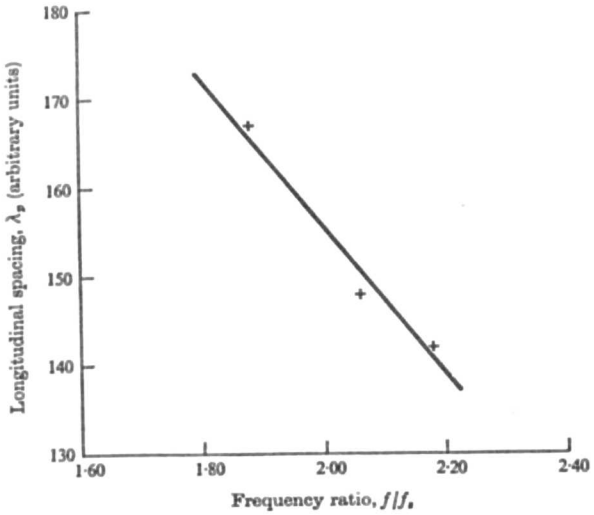


Variation of longitudinal inter-vortex spacing with frequency

Figure 4.40a

The three co-linear data points in figure 4.40a lie on a line of equation:

$$\frac{a}{D} = -4.25\hat{f} + 13. \tag{4.46}$$



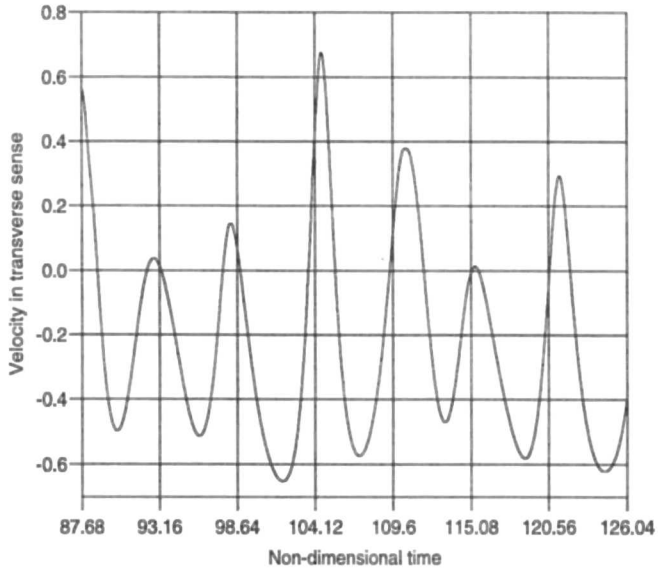
The longitudinal vortex spacing λ_p, measured from photographic negatives, as a function of in-line vibration frequency f/f_s. +, photographic measurements; ——, fitted straight line, $\lambda_p = 322{\cdot}50 + 84{\cdot}41 f/f_s$.

From Griffin and Ramberg (1976).

Figure 4.40b

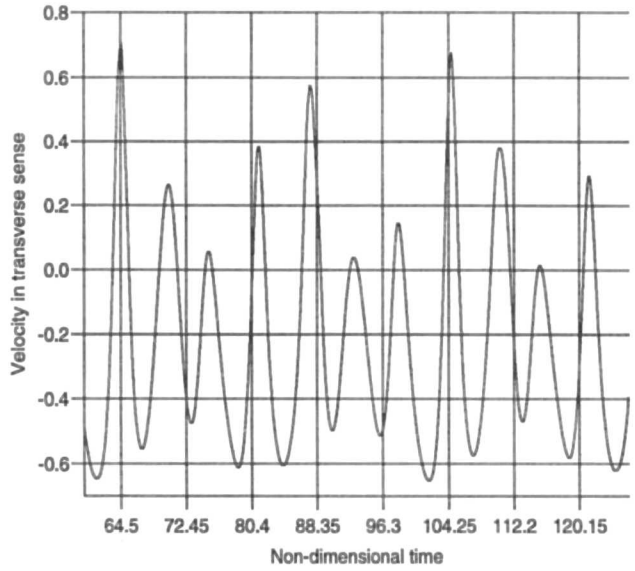
If samples of the transverse velocity fields are taken for the other weak wave cases (1,9,11,15) for which no regular street is observed, there appears a basic component of fluctuation which has a period approximately equal to the natural shedding period of the cylinder in steady incident flow; this period, non-dimensionalised, is the reciprocal of the Strouhal number. Figure 4.41 is a plot for case 15. (The increment of the x-axis is set equal to τ_n^*, the non-dimensionalised natural period of shedding).

Figure 4.42 is a plot of the same data as in figure 4.41, but the increment of the x-axis is set equal to τ_w^*. This figure shows that the peaks in transverse velocity coincide approximately with intervals of time which are divisible by an integer number of natural periods and wave periods.



Transverse velocity sampled at $x/D = 2.5,\ y/D = 1.5$. Case 15.

Figure 4.41



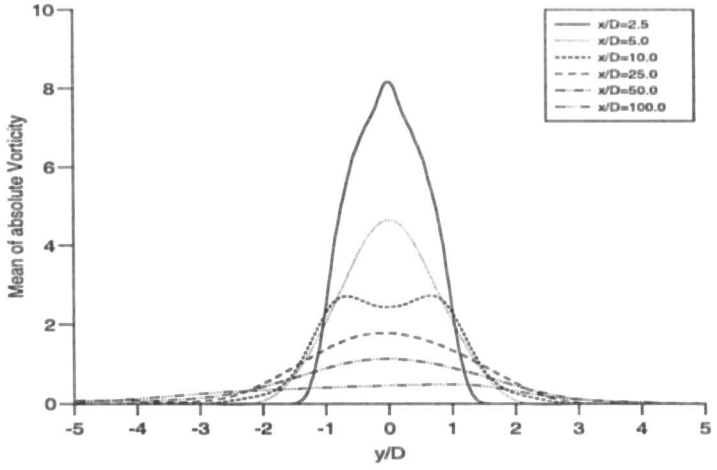
Transverse velocity sampled at $x/D = 2.5,\ y/D = 1.5$. Case 15.

Figure 4.42

All velocity time traces of the unsynchronised cases (1,9,11,15) exhibit the presence

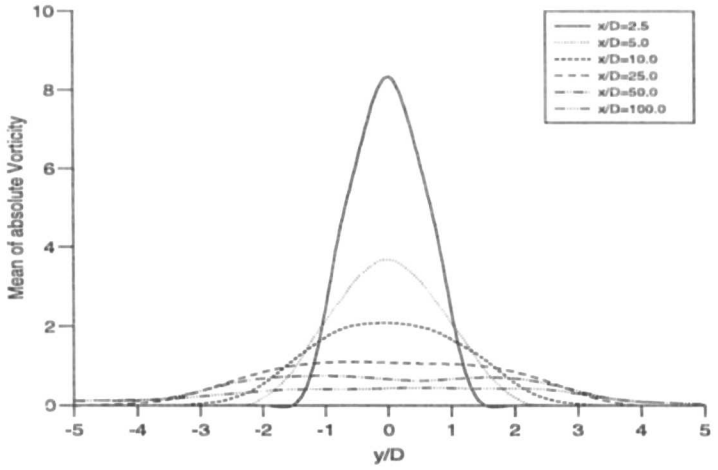
of a beat frequency.

Time-average information of the weak wave cases also shows differences between the wakes of cases which are synchronised with the wave, and those which are not. Figure 4.43 is a plot of $\overline{|\omega|}$ versus y/D for case 1. The curves are smooth and bell-shaped except for the data at $x/D = 10$, which exhibits a minimum at $y/D = 0$. Figure 4.44 is a plot of case 9; the curves are all smooth, bell-shaped, and become flattened as x/D increases. Examples of locked-in shedding are shown in figure 4.45 (case 5) and figure 4.46 (case 7). In the near wake it may be seen that the profiles of $\overline{|\omega|}$ have 'shoulders', which are more pronounced in case 5. The existence of these 'shoulders' is probably due to the effects of lock-in modifying the formation length, and shifting the thin free shear layers into the recording plane. This hypothesis must be a tentative one, since no detailed examination of the formation region was carried out.



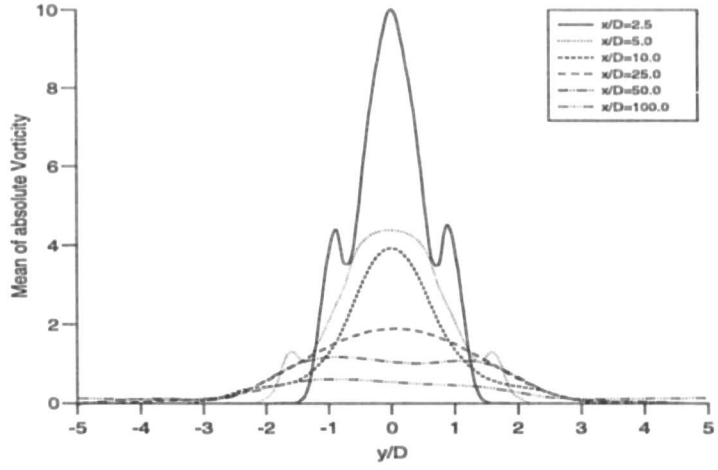
Time-average of absolute vorticity. $Re = 150$. Case 1.

Figure 4.43



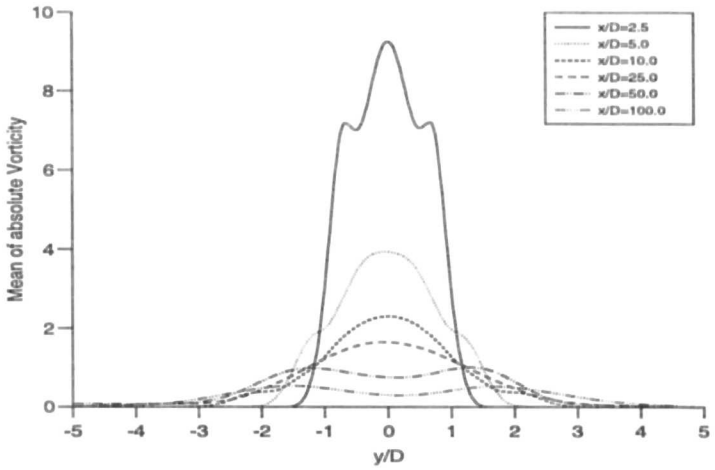
Time-average of absolute vorticity. $Re = 150$. Case 9.

Figure 4.44



Time-average of absolute vorticity. $Re = 150$. Case 5.

Figure 4.45



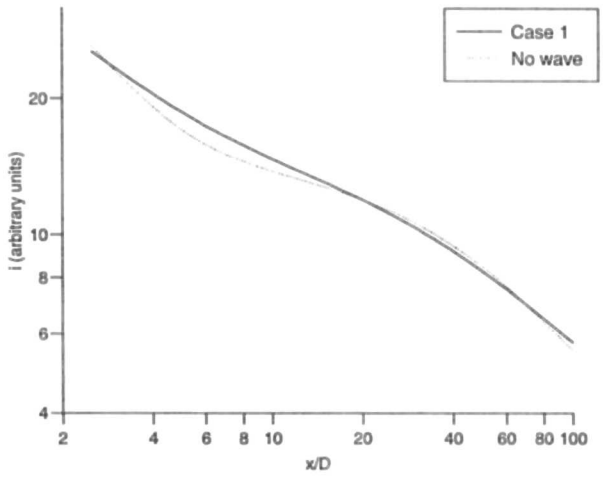
Time-average of absolute vorticity. $Re = 150$. Case 7.

Figure 4.46

Plots of the decay in the time-average absolute vorticity termfor the various wave cases are shown in figures 4.47 through to 4.54. Several points of interest are to be made concerning the shapes of these curves for the different wave cases. Consider first the cases for which the vortex shedding is not synchronised to the wave; i.e. cases 1,9,11,13 and 15 . The curves for these cases bare a close resemblance to the steady incident flow case (plotted on each figure as a dotted line), although, in general, all curves are flatter, and do not display such a prominent delineation between the three different regions downstream. In general, the near- and mid-wake regions (i.e. up to $x/D \approx 40D$) follow the steady incident flow case very closely, although the rate of decay of activity of the flow is slightly weaker for all cases except 15 in the near-wake. In the far-wake region, the rate of decay is flatter in all cases so that at $x/D = 100$ the value of activity of the flow in absolute terms is greater for the wave cases.

Paradoxically, the most interesting cases are those for which the wake is regular,

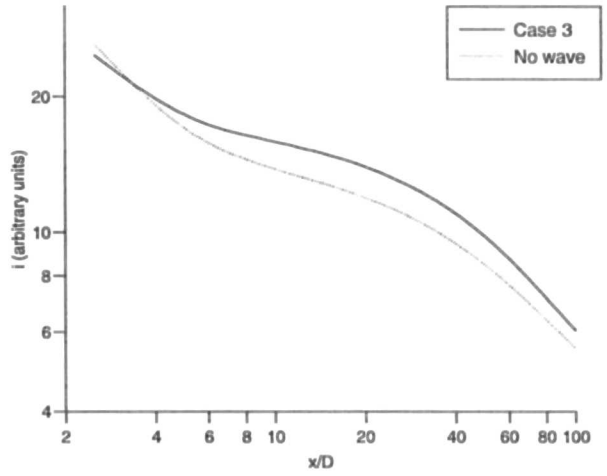
and the vortex shedding is synchronised to the wave (cases 3,5 and 7). The first thing to note about these data (figures 4.48, 4.49 and 4.50) are the large differences in absolute terms from the steady incident flow case. These differences arise because of the altered streamwise inter-vortex spacing in the wake. However, the rate of decay of the time-average absolute vorticity term is very different in each of the cases. Case 5 shows a remarkably similar form to the steady incident flow case; if the data from case 5 were to be shifted downwards by a constant amount, the agreement between the two sets of data would be very close. So although the level of activity of the flow in case 5 is much greater, the rate at which this activity decays with distance downstream is very similar to the steady incident flow case. Case 3 demonstrates a decay rate in the near-wake which is weaker than the steady incident flow case, and one in the far-wake which is slightly greater. The reverse is true of case 7, which lies at the other boundary of the lock-in region, i.e. the initial decay rate is stronger than the steady incident flow case, but the far-wake rate is weaker. In both cases, however, the value of the time-average absolute vorticity flux is greater at $x/D = 100$ than in the steady incident flow case.



Decay of the time-average of absolute vorticity with distance downstream.

Case 1.

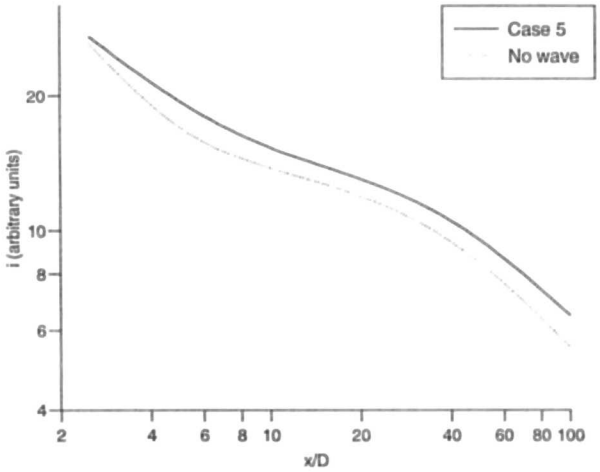
Figure 4.47



Decay of the time-average of absolute vorticity with distance downstream.

Case 3.

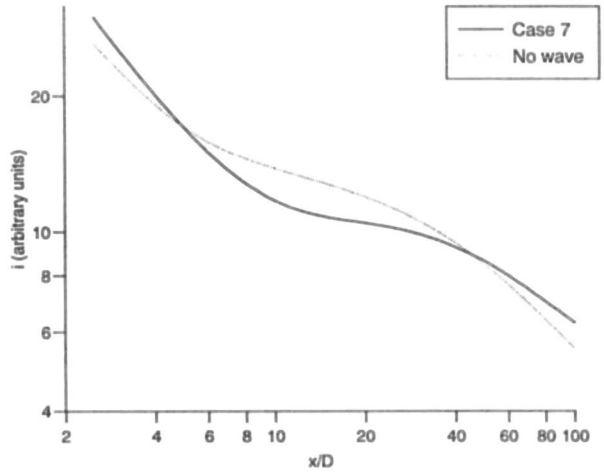
Figure 4.48



Decay of the time-average of absolute vorticity with distance downstream.

Case 5.

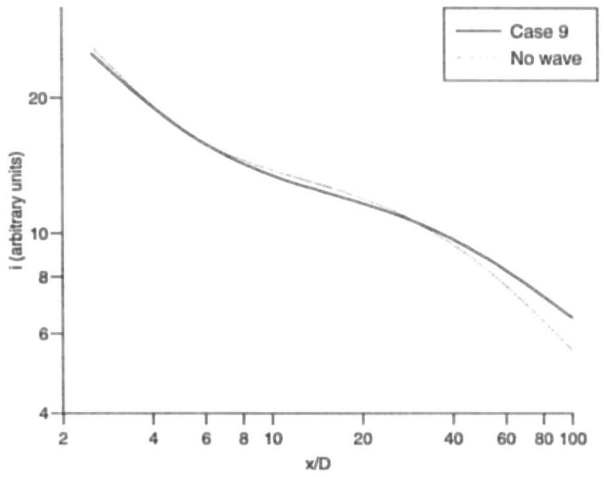
Figure 4.49



Decay of the time-average of absolute vorticity with distance downstream.

Case 7.

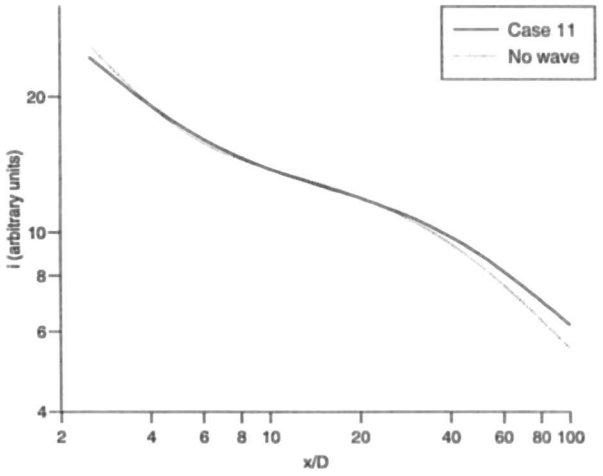
Figure 4.50



Decay of the time-average of absolute vorticity with distance downstream.

Case 9.

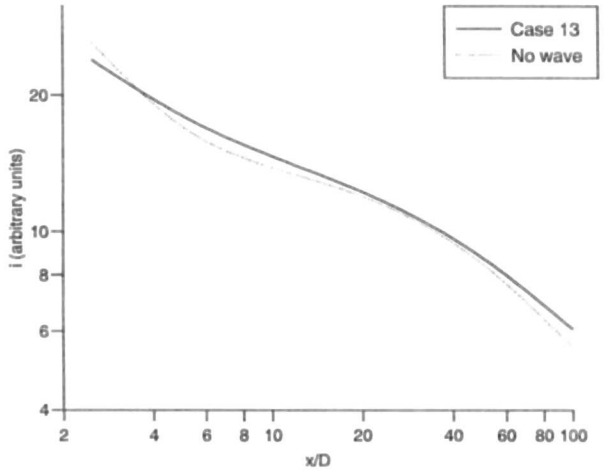
Figure 4.51



Decay of the time-average of absolute vorticity with distance downstream.

Case 11.

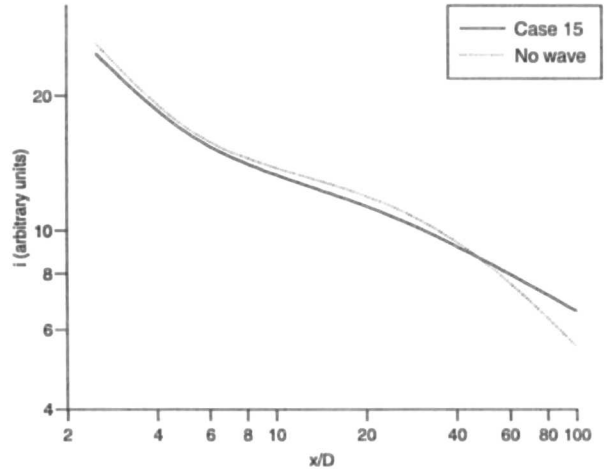
Figure 4.52



Decay of the time-average of absolute vorticity with distance downstream.

Case 13.

Figure 4.53



Decay of the time-average of absolute vorticity with distance downstream.

Case 15.

Figure 4.54

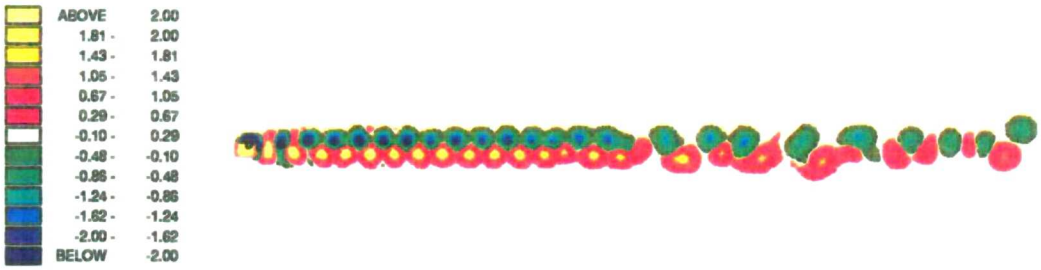
Strong Waves

The strong wave cases ($0.192 \leq \hat{h} \leq 0.633$) generally have broader wakes, and demonstrate a rich variety of vortex configurations. Figures 4.55 to 4.70 are the vorticity contour and point vortex plots for these cases. Again, they are arranged in an order of descending frequency, increasing amplitude. The flow is from left to right, and the waves are propagating from left to right.



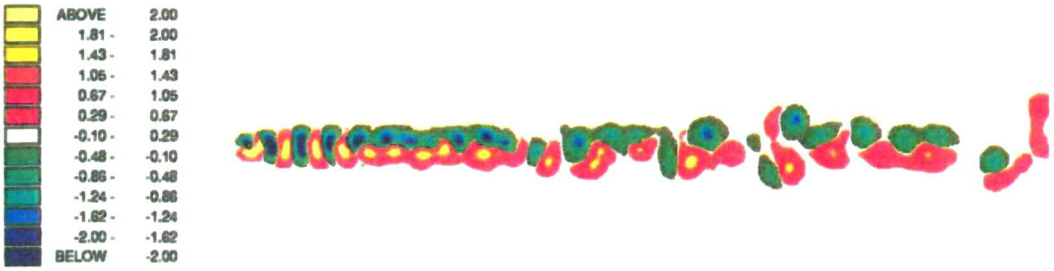
Vorticity contours. $Re = 150$. Case 2.

Figure 4.55



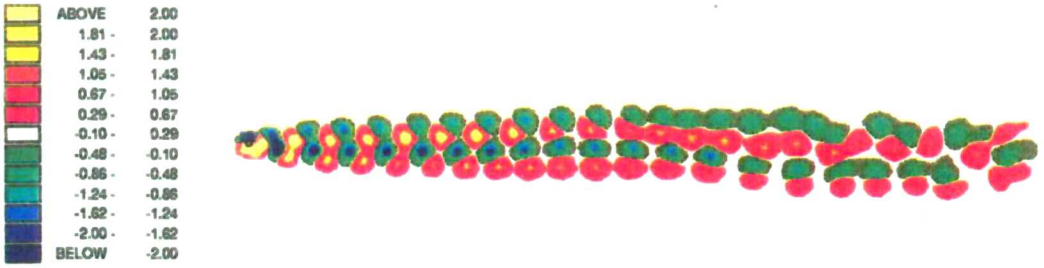
Vorticity contours. $Re = 150$. Case 4.

Figure 4.56



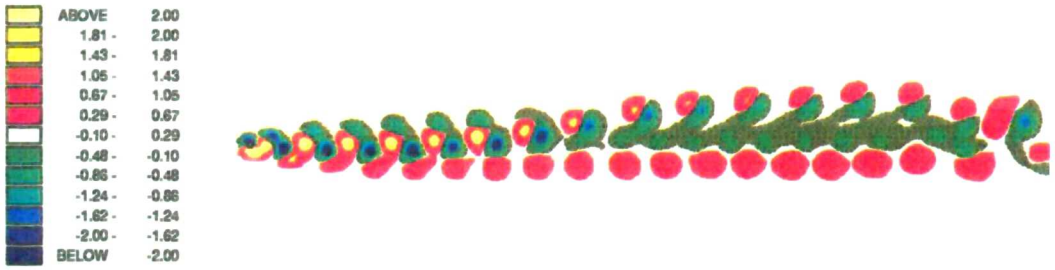
Vorticity contours. $Re = 150$. Case 6.

Figure 4.57



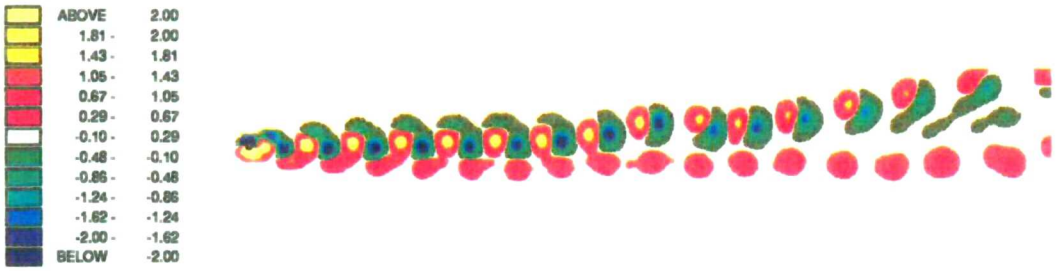
Vorticity contours. $Re = 150$. Case 8.

Figure 4.58



Vorticity contours. $Re = 150$. Case 10.

Figure 4.59



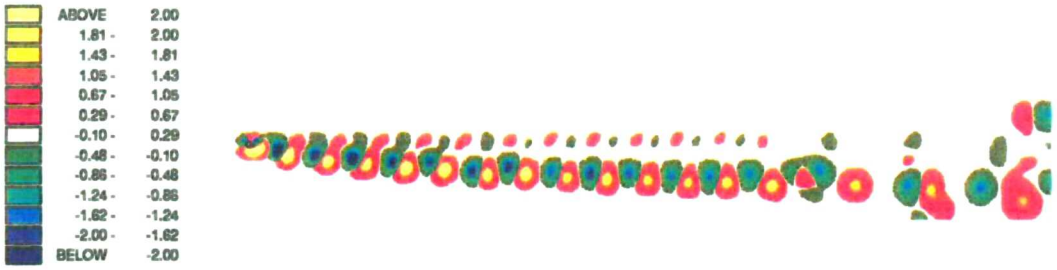
Vorticity contours. $Re = 150$. Case 12.

Figure 4.60



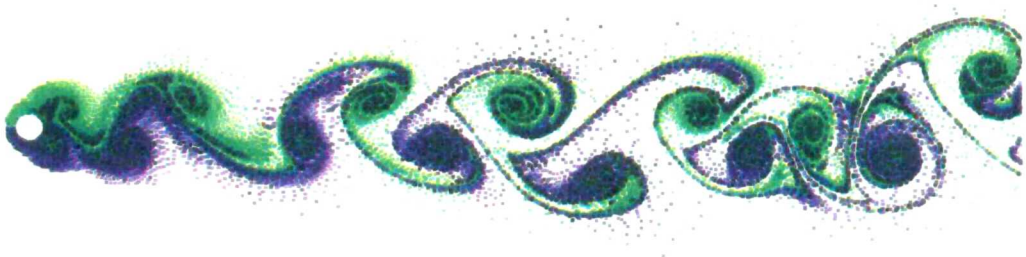
Vorticity contours. $Re = 150$. Case 14.

Figure 4.61



Vorticity contours. $Re = 150$. Case 16.

Figure 4.62



Point vortices. $Re = 150$. Case 2.

Figure 4.63



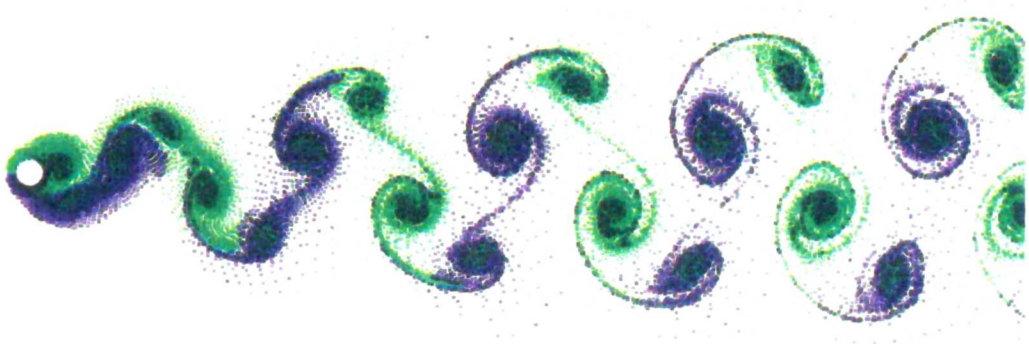
Point vortices. $Re = 150$. Case 4.

Figure 4.64



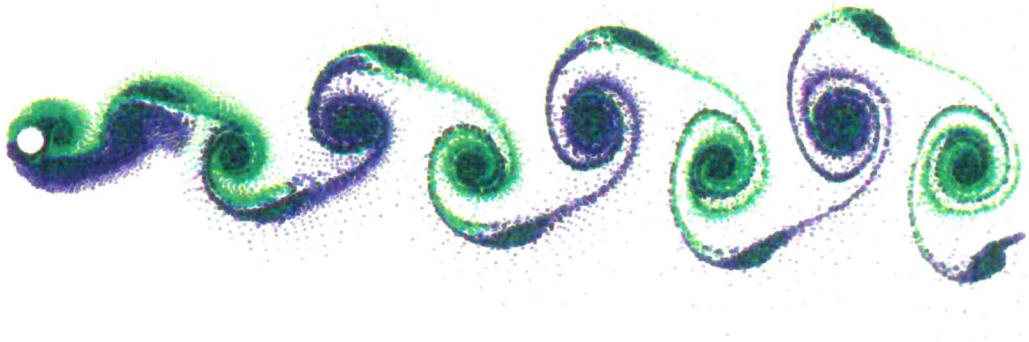
Point vortices. $Re = 150$. Case 6.

Figure 4.65



Point vortices. $Re = 150$. Case 8.

Figure 4.66



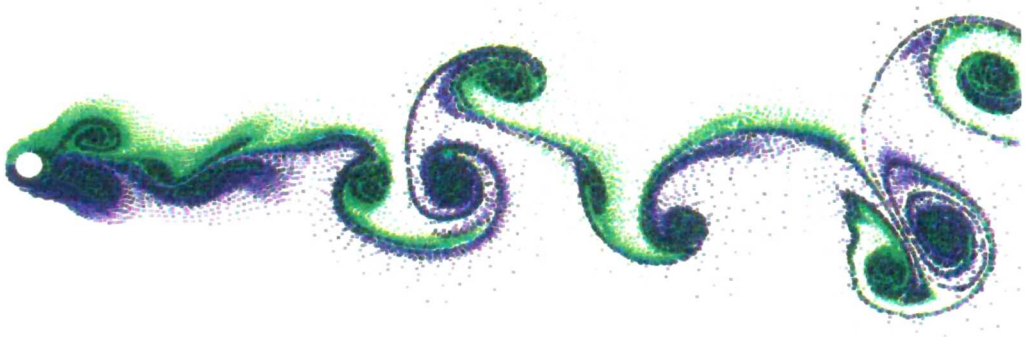
Point vortices. $Re = 150$. Case 10.

Figure 4.67



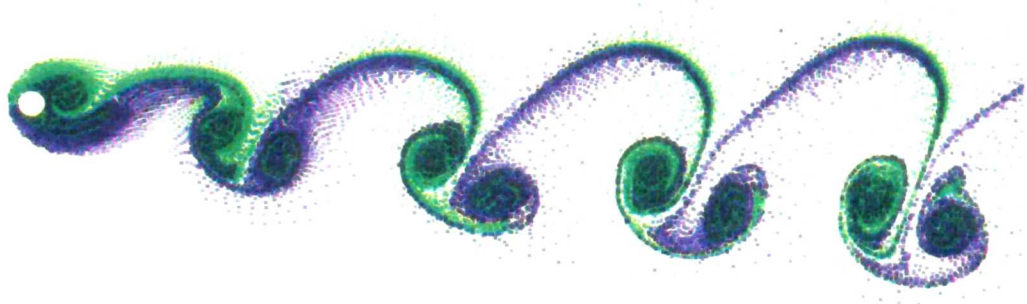
Point vortices. $Re = 150$. Case 12.

Figure 4.68



Point vortices. $Re = 150$. Case 14.

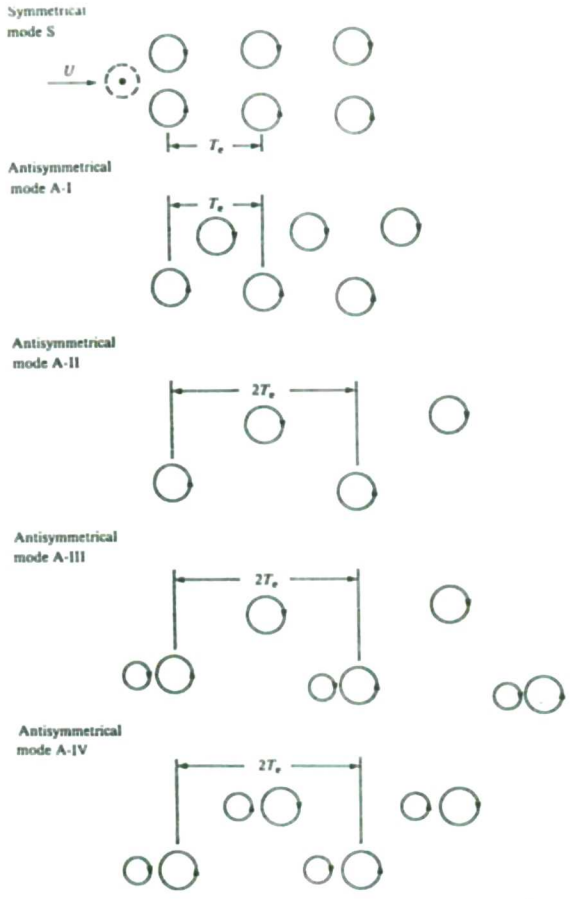
Figure 4.69



Point vortices. $Re = 150$. Case 16.

Figure 4.70

Ongoren and Rockwell (1988) have examined the near wake structure of a cylinder undergoing in-line oscillations, and present extensive flow visualisation evidence of the various modes that occur as a result of wave/cylinder synchronisation. They present four basic antisymmetric modes and one symmetric mode of shedding; their figure showing these modes is reproduced below in figure 4.71.



Basic modes of shedding (from Ongoren and Rockwell (1988)).

Figure 4.71

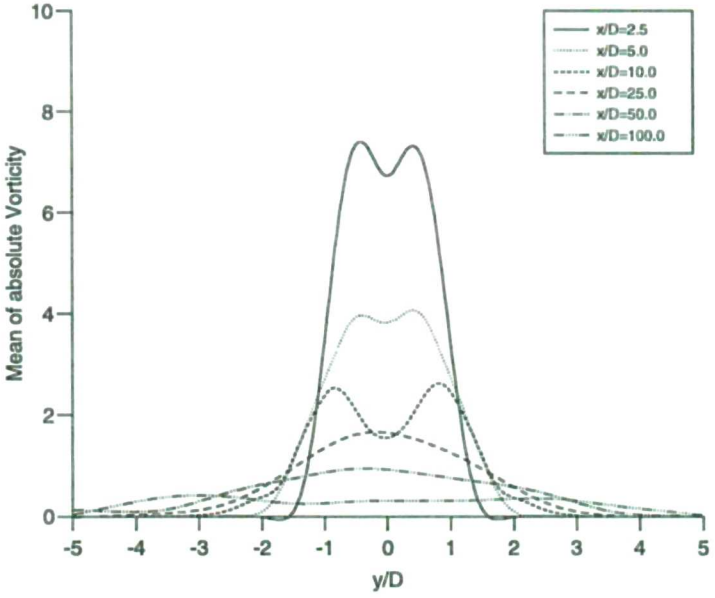
In the present data there is no evidence of a sustained symmetric shedding mode, and the antisymmetric mode A-II is also absent. Rather, it is found that in for example case 12, point vortex plots suggest the presence of a mode A-II type in the near wake, but further downstream it may clearly be seen that a weaker vortex grows from the interconnecting free shear layer between the primary vortices, and begins to establish itself about $30D$ downstream of the cylinder; this mode is similar to the A-III mode. In any case, the wake patterns described here are often not of a single mode, and a variety of modes sometimes appear in the long term development of

the wake. Ongoren and Rockwell note that the A-II mode is not present for in-line oscillations, but may appear in cases for which the oscillation and free stream are not aligned. The appearance of a sustained symmetric shedding mode is only evident in cases for which the non-dimensional frequency is much higher than that tested here (e.g. $\hat{f} = 3$), or indeed, if the amplitude of the wave is large. The latter case is an example of a 'pulsatile' flow, in which a weak steady current is added to a relatively strong oscillatory component; these are not the considerations of the present work, but Zhou (1994) presents a study. Flow visualisation carried out by the author, and presented in chapter 6, shows that for very strong wave cases ($\hat{u} \approx 1$), a symmetric shedding mode persists many diameters downstream, but eventually decays to an antisymmetric mode, with a lengthscale very much greater than that of the von Kármán vortex street of the unperturbed case. It should be noted that for the present results the start-up procedure promotes an antisymmetric mode, and in all cases an antisymmetric configuration is realised over the first few cycles of shedding.

Case 2 is an example of mode I shedding; in terms of modifications that appear in the wake, it is quite similar to the weaker wave case (figure 4.23) at the same frequency. The inter-vortex spacing is not regular, and there is some evidence of vortices 'bunching' in the near-wake, with the formation of vortex pairs far downstream (figure 4.55). Plots of the time-average values of $\overline{|\omega|}$ demonstrate that close to the cylinder, the response of this wake is similar to the weaker wave case. Figure 4.72 is a plot of this case.

The inflexion points in the curves for $x/D = 2.5, 5., 10.$ are an indication that the transverse inter-vortex spacing is somewhat greater in this case. At $x/D = 25.$, the two cases are similar, but beyond these values of x/D, the stronger wave case exhibits a greater transverse broadening. Plots of the vorticity contours for these

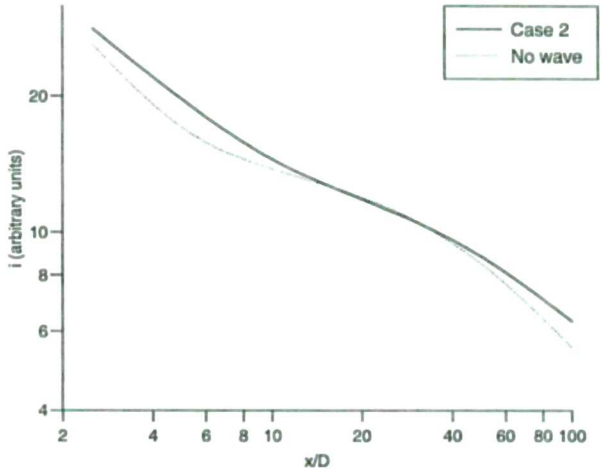
two cases confirm that case 2 has a far-wake which is broader, and for which the longitudinal inter-vortex spacing is increasing with distance downstream. Interestingly, plots of the streamwise decay of the time-average of absolute vorticity (see figures 4.73 and 4.47) show that in terms of the activity of the flow in the wake, the two cases are very similar.



Time-average of absolute vorticity. $Re = 150$. Case 2.

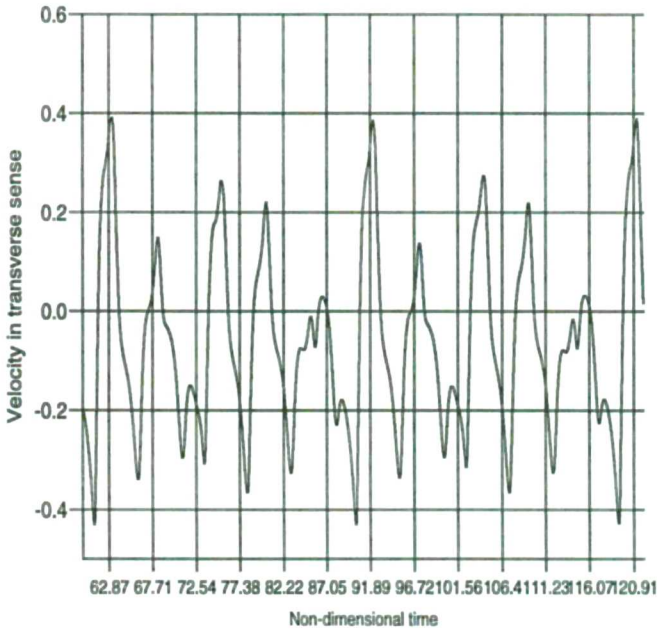
Figure 4.72

Figure 4.74 is a plot of the time trace of case 2 at the station $x/D = 2.5$, $y/D = 1.5$ for which the increment on the x-axis has been set equal to twice the period of the wave. The amplitude of the signal is modulated, and the flow is seen to repeat itself every twelve cycles of the wave.



Decay of the time-average of absolute vorticity with distance downstream. Case 2.

Figure 4.73



Transverse velocity sampled at $x/D = 2.5,\ y/D = 1.5$. Case 2.

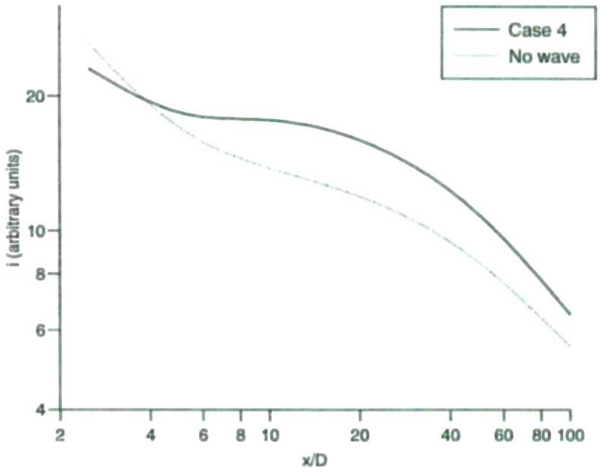
Figure 4.74

It is unclear to the author why the lowest frequency periodicity is equal to twelve wave cycles: one might expect the existence of a beat frequency, whose non-dimensional period would be equal to $(0.5f_w^* - f_n^*)^{-1} \approx 40$. Some peaks within the periodic range are separated by a length of time equal to the natural shedding period of the flow, but most are not. In the weaker wave case, the signal is also modulated, but the non-dimensional period is definitely equal to τ_n^*. Thus the stronger wave case is synchronised, whilst the weaker falls below the threshold for lock-in.

Case 4 is the special case of $\hat{f} = 2$, i.e. the wave frequency is exactly twice the natural shedding frequency. The wake is an example of the A-I type mode, although the transverse inter-vortex spacing is larger than the steady incident flow case, and has a value of $2.75D$ in the near-wake (see figure 4.64). This compares with a value of $1.5D$ for the steady incident flow case. The streamwise inter-vortex spacing has the same value of $4.75D$. Figure 4.56 shows that the wake undergoes a transition at a distance of approximately $70D$ from the cylinder, after which the vortex structures become larger and the streamwise inter-vortex spacing increases; meanwhile, the wake undergoes very little broadening, even far from the cylinder. Figure 4.75 is a plot of the variation in the time-average absolute vorticity term with streamwise distance for this case, and shows that the activity in the wake decays only very slowly in the mid-wake. Interestingly, the shape of the curve in figure 4.75 is similar to that of the corresponding weak wave case, i.e. case 3 (see figure 4.48): the decay rate is weaker than the steady incident flow case over the near-wake, but stronger in the far-wake.

If the frequency of the wave is again lowered, a change in the mode of the wake occurs. Figure 4.65 is a plot of the point vortices for case 6 ($\hat{f} = 1.825$). In the near

wake it may clearly be seen that a symmetric mode is established over the region $7.5D \leq x \leq 16D$, but not of the type described in figure 4.71.



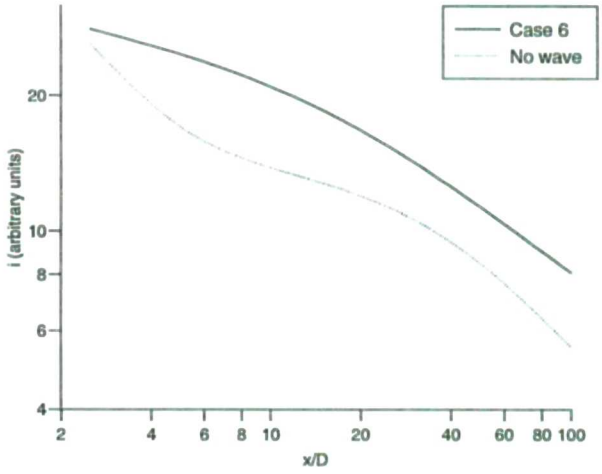
Decay of flux of time-average of absolute vorticity with distance downstream.

Case 4.

Figure 4.75

Although the vortices are positioned symmetrically over this region, the **signs** of the vortices in the streamwise direction are alternate. In fact, this configuration is pretty close to the antisymmetric mode A-IV. Beyond $x = 16D$ the like-signed vortices begin to coalesce, and an antisymmetric configuration is established. There is quite a high proportion of the vorticity contained within the free shear layers that connect the concentrated vortices; this vorticity is drawn into the main wake, and a complicated flow pattern results. Far downstream we see that the vortex structures enlarge, and begin to break up.

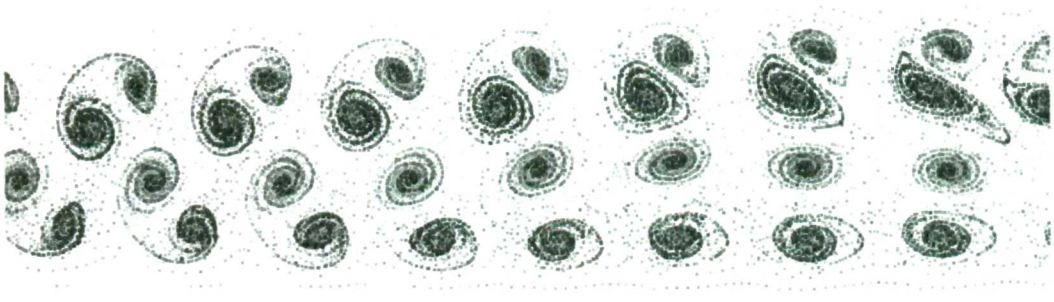
Figure 4.76 is a plot of the variation of the time-average absolute vorticity term versus downstream distance for case 6. It may be seen that the rate of decay of the flux varies quite smoothly with distance downstream.



Decay of the time-average of absolute vorticity with distance downstream. Case 6.

Figure 4.76

At lower wave frequencies (case 8), a beautiful double vortex street is observed (figure 4.66). This is an example of mode A-IV, but one in which the secondary vortices have near equal strength. Figure 4.58 shows that this configuration is quite persistent and exists for many diameters downstream. The vortex pairs undergo a gradual rotation, so that by $x \approx 65D$ a symmetric configuration is realised:



Symmetric mode realised at $x \approx 65D$. Case 8

Figure 4.77

This in itself is reasonably stable, and exists intact up to about $x = 110D$. Very soon after this, the wake begins to undulate weakly and it is probable [3] , that further downstream the wake adopts an antisymmetric configuration with a lengthscale many times that of the von Kármán value.

Detemple and Eckelmann (1989) carried out experiments in which the low Reynolds number wake of a circular cylinder is excited by sound waves, and they report flow visualisation patterns which are analogous to those found by other researchers for longitudinally oscillating cylinders (e.g. Couder and Basdevant (1986) and Griffin and Ramberg (1976)). At $\hat{f} = 1.5625$, they demonstrate the appearance of what they term "Sea-horses". Figure 4.78 is a plot of their result for this frequency ratio. It should be noted that although they present quantitative frequency data, the amplitude of the sound is a qualitative aspect.



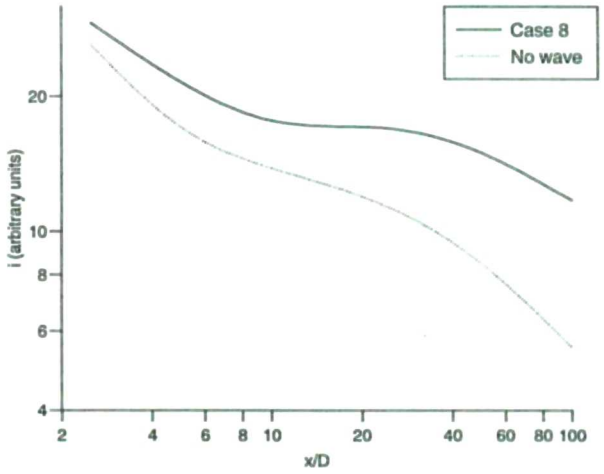
"Sea-horse" vortex configuration. From Detemple and Eckelmann (1989).

Figure 4.78

Figure 4.79 shows a plot of the variation of time-average absolute vorticity term

[3]This is speculation, since an insufficient length of wake is modelled.

with distance downstream. It may be seen that up to $x \approx 10D$, the decay matches the steady incident flow case reasonably well, but beyond this the decay slows dramatically, so that by $x = 100D$ $\bar{i}$ is four times the value of the steady incident flow case. The high value of $\bar{i}$ results from the symmetric alignment of the vortices, and the fact that there is little if any annihilation of vorticity through vortices tearing each other or undergoing partial merging.



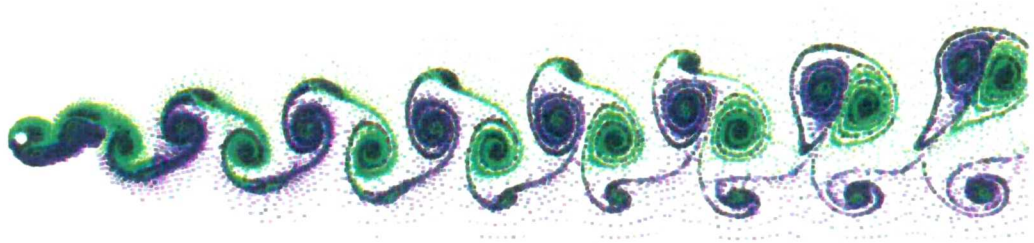
Decay of flux of time-average of absolute vorticity with distance downstream.

Case 8.

Figure 4.79

Cases 10 ($\hat{f} = 1.3$) and 12 ($\hat{f} = 1.2$) have similar wake structures. The arrangement of vortices in the near-wake is virtually co-linear, and the transverse inter-vortex spacing has reduced to $1.5D$ and D respectively. One particularly interesting feature is that the vortex rows have interchanged positions when compared with the classical von Kármán vortex street, i.e. vortices with -ve circulation form the top row, whilst vortices with +ve circulation form the lower row. This is characteristic of a typical wake configuration of a thrusting body. The streamwise inter-vortex spacing is approximately double that of the von Kármán value, taking the values

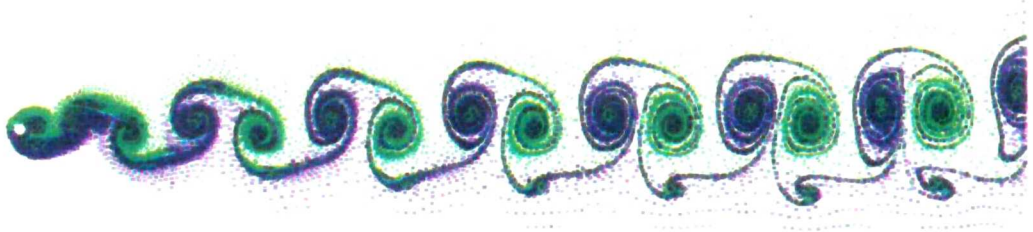
of $8.125D$ and $8.75D$ respectively. These are both interesting cases, since over the length of the wake which has been modelled, they might reasonably make a claim of exhibiting several modes of vortex structure: the near-wake is close to mode A-II (more so in case 12); further downstream the free shear layer connecting the primary vortices starts to roll up, so that at $x \approx 30D$ (case 10), a mode A-IV is established. Figure 4.80 is a point vortex plot of case 10 over a substantial length of the wake. It shows that the secondary vortex which develops from the interconnecting free shear layers decays in the upper row (due to the rising vortex pair), whilst that which forms in the lower row survives and continues to roll up. The primary vortex pair, well established by $x = 50D$, self-convects in a positive transverse direction and actually unwinds this secondary vortex; this is probably the case since figure 4.80 shows that the small concentrated vortex in the upper shear layer suddenly disappears between $50D < x < 60D$, whilst the shear layer stays intact, and there is no evidence of vortices merging. The primary counter-clockwise vortex has caused the concentrated vorticity in the secondary vortex to be redistributed back through the free shear layer. The importance of competition in the process of primary vortex pairing is highlighted in this case; it may be seen that only a very fine adjustment in initial primary vortex spacing is required so that the vortex pairs which form downstream should in fact be directed in a negative transverse sense. If this had been the case of course, the resultant wake would have been an image of the current one about the x-axis. With the removal of the upper secondary vortex, the wake is configured to a A-III type mode, except that the weaker vortex is the lone vortex. Figure 4.81 is a plot of the point vortices for case 12, and again shows the development of the secondary vortex in the free shear layer. On this occasion however, the secondary vortex in the upper shear layer is short lived, and never really rolls up properly.



Point vortices. $Re = 150$. Case 10.

Figure 4.80

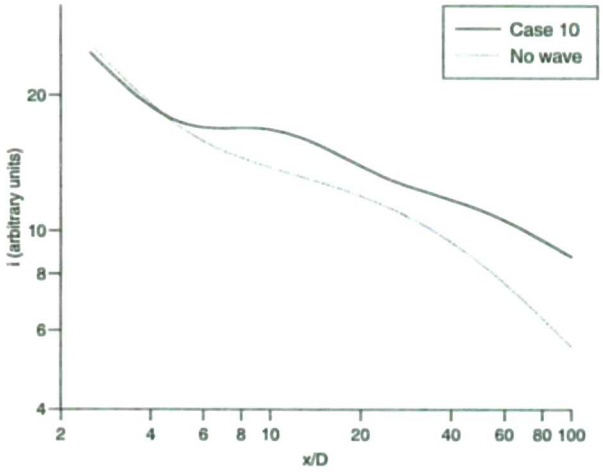
The point on the upper shear layer which is beginning to thicken, and would represent the origin of formation of the secondary vortex, is actually quite close to its primary vortex; the effect of this proximity of the primary vortex is to pull and stretch the shear layer, so inhibiting the roll up of the secondary vortex. By contrast, the thickening that occurs in the lower shear layer is well away from its primary vortex (and increasingly so due to the self-induced velocity field that the two primary vortices exert), and thus the influence of the latter is insufficient to prevent roll up.



Point vortices. $Re = 150$. Case 12.

Figure 4.81

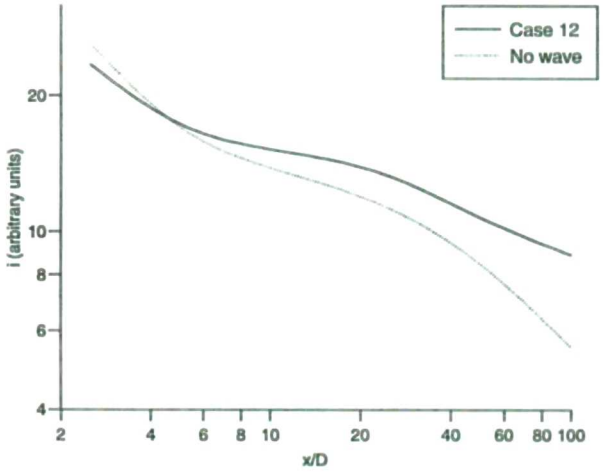
Figures 4.82 and 4.83 are plots of the variation in the time-average absolute vorticity flux for cases 10 and 12 respectively.



Decay of the time-average of absolute vorticity with distance downstream.

Case 10.

Figure 4.82



Decay of the time-average of absolute vorticity with distance downstream.

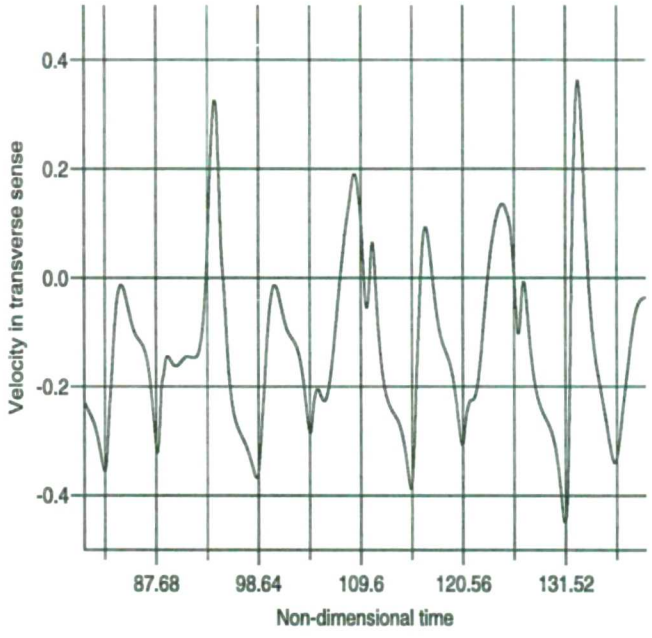
Case 12.

Figure 4.83

A marked change in the decay of this quantity with distance downstream is evi-

dent, if compared with the previous case 8 (figure 4.79). In these two cases, the decay rate is much closer to the steady incident flow case, and the differences in the value of activity in the wake are not so great. In the near-wake, both sets of data are very similar to the steady incident flow case.

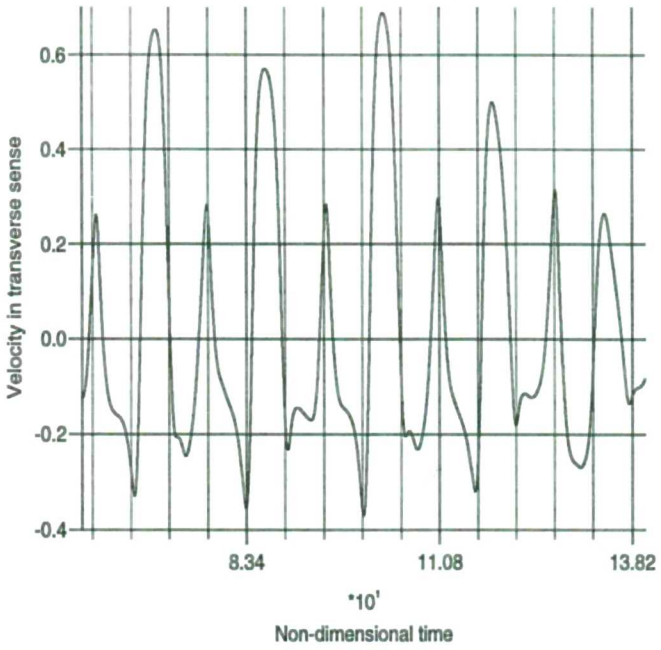
At $\hat{f} = 1.0$ (case 14) samples of velocity in the near wake indicate that there is no periodicity associated with this flow:



Transverse velocity sampled at $x/D = 2.5$, $y/D = 1.5$. Case 14.

Figure 4.83

However, further downstream ($x = 10D$), samples of the transverse velocity demonstrate a periodicity which is equal to three periods of the natural shedding period or the wave period.

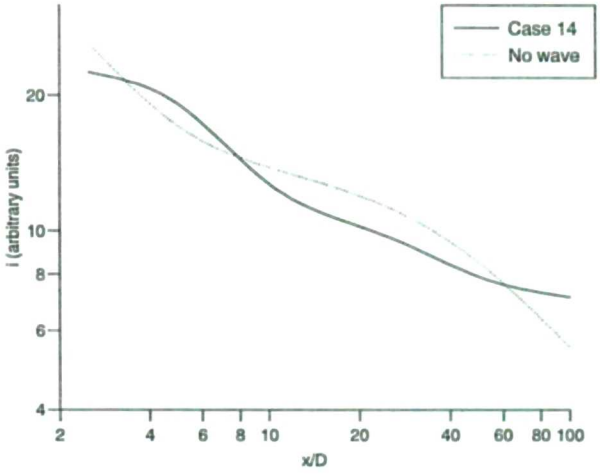


Transverse velocity sampled at $x/D = 10.$, $y/D = 1.5$. Case 14.

Figure 4.84

The plot of point vortices (figure 4.69) shows that at $t^* = 165$ the vortex formation process is symmetric, and that the near-wake is irregular. The wake is neither symmetric nor antisymmetric, but consists of pairs of primary vortices which have formed from vortex triplets; in between these three vortices are weaker vortices. Figure 4.61 shows that the wake broadens tremendously due to the movement of vortex pairs away from the main wake. The differences between this case and case 13, which has the same frequency but smaller amplitude, are quite striking; the latter is an example of the A-I mode, and this structure is maintained very far downstream. Here, the transverse broadening of the wake occurs very close to the cylinder. Figure 4.85 is a plot of the variation of the time-average absolute vorticity flux versus distance downstream. It shows that this is the first strong wave case presented for which the activity is actually less than the steady incident flow value

over a substantial portion of the wake ($8 < x/D < 60$).

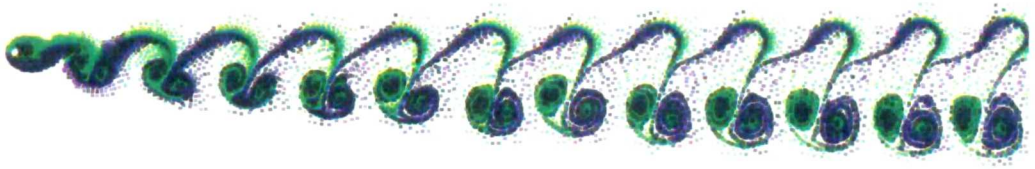


Decay of the time-average of absolute vorticity with distance downstream.

Case 14.

Figure 4.85

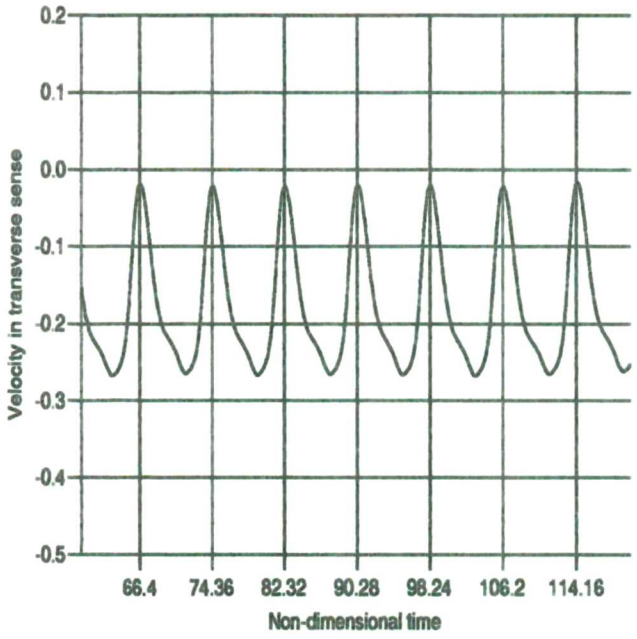
At a frequency **below** the natural shedding frequency (case 16), a mode type similar to A-III develops. Again, the weaker of the three vortices is the lone vortex, which develops from instabilities in the free shear layers that connect the primary vortex pairs. Figure 4.70 is a point vortex plot of the near-wake and shows that immediately after being shed, the two primary vortices form a pair. Figure 4.62 is a vorticity contour plot which includes the far-wake and shows the development of the third, weaker vortex. The streamwise spacing between the vortices becomes nearly equal, so that convection of a pair from the main wake becomes limited (see figure 4.86).



Point vortices. $Re = 150$. Case 16.

Figure 4.86

Samples of the transverse velocity at $x/D = 2.5$, $y/D = 1.5$ show that the shedding is locked in, and has a period equal to the wave period. Figure 4.87 is a plot of this, for which the increment of the x-axis has been set equal to the non-dimensional wave period.



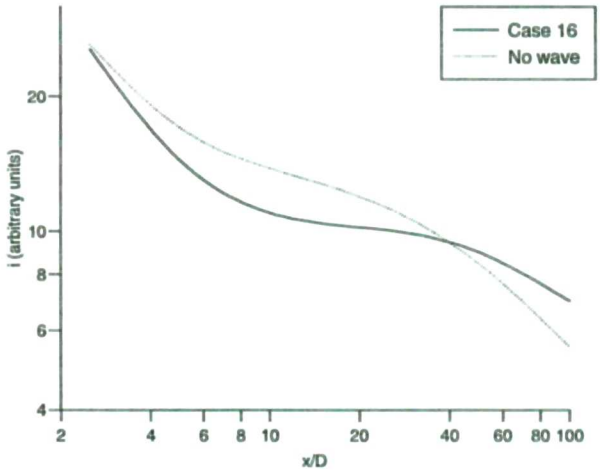
Transverse velocity sampled at $x/D = 2.5$, $y/D = 1.5$. Case 16.

Figure 4.87

This is the first case in which the shedding has locked on to the wave period rather

than twice the wave period, and it follows that there must exist a second lock-in region in the $(\hat{h}, \hat{f})$ parameter space for $\hat{f} < 1$. Detemple and Eckelmann (1989) report lock-in for the range $0.53 < \hat{f} < 2.46$. For $0.77 < \hat{f} < 1.16$, they report that the vortex shedding experiences lock-in at the driving frequency, and over $0.53 < \hat{f} < 2.46$ the vortex shedding experiences lock-in at half the driving frequency. In the overlapping range, the mode of lock-in is unpredictable, and sometimes may not occur.

Figure 4.88 shows the decay of the time-average absolute vorticity flux versus distance downstream. It may be seen that up to $x/D = 40$, the activity in the wake is substantially less than is the case for steady incident flow. Beyond $x/D = 40$, the rate of decay levels off, so that in the far-wake the activity in the wave case is greater.



Decay of the time-average of absolute vorticity with distance downstream. Case 16.

Figure 4.88

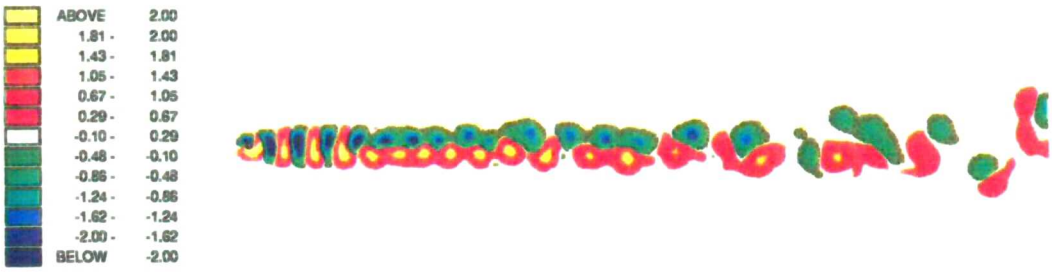
It is of interest at this point to check the effects of the phase term associated with the wavelength of the wave in the potential velocity field, i.e. to discover what changes

to the flow field occur if the wave is modelled as a planar oscillatory motion, for which all points of the flow move in phase with each other. This may easily be done here by removing the phase term associated with the wave, so that the imposed velocity field is again equation 4.39 , but no incremental velocities are added to the motion of the vortices themselves, i.e. equation 4.40 becomes simply:

$$u_v = u_p + u_r$$

$$v_v = v_p + v_r \tag{4.47}$$

where the subscripts are the same as those used in equation 4.40. This flow problem is now hydrodynamically equivalent to the case of applying in-line oscillations to a cylinder in a steady free stream. Case 6 is selected as a test case, because the amplitude of the wave motion is large, and the wavelength is relatively small; it is presupposed that a smaller wavelength has a greater 'concertina' effect on the vortices in the wake. Thus we expect case 6 to be one of the cases most affected by the effects of wavelength. Figure 4.89 is a vorticity contour plot of case 6 with planar oscillatory flow only, and this figure may be directly compared with figure 4.57 for the original case 6.



Vorticity contour plot. Case 6 with planar oscillatory flow only.

Figure 4.89

In the near wake, the differences between this result and that presented in figure 4.57 are barely perceptible. Far from the body there are slight differences in the distribution of vorticity, with case 6 displaying a somewhat more disrupted wake structure; in general, the wake is more spread in case 6, so for instance the presence of a vortex pair at $x/D \approx 100$ is not evident in the planar oscillatory case. This result indicates that the effects of wavelength, even in this particularly testing example, are weak, and probably of a 'second order'.

1.4.2.3 Turbulence Modelling

So far the two-dimensional results have been confined to a low Reynolds number regime in which the flow is known to be laminar. In order to apply the computational model at more practical Reynolds numbers, some different representation of the small scales of the wake motions is required, since direct simulation is not a possible option at present. An in-depth study of various wave cases at high Reynolds numbers has not been carried out here, but the inherent difficulties in modelling the turbulent wake of a circular cylinder in waves are recognised, and the solution to a prototype wave case is presented. Most turbulence models have been developed in the study of internal flow problems, particularly with regard to turbulent boundary layers, and less work has been carried out in modelling the turbulence in wake flows behind bluff bodies. One of the problems of modelling flows past circular cylinders at moderate to high Reynolds numbers is that turbulence is not present in the boundary layers until the critical Reynolds number of around 250,000, but resides in the formation region and in the primary vortex structures in the wake. The detailed experiments of Cantwell and Coles (1983) for flow past a circular cylinder at $Re = 140,000$ show that the effects of history and transport are of crucial impor-

tance in the description of turbulent mechanisms within the wake. Rodi (1992) has made comparisons between an eddy viscosity type model and a full Reynolds stress model for flow past bluff bodies. The eddy viscosity model is the widely used k-ε model. Franke et al (1989) evaluated Cantwell and Coles' data for vortex shedding past a circular cylinder and found that substantial regions exist where the eddy viscosity is *negative*; Rodi suggests this weakens the case for employing an eddy viscosity approach to modelling turbulence in these flow scenarios. However, his results obtained via a Reynolds stress model for flow past a circular cylinder are apparently less good than those achieved with the simpler two equation transport model.

Beyond a Reynolds number of about 170, the flow past a slender circular cylinder becomes mildly three-dimensional; at higher Reynolds numbers the wake is said to be turbulent in that the frequency content of the wake is comprised of a multitude of components; in particular, there exists a random velocity field on top of the principal periodic velocity component. The presence of a strong periodic velocity term together with the high frequency random fluctuations poses many problems for any turbulence model. It is generally thought (e.g. see Rodi (1992)) that the only proper way forward is to solve the three-dimensional Navier Stokes equations as a Large Eddy Simulation, in which the very fine motions are treated as being isotropic within each computational element [4] and a simple model such as the Smagorinsky (1963) model is used to model the turbulent stresses; all motions greater than the element size are resolved at the mesh nodes. However, Large Eddy Simulation is computationally very costly, and in spite of the all caveats noted above, a two-equation turbulence model is developed here, and used to calculate the flow past a circular cylinder at a Reynolds number of 10^4.

[4] In Large Eddy Simulations the Navier-Stokes equations are averaged over a *small* region of space, which is equivalent to a low-pass filtering of the equations in Fourier space. The size of the chosen filter is not necessarily equal to the size of the computational element.

If the instantaneous velocity field is decomposed into a phase average (i.e. an ensemble or time average at constant phase in the shedding process), and a random fluctuating turbulent component, we have:

$$\vec{u} = < \vec{u} > + \vec{u}\,' \tag{4.48}$$

Reynolds averaging is over all unsteady components. In the present case part of the large scale time dependence is captured by the numerical mesh solution and the part comprising mainly subgrid motions must be modelled. Here a two-dimensional grid scale solution is being computed and hence the subgrid modelling should include all scales in the third dimension. Equations which are the same as the Reynolds averaged equations are derived by requiring that $\overline{\vec{u}\,'} = 0$, where $\bar{}$ denotes a time average, and that the correlation between the random component and the grid scales is zero. The $\vec{u}\,'$ are not captured by the numerical model, but their effect is felt through the inclusion of additional stress terms in the momentum equations.

A k-ε two equation transport model is developed here, and in this model the three components of $\vec{u}\,'$ have equal magnitude (i.e. isotropy is implied) and the eddy viscosity is expressed as: $\nu_t = C_\mu k^2/\varepsilon$, where $k = \frac{3}{2}\overline{\vec{u}\,'^2}$. The total energy per unit mass at any point in the flow is the sum of the resolved energy $\frac{1}{2}(u^2 + v^2)$ and the turbulent kinetic energy k.

The turbulence model presented here is the standard high Reynolds number k-ε model with the conventional coefficients:

$$\frac{\partial k}{\partial t} + (\vec{u} \cdot \nabla)k = \nabla((\frac{\nu_t}{\sigma_t} + \nu)\ \nabla k) + (P - \varepsilon) \tag{4.49}$$

$$\frac{\partial \varepsilon}{\partial t} + (\vec{u} \cdot \nabla)\varepsilon = \nabla((\frac{\nu_t}{\sigma_\varepsilon} + \nu)\, \nabla\varepsilon) + \frac{C_{\varepsilon_1}\varepsilon P}{k} - \frac{C_{\varepsilon_2}\varepsilon^2}{k} \tag{4.50}$$

where P is the production term and is equal to $\frac{\nu_t}{2}|\nabla\vec{u} + \nabla\vec{u}^T|^2$, and $C_\mu = 0.09$, $\sigma_t = 1.0$, $\sigma_\varepsilon = 1.3$, $C_{\varepsilon_1} = 1.44$, $C_{\varepsilon_2} = 1.92$.

In common with the vortex method, these two transport equations are solved by splitting the equations into convective and diffusive operators. Convection is carried out by particle, and diffusion and source terms are handled on the mesh. The k and ε fields are represented as:

$$k = \sum_i K_i \delta(\vec{x} - \vec{x}_i) \tag{4.51}$$

$$\varepsilon = \sum_i E_i \delta(\vec{x} - \vec{x}_i) \tag{4.52}$$

where K and E are integral quantities over elementary fluid volumes of turbulent kinetic energy and dissipation rate respectively.

The Boussinesq eddy viscosity concept is used to relate the Reynolds stresses to the mean flow, i.e.

$$-\overline{u_i' u_j'} = \nu_t(\frac{\partial u_i}{\partial x_j} + \frac{\partial u_j}{\partial x_i}) - \frac{2}{3}k\delta_{ij} \tag{4.53}$$

When this expression for the Reynolds stresses is substituted into the momentum equations, and the curl of these equations is taken, we have the following equation for the transport of vorticity:

$$\frac{\partial \omega}{\partial t} + (\vec{u} \cdot \nabla)\omega = \nabla^2(\nu_e \omega) + S \tag{4.54}$$

where $\nu_e = \nu_t + \nu$, and:

$$S = 2\left(\frac{\partial^2(\nu_t \frac{\partial u}{\partial y})}{\partial x^2} - \frac{\partial^2(\nu_t \frac{\partial v}{\partial x})}{\partial y^2} + \frac{\partial^2(\nu_t(-\frac{\partial u}{\partial x} + \frac{\partial v}{\partial y}))}{\partial x \partial y}\right) \tag{4.55}$$

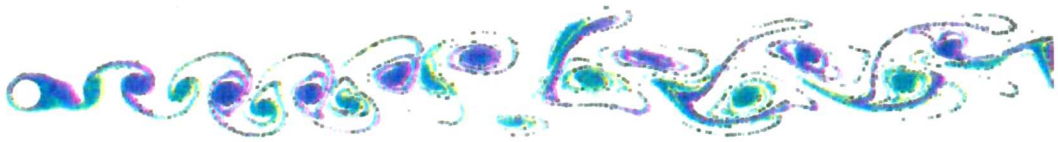
Sugavanan and Wu (1982) drop the source term S, and Smith and Stansby (1989) follow the same procedure. Here, S is likewise set to zero in the turbulence model.

The boundary conditions for the k-ε model are problematic: the most common approach is to use wall functions which are empirical equations relating the shear stress at the wall to the velocity at the first node off the wall assuming a certain turbulent velocity profile in the boundary layer. The boundary layers at high Reynolds numbers tend to be thin (i.e. their scale is much smaller than typical length scales in the flow), and they therefore require very fine elements to capture them; often, this is impractical, and so the idea of wall functions is to assume a given profile in the boundary layer and by having at least one computational point within the boundary layer (typically in the logarithmic region - near to the edge of potential region) approximately resolve the stresses at the wall. This method has been used by many researchers, e.g. Franke and Rodi (1991) for flow past a square cylinder, Begue, Cardit and Pironneau (1988) for flow past a circular cylinder. For a review of low Reynolds number turbulence models and near wall treatments see Patel, Rodi and Scheurer (1984).

The method presented here forces the turbulent kinetic energy to zero (actually to 10^{-20}) at the first point off the wall; the value of the dissipation rate is set as a function of the local production P. This is done by considering the source terms in the transport equation for ε, which are: $C_{\varepsilon_1}\frac{\varepsilon}{k}P - C_{\varepsilon_2}\frac{\varepsilon^2}{k}$. As $k \to 10^{-20}$ this source

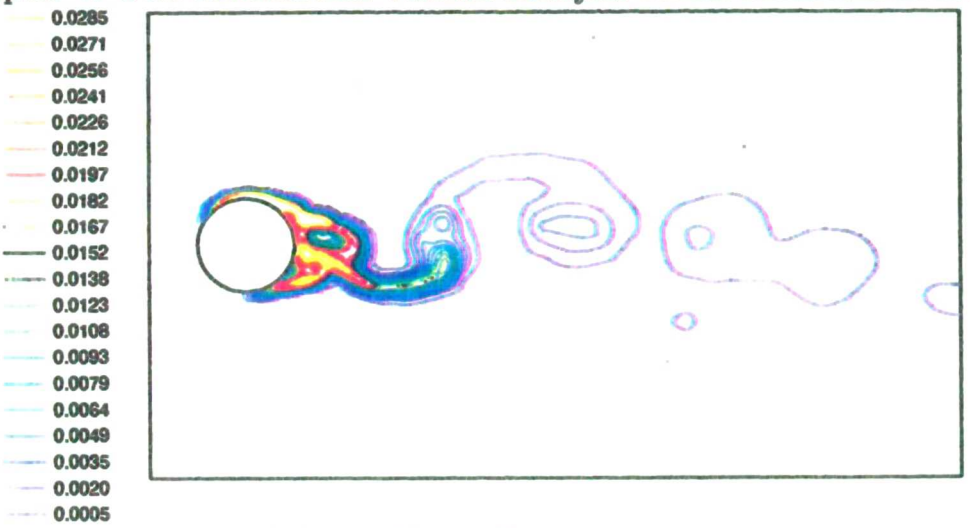
term becomes very large, unless $\varepsilon = \frac{C_{\varepsilon_1}}{C_{\varepsilon_2}}.P$. These conditions are applied through manipulation of the main diagonal and source terms in the discretized equations for k and ε.

Figure 4.90 is a plot of the point vortices for steady incident flow past a cylinder at a Reynolds number of 10^4. The two colours represent the sign of the vorticity, blue being negative and green positive. The shed vortices lie much closer to the centreline than in the low Reynolds number cases, and vertical spacing is approximately $0.34D$. Figures 4.91, 4.92, 4.93 are plots of k, ε, and ν_t for the same case. There is no evidence of significant k near to the front of the cylinder, and most of the production of k is due to shear at the top and bottom of the cylinder, where the gradients $\frac{\partial q}{\partial r}$ are largest. Once generated, k is convected into the formation region along the rolling-up shear layers, and only a small fraction becomes ingested into the shed vortex centres.



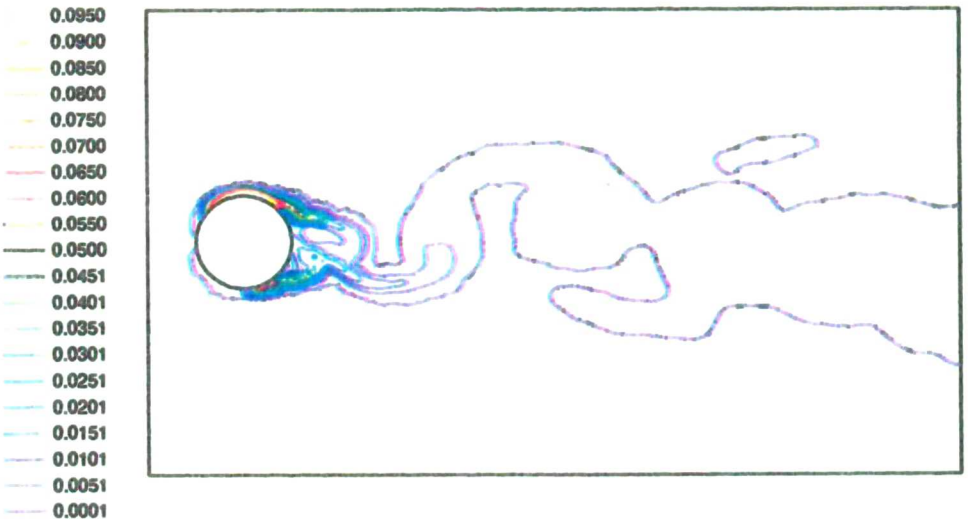
Steady incident flow Reynolds number = 10^4

Figure 4.90



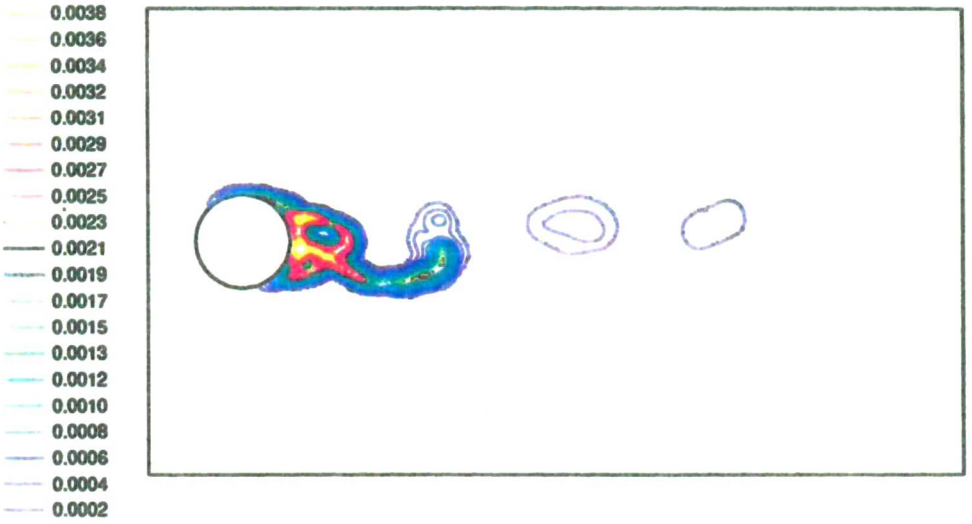
Turbulent Kinetic Energy contours

Figure 4.91



Dissipation rate contours

Figure 4.92



Eddy viscosity contours

Figure 4.93

The tight rolling up of the shear layer to form Bloor or Gerrard vortices results in fluctuations of velocity at fine scales and a modal transfer towards higher frequencies in the energy spectrum. These shear layer instabilities are two dimensional at their inception, but at higher Reynolds numbers three-dimensional instabilities develop.

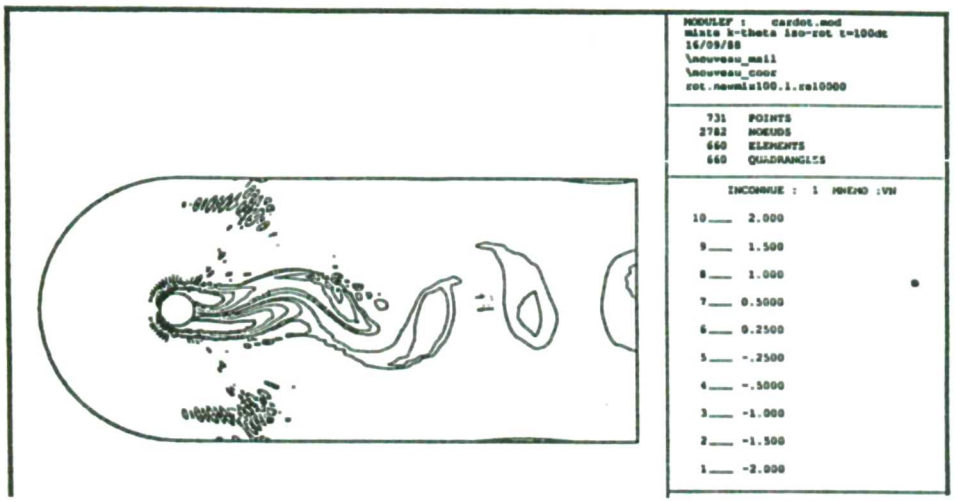
Figure 4.91 indicates that a quite high instantaneous turbulence intensity (defined as u'/U_c) of about 35% occurs in the shear layer; behind the cylinder and in the formation region a lower value of about 20% is attained. Comparison of figures 4.91, 4.92, and 4.93 demonstrates that although k is high in the shear layers, the eddy viscosity ν_t has its peaks primarily in the formation region; it exists also in the nearest shed vortex (lower row) to the formation region and in the interconnecting vortex sheet that links this vortex to the formation region. Some of the turbulent kinetic energy becomes entrained into the cores of the primary von Kármán vortices as they form. The transport of k along the fine structures that are the free shear layers and the vortex sheets that connect the von Kármán vortices is a very important effect in

the behaviour of turbulent wakes behind cylinders, and must be modelled carefully. The technique of introducing an integral quantity of k and ε and convecting these as a Lagrangian step introduces minimal numerical diffusion into the method and thus the fine structures of the k and ε distributions are maintained through the time integration.

Near to the surface of the cylinder the k-ε equations are source dominated; ε 'follows' k, such that any rapid rise in k is matched by a rise in ε. In the formation region, and certainly at the vortex cores, the production term is weaker, and the transport equations less source dominated. A maximum turbulent viscosity of about 25ν is reached at the centreline, next to the back of the cylinder. In the cores of the first few shed vortices the eddy viscosity has dropped to about 4ν.

The turbulence model here simulates the additional dissipative stresses arising through random fluctuations in the velocity field, and the effect is to decrease the local Reynolds number just behind the cylinder and help stabilise the formation process. About $10D$ downstream from the cylinder the periodic wake structure tends to break down over quite short distances, and is replaced by a new regular vortex structure of about twice the scale of the initial von Kármán street. The two regions of regularly spaced vortices are separated by a vortex pair which has begun to eject from the main wake. So far as the author is aware, the only computation for flow past a circular cylinder at a Reynolds number of 10^4 has been performed by Begue, Cardot and Pironneau (1988). Figure 4.94 is a plot of vorticity contours from their results for steady incident flow past a circular cylinder. Unfortunately, this plot does not extend very far into the wake, so comparison with the present results is limited. The results of Begue et al are obtained using a modified k-ε equation with wall functions. There are considerable differences between the results presented here and those of

Begue et al, principally that the formation region in the latter case is much longer, and the streamwise inter-vortex spacing is about twice the size. The apparently spurious creation of vorticity at $x/D \approx 1$, $y/D \approx \pm 3$ is probably due to mesh effects; the far boundary is quite close in this computation, and the mesh is coarse. Also, the time step is very large by comparison with that used in the present results.

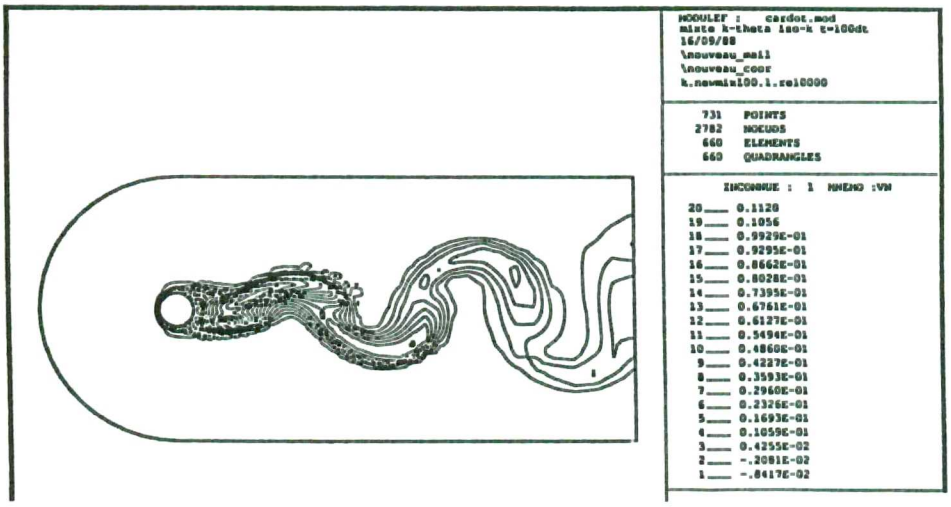


Vorticity contours for flow past a circular cylinder at $Re = 10^4$

From Begue, Cardot and Pironneau (1988)

Figure 4.94

The values of turbulent kinetic energy are shown in figure 4.95. The values obtained by Begue et al are higher than those of the present results, by a factor of about three. The point of maximum k lies further from the cylinder, and k is transported further into the wake; the unrealistic negative values of k are presumably to do with the contour package. Values of ν_t obtained by Begue et al are typically eight times greater than those obtained here.



Turbulent kinetic energy contours for flow past a circular cylinder at $Re = 10^4$

From Begue, Cardot and Pironneau (1988)

Figure 4.95

Figure 4.96 is a photograph by Thomas Corke and Hassan Nagib appearing in "An Album of Fluid Motion" which shows the flow visualisation of a circular cylinder at this Reynolds number. The flow patterns are elucidated by the entrainment of a marker in the irrotational flow into the vortex structures behind the cylinder. In this picture it is not clear what is happening in the formation region, as no marker has been entrained there. However, the relative spacing of the vortices is clearly shown; the streamwise inter-vortex spacing is approximately $4D$, and the lateral inter-vortex spacing is approximately D. Immediately below this photograph is a magnified plot of the vortices in the simulation presented here. The vortices in the latter case appear to be shifted about $D/2$ upstream of those in the flow visualisation. Also, the vortices are almost placed co-linearly, which might be an indication that there is insufficient diffusion in the computation.

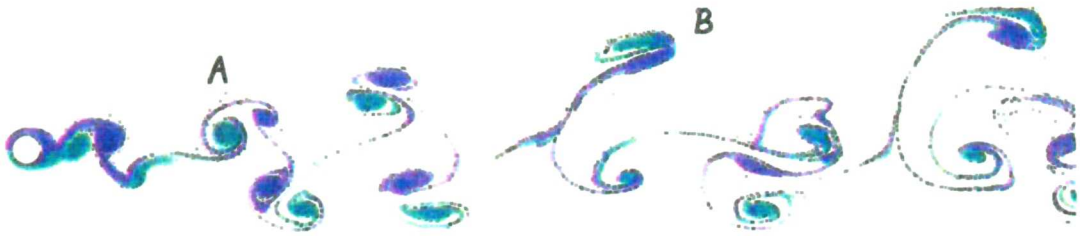


Flow visualisation (top) and numerical computation (bottom) of flow past a circular cylinder at $Re = 10^4$

Figure 4.96

Figure 4.97 is a vortex plot of the wave case at the same Reynolds number in which $\hat{\lambda} = 30$, $\hat{f} = 1.8$, $\hat{u} = 0.5$; the two colours again represent the sign of vorticity, blue being negative and green positive. The wake is characterised by the formation of pairs of near equal strength vortices, which move away from the wake centreline under the influence of their self-induced velocity fields. A few diameters from the cylinder their orientation is such that the initial direction of motion of the pair is outwards and back towards the cylinder (A). As the vortex pair moves outwards and into a region of reduced velocity deficit, it experiences a higher free stream value and is convected downstream quickly; meanwhile the self-induced velocity vector rotates so that it now faces outwards and away from the cylinder (B). Still further downstream the rotation is complete and the pair begins to re-enter the main wake. The streamwise distance between the ejected pairs is seen to grow, and this is a result

of the combination of the free stream and the rotating self-induced velocity vector. Spreading in a transverse sense is rapid and the rate of change of this quantity with respect to downstream distance is largest a few diameters from the cylinder where ejection begins to take place. This contrasts with the steady incident flow case in which the transverse growth is gradual.

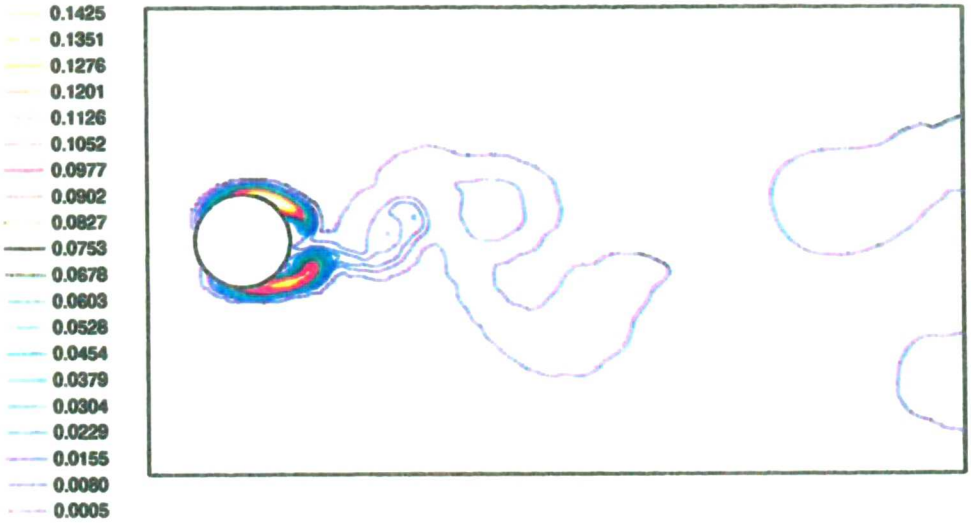


Point vortices. $Re = 10^4$. $\hat{\lambda} = 30$; $\hat{f} = 1.8$; $\hat{u} = 0.5$.

Figure 4.97

Figures 4.98, 4.99 and 4.100 are contour plots of k, ε, and ν_t. The most immediately clear difference between this wave case and the steady incident case is that the levels of k are relatively higher around the cylinder. The turbulence intensity has a maximum of about 40% in the shear layers. It is to be expected that, in general, the wave cases (particularly with high $\hat{u}$) will demonstrate increased turbulent fluctuations in the formation region since the vortices which are beginning to form there are subject to a quite large oscillatory velocity components and are convected closer to the cylinder. The increased levels of turbulence in the formation region results in a relative increase in the levels of turbulence which is washed into the vortex cores.

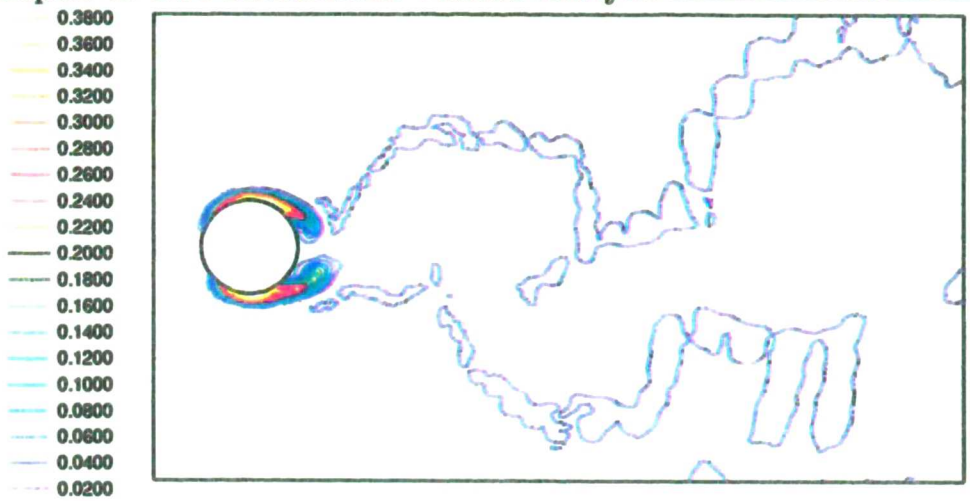
Nevertheless, the decay of turbulence in the wake is rapid and intensities are down to about 5% within a few diameters.



Contour plot of Turbulent Kinetic Energy.

$Re = 10^4$. $\hat{\lambda} = 30$; $\hat{f} = 1.8$; $\hat{u} = 0.5$.

Figure 4.98



Contour plot of Dissipation rate.

$Re = 10^4$. $\hat{\lambda} = 30$; $\hat{f} = 1.8$; $\hat{u} = 0.5$.

Figure 4.99



Contour plot of Turbulent Viscosity.

$Re = 10^4$. $\hat{\lambda} = 30$; $\hat{f} = 1.8$; $\hat{u} = 0.5$.

Figure 4.100

Chapter 5

Three-dimensional Viscous Analysis

5.1 Introduction

The theory, implementation and results of a three-dimensional numerical method are presented in this chapter. This method is used to model the flow characteristics of the wake of a circular cylinder in a combination of a steady free stream and surface gravity waves. Three-dimensional vortex dynamics are first investigated in the more straightforward case of a tapered cylinder in a steady flow.

The work presented in this thesis so far has examined the modifications which take place in the wake as a result of a two-dimensional progressive wave train, which models the presence of a surface gravity wave. However, it has long been recognised (e.g. Williamson (1995)) that in the case of a two-dimensional incident flow past a nominally two-dimensional body, the rôle of three-dimensional instabilities in the development of the wake is of crucial importance. On this basis, the case of a circular cylinder translating into surface gravity waves, for which the incident

flow is highly three-dimensional, should therefore merit an investigation into the three-dimensional aspects of the wake flow. Unfortunately, the number of degrees of freedom that exist in the three-dimensional numerical problem is very large, and so the range of scenarios that may be studied numerically is rather limited. It is not the purpose here to repeat the cases presented in the two-dimensional analysis, nor would this be a realistic prospect. Rather, the aim is to determine and understand the three-dimensional vortex dynamics that take place in the wake of a circular cylinder translating into a typical sea wave, and to make comparisons,where appropriate, with the corresponding two-dimensional data. Since this study is concerned with relatively weak waves, the strength of the two components of vorticity which are generated at the cylinder surface and are orthogonal to the principal spanwise component will tend to be small. Furthermore, no attempt is made to model any deflections of the free surface in the approximation presented here.

The numerical method which is developed here is essentially an extension of the two-dimensional viscous vortex method described earlier on in this thesis. The three-dimensional Lagrangian vortex object used is the **vorton**, which is discussed in section 5.2.4. The mesh solution is based around a piecewise-linear Galerkin Finite Element method, with discretization over tetrahedral elements. Several factors encouraged the adoption of this approach, including the fact that a three-dimensional Finite Element mesh generation package was already available in the department of Aeronautics (FELISA package). In addition, analytic integration and algorithms in general are simpler for four noded elements, and in terms of accuracy, the spatial compactness of the tetrahedron offers advantages over, for example, the hexahedron. The mesh generator used here is of the Advancing Front type, and was developed for use in inviscid transonic flow problems, although is also suited to low Reynolds number viscous problems; more details of this particular program can be found in

Peraire, Morgan and Peiro (1990). The mesh generator produces fully unstructured general meshes, whose element density may be modified by the inclusion of point, line and triangular source distributions.

5.2 Numerical Method

5.2.1 Introduction

Consider the general differential equation:

$$A(\phi) + Q = 0 \tag{5.1}$$

where A is a linear operator and Q is independent of ϕ. There is an associated boundary equation:

$$B(\phi) + q = 0 \tag{5.2}$$

where B is a linear operator and q is independent of ϕ. For instance, Dirichlet and Neumann boundary conditions are represented as:

$$\begin{aligned} B(\phi) = \phi \quad &; \quad q = -\phi^0 \quad on\ \Gamma_D \\ B(\phi) = -\frac{\partial \phi}{\partial n} \quad &; \quad q = -q^0 \quad on\ \Gamma_N \end{aligned} \tag{5.3}$$

If ϕ is approximated by the function $\hat{\phi} = \sum \phi_i N_i$, where N_i are the global trial functions (also shape functions), and ϕ_i is the value of the function ϕ at node i, it is generally true that $\hat{\phi}$ will not be an exact solution to (5.1). Upon substitution, there is a residual in the domain Ω of R_Ω, and a residual at the boundary R_Γ:

$$R_\Omega = A(\hat{\phi}) + Q \tag{5.4}$$

$$R_\Gamma = B(\hat{\phi}) + q \ . \tag{5.5}$$

The general method of weighted residuals (MWR), of which Finite Elements is an example, requires that the integral of these residuals, multiplied by a suitable test function (also weighting function), be equal to zero, i.e. :

$$\int_\Omega R_\Omega W \ d\Omega + \int_\Gamma R_\Gamma \overline{W} \ d\Gamma = 0 \quad l = 1, 2, 3, ... \tag{5.6}$$

where $\overline{W}$ is another suitable test function, not necessarily equal to W. Now,

$$\int_\Omega R_\Omega W \ d\Omega = \sum_{e=1}^{n_e} \int_{\Omega^e} R_\Omega W \ d\Omega \tag{5.7}$$

and,

$$\int_\Gamma R_\Gamma \overline{W} \ d\Gamma = \sum_{e=1}^{n_e} \int_{\Gamma^e} R_\Gamma \overline{W} \ d\Gamma \tag{5.8}$$

provided that $\sum_{e=1}^{n_e} \Omega^e = \Omega$, and $\sum_{e=1}^{n_e} \Gamma^e = \Gamma$. Γ^e denotes that part of the boundary of element Ω^e which lies on Γ. If equation (5.6) is satisfied for a very large number of arbitrary functions W and $\overline{W}$, then the approximation $\hat{\phi}$ must approach the exact solution ϕ. In the Galerkin formulation of the Finite Element method, the test functions are the same as trial functions, i.e. $W = N$. One of the attractive properties of this approach is that the discretization of a Laplacian operator results in a symmetric stiffness matrix; in addition, the implementation of homogeneous Neumann type boundary conditions is particularly straightforward.

In the present three-dimensional method, the velocity-vorticity formulation is employed. As in the two-dimensional case, the vorticity transport equation is solved using an operator split approach, in which the convection of vorticity is performed using vortons, and changes in the vorticity field arising from the processes of diffusion **and** stretching are calculated at the node points of the mesh; these changes are interpolated back on to the vortons prior to the convection step.

The fields of velocity and vorticity are approximated by a piecewise linear spatial variation over the elements in the domain. The representation is therefore:

$$\vec{\omega}(\vec{x},t) \approx \vec{\tilde{\omega}} = \sum_{i=1}^{n_p} \vec{\omega}_i N_i \tag{5.9}$$

$$\vec{u}(\vec{x},t) \approx \vec{\tilde{u}} = \sum_{i=1}^{n_p} \vec{u}_i N_i \tag{5.10}$$

where n_p is the number of nodes, and N_i the shape function at node i. A typical tetrahedral element (e) is shown in figure 5.1.

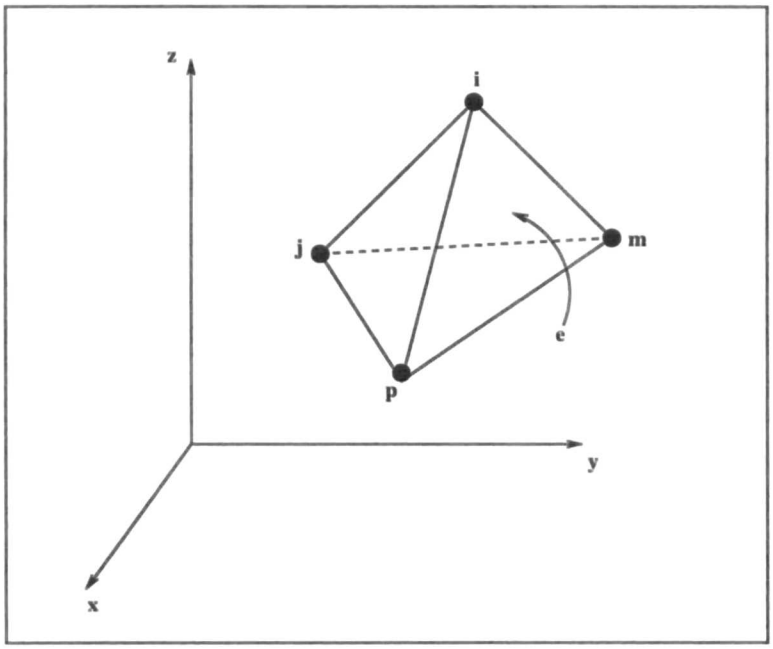
The connectivity between elements and nodes is arranged under the consistent node numbering system of an anticlockwise order of three nodes from any one of the nodes, e.g. $pijm$, $ipmj$, $mipj$ etc... The shape functions are linear over this element, and are given by:

$$N_i^e = \alpha_i^e + \beta_i^e x + \gamma_i^e y + \delta_i^e z \tag{5.11}$$

$$N_j^e = \alpha_j^e + \beta_j^e x + \gamma_j^e y + \delta_j^e z \tag{5.12}$$

$$N_m^e = \alpha_m^e + \beta_m^e x + \gamma_m^e y + \delta_m^e z \tag{5.13}$$

$$N_p^e = \alpha_p^e + \beta_p^e x + \gamma_p^e y + \delta_p^e z \tag{5.14}$$



Tetrahedral element

Figure 5.1

where,

$$\vec{\omega}^e = \frac{1}{6V^e}[\ (\ \alpha_i^e + \beta_i^e x + \gamma_i^e y + \delta_i^e z) \ \vec{\omega}_i \ +$$

$$(\ \alpha_j^e + \beta_j^e x + \gamma_j^e y + \delta_j^e z) \ \vec{\omega}_j \ +$$

$$(\ \alpha_m^e + \beta_m^e x + \gamma_m^e y + \delta_m^e z) \ \vec{\omega}_m \ +$$

$$(\ \alpha_p^e + \beta_p^e x + \gamma_p^e y + \delta_p^e z) \ \vec{\omega}_p \ ] \qquad (5.15)$$

and

$$6V^e = det \begin{vmatrix} 1 & x_i & y_i & z_i \\ 1 & x_j & y_j & z_j \\ 1 & x_m & y_m & z_m \\ 1 & x_p & y_p & z_p \end{vmatrix} \tag{5.16}$$

$$\alpha_i^e = det \begin{vmatrix} x_j & y_j & z_j \\ x_m & y_m & z_m \\ x_p & y_p & z_p \end{vmatrix} \qquad \beta_i^e = -det \begin{vmatrix} 1 & y_j & z_j \\ 1 & y_m & z_m \\ 1 & y_p & z_p \end{vmatrix}$$

$$\gamma_i^e = -det \begin{vmatrix} x_j & 1 & z_i \\ x_m & 1 & z_j \\ x_p & 1 & z_m \end{vmatrix} \qquad \delta_i^e = -det \begin{vmatrix} x_j & y_j & 1 \\ x_m & y_m & 1 \\ x_p & y_p & 1 \end{vmatrix} \tag{5.17}$$

Definitions for the other coefficients are cyclic rearrangements of the above. Similar expressions are used for the velocity field over the element.

5.2.2 Velocity Equation

For a given distribution of vorticity, the problem is to solve:

$$\nabla^2 \vec{u} = -\nabla \wedge \vec{\omega} \qquad in\ \Omega \tag{5.18}$$

with boundary conditions:

$$\vec{u} \cdot \vec{n} = 0 \qquad on\ \Gamma_s \tag{5.19}$$

$$\vec{u} = \vec{u}^{\,0} \qquad on\ \Gamma_D \tag{5.20}$$

$$\frac{\partial \vec{u}}{\partial n} = 0 \qquad on\ \Gamma_N \tag{5.21}$$

where $\Omega = \bigcup_{e=1}^{n_e} \Omega_i^e$, Γ_s is the portion of the boundary coincident with a solid surface, Γ_D is the portion of the boundary where $\vec{u}$ is specified (Dirichlet), and Γ_N is the portion of the boundary where outlet conditions are specified ($\Gamma = \Gamma_s + \Gamma_D + \Gamma_N$). The Finite Element approximation becomes:

$$\int_\Omega (\nabla^2 \vec{u} + \nabla \wedge \vec{\omega}) N_l \, d\Omega + \int_{\Gamma_s} \frac{\partial \hat{u}}{\partial n} \overline{W}_l \, d\Gamma_s = 0, \qquad l = 1, 2, \ldots, n_p \tag{5.22}$$

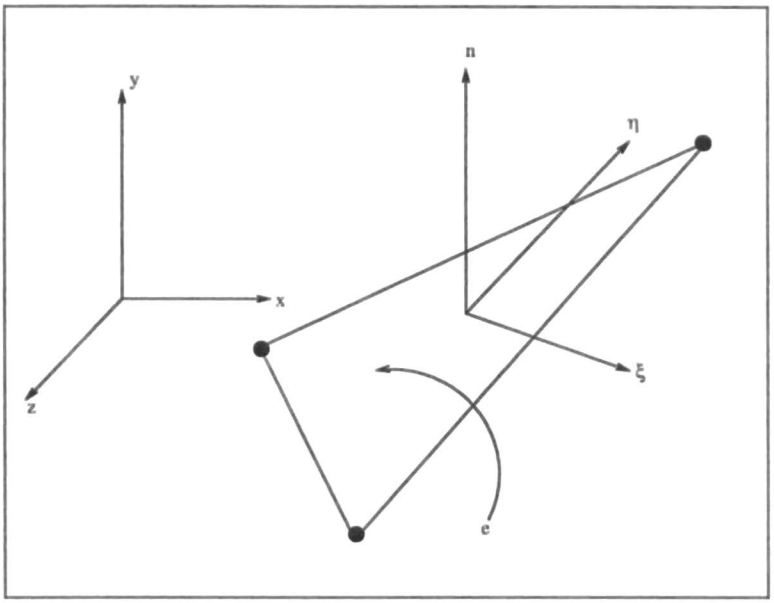
Inserting the expansions for $\vec{u}$ and $\vec{\omega}$, and using Green's lemma, we get:

$$-\int_\Omega \nabla N_i . \nabla N_l \, d\Omega\{\vec{u}_i\} + \int_\Gamma \frac{\partial \vec{u}}{\partial n} . N_l \, d\Gamma + \int_\Omega (\nabla \wedge N_i) N_l \, d\Omega\{\vec{\omega}_i\}$$

$$+ \int_{\Gamma_s} \frac{\partial \vec{u}}{\partial n} \overline{W}_l \, d\Gamma_s = 0 \qquad l = 1, 2, \ldots, n_p \tag{5.23}$$

where $\vec{n}$ is the unit normal vector out of the element.

Equation (5.23) is a vector equation for the three components of velocity, which are uncoupled from each other everywhere except at Γ_s. Defining a local coordinate system on each element on Γ_s, and denoting all variables in this system by superscript e:



Solid surface boundary element axis system

Figure 5.2

$$\vec{u}^{\,(e)} = [\beta]\vec{u} \tag{5.24}$$

where $[\beta]$ is the direction cosine matrix,

$$\rightarrow \vec{u} = [\beta]^T \vec{u}^{\,(e)} \tag{5.25}$$

since both axis systems are orthogonal.

In order to satisfy $\vec{u}.\vec{n} = 0$ on Γ_s, the velocity at nodes on the solid surface is projected such that $\vec{u}^*.\vec{n}_i = 0$, where $\vec{n}_i$ is the normal at node i (and is an average of the normals of all surface elements that connect to node i) and $\vec{u}^*$ is an intermediate velocity. By continuity and the vorticity-velocity relationship, the normal flux over each surface element is then expressed as:

$$\frac{\partial u}{\partial n} = -\beta_{11}\left(\frac{\partial u_\xi}{\partial x_i} + \frac{\partial u_\eta}{\partial \eta}\right) + \beta_{21}\left(\frac{\partial u_n}{\partial x_i} + \omega_\eta\right) + \beta_{31}\left(\frac{\partial u_n}{\partial \eta} - \omega_\xi\right) = q_u$$

$$\frac{\partial v}{\partial n} = -\beta_{12}(\frac{\partial u_\xi}{\partial x_i} + \frac{\partial u_\eta}{\partial \eta}) + \beta_{22}(\frac{\partial u_n}{\partial x_i} + \omega_\eta) + \beta_{32}(\frac{\partial u_n}{\partial \eta} - \omega_\xi) = q_v$$

$$\frac{\partial w}{\partial n} = -\beta_{13}(\frac{\partial u_\xi}{\partial x_i} + \frac{\partial u_\eta}{\partial \eta}) + \beta_{23}(\frac{\partial u_n}{\partial x_i} + \omega_\eta) + \beta_{33}(\frac{\partial u_n}{\partial \eta} - \omega_\xi) = q_w \tag{5.26}$$

The velocity equations become, on setting $\overline{W}_l = -N_l$:

$$\int_\Omega \nabla N_i.\nabla N_l \, d\Omega \, \{u_i\} = \int_\Omega \frac{\partial N_i}{\partial y} N_l \, d\Omega\{\omega_{zi}\} - \int_\Omega \frac{\partial N_i}{\partial z} N_l \, d\Omega\{\omega_{y_i}\} + \int_{\Gamma_s} q_u N_l d\Gamma_s \quad l = 1, 2, \ldots, n_p \tag{5.27}$$

$$\int_\Omega \nabla N_i.\nabla N_l \, d\Omega \, \{v_i\} = \int_\Omega \frac{\partial N_i}{\partial z} N_l \, d\Omega\{\omega_{xi}\} - \int_\Omega \frac{\partial N_i}{\partial x} N_l \, d\Omega\{\omega_{zi}\} + \int_{\Gamma_s} q_v N_l d\Gamma_s \quad l = 1, 2, \ldots, n_p \tag{5.28}$$

$$\int_\Omega \nabla N_i.\nabla N_l \, d\Omega \, \{w_i\} = \int_\Omega \frac{\partial N_i}{\partial x} N_l \, d\Omega\{\omega_{y_i}\} - \int_\Omega \frac{\partial N_i}{\partial y} N_l \, d\Omega\{\omega_{xi}\} + \int_{\Gamma_s} q_w N_l d\Gamma_s \quad l = 1, 2, \ldots, n_p \tag{5.29}$$

Once integrated over all the elements and assembled into a global matrix, the following system is solved:

$$[K]\{u\} = \{S_u\} \tag{5.30}$$

$$[K]\{v\} = \{S_v\} \tag{5.31}$$

$$[K]\{w\} = \{S_w\} \tag{5.32}$$

Rather than loop over the elements whilst calculating the local element stiffness

matrix, $[K]$ is assembled prior to the time march, and thus represents a global nodal stiffness matrix. Typically in an unstructured tetrahedron element mesh there are five times the number of elements as there are nodes; thus the loops over elements take roughly five times the computational effort. $[K]$ is a discretization of the Laplacian, and is a symmetric matrix; only the upper triangular part is stored. Because the mesh is fully unstructured, $[K]$ has no structure, and it is stored in a Compressed Row Storage (CRS) format. The CRS format puts subsequent non-zeros of the matrix in contiguous memory locations, and therefore also requires two additional integer pointer arrays. These are assembled in a pre-processing program. Once formed, the system is solved using a Preconditioned Conjugate Gradient Method; the preconditioning method used is diagonal scaling, since its implementation is straightforward. An Incomplete Cholesky Conjugate Gradient method was implemented, which resulted in approximately a factor of four reduction in the number of iterations to convergence, but it was found that the extra costs contained in the forward/backward substitution stage, together with the large memory allocation required to store the factored matrix (there are two: one for velocity, one for diffusion) made the approach less elegant and less effective than was initially perceived. Computations presented here were carried out on a Silicon Graphics 4000 Workstation, for the most part with $16Mb$ of memory, which was later updated to $48Mb$. Although the processor speed of this machine is relatively quick, the limitations of the memory size can cause severe deterioration in the throughput of data once the physical memory limit is reached.

Once u,v, and w have been solved, values at the solid surface will in general not satisfy $\vec{u}.\vec{n} = 0$. Projections of the velocity field at the solid surfaces are again made, modifying the boundary flux terms $\int_{\Gamma_s} q_u N_l d\Gamma_s$, $\int_{\Gamma_s} q_v N_l d\Gamma_s$ and $\int_{\Gamma_s} q_w N_l d\Gamma_s$ in equations 5.27, 5.28 and 5.29. The volume source terms do not change and are

stored in separate vectors for each component of velocity. The system is re-solved until there is no further change in the solid surface velocities. Convergence is typically achieved in about five outer loops of iteration, with a greatly decreasing amount of effort per outer iteration. It is found that over-projection of the velocity field at the solid surfaces (i.e. 'over-relaxation') produces a faster rate of convergence in the velocity solver.

5.2.3 Diffusion and stretching equation

The following describes the approach taken to solve the diffusion and stretching of vorticity. The solution to these equations gives $\vec{\omega}^*$, an intermediate vorticity field. The final vorticity field $\vec{\omega}^{n+1}$ is found by convecting $\vec{\omega}^*$. The equations to be solved are:

$$\frac{\partial \vec{\omega}}{\partial t} = \nu \nabla^2 \vec{\omega} + (\vec{\omega} \cdot \nabla)\vec{u} \qquad in\ \Omega \tag{5.33}$$

$$\frac{\partial \vec{\omega}}{\partial n} = \vec{q}^{\,0} \qquad on\ \Gamma_s \tag{5.34}$$

$$\frac{\partial \vec{\omega}}{\partial n} = 0 \qquad on\ \Gamma_N \tag{5.35}$$

$$\vec{\omega} = \vec{\omega}^{\,0} \qquad on\ \Gamma_D \tag{5.36}$$

At a slip surface, the only non-zero component of vorticity is the component normal to the wall (i.e. a vortex cannot meet a slip surface at any angle other than 90^o and $\vec{\omega} \wedge \vec{n} = 0$, $\frac{\partial \vec{\omega} \cdot \vec{n}}{\partial n} = 0$ there). At a wall, only in-plane components of vorticity exist, i.e. $\vec{\omega} \cdot \vec{n} = 0$; the normal gradients of the two in-plane components are calculated using a method similar to that employed by Koumoutsakos, Leonard and Pépin (1994).

The production of a vorticity flux over the time step is related to the surface integral of a vortex sheet, which is the current slip velocity value, i.e. :

$$\oint \vec{u}_s \, d\vec{s} = - \oint \int_t^{t+\Delta t} \frac{\partial \vec{\omega}}{\partial n} \, dt \, d\vec{s} \tag{5.37}$$

For a Crank-Nicholson treatment of the diffusion term (used here), this gives the condition:

$$\frac{1}{2} \left(\frac{\partial \vec{\omega}^{(t+\Delta t)}}{\partial n} + \frac{\partial \vec{\omega}^{(t)}}{\partial n} \right) = - \frac{\vec{u}_s \wedge \vec{n}}{\nu \Delta t} \tag{5.38}$$

The Finite Element discretization follows the same lines as in the velocity equations, with the addition of a 'mass' matrix M which comes about through integration of the $\frac{\partial \vec{\omega}}{\partial t}$ term, and the inclusion of the stretching terms, which are treated explicitly. The Crank-Nicholson method is used for the diffusion term. A typical form of integration of the vortex stretching component gives, for example, in the x-component equation, the following three terms:

$$\begin{aligned} \int_\Omega N_i \frac{\partial N_j}{\partial x} N_l \, d\Omega \{\omega_{x_i}^n u_j\} \quad &+ \quad \int_\Omega N_i \frac{\partial N_j}{\partial y} N_l \, d\Omega \{\omega_{y_i}^n u_j\} \\ &+ \quad \int_\Omega N_i \frac{\partial N_j}{\partial z} N_l \, d\Omega \{\omega_{z_i}^n u_j\} \end{aligned} \tag{5.39}$$

However, equation (5.33) may be written in the following form:

$$\frac{\partial \omega_x}{\partial t} = \nu \nabla^2 \omega_x + \nabla \cdot (u \vec{\omega}) \tag{5.40}$$

$$\frac{\partial \omega_y}{\partial t} = \nu \nabla^2 \omega_y + \nabla \cdot (v \vec{\omega}) \tag{5.41}$$

$$\frac{\partial \omega_z}{\partial t} = \nu \nabla^2 \omega_z + \nabla \cdot (w \vec{\omega}) \tag{5.42}$$

by requiring that $\nabla \cdot \vec{\omega} = 0$. Use may then be made of the 'product approximation' or 'group representation' method (Christie et al (1980)) to permit a more accurate representation of the stretching terms. After integration over an element Ω^e, the three transport equations for vorticity then become:

$$\int_{\Omega^e} \left(\frac{1}{2} \nabla N_i \nabla N_l + \frac{1}{\nu \Delta t} N_i N_l \right) \, d\Omega^e \, \{\omega^*_{x\,i}\} =$$

$$\int_{\Omega^e} \left(\frac{1}{2} \nabla N_i \nabla N_l + \frac{1}{\nu \Delta t} N_i N_l \right) \, d\Omega^e \, \{\omega^n_{x\,i}\}$$

$$+ \int_{\Omega^e} \frac{\partial N_l}{\partial x} N_i \, d\Omega^e \left\{ \left(u\omega^n_x + u\omega^n_y + v\omega^n_z \right)_i \right\}$$

$$+ \int_{\Gamma_s} \frac{\partial \hat{\omega}^n_x}{\partial n} N_l \, d\Gamma_s \quad l = 1, 2, \ldots, n_p \tag{5.43}$$

$$\int_{\Omega^e} \left(\frac{1}{2} \nabla N_i \nabla N_l + \frac{1}{\nu \Delta t} N_i N_l \right) \, d\Omega^e \left\{ \omega^*_{y_i} \right\} =$$

$$\int_{\Omega^e} \left(\frac{1}{2} \nabla N_i \nabla N_l + \frac{1}{\nu \Delta t} N_i N_l \right) \, d\Omega^e \left\{ \omega^n_{y\,i} \right\}$$

$$+ \int_{\Omega^e} \frac{\partial N_l}{\partial x} N_i \, d\Omega^e \left\{ \left(v\omega^n_x + v\omega^n_y + v\omega^n_z \right)_i \right\}$$

$$+ \int_{\Gamma_s} \frac{\partial \hat{\omega}^n_y}{\partial n} N_l \, d\Gamma_s \quad l = 1, 2, \ldots, n_p \tag{5.44}$$

$$\int_{\Omega^e} \left(\frac{1}{2}\nabla N_i \nabla N_l + \frac{1}{\nu\Delta t} N_i N_l\right) \, d\Omega^e \, \{\omega^*_{z\,i}\} =$$

$$\int_{\Omega^e} \left(\frac{1}{2}\nabla N_i \nabla N_l + \frac{1}{\nu\Delta t} N_i N_l\right) \, d\Omega^e \, \{\omega^n_{z\,i}\}$$

$$+ \int_{\Omega^e} \frac{\partial N_l}{\partial x} N_i \, d\Omega^e \left\{\left(w\omega^n_x + w\omega^n_y + w\omega^n_z\right)_i\right\}$$

$$+ \int_{\Gamma_s} \frac{\partial \hat{\omega}^n_z}{\partial n} N_l \, d\Gamma_s \quad l = 1, 2, \ldots, n_p \tag{5.45}$$

After assembly over all the elements this gives a system to be solved which is of the type:

$$[K + M]\{\omega_x\} = \{S_{\omega_x}\} \tag{5.46}$$

$$[K + M]\{\omega_y\} = \{S_{\omega_y}\} \tag{5.47}$$

$$[K + M]\{\omega_z\} = \{S_{\omega_z}\} \tag{5.48}$$

Since $[M]$ is also symmetric, $[K + M]$ is a symmetric matrix, and this system is solved in a similar manner to the velocity problem by using the Conjugate Gradient method with a diagonal scaling preconditioner.

5.2.4 Vortons

A vorton is a dimensionless, undeformable vortex object. It is a vortical singularity corresponding to a three-dimensional δ-singularity of the vorticity field. A vorton is thus the three-dimensional analogue of the two-dimensional point vortex. The

point vortex is an infinitely long, straight line vortex which, when intersecting an orthogonal analysis plane becomes a point there; since it extends to infinity, and its circulation is constant throughout, it represents a solenoidal vorticity field, and thus the divergence of vorticity is everywhere zero. The vorton, on the other hand, 'terminates' in space, and is therefore a vortex monopole. The problem of maintaining a divergence free vorticity field from a finite set of evolving vortons in a general incompressible flow is one of the principal arguments against the use of this object (Saffman and Meiron(1986)). Nevertheless, the use of vortons is becoming more popular because of the simplicity and flexibility that they offer in terms of tracking complex three-dimensional flow structures. In addition, the particular problems which are addressed in this thesis are well suited to this representation, since any errors in divergence which may develop are washed downstream with the flow, and cannot accumulate in the vicinity of the cylinder. The problem of circulating internal flows, such as a cavity driven problem, might require a more cautious approach.

The vorticity field $\vec{\omega}$ is represented as the sum of a finite set of vortons:

$$\vec{\omega}(\vec{x},t) = \sum_{\alpha} \vec{\kappa}_{\alpha}(t)\delta(\vec{x} - \vec{x}_{\alpha}) \ . \tag{5.49}$$

A Biot-Savart volume integral of this elementary representation of the vorticity field gives the following induced velocity field in the neighbourhood of a single vorton α:

$$\vec{u}(\vec{x},t) = \frac{\vec{\kappa}_{\alpha} \wedge (\vec{x} - \vec{x}_{\alpha})}{4\pi|\vec{x} - \vec{x}_{\alpha}|^3} \tag{5.50}$$

In the absence of viscosity, the **strength** of vortons remains a function of time because of the stretching term which exists in the three-dimensional vorticity transport equation. In pure particle methods, the evolution of the vortons would normally be

represented as:

$$\frac{d\vec{x}_\alpha}{dt} = \vec{u}_\alpha(\vec{x}_\alpha, t) \; ; \; \frac{d\vec{\kappa}_\alpha}{dt} = (\vec{\kappa}_\alpha \cdot \nabla)\vec{u}_\alpha(\vec{x}_\alpha, t) \tag{5.51}$$

where the first equation represents the changes in the vorticity field due to convection, and the second due to vortex stretching. Saffman and Meiron (1986) show that the above formulation does not constitute a weak solution to the vorticity transport equation, and thus the invariance of vorticity and momentum are violated. However, Winckelmans and Leonard (1988) show that by using a different expression for the vortex stretching term, a weak solution is obtained. They implement the following form of the evolution equations for the vortons:

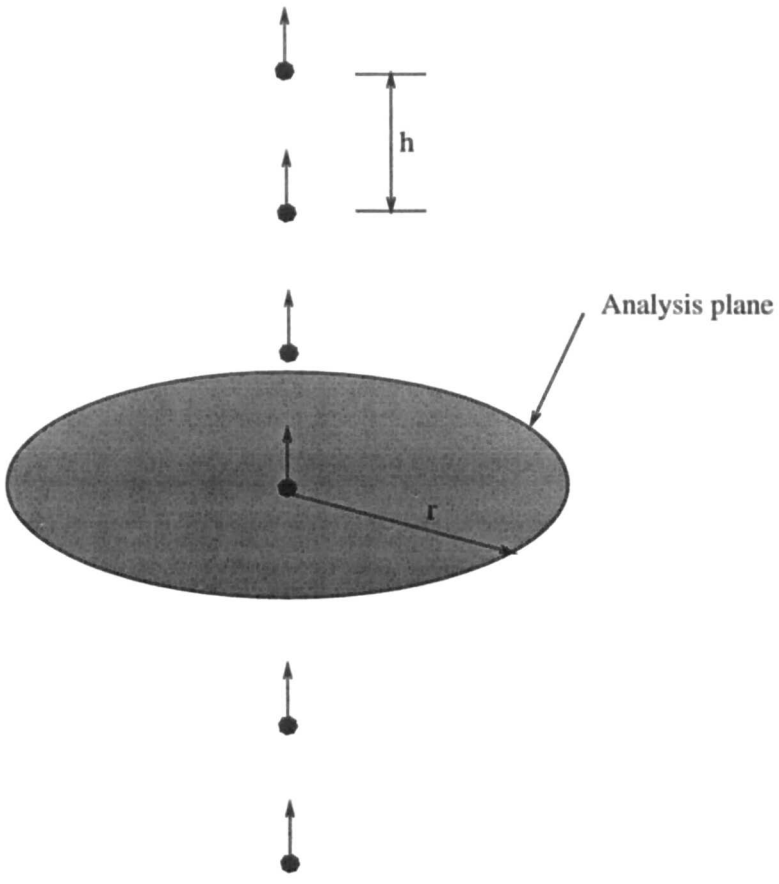
$$\frac{d\vec{x}_\alpha}{dt} = \vec{u}_\alpha(\vec{x}_\alpha, t) \; ; \; \frac{d\vec{\kappa}_\alpha}{dt} = (\vec{\kappa}_\alpha \cdot \nabla^T)\vec{u}_\alpha(\vec{x}_\alpha, t) \; . \tag{5.52}$$

The transpose form is derived from standard form using the relationship: $\vec{\omega} = \nabla \wedge \vec{u}$.

In the present method, the stretching term is included in the solution to the vorticity transport equation, which is obtained from a Finite Element solution over the discretized domain; the vorticity is therefore by definition a weak solution to the transport equation. Details of the method are presented in the following section.

As a final note to the idea of using vortons in the modelling of incompressible flows, consider the simple example of the straight line vortex. The line vortex may be modelled by a set of colinear, equidistant vortons, with inter-vorton spacing h. The line vortex is parallel to the z-axis, and the circulation of the line vortex is $\Gamma = 2\pi$ (say); the strength of each vorton is Γh. If $q = (u^2 + v^2)^{1/2}$, it is known that $q = \Gamma/2\pi r$, where $r = (x^2 + y^2)^{1/2}$ so that the integral of the velocity along any con-

tour (on a plane orthogonal to the line vortex) that includes the vortex has the value Γ. This is not true for a single vorton, and any line integral of the velocity field that includes the vorton will not, in general be equal to Γ. (The surface integral around any volume that encloses the vorton has the constant value $|\vec{\kappa}|$). The question is how well does a series of vortons model the line vortex? The problem is considered by examining the variation in the velocity q that is induced at a radial distance r from the vortex as a function of the spacing parameter h/r, and comparing it with the line vortex result. Figure 5.3 is a schematic of the problem.



Schematic of vorton problem

Figure 5.3

Now $\vec{\kappa} = (0, 0, \kappa_z)$, and in the case of an analysis plane that intersects one of the vortons:

$$q(r) = \frac{\kappa_z}{4\pi}\left[\frac{1}{r^2} + \frac{2r}{(r^2+h^2)^{\frac{3}{2}}} + \frac{2r}{(r^2+(2h)^2)^{\frac{3}{2}}} + \frac{2r}{(r^2+(3h)^2)^{\frac{3}{2}}} + ...\right] \tag{5.53}$$

on the plane, where the factor of 2 comes from considering contributions from vortons above and below the plane. In the case of an infinite line vortex model, this becomes:

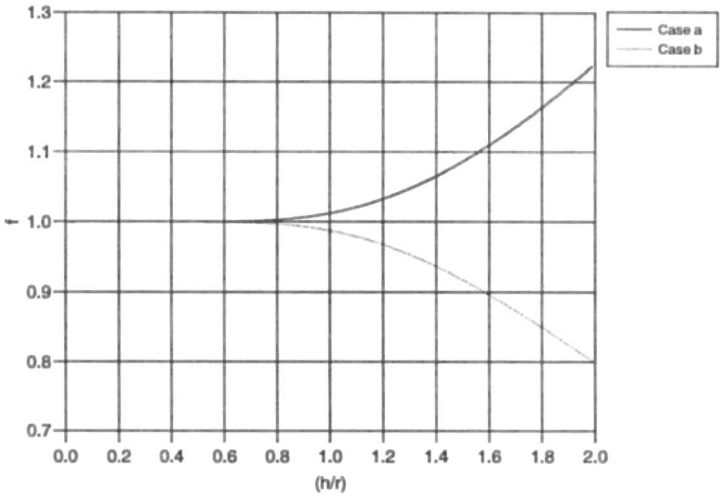
$$q(r) = \frac{\kappa_z}{4\pi}\left[\frac{1}{r^2} + \frac{2}{r^2}\sum_{m=1}^{\infty}\frac{1}{(1+m^2(\frac{h}{r})^2)^{\frac{3}{2}}}\right] \tag{5.54}$$

For the line vortex, we have: $rq(r) = 1\ \forall r$, so we are interested in how well the function:

$$f = \frac{1}{2}\left[\frac{h}{r} + 2\frac{h}{r}\sum_{m=1}^{\infty}\frac{1}{(1+m^2(\frac{h}{r})^2)^{\frac{3}{2}}}\right] \tag{5.55}$$

approximates the value 1. Figure 5.4 is a plot of the variation in f with h/r. It shows the case of the analysis plane intersecting a vorton (case a), and the case of the analysis plane lying midway between two vortons (case b). In the former case $q \to \infty$ as $r \to 0$, and in the latter case, $q \to 0$ as $r \to 0$.

Figure 5.4 shows the limitations of the vorton model: far from the vortex axis, the model is indistinguishable from the line vortex, but as the axis is approached, the 'granular' quality of the vorton model becomes apparent. In any case, for $r > 1.25h$ in all planes of analysis, the array of vortons models the line vortex velocity field very well.



Vorton model representation of an infinite straight line vortex.

h/r is the vorton spacing ratio. In the case of the line vortex $f = 1.0\ \forall r$.

Figure 5.4

It should be emphasised here that a Cloud-in-Cell method cannot model vortex structures smaller than the element size, so although it may appear unfortunate that at a spacing ratio of $h/r = 1.0$ the vorton model does not perform so well (this having implications for element aspect ratios), the modelling of a single line vortex is not the goal of a Cloud-in-Cell approach.

5.2.5 Interpolation between Vortons and Mesh Nodes

The solution to equation 5.18 requires values of vorticity at the mesh nodes. This is achieved by interpolating information between the current set of vortons and the mesh nodes. After the solutions to equations 5.46, 5.47 and 5.48 have been obtained, the **changes** to the vorticity field on the nodes must be interpolated back to the particles. Vortons carry an integral value of vorticity, and have units $\left[\frac{l^3}{t}\right]$. This quantity (termed 'vortonicity' here for want of a better word) is interpolated to the nodes, so that for instance, the vortonicity of a vorton (integer label v) residing in

an element e is interpolated to the four nodes of e (i, j, p, m) using the same linear shape functions as in the Finite Element discretization:

$$\vec{\kappa}_i = \vec{\kappa}_v \left(\alpha_i^e + \beta_i^e x_v + \gamma_i^e y_v + \delta_i^e z_v\right) \tag{5.56}$$

$$\vec{\kappa}_j = \vec{\kappa}_v \left(\alpha_j^e + \beta_j^e x_v + \gamma_j^e y_v + \delta_j^e z_v\right) \tag{5.57}$$

$$\vec{\kappa}_p = \vec{\kappa}_v \left(\alpha_p^e + \beta_p^e x_v + \gamma_p^e y_v + \delta_p^e z_v\right) \tag{5.58}$$

$$\vec{\kappa}_m = \vec{\kappa}_v \left(\alpha_m^e + \beta_m^e x_v + \gamma_m^e y_v + \delta_m^e z_v\right) \tag{5.59}$$

By definition, the integral of the shape functions over the element is unity, implying that vortonicity is conserved after the interpolation process, i.e. :

$$\vec{\kappa}_i + \vec{\kappa}_j + \vec{\kappa}_p + \vec{\kappa}_m = \vec{\kappa}_k \tag{5.60}$$

The vortonicity at each node is calculated through the successive summation of all vortons which are inside all elements to which that node is connected. The summation of shape functions of all vortons that contribute is stored for each node $(S_i;\ i = 1, 2, ..., n_p)$ and this value is used in the re-interpolation process after the field equations have been solved. Once the vortonicity at each node has been calculated, the vorticity there is evaluated by dividing through by a node 'volume' $(V^i;\ i = 1, 2, ..., n_p)$, which is derived as being a quarter of the sum of all the volume elements which connect to that node. For simplicity, a two-dimensional analogue is shown in figure 5.5.

Note that the sum of the volumes associated with the nodes is equal to the volume of the domain Ω.

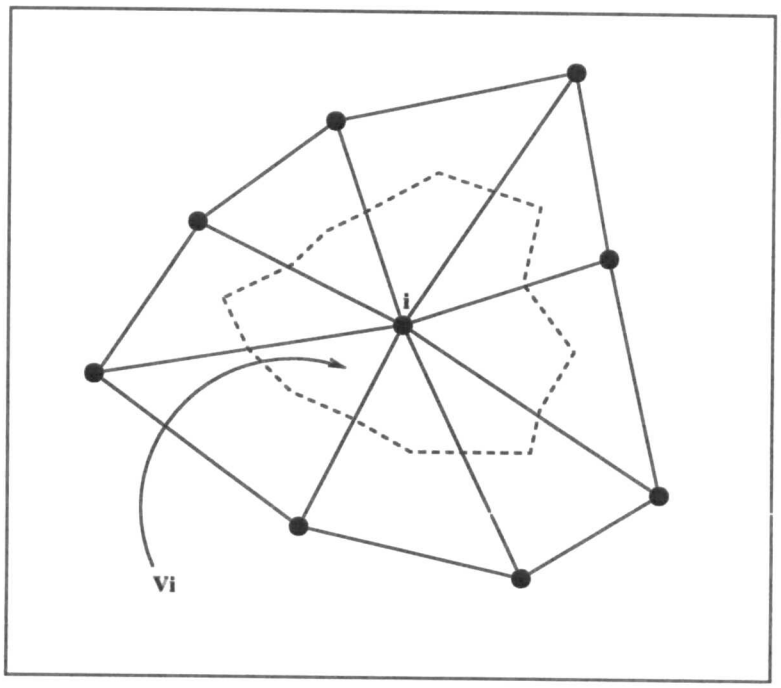


Figure 5.5

Node Volume Analogue

Once the field equations have been solved over Δt, changes in vorticity at each node are re-interpolated back to the particles:

$$\vec{\kappa}_v^{\,n+1} = \vec{\kappa}_v^{\,n} + \delta\vec{\kappa}_v \tag{5.61}$$

where,

$$\delta\vec{\kappa}_v = \frac{\delta\vec{\omega}_i V^i}{S_i}[\alpha_i^e + \beta_i^e x_v + \gamma_i^e y_v + \delta_i^e z_v]$$

$$+ \frac{\delta\vec{\omega}_j V^j}{S_j}[\alpha_j^e + \beta_j^e x_v + \gamma_j^e y_v + \delta_j^e z_v]$$

$$+ \frac{\delta\vec{\omega}_p V^p}{S_p}[\alpha_p^e + \beta_p^e x_v + \gamma_p^e y_v + \delta_p^e z_v]$$

$$+\frac{\delta\vec{\omega}_m V^m}{S_m}[\alpha_m^e + \beta_m^e x_v + \gamma_m^e y_v + \delta_m^e z_v] \tag{5.62}$$

If $\delta\vec{\omega} \neq 0$ at a node, and $S = 0$ (i.e. no vortons contributed to this node), a new vorton is placed at the node, with a vortonocity equal to $(\delta\vec{\omega} \times V^{node})$.

5.2.6 Vorton Convection and Tracking

Once the velocity field has been ascertained at the node points, values are interpolated to the positions of each of the vortons within an element. The velocity field varies linearly through an element, so if the values of velocity at nodes i, j, p, m of element e are designated by $\vec{u}_i, \vec{u}_j, \vec{u}_p, \vec{u}_m$ respectively, the velocity at the point in space coincident with vorton v is given by:

$$\vec{u}_v = \vec{u}_i N_i^e(\vec{x}_v) + \vec{u}_j N_j^e(\vec{x}_v) + \vec{u}_p N_p^e(\vec{x}_v) + \vec{u}_m N_m^e(\vec{x}_v) \tag{5.63}$$

The position of each vorton is then updated according to:

$$\vec{x}_v^{n+1} = \vec{x}_v^n + \vec{u}_v^n \Delta t \tag{5.64}$$

After the vortons have been convected, their positions with respect to the volume elements need to be found. The shape functions over the elements are used to keep track of the vortons. Each vorton has a volume element integer identifier attached to it, and each volume element has a list of the four volume elements which are face neighbours. If an element borders a surface boundary triangle, that neighbour has an integer identifier of 0. To check if a vorton is resident in an element, the value of the shape function for each of the nodes is checked: if all are positive the vorton lies

within the element; if not, the search direction begins in the most negative sense. If the search direction encounters a 0, it goes back to the next most likely direction (i.e. next most negative shape function) and so forth.

The order of element neighbours is arranged (in the pre-processor) to be consistent with the node numbering convention of each element, e.g. neighbour number 1 of e has a common face with e which is opposite to node number 1 of e. This allows for a more efficient searching algorithm.

5.2.7 Summary of Code

The following is the layout of the algorithmic structure of the three-dimensional code developed here. It only includes the principal components within the time-stepping loop, so for instance, the algorithms concerned with releasing passive markers, or sampling data from various points in space, are not included.

- Interpolate from vortons to mesh nodes.

- Calculate source terms in velocity equations, and solve for velocity at node points.

- Calculate source terms in diffusion/stretching equations, and solve for vorticity.

- Interpolate changes in vorticity at nodes back to vortons.

- Interpolate velocity field to vortons.

- Convect vortons over the time step.

• Search for vortons.

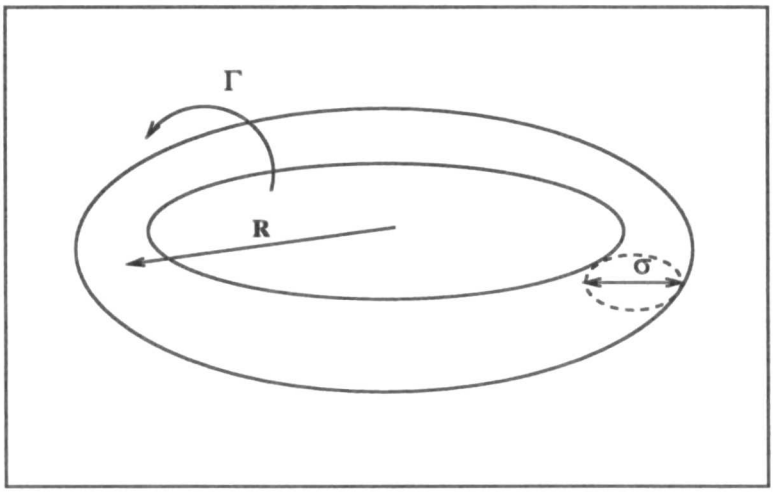
5.2.8 Validation of Code

Full validation of a three-dimensional general purpose viscous code is a difficult and time consuming task. In no way does this section claim to have achieved this, but certain preliminary tests were carried out to check the veracity of the algorithms developed here. At the lowest level, the convection and searching algorithms were tested by modelling the propagation of an inviscid vortex ring, and comparing the self-induced velocity with an analytic results.

The first two terms in a series for the velocity of a thin single vortex ring are given (Widnall, Bliss, Tsai (1966)) by:

$$v = \frac{\Gamma}{4\pi R}\left[\ln\left(\frac{8R}{\sigma}\right) - \frac{1}{4}\right] \tag{5.65}$$

where Γ is the circulation, R the radius, and σ the core size (figure 5.6).



Configuration of vortex ring

Figure 5.6

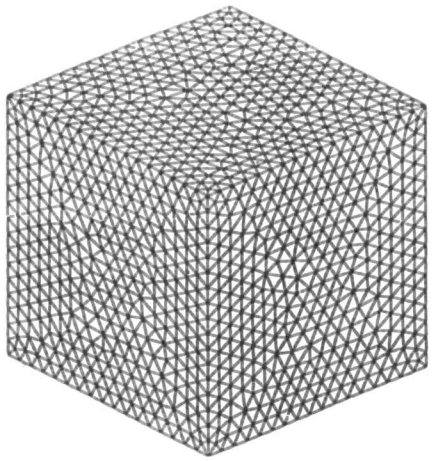
As $\sigma \to 0,\ v \to \infty$.

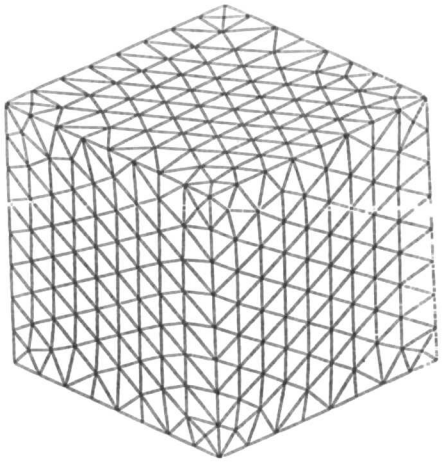
The single vortex ring was modelled by 100 vortons distributed azimuthally and regularly; the theoretical core size is therefore zero, but an effective core size results as a function of the mesh density and interpolation method between particle and element. Basically, the ring takes on a core size proportional to some minimum dimension of the mesh. Thus, the finer the mesh, the faster the ring is expected to propagate. Figure 5.7 is a plot of the three different sized meshes used and the corresponding vortex ring velocity in each; h is the typical spacing between nodes. It may be seen that reduction in element size leads to an increase in velocity - indicating that the effective core size of the vortex is reduced. The observed velocities for the coarse, medium and fine meshes are: $v_c = 0.0598$; $v_m = 0.0778$; $v_f = 0.0882$ Equation 5.65 may be re-arranged to give:

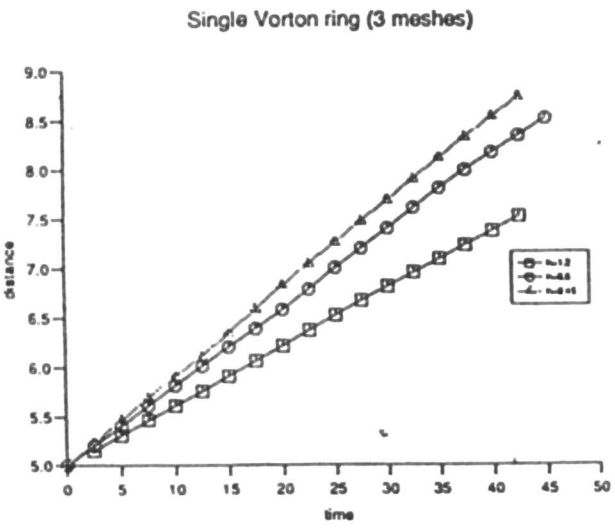
$$\sigma = 8R\exp^{-[\frac{4\pi Rv}{\Gamma}+\frac{1}{4}]} \tag{5.66}$$

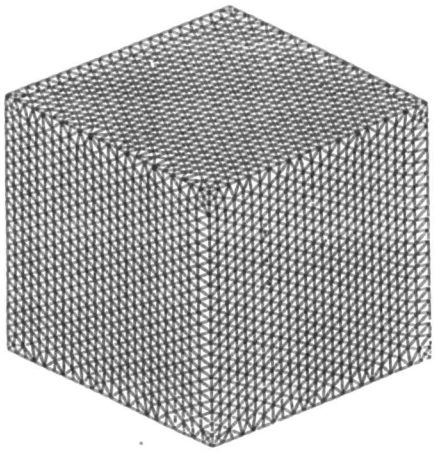
This gives: $\sigma_c = 2.380$; $\sigma_m = 1.353$; $\sigma_f = 0.975$.

These values are slightly less than twice the corresponding typical element sizes, indicating that the ring of singular particles is smeared, on average, across two elements.







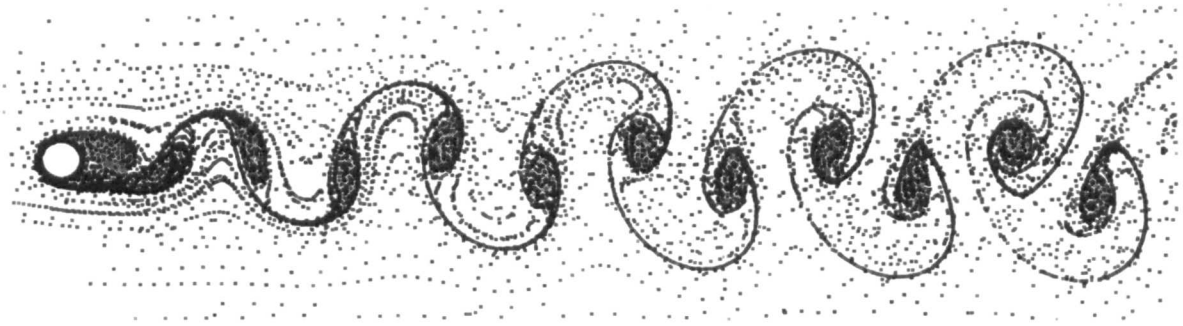


Three meshes and corresponding ring position versus time.

Figure 5.7

In order to compare this code with the two-dimensional vortex method, the steady uniform incident flow past a cylinder at a Reynolds number of 200 was modelled.

To maintain a two-dimensional flow, symmetry planes were used at the ends of the cylinder and the mesh was generated such that the height of the cylinder was half of the diameter. This prevented the generation of any spanwise instabilities at this Reynolds number, which are of larger lengthscales. The objectives of this test were to establish the complete viscous algorithm (except for the stretching terms) without the complications of a truly three-dimensional flow. Pressure at all nodes was calculated from the solution to a Poisson equation (see Appendix C), and forces on the cylinder were evaluated by integration of the pressures and skin friction components around the cylinder. The shedding frequency was measured ($S = 0.196$) and found to be in good agreement with the two-dimensional data at this Reynolds number, as was the drag force coefficient ($\overline{C_D} = 1.3$). Figure 5.8 is a plot of a spanwise slice of vortons; in this computation the cutoff value of vorticity was extremely small, resulting in the appearance of extremely weak vortons far from the wake, which come about through diffusion.



Vorton plot of steady incident flow at Reynolds number of 200

Figure 5.8

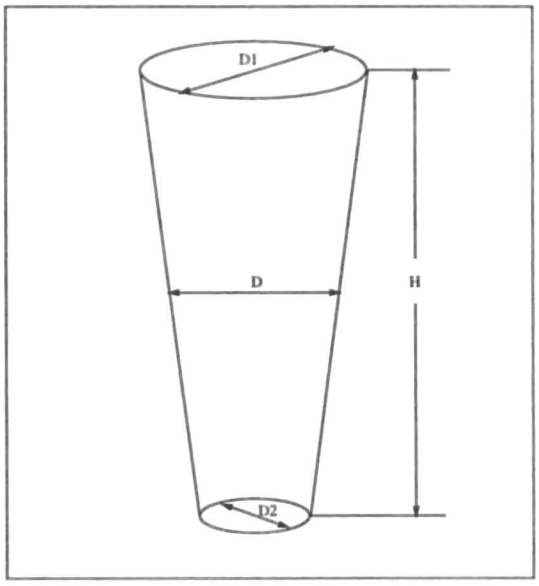
5.3 Results

5.3.1 Tapered Cylinder

The flow behind linearly, mildly tapered cylinders is a simple example of a three-dimensional wake flow, and makes for an excellent starting point in the study of flow past more complicated three-dimensional bodies, or indeed, three-dimensional incident flow past a quasi two-dimensional body, such as the case of a circular cylinder translating into free surface waves. The tapered cylinder is characterised by a taper ratio, which is normally defined as:

$$T_R = H/(D_1 - D_2) \tag{5.67}$$

where H is the height of the cylinder, and D_1, D_2 are the cylinder diameters at the ends of the cylinder. A mildly tapered cylinder is one for which $T_R \geq 40$.



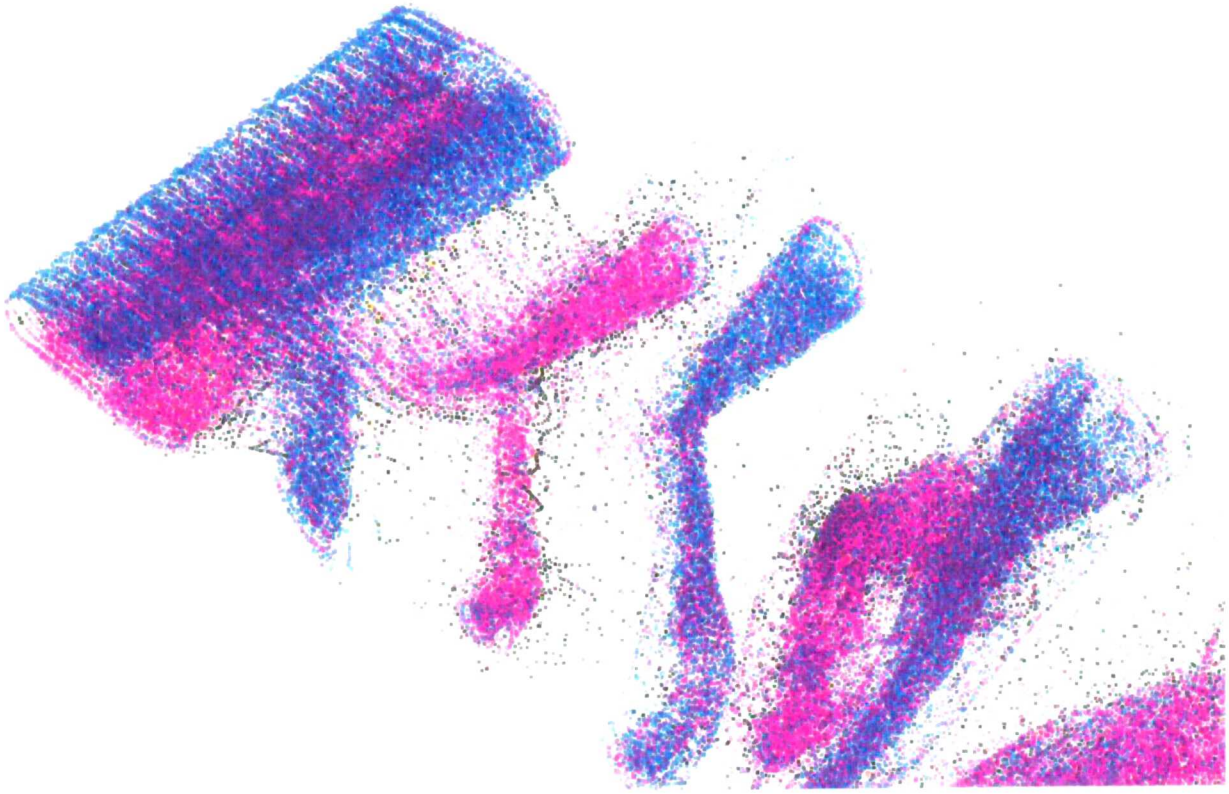
Tapered cylinder geometry

Figure 5.9

Tapered cylinders are of course important in their own right, as there are many examples of this type of structure in engineering: for instance, chimney stacks and cooling towers in power stations are examples of large-scale mildly tapered cylinders. The study of flow past tapered cylinders was initiated by Gaster (1969), who reported the existence of two frequencies in the wake, one of which was an order of magnitude lower than the principal one; in a later experiment, he reports the presence of a cellular shed vortex structure, i.e. one in which the vortices are shed in discrete 'blocks' in the spanwise sense. Van Atta and Piccirillo (1990) also found cellular structure behind tapered cylinders, and showed that the difference in shedding frequencies between adjacent spanwise cells was a constant. At the interface between two cells, a shed vortex undergoes a splitting or dislocation, resulting in the formation of Y-shaped vortices in the wake.

Flow visualisation experiments on a tapered cylinder with $T_R = 40$ were carried out by the author, and the results are presented in chapter 6.

Numerical simulations have been carried out on a tapered cylinder with $T_R = 40$, and at a Reynolds of 200, based on the mid-span diameter. The aspect ratio of this cylinder is 8, based on the mid-span diameter. Figure 5.10 is a plot of the vortons for this case. It quite clearly shows the Y-shaped vortices that occur as a result of dislocations. In this plot the larger end is at the top, and the vortons are coloured according to the sign of their component in the spanwise direction, i.e. blue vortons indicate positive spanwise vorticity, red vortons negative spanwise vorticity. The planes that intersect the cylinder ends are modelled as symmetry planes (i.e. slip solid surfaces). The vortices intersect these planes orthogonally.



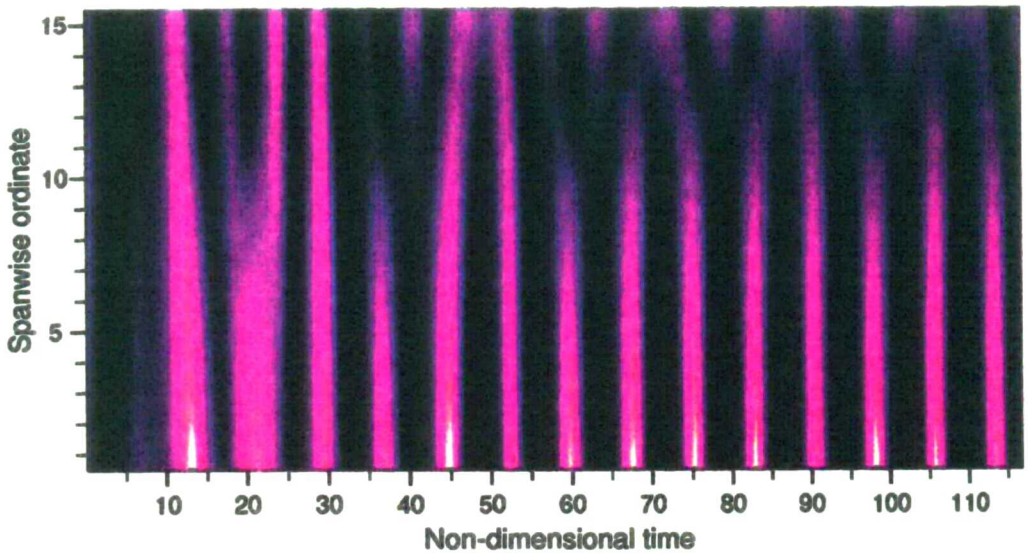
Vorton plot. Tapered cylinder, $T_R = 40$.

Figure 5.10

The transverse velocity is monitored close to the cylinder over the entire span. Sample stations are created at $x/D = 1.5$, $y/D = 0.75$ at 32 points in the spanwise direction. Recordings of the time history of the transverse velocity are presented in figure 5.11. Near to the cylinder there is a high phase correlation from the larger end to the mid-span. The discontinuity in frequency occurs nearer to the smaller

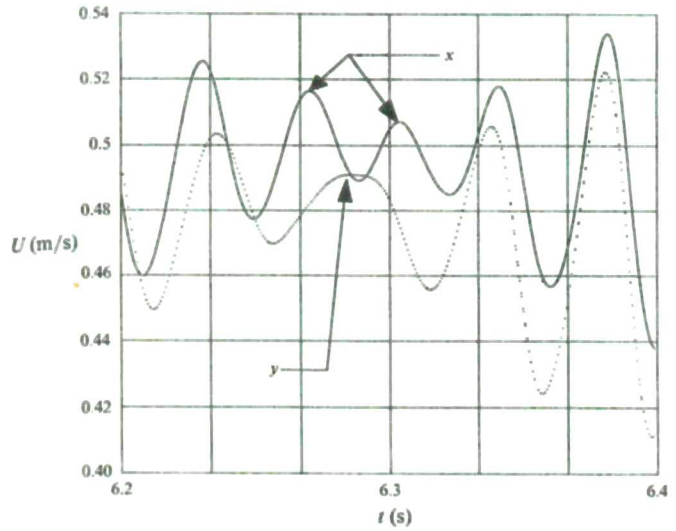
end. The spanwise correlation is high for about 70% of the cylinder length from the larger end. The flow is essentially determined by the larger end, which is dominant, and the transverse velocity pattern repeats itself (approximately) every 5 larger period shedding cycles, giving a beat frequency of $5f_1$. A velocity time trace made by Piccirillo and Van Atta (1993) at two opposite ends of a cell is shown in figure 5.12, and shows the point at which a vortex dislocation occurs.

Piccirillo and Van Atta (1993) found that the non-dimensionalised cell size became a constant value for a range of taper ratios at Reynolds number greater than about 100. Figure 5.13 is a reproduction of their figure for the non-dimensional cell size versus the Reynolds number at the centre of the cell. Included on this figure is the data for the case run here; only the larger cell is plotted, which concurs very well with their data. The cylinders used by Piccirillo and Van Atta are of an aspect ratio roughly 5 to 6 times greater than the cylinder tested here, and so the possible number of cells generated is higher. Their data indicate that the cell sizes decrease slowly in the direction of the smaller end. The second cell in the data presented here (i.e. that nearer the smaller end) has been foreshortened, because the cylinder ends in the symmetry plane, and therefore including the non-dimensional size of this cell in figure 5.13 would be misleading. The fact that the smaller cell size, non-dimensionalised, is so far off the other data reinforces the idea that the wake is dominated by the larger end. The cellular shedding pattern is established from the large end towards the smaller end, rather than *vice versa*. Roughly speaking, a cylinder of aspect ratio of 12 at this taper ratio should include two complete cells.



Transverse velocity at $x/D = 1.5$, $y/D = 0.75$.

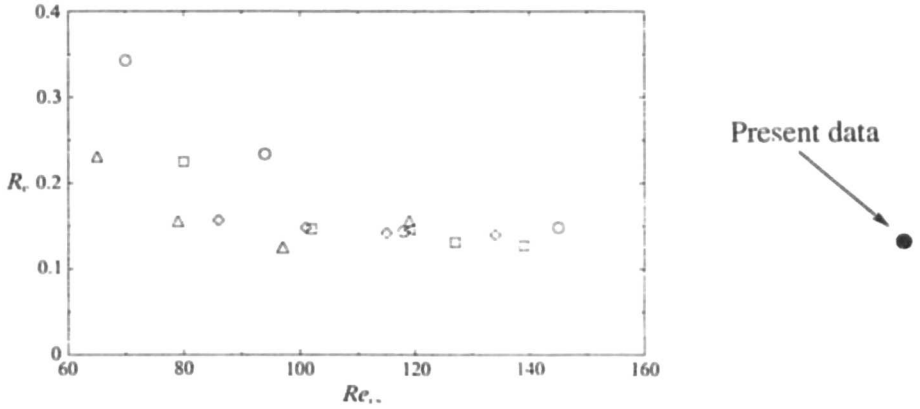
Figure 5.11



Comparative velocity time trace at two adjacent measuring stations, on opposite sides of a cell boundary, as a vortex split occurs. Note the two peaks marked by x, which correspond to one peak, marked by y, in the other signal. --, $Z = 4.5$ cm; ..., $Z = 4.9$ cm.

From Piccirillo and Van Atta (1993)

Figure 5.12



Non-dimensionalized cell size R_c plotted against Re_c for all cylinders: ○, 100:1 cylinder: □, 75:1; ◇, 60:1; △, 50:1; ◁, data of Noack *et al.* (1991).

From Piccirillo and Van Atta (1993)

Figure 5.13

Figure 5.14 is a reproduction of data from Piccirillo and Van Atta of the cell Strouhal number versus cell midpoint Reynolds number with the present data included. There is a reasonable amount of scatter on the data, and the results presented here fall below the best fit curve of $St_e = 0.195 - 5.0/Re$, particularly in the higher Reynolds number case of $Re_{em} = 206$. It is difficult to attribute the causes for the rather low values seen, which may be physical, and connected to the three-dimensional character of the flow; certainly for the straight cylinder, there is a discontinuity in the Strouhal number curve at these Reynolds numbers. Another possibility is that

the source of the apparent discrepancy is related to insufficient spatial resolution of the mesh, specifically the effects of elongated (spanwise) elements. The mesh used here is quite coarse, and consists of approximately 160,000 elements. It is clear that further research is required in this area. The numerical data of Jespersen et al (1991) is included in Piccirillo and Van Atta's figure, which shows their data to be slightly higher than the best fit curve. Jespersen et al used a mesh of $64 \times 64 \times 64$ elements, and ran their code on the parallel Connection Machine. Their Strouhal number data for straight cylinders is also quite high, being 0.185 at $Re = 122.5$; at $Re = 200$, the range of their recorder Strouhal number was $0.204 \rightarrow 0.208$, depending on the time differencing scheme used.

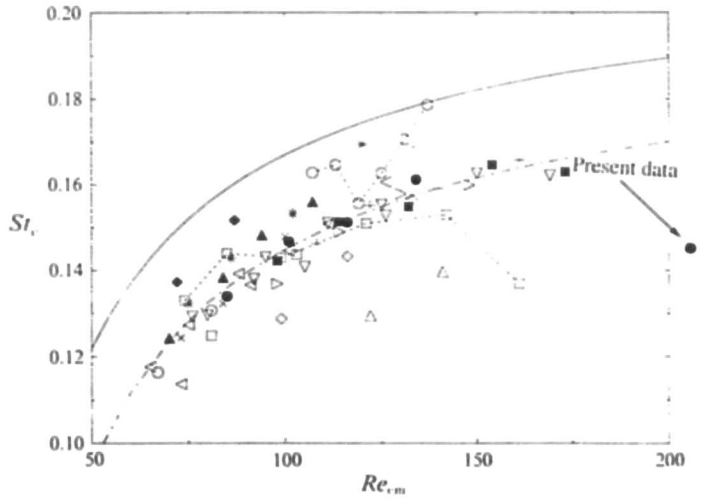
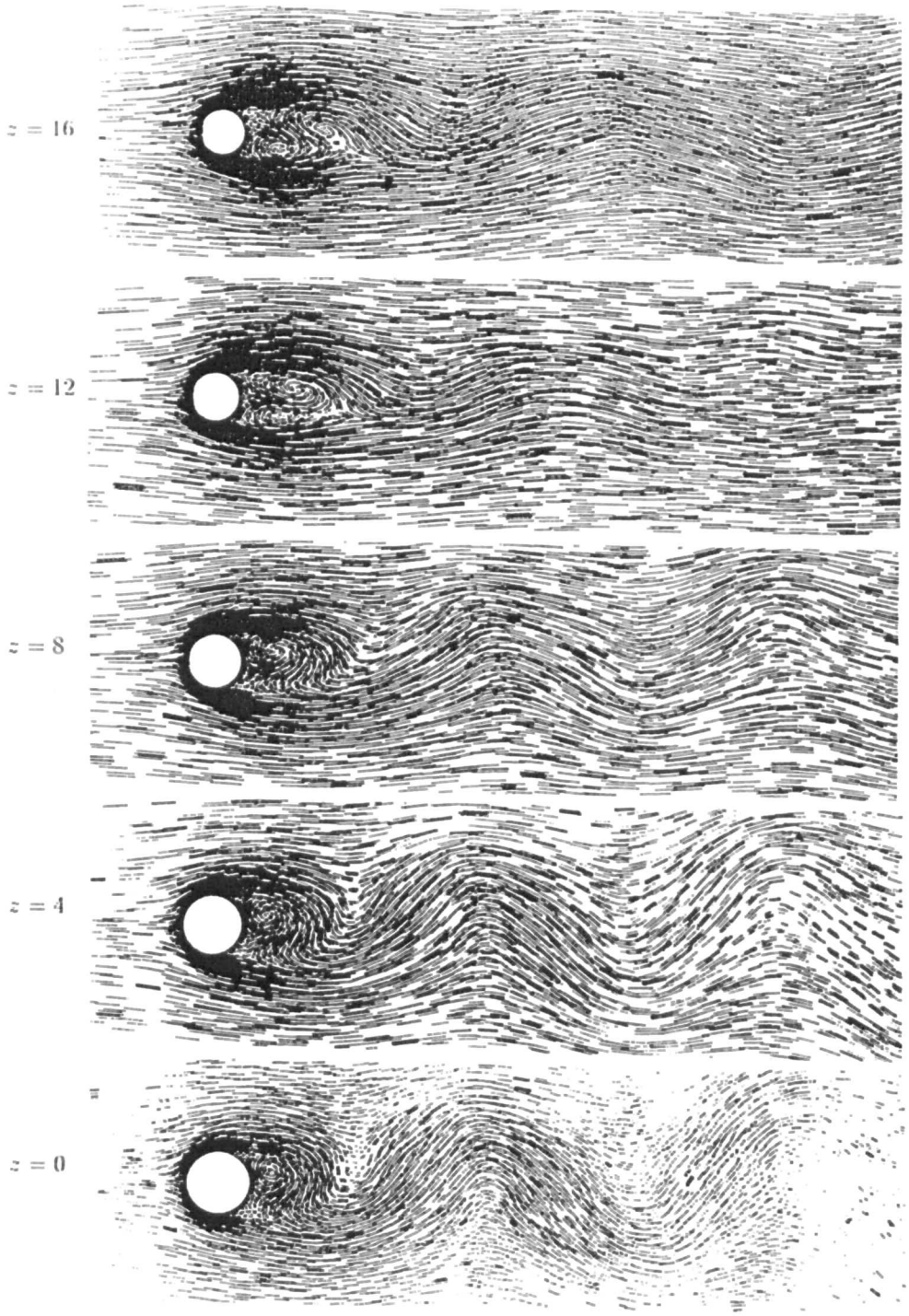


FIGURE 8. Cell Strouhal numbers versus cell midpoint Reynolds number: ○, run 11; □, run 12; ◇, run 13; △, run 14; ◁, run 21; ▽, run 22; ▷, run 23; +, run 24; ×, run 31; •, run 32; ●, run 33; ■, run 34; ◆, run 41; ▲, run 42; ◀, run 43; ▼, run 44; ○---○, data of Jespersen & Levit (1991); □---□, data of Noack *et al.* (1991); —, Roshko curve; - - -, best-fit curve to the data.

From Piccirillo and Van Atta (1993)

Figure 5.14

Figure 5.15 is a plot of the velocity vectors of the present data on various spanwise planes, and shows the phase changes in shedding with spanwise distance.



Velocity vectors at various spanwise locations.

Figure 5.15

5.3.2 Wave Flows

This section describes the numerical work carried out on the simulation of the steady translation of a long circular cylinder into free surface gravity waves. The free surface is approximated by the usual linearised wave boundary conditions.

The linearised wave problem is to solve the Laplacian for the velocity potential:

$$\nabla^2 \phi = 0 \tag{5.68}$$

subject to the following boundary condition at the free surface:

$$\frac{\partial^2 \phi}{\partial t^2} = -g \frac{\partial \phi}{\partial z} \quad on \; z = 0 \tag{5.69}$$

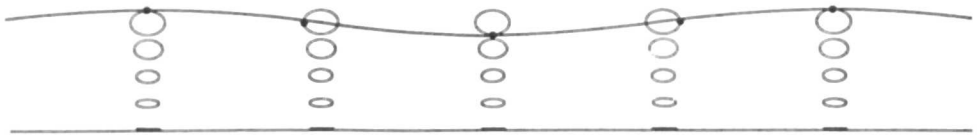
where z is a vertical ordinate with origin at the mean free surface, and is positive upwards. The boundary condition at the bottom ($z = -h$) is $\frac{\partial \phi}{\partial n} = 0$, i.e. there is no normal component of velocity. The solution to equation 5.68 for a finite but arbitrary depth h is:

$$\phi = \phi_0 \cosh\left[k(z+h)\right] e^{i(\omega t - kx)} \; . \tag{5.70}$$

This represents the solution to a sinusoidal wave propagating in the positive x-direction. The angular frequency of the wave may be evaluated using equation 5.69:

$$\omega^2 = gk \tanh kh \; . \tag{5.71}$$

The gradient of equation 5.70 yields particle paths which are shown in figure 5.16:



Particle paths for 'long' waves. From Lighthill (1978)

Figure 5.16

The velocity field is given by $\nabla\phi$:

$$u_w = k\phi_0 \cosh[k(z+h)] \sin(\omega t - kx) \tag{5.72}$$

$$v_w = 0 \tag{5.73}$$

$$w_w = k\phi_0 \sinh[k(z+h)] \cos(\omega t - kx) \ . \tag{5.74}$$

This velocity field satisfies $\nabla \cdot \vec{u}_w = 0$ and $\nabla \wedge \vec{u}_w = 0$. However, the problem with using this potential velocity field as part of the solution to the Navier-Stokes equations is that there exists a finite vertical component of velocity at the free surface due to the linearised wave theory applying a boundary condition at the (plane) mean free surface $z = 0$. It is convenient to use this surface, as opposed to the true free surface as the upper boundary of the mesh used for the vorticity field calculations. So vorticity is convected **out** of the computational domain where $w_w > 0$ and **into** the domain where $w_w < 0$. Numerically, this is not viable since total vorticity is lost out of the mean free surface in some regions, and an unknown quantity of vorticity enters through the mean free surface over other regions. One approach around this problem is to 'track' the free surface itself, which requires the mesh to move.

However, this can be quite complicated, and requires the re-evaluation of the global stiffness matrix every time step, or at least, every few time steps if the wave period is very long. The approach adopted here is to maintain the potential wave field with the linearised boundary condition, but apply a transformation with respect to z to the vorticity field immediately after convection of the vortons.

Consider first the potential velocity field. Imposing a mean current on the wave solution, which represents the relative velocity of the towed cylinder and hence does not affect the free surface boundary condition, the imposed potential velocity field in the vicinity of a circular cylinder of a radius of r_c is given by:

$$u(\vec{x},t) = [U_c + k\phi_0 \cosh[k(z+h)] \sin(\omega t - kx)] \left[1 - \frac{r_c^2(x^2-y^2)}{(x^2+y^2)^2}\right] \tag{5.75}$$

$$v(\vec{x},t) = -2[U_c + k\phi_0 \cosh[k(z+h)] \sin(\omega t - kx)] \frac{r_c^2 xy}{(x^2+y^2)^2} \tag{5.76}$$

$$w(\vec{x},t) = k\phi_0 \sinh[k(z+h)] \cos(\omega t - kx) \tag{5.77}$$

The above potential solution admits a very weak violation of continuity of velocity (see Appendix D).

The approach adopted here may be summarised as follows:

• at the beginning of the time march ($\vec{\omega} = 0$ everywhere) the potential velocity field is used in the diffusion/stretching equation for vorticity to give $\vec{\omega}^*$;

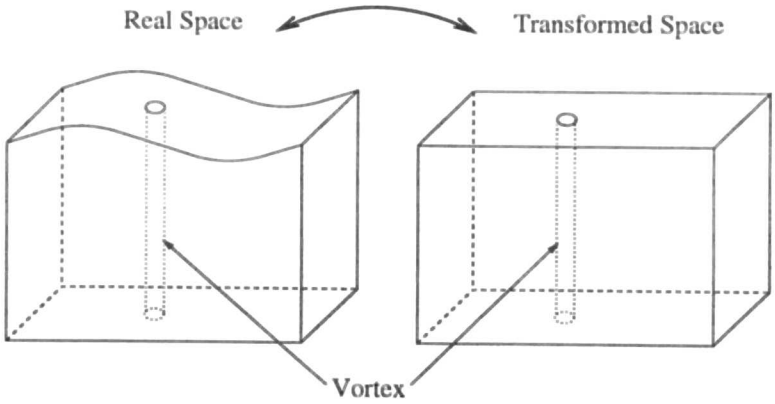
• once this field has been evaluated, vortons are created and convected over the time step using the original potential velocity field to give $\vec{\omega}^{**}$;

• the vortons are then mapped back to the computational domain using the exact opposite of the vertical potential velocity; in doing so, the vorticity field is changed by (a) convection, (b) stretching. The new vorticity field may then be explicitly calculated, and is the value at the end of the time step, i.e. is $\vec{\omega}^{n+1}$;

• in the following time step, the rotational velocity field is non-zero, and is included in the velocity field used in the evaluation of changes in the vorticity field due to stretching.

The above process basically allows the vorticity field to penetrate the free surface, and then applies a mapping to return the vorticity field to the computational domain, whilst modifying the vorticity field by adjusting the convection and stretching terms as necessary. The numerical implementation of the above is simplified, in that the transformation of the z-ordinate is carried out in the diffusion/stretching equation for vorticity by setting the vertical potential component of velocity to zero in the stretching terms. In addition, the applied convection velocity does not include the vertical potential term. It should be stressed however, that the slip velocity on the cylinder which arises due to the complete potential velocity field is included, so that the correct amount of transverse and streamwise vorticity is generated at the cylinder surface. Figure 5.17 is a schematic of the transformation.

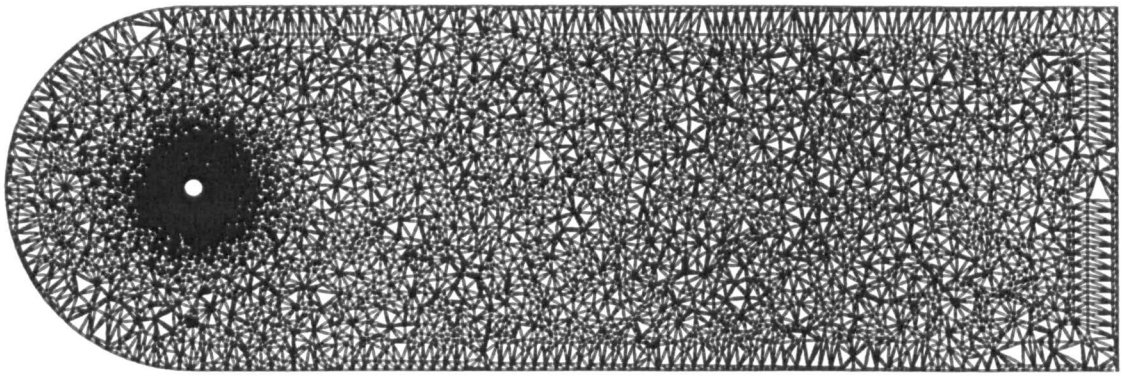
A typical mesh used in the three-dimensional wave problem is shown in figures 5.18 and 5.19. Figure 5.18 is an x-y plane through the mesh, and figure 5.19 shows both an x-z and a y-z plane. The mesh is first generated over the interval $0 \leq z \leq 1.0$, and then stretched in the z-direction, so that the aspect ratio of the cylinder is 16.



Schematic of transformation in three-dimensional wave case

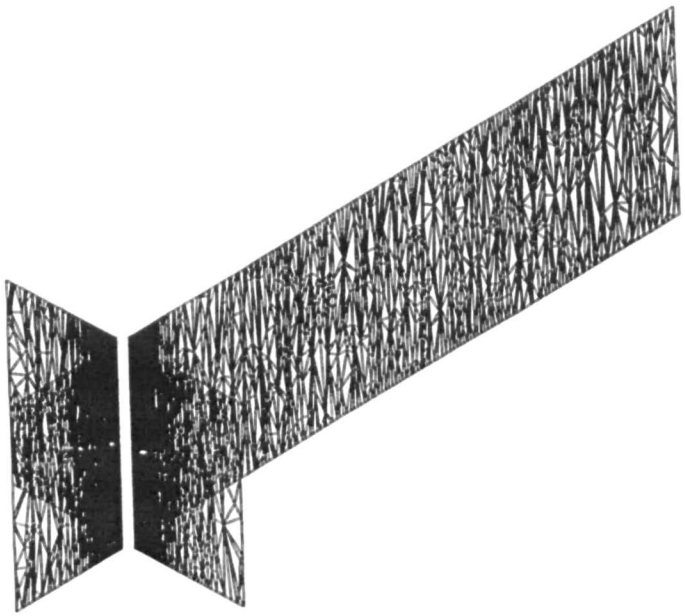
Figure 5.17

The mesh comprises 399561 tetrahedral elements, 85866 nodes, and 67664 triangular boundary elements. Line sources are placed at the origin (i.e. centre of cylinder) to increase the element density near to the cylinder.



x-y plane in a typical mesh.

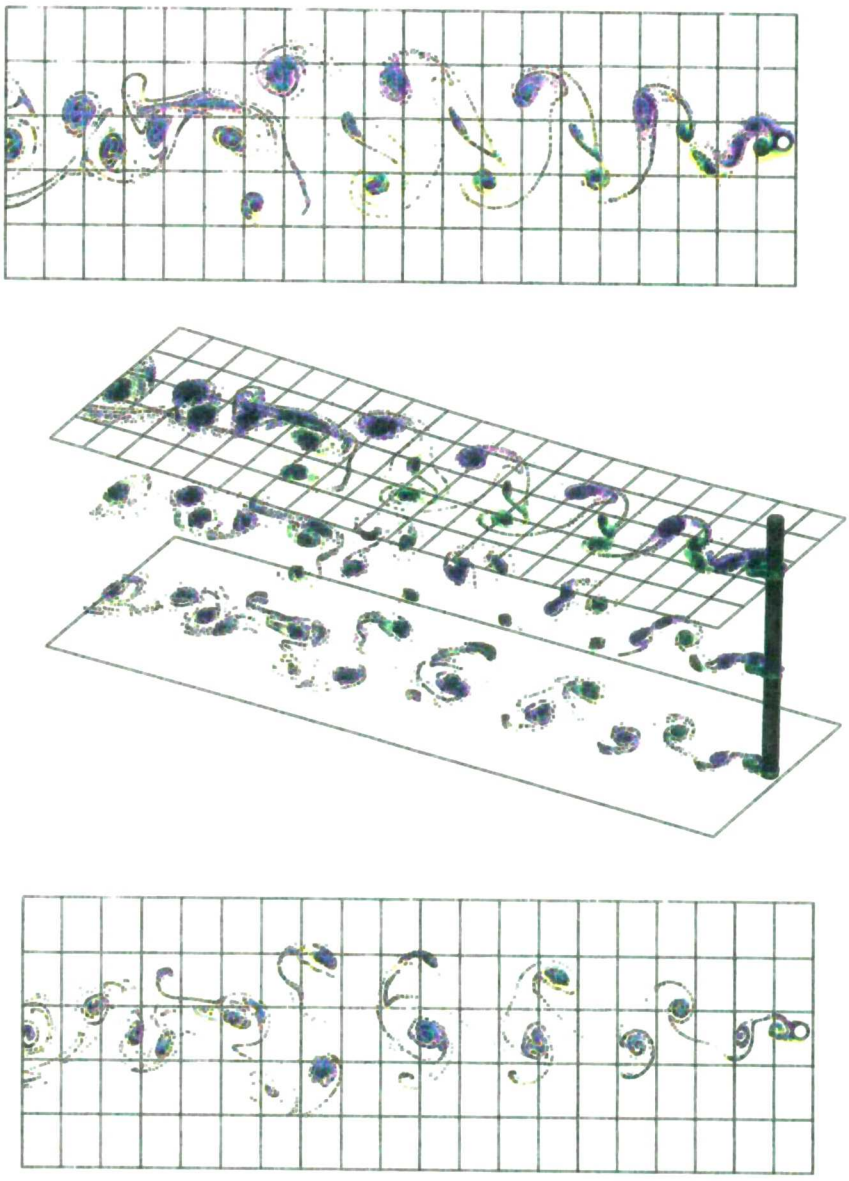
Figure 5.18



x-z and y-z planes in a typical mesh.

Figure 5.19

A case is run for which $Re = 150$; $\hat{\lambda} = 60$; $\hat{f} = 1.8$; $\hat{u} = 0.5$. Figure 5.20 shows the vortons at a non-dimensional time of $t^* = 68.4$. The two colours represent positive and negative values of the z-component of vorticity. The top plot is a plan view on to the free surface; the middle plot is a three-dimensional perspective of the flow field, and the bottom plot is a plan view of the flow at $z = -h$. The middle plot shows only three slices of the vorton field, otherwise the image would be too complicated to interpret. At this point in the computation there are just over 2×10^6 vortons in the field. Here, the free surface is shown as a grid. The cylinder is travelling from left to right, the waves from right to left, and the viewer is looking down on the cylinder; a small length of cylinder is drawn protruding through the free surface.



Vorton plot. $Re = 150$; $\hat{\lambda} = 60$; $\hat{f} = 1.8$; $\hat{u} = 0.5$.

Figure 5.20

The length of the cylinder is approximately equal to $\lambda_w/4$, meaning that the u-component of the wave velocity field spans the approximate range: $\hat{u} : 0.2 \rightarrow 0.5$ between the bottom ($z = -h$), and the free surface ($z = 0$). Figure 5.20 shows that near to the free surface the vortex shedding is almost symmetric. In the bottom plane the near-wake resembles the von Kármán vortex street. The middle plane near-wake flow is quite similar to the two-dimensional result of Case 6, and the correlation between this plane and the free surface is high over this region. It is difficult to visualise what is happening to the vortices in the wake in a three-dimensional sense; the flow behind the tapered cylinder was shown to be structurally quite simple, but what form of vortex connection is taking place here is hard to say. More insight may be gained by forming iso-vorticity surfaces from the data, and examining the way in which these 'structures' behave in the wake.

Chapter 6

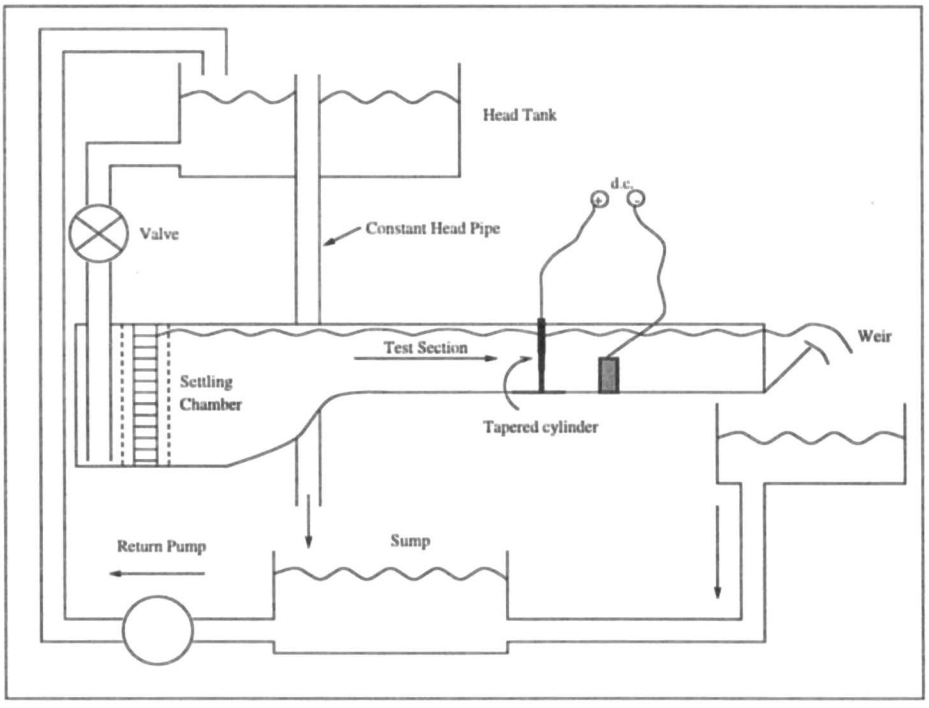
Experimental Work

6.1 Tapered Cylinder

In conjunction with the numerical simulation of flow past a mildly tapered cylinder, certain flow visualisation experiments are carried out on a tapered cylinder in a water flume in the hydraulics laboratory of the Department of Aeronautics at Imperial College. The working section is $0.6m$ wide and about $0.65m$ deep. The water flow rate is controlled by lowering or raising the weir, or by turning the valve which is located upstream of the working section. The flow past a cylinder of taper ratio $T_R = 40$, and at a Reynolds of 200 (based on mid-span diameter) is recorded. The water flow speed at this Reynolds number is $1cm/s$. Flow visualisation is performed using a precipitation technique, which is an effective technique for low speed flows. The practical details and technical procedures for using the electrolytic precipitation technique are detailed by Honji, Taneda and Tatsuno (1980).

Here, a thin strip of rolled solder the length of the cylinder is attached to the front of the cylinder and is connected to the anode of a low voltage d.c. supply. Once the solder has been attached to the surface of the cylinder, fine emery-paper is used to smooth the surface carefully to ensure minimal interruption to the boundary layer.

The cathode of the d.c. supply is connected to a large steel plate placed many body lengths from the cylinder in the water; when the current is switched on a whitish precipitate forms at the anode, and is carried away into the shear layers, marking the flow patterns. In the results presented here, the very thin strip of solder is placed to one side of the stagnation line so that only one shear layer and vortex row are illuminated. The experimental set-up at the time of the tests is shown in figure 6.1. Increasing the voltage results in more precipitate being generated, but too high a voltage causes the formation of quite large bubbles at the anode. The optimum voltage in this case was found to be around $20V$.



Schematic of experimental setup for tapered cylinder.

Modified from Savvides (1994).

Figure 6.1

There was a certain amount of difficulty experienced with the cylinder end conditions. At first, circular end-plates of diameter $20cm$ were attached; unfortunately,

the boundary layers which developed on the end-plates strongly interfered with the shedding vortices. The quite low aspect ratio of the cylinder (8) means that over short streamwise distances, the wake structure becomes almost entirely engulfed by the multi-component vorticity generated at the end-plates. Smaller end-plates were tried, but with not much more success. Tests were then carried out extending the cylinder by two constant diameter cylinders at either end, so that any end-effects were far from the tapered cylinder. Figure 6.2 is a diagram of the actual tapered cylinder which was used.

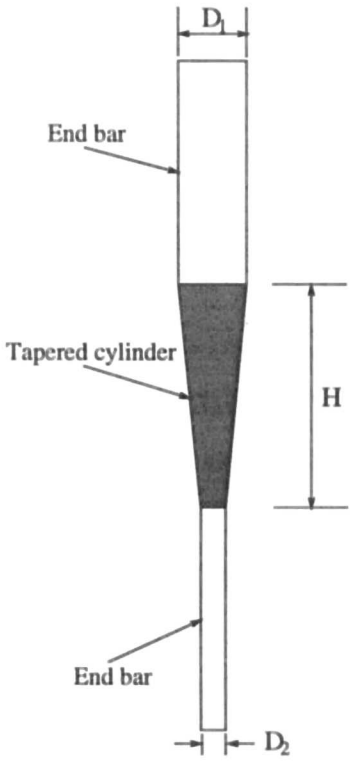


Diagram of tapered cylinder used in flow visualisation experiment.

Figure 6.2

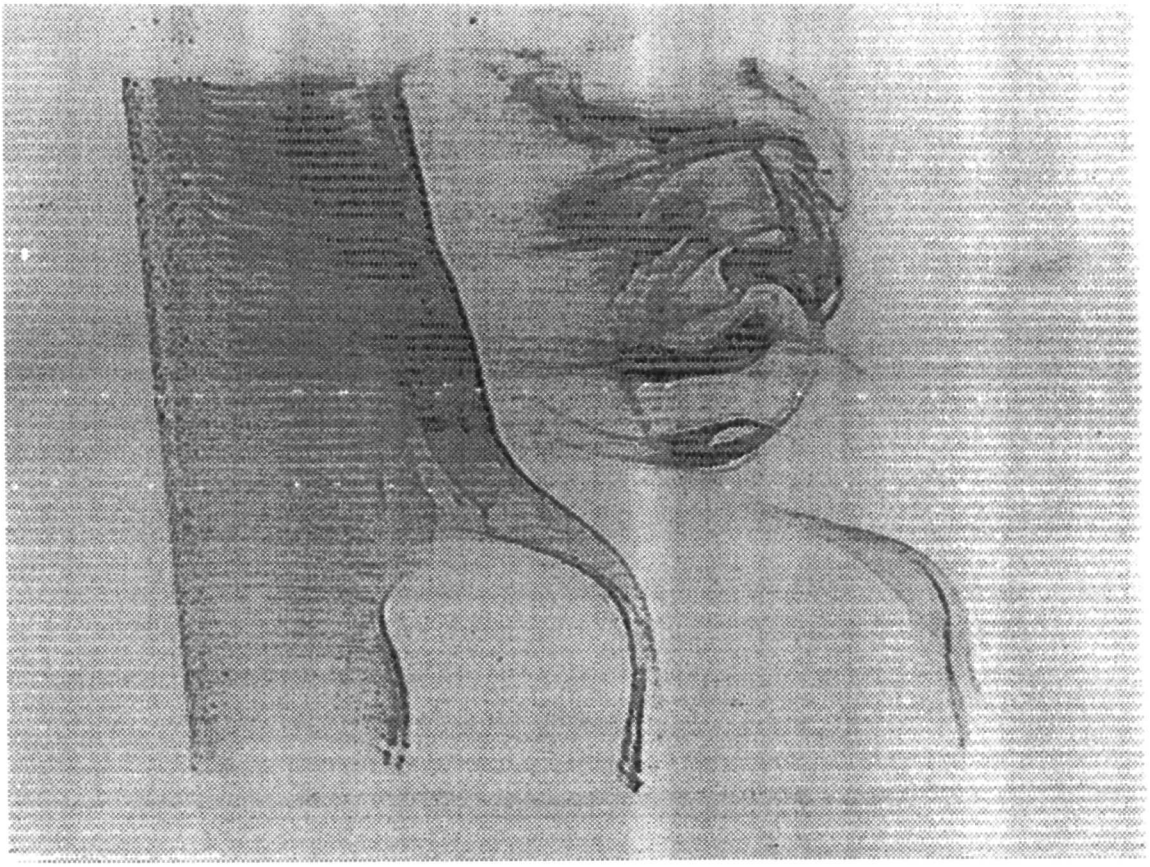
Although there is a discontinuity in geometry at the ends of the tapered cylinder, this arrangement allows the vortices to cross smoothly the planes which divide the

region of interest and the artificial extensions. The shed vortices that are observed meet the planes orthogonally.

The cylinder is arranged in the flume with the larger end towards the free surface, and the smaller end towards the bottom. The extension to the larger end penetrates the free surface, whilst the extension to the lower end has an end-plate attached, and is close to the floor of the flume. Only the solder strip on the tapered cylinder is exposed to the water. A 5 watt argon ion laser is used to illuminate a thin vertical plane of the wake; the beam is directed underneath the working section, whereupon it passes through a cylindrical lens, which diverges the beam in to a light sheet, and is reflected upwards into the water. The laser sheet illuminates approximately 4 lengths of the cylinder in the streamwise direction.

The precipitate is filmed using a video camera, and certain frames from the film are 'digitised' on a Silicon Graphics Workstation. Figure 6.3 is an example of one such digitisation, and shows the bi-cellular shedding pattern of this tapered cylinder. The actual cylinder is just visible. With the naked eye up to about 6 vortices near the smaller end are clearly seen, but the video film is not as good.

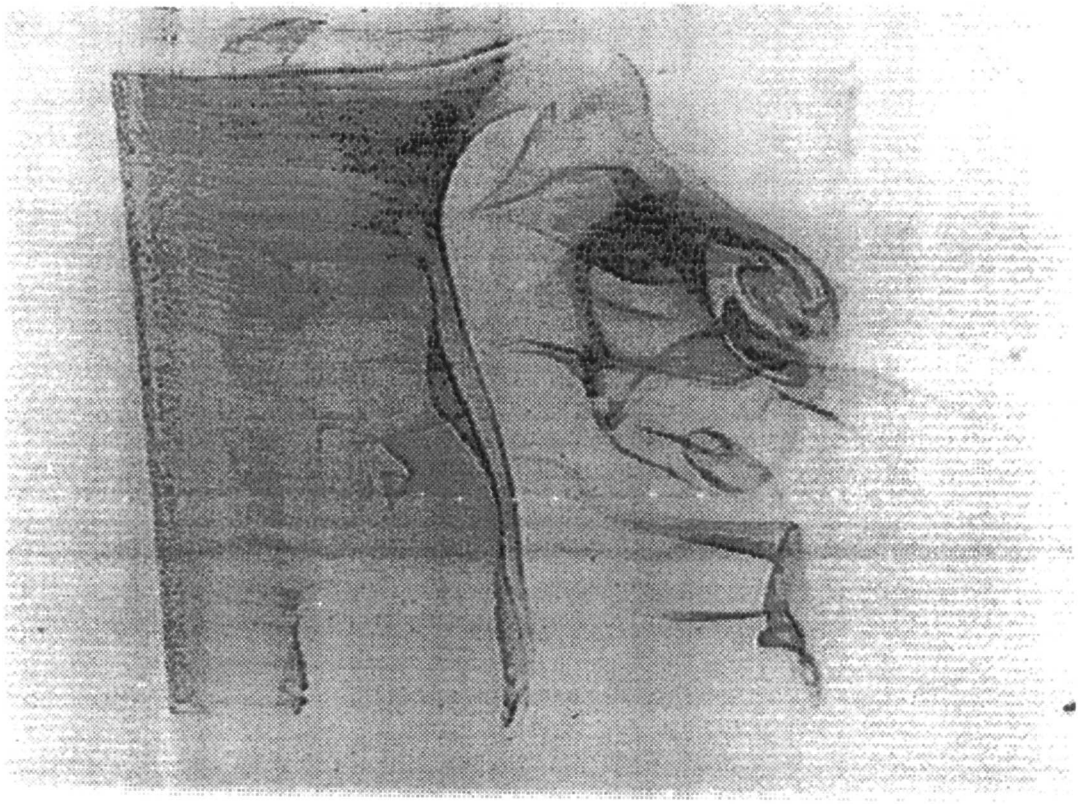
Since vortex lines formed by the rolled up shear layers must be continuous, the disparity in shedding frequency at the ends results in a dislocation or splitting of the vortex. Note that the spanwise point at which the dislocation takes place, and which marks the boundary between the two shedding cells, is in good agreement with the numerical simulations presented earlier on in chapter 5, and occurs at about 70% of the length of the cylinder from the larger end. Both the numerical cylinder and the tapered part of the real cylinder are exactly the same, and are under approximately the same conditions.



Precipitate in the wake of a tapered cylinder. Bi-cellular shedding.

Figure 6.3

It is not clear from figure 6.3 what is happening to the vortex which is shed from the larger end of the cylinder further downstream, although apparently a strong component of streamwise vorticity has developed. Figure 6.4 shows the case when a vortex has been shed in-phase over almost the entire length of the cylinder.



Precipitate in the wake of a tapered cylinder. In-phase shedding.

Figure 6.4

The experiments carried out on the tapered cylinder show that, for these water flow speeds, the electrolytic precipitation technique is an excellent way of realising three-dimensional vortex structures. A good qualitative agreement is found between the flow visualisation experiments presented here, and the three-dimensional numerical analysis, presented in chapter 5.

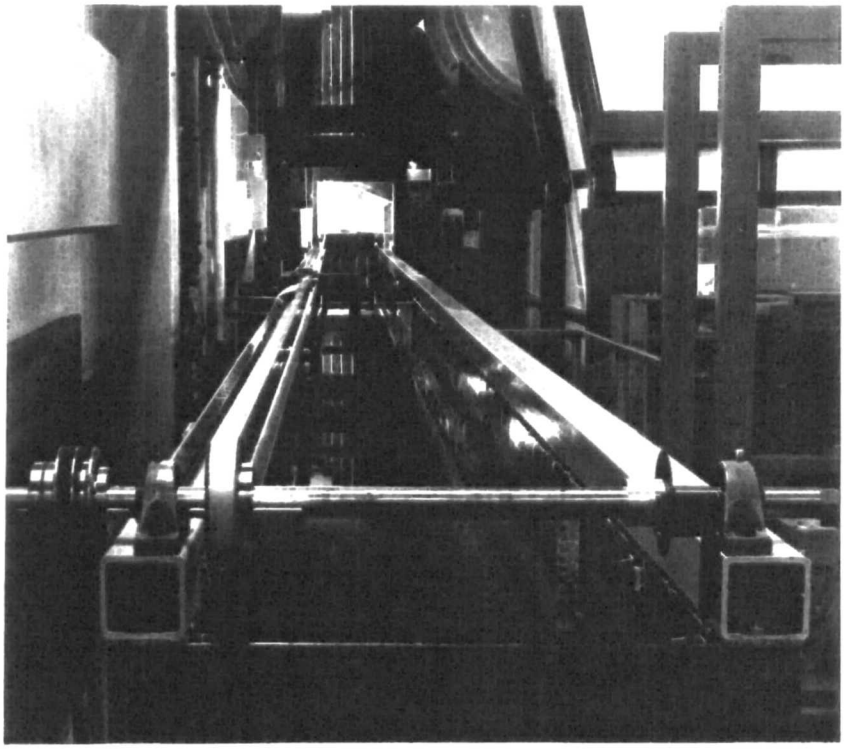
6.2 Wave Flows

6.2.1 Experimental Facility

A series of flow visualisation experiments are carried out in the $20m$ wave flume in the Department of Aeronautics, Imperial College. The working section of this flume is $0.6m$ wide, 3 metres long, and typically has about $0.8m$ of water in. The twin-paddles which create the waves at one end may be driven over the frequency range of $0.5 \rightarrow 2.5\ Hz$, giving a range of wavelengths of between $6.25m$ to $0.25m$. A signal generator is used with a sinusoidal output signal. Wave heights up to about $150mm$ may be generated.

Major structural modifications to the wave flume were necessary to facilitate the towing of the cylinder through the tank. A towing system was designed based on a single specialised track with linear bearings, which provide a smooth and accurate means for translating the cylinder. The load bearing capability of the bearings is very high, and the torsional rigidity is sufficiently great to allow the use of a cantilevered carriage system. This provides greater access and convenience to the operator. The linear bearings and track are of type HSR-HA35 from Unimatic Engineers Ltd., London. The belt is $32mm$ wide, and is of type BRECOflex® T10 from Transmission Developments Co. (G.B) Ltd., Poole, Dorset. Since the access space around the flume is rather restricted, two simple plummer block pulleys are used at either end of the flume for the $40m$ timing belt. The belt itself is supported along the interior of the flume by a series of small rollers, about $5m$ apart. Maximum belt sag without the rollers in place is about $70mm$. The motor used is a $3.75\ kW$ Thrige-Scott d.c. motor, with a 25:1 gearbox. The motor is positioned underneath the flume, and mounted on a purpose built frame; drive to one of the plummer block pulleys is achieved via a short drive belt. Since there were no electrical safeguards in place to prevent the carriage from over-running and impacting the plummer blocks

at the ends of the track in the event of a mishap, a mechanical fail-safe was introduced in the form of a breaking clutch system between the motor and the driven shaft. If the carriage offers too much resistance, a plastic link in the clutch shears, decoupling the motor from the carriage. This system was designed by Joe Meggyesi from the Technician staff, Department of Aeronautics. Figure 6.5 is a photograph of the experimental facility, viewed from the beach end towards the paddles.



View of the $20m$ Wave Flume from the beach end.

Figure 6.5

The BRECOflex® T10 timing belt is joined at the carriage through a ratchet system

designed by Joe Meggyesi from the Technician staff in the Department of Aeronautics.

Figure 6.6 is a diagram showing details of the modifications made to the existing flume.

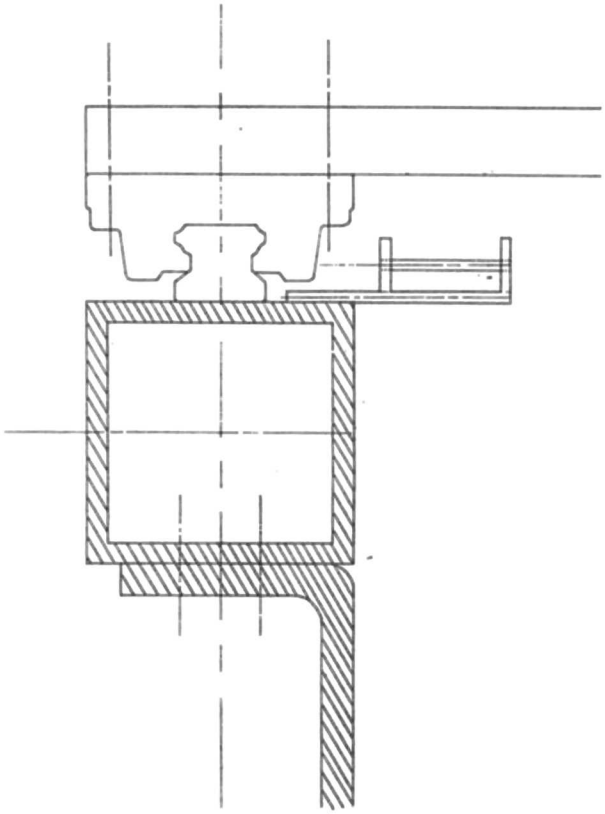
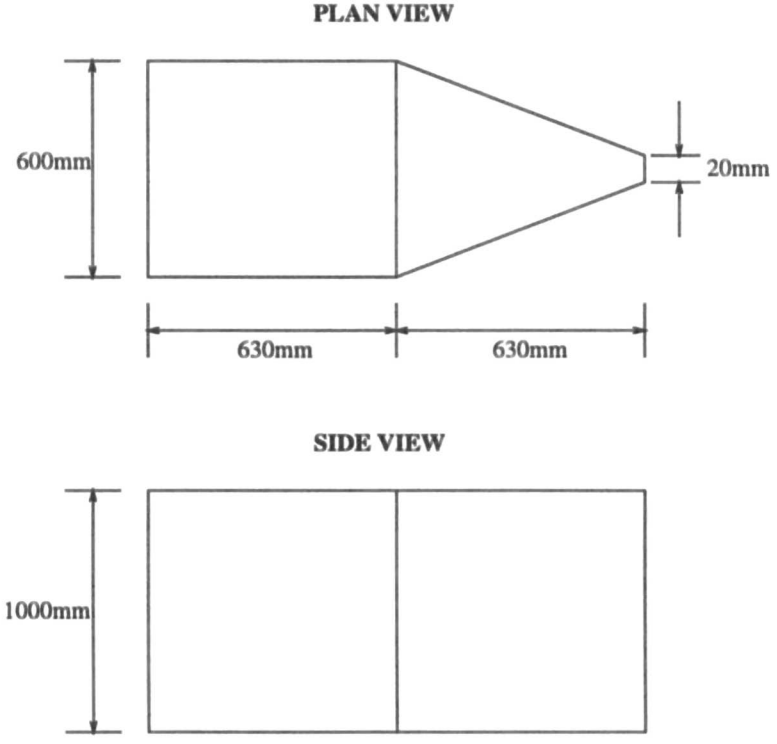


Diagram showing cross section of track, linear bearing, and $100mm$ thick support sections.

Figure 6.6

The beach that existed at the time was a 6:1 sloping wooden beach, and posed difficulties for the new carriage system because it took up about $6m$ of the tank and fouled the cylinder not far from the working section. It was also found to

produce quite significant reflections, and this was particularly noticeable for weak waves (with heights of the order of $1cm$). A new type of beach was tested, which was based on the foam [1] 'wedge' type seen in practice in the Civil Engineering Department of Imperial College. Apart from the benefit of not intruding into the flume more than just over a metre, this beach performed extremely well over all ranges of wavelength of waves, and produced minimal reflections and monochromatic waves over the working section. The quality of the waves was judged by viewing the wave train over the entire length of the flume; no electrical device was used to check the waveforms generated. Figure 6.7 shows the dimensions of the beach which was used.



Foam beach used in Wave Flume.

Figure 6.7

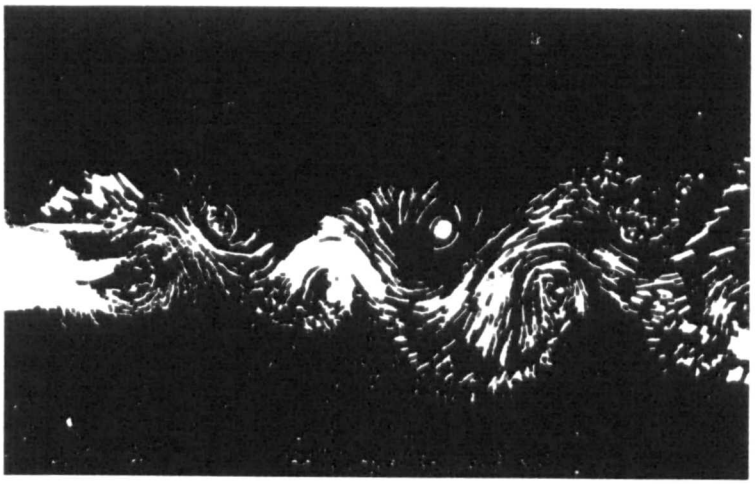
[1] Foam block were purchased from Declon, Corby, Northants.

6.2.2 Surface Flow Visualisation

The objectives of these experiments are to visualise the free surface vortices of the wake of a vertical cylinder translating steadily into waves. These surface flow visualisation data are compared qualitatively with the two-dimensional viscous analysis presented in chapter 4, as well as the experiments of other researchers. In comparing the present data with the numerical simulations, it should be recalled that the two sets of data are at different Reynolds numbers, so that the crucial process of vortex formation and shedding is perhaps subject to Reynolds number effects.

The cylinder in this case penetrates the free surface, and has minimum clearance at the bottom of the flume. Two methods of flow visualisation are tried. The first involves delivering small polystyrene beads as seed particles from a nozzle device attached to the front of the cylinder; the polystyrene beads are buoyant. These experiments are carried out on a $50mm$ diameter cylinder at a Reynolds number of around 10^4; the surface elevation in these cases is typically a few centimetres. It is desirable to use particles as small as possible (whilst still being able to visualise them effectively) so that they remain passive. However, many problems were encountered with this approach, and it was found that the large distortions of the surface and the high Reynolds number made visualisation difficult. In addition, an even delivery of particles could not be guaranteed, and once on the water surface, particles tended to 'clump' together to form groups of islands. This may have been the result of some electrical charge on the particles. The patterns formed by the particles are photographed using a long exposure so as to produce instantaneous streaklines. The camera itself is mounted above the water surface, and fixed with respect to the flume. Figure 6.8 shows the case of the cylinder translating into water with no waves present. The classical von Kármán vortex street may be observed. Figure 6.9 is a case with waves, for which the wavelength of the wave is 20 diameters,

and the height from the mean free surface is half the cylinder diameter. It is difficult to discern any particular structures in the wake in the latter case, except perhaps very close to the back of the cylinder.



Cylinder in steady translation. No waves. Polystyrene bead visualisation.

Figure 6.8



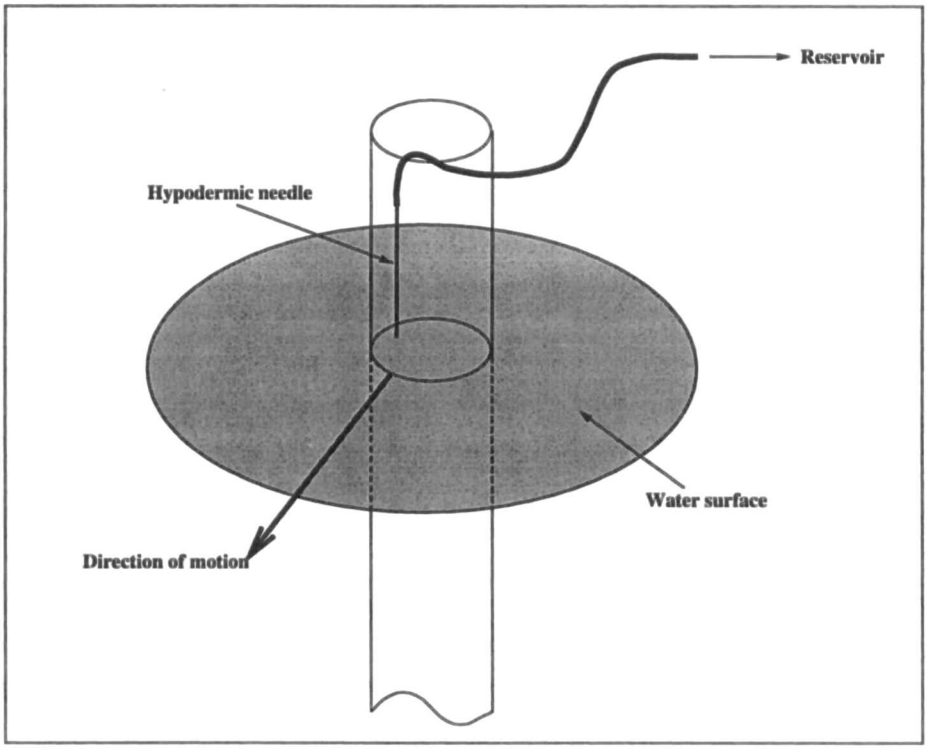
Cylinder in steady translation. With waves. Polystyrene bead visualisation.

Figure 6.9

In response to these problems, a smaller diameter cylinder was used in conjunc-

tion with weaker waves. The Reynolds number in these cases is 600. The cylinder diameter is $1.0cm$, and the carriage travels at a speed of $6.0cm/s$. The speed of the carriage is first calibrated by measuring the time taken to travel a certain distance down the flume; markings were then made on the potentiometer which controls the motor. With the powerful motor used, it was found that the speed of the carriage is independent of the load placed on the motor.

The particles from the first experiment were replaced by a solution of potassium permanganate, which is bled on to the front part of the cylinder via a hypodermic needle; this helps maintain an even, minimal flow rate whilst avoiding the formation of droplets of the dye. A schematic of the experimental set-up is shown in figure 6.10.



Schematic of dye delivery system.

Figure 6.10.

The dye is gravity-fed from the reservoir, which is attached to the carriage. The

end of the hypodermic needle is placed about a centimetre above the wetted part of the cylinder, so that in cases for which waves are present, there is likely to be a deficit of dye when a trough is at the cylinder, and an excess when a peak is at the cylinder, although in practice, the biggest problem was found to be distributing an equal amount of dye to both sides of the cylinder.

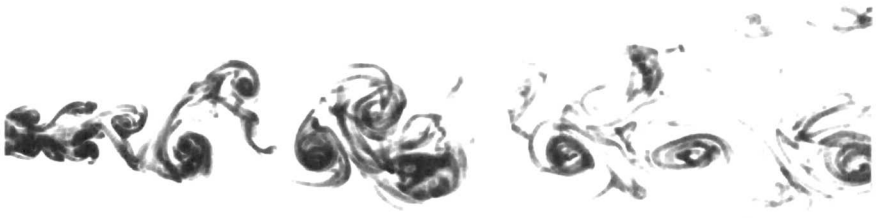
Photographs of the flow patterns are taken by a camera fixed to the flume about $40cm$ above the water surface. Two 1000 Watt tungsten lights either side of the working section to provided illumination. Fairly high speed (400 ASA) black and white film was used. The floor of the flume is covered by a white board, in order to set-off the surface dye. Figure 6.11 demonstrates the formation of the classical von Kármán vortex street which remains stable up to about 30D downstream; thereafter structure in the flow patterns becomes much less distinct and there is a small but fairly abrupt change in the wake width. There is a slight bias in concentration of dye which makes the vortices on the lower row appear a little darker.



Cylinder in steady translation. No waves. Dye visualisation.

Figure 6.11

Figure 6.12 demonstrates the effect of adding a wave. In this case $\hat{\lambda} = 30$, $\hat{f} = 1.85$, $\hat{u} = 0.5$, where the same definitions of the non-dimensional parameters apply, i.e. $\hat{\lambda} = \lambda_w/D$, $\hat{f} = f_w/f_n$, $\hat{u} = u_w/U_c$. The peak-to-peak wave height in this case is $4mm$; this value is measured off a ruler affixed to the side of the working section. The non-dimensional frequency of 1.85 includes the encounter frequency due to the steady forward motion of the cylinder; in this case with $\lambda_w = 30cm$, and with the cylinder travelling at $6.0cm/s$, the incremental frequency is equal to $0.06/0.3 = 0.2Hz$. Data in the literature for the Strouhal number of $Re = 600$ tend to be quite spread, so that selecting a value of f_n is difficult. Data presented at the IUTAM Symposium (Gőttingen (1992)) by various researchers is used here: ignoring the extreme values presented, the mean of data from Chaplin (2-D computation), Unal (2-D computation), and Norberg (experiment) at this Reynolds number gives a Strouhal number of 0.217, so that in the present experiments the natural shedding frequency is $1.3Hz$.

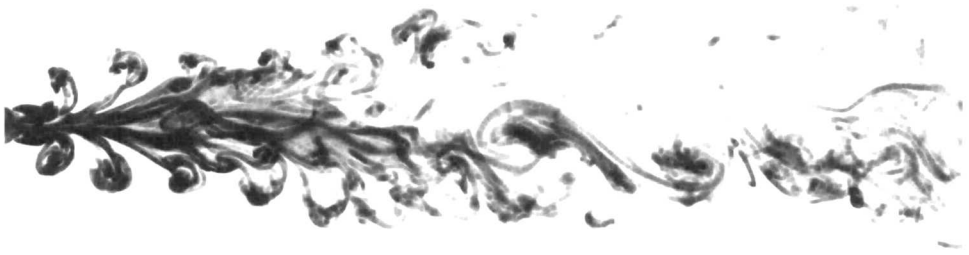


Cylinder in steady translation. $\hat{\lambda} = 30$, $\hat{f} = 1.85$, $\hat{u} = 0.5$. Dye visualisation.

Figure 6.12

There are several points of interest in figure 6.12, when compared with the steady result (figure 6.11). Reasonably far from the cylinder, the wake is of an anti-symmetric configuration; individual vortices are certainly still apparent up to $30D$ in the lower row, although in the upper row the concentration of dye is weaker, and the structure not so clear. From figure 6.12, the longitudinal inter-vortex spacing is measured as being approximately $4.7D$, compared with $4.25D$ for the steady case. Near to the back of the cylinder, the vortex configuration is symmetric, but it becomes anti-symmetric at a distance of about $3.5D$ from the cylinder. The lateral growth of the wake is weak, and is very similar to the steady result. The parameters for this case lie in-between two cases in the two-dimensional viscous analysis results, namely case 4 ($\hat{\lambda} = 30,\ \hat{f} = 2.0,\ \hat{u} = 0.5$), and case 6 ($\hat{\lambda} = 30,\ \hat{f} = 1.825,\ \hat{u} = 0.5$). Figures 4.56 and 4.57 are point vortex plots of these two cases, and may be directly compared with figure 6.12, since the cylinder is the same size in all plots though of course there is a small parallactic effect in the latter. The experimental data more closely resembles case 4, in which the vortex shedding consists, in principal, of regularly spaced oppositely signed vortices. At a streamwise distance of about $22D$ however, the presence of large loops of the interconnecting vortex sheets (in the lower row - see figure 6.12) has much in common with the structures seen in the data for case 6.

In the case of very strong waves, a totally different wake structure is observed. Figure 6.13 is a photograph of the wake for a case identical to the one presented in figure 6.12, except for the change to the wave amplitude, i.e. $\hat{u} = 1.0$. The wave induced velocity field at the water surface now has a maximum magnitude equal to the forward speed of the cylinder. The height of the waves in this case is approximately $9mm$.



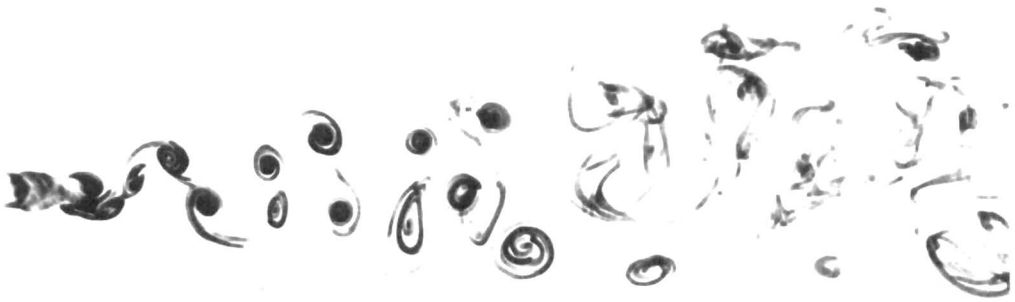
Cylinder in steady translation. $\hat{\lambda} = 30$, $\hat{f} = 1.85$, $\hat{u} = 1.0$. Dye visualisation.

Figure 6.13

Vortex pairs are formed on both sides of the cylinder, and are shed in phase to give a symmetric configuration in the wake. The pairs form very close to the back of the cylinder. The vortices which form the pairs are apparently not of equal strength since each pair rolls back into the main wake, and merges at a distance of approximately $10D$ from the back of the cylinder. Beyond this distance, the flow patterns are extremely complicated, and it is difficult to discern any clear vortical structure until the formation of the large scale structures at $x = 15D$; two large vortices of negative circulation may be observed at and beyond this distance. Interestingly, a faint but continuous trace of dye may just be seen which connects the upstream large vortex to the centreline of dye immediately behind the cylinder, away from which the initial vortex pairs move. The two large vortices resemble a Kelvin-Helmholtz type instability of a free shear layer.

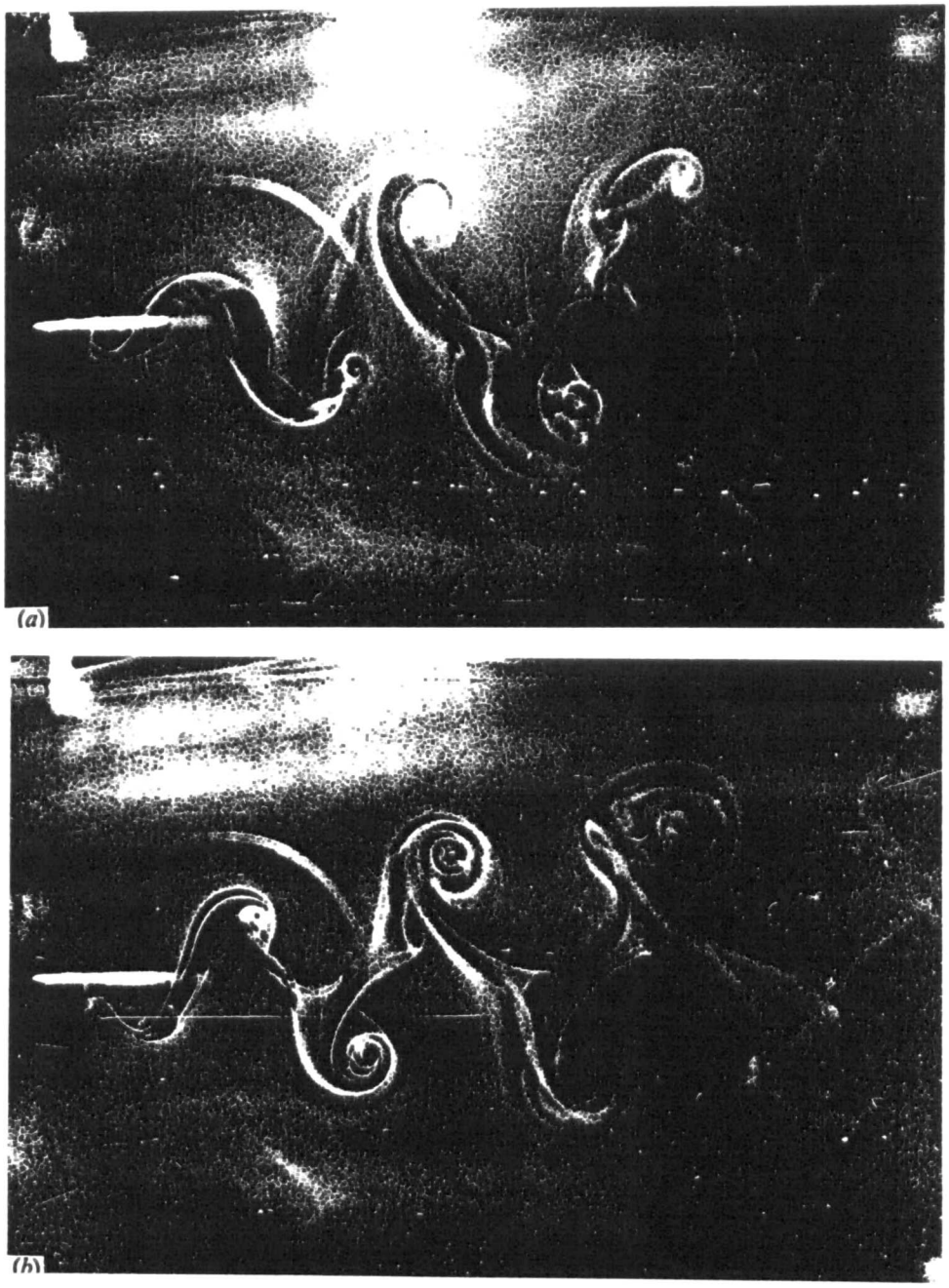
Waves of longer wavelength and lower frequency have a greater effect on the trans-

verse spreading of the wake. Figure 6.14 is a photograph of the wake for a wave of $\hat{\lambda} = 60$, $\hat{f} = 1.31$, $\hat{u} = 0.5$. The quite beautiful vortex patterns that emerge in the wake are similar to the "Sea-horses" of Detemple and Eckelmann (1989) which result from an acoustic excitation of the wake of a circular cylinder; their data shows this pattern to occur at a non-dimensional frequency of 1.5625. Griffin and Ramberg (1976) present similar structures for in-line oscillations of a cylinder plus a steady current, and their data for $\hat{f} = 1.74$ and $\hat{f} = 1.92$ are shown in figure 6.15. There are certain differences between the patterns shown here, and those of Griffin and Ramberg: in the latter case, the two neighbouring vortices in either row are much closer together; in the present data this separation distance is of roughly the same size as the transverse distance separating the vortex rows.



Cylinder in steady translation. $\hat{\lambda} = 60$, $\hat{f} = 1.31$, $\hat{u} = 0.5$. Dye visualisation.

Figure 6.14



From Griffin and Ramberg (1976).

(a):$\hat{f} = 1.74$; (b):$\hat{f} = 1.92$

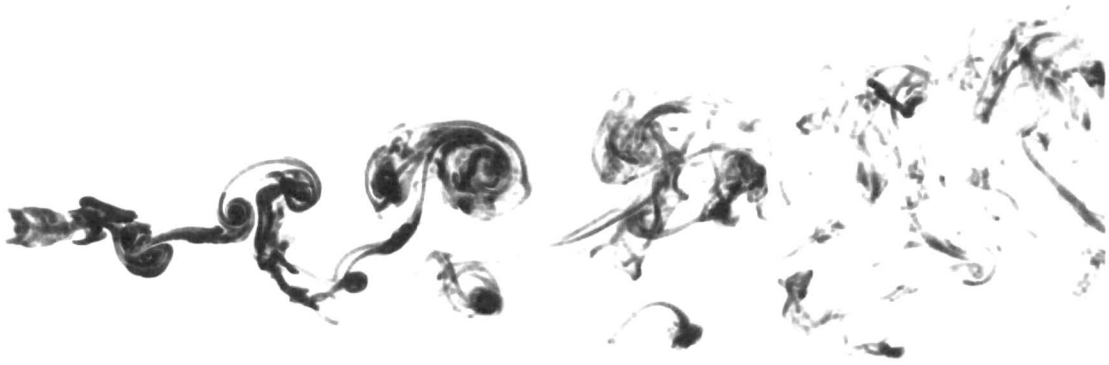
Figure 6.15

The parameters of this case lie in between those of case 8 and case 10 of the two-dimensional viscous analysis data (figures 4.66 and 4.67 respectively). The structure of the near wake in the experiment most closely resembles that of case 8 (figure 4.66), although the inter-vortex spacing is not quite as small as that of the numerical simulation. At a streamwise distance of about $20D$ from the cylinder, this double street pattern is lost in favour of a vortex configuration of the mode type A-III described by Ongoren and Rockwell. A single vortex is observed in the lower row, whilst the flow field in the upper row has become quite complex. The vorticity contour plot for case 10 (figure 4.67) shows a similar behaviour at around $x = 35D$.

If the wave height is increased, so that $\hat{u} \approx 1$, a substantial portion of the near wake is of a symmetric configuration. In this regime, very close to the back of the cylinder there are two sets of vortex pairs either side of the cylinder, whose instantaneous velocity is directed in a transverse sense to the flow. Downstream, there is a further set, and thereafter the wake becomes anti-symmetric, with regular inter-vortex spacing. The longitudinal inter-vortex spacing is greater than the steady flow case, and is measured to be about $5D$; the transverse spacing is also large, and has the value of approximately $3D$.

For still longer wavelength, lower frequency waves, a different flow pattern emerges. Figure 6.16 is a photograph for the case $\hat{\lambda} = 100$, $\hat{f} = 1.03$, $\hat{u} = 0.5$. The wake is characterised by the presence of large vortex pairs in the upper half plane, and a single vortex in the lower half plane. The vortex pairs convect quite rapidly in a transverse sense, so that at a streamwise distance of about $30D$ from the cylin-

der, the wake is very broad; dye has spread over approximately twice the transverse distance there when compared with the steady flow result. The parameters for this case lie between those of cases 14 ($\hat{\lambda} = 100,\ \hat{f} = 1.00,\ \hat{u} = 0.5$) and 12 ($\hat{\lambda} = 100,\ \hat{f} = 1.197,\ \hat{u} = 0.5$) of the two-dimensional viscous analysis data, although they are much closer to case 14. Figures 4.68 and 4.69 are the point vortex plots for cases 12 and 14 respectively.



Cylinder in steady translation. $\hat{\lambda} = 100$, $\hat{f} = 1.03$, $\hat{u} = 0.5$. Dye visualisation.

Figure 6.16

There are similarities between the experimental result and the numerical data. Figure 6.17 is a plot of the numerical data for case 14, where much more of the wake is shown.



Point vortices. $Re = 150$. Case 14. Expanded view.

Figure 6.17

Figure 6.17 is fairly close to being a mirror image [2] of the experimental data; the vortex pairs in this case are in the lower half plane, and the single vortex is almost directly above the corresponding pair. Notice also that in between the single vortex and the next downstream vortex pair there exists a smaller vortex in the connecting free shear layer. This is just observable in the experimental data of figure 6.16 between the two vortex pairs closest to the cylinder. Further downstream there is no evidence of a formed vortex at this location (also true of the numerical data), which may be related to the local strain field exerted by the rapid transverse motion of the next downstream vortex pair. The formation of the first vortex pair in the numerical data occurs further from the cylinder than in the experimental data; indeed, the entire wake pattern is more stretched in the longitudinal sense, and the vortex pairs themselves travel a smaller distance in the transverse sense. This may be a result of the difference in Reynolds number between the two sets of data.

[2] The decision of the wake to bias itself to one particular direction is probably determined by the favoured amplification of noise terms from an impulsive start.

Chapter 7

Conclusions

An investigation has been carried out into the effects of a vertical cylinder translating steadily into waves. This work has been concerned with weak waves, i.e. waves for which the wave height is a fraction of the cylinder diameter, and the particle orbital speed is a fraction of the forward speed of the cylinder. Numerical investigations have been carried out together with surface flow visualisation. The numerical investigations comprised three levels of idealisation to the physical problem: (a) an inviscid study of the wake dynamics using point vortices, (b) a viscous two-dimensional study using a hybrid Finite Volume / particle method developed here, (c) a viscous three-dimensional study using a hybrid Finite Element / vorton method developed here.

A linearised stability analysis of a von Kármán vortex street which has been quasi-statically perturbed by a finite strength wave shows that this general configuration is unstable to infinitesimal disturbances. *Numerical* integration of the full non-linear equations of motion, including the velocity field of an in-line progressive wave train, shows that small errors in the exact conditions in the flow grow exponentially, until such time as an opposite signed vortex pair ejects from the wake, and then

proceeds in a transverse direction ad infinitum. One vortex pair per wavelength of the wave is created. At later instants, other vortex pairs eject from the central wake.

A linearised stability analysis of a wake configuration for which there exists a sinusoidal variation in vortex strengths shows that such a configuration is unstable to infinitesimal disturbances. A numerical integration of the full non-linear equations of motion shows that, for the same wave parameters, the rate of degeneration of the wake is much more rapid than in the case of a constant strength vortex wake undergoing perturbations due to a progressive in-line wave.

A more realistic representation of the true physical problem was achieved by performing two-dimensional viscous simulations of the flow cases. The range of wave cases which were tested spanned $0.69 \leq \hat{f} \leq 2.265$; two wave velocity amplitudes were tested over this range of $\hat{f}$: $\hat{u} = \frac{u_w}{U_c} = 0.2$ (where u_w is the amplitude of the wave velocity, U_c is the cylinder speed), and $\hat{u} = 0.5$. In the former case, structural changes to the wake are minimal, and there is little evidence of vortex pairing. The effects of synchronisation between the wave and the vortex shedding were noted in some of these cases ($\hat{f} = 2.0, 1.825, 1.565$). Here, the shedding frequency is exactly half of the wave frequency. The wakes of these particular cases retain a regular staggered vortex street configuration for large distances downstream, and the longitudinal inter-vortex spacing is found to obey the equation: $\frac{a}{D} = -4.25\hat{f} + 13$. Also, the existence of a beat frequency in transverse velocity signals close to the cylinder is absent in these cases, but not in cases outside the lock-in region ($\hat{f} = 2.265, 1.295, 1.2, 1.$). The wakes of flow cases outside the region of lock-in are more disrupted than those inside. In the near-wake, the inter-vortex spacing is no longer regular, and the overall shape of the wake is mildly jagged. Large vortex structures develop in the far-wake. These vortices are not so compactly arranged, and

tend to spread out in a longitudinal sense, with the lengthscale of the vortex structures increasing with distance downstream. Higher strength wave cases ($\hat{u} = 0.5$) demonstrate a variety of vortex modes in the wake, and generally have much broader wakes. Vortex pairing is strongly in evidence. At a wave frequency higher than twice the natural frequency ($\hat{f} = 2.265$) the near wake to a certain extent resembles the regular von Kármán vortex street, although the vortices are 'bunched' in certain regions, and stretched out in others. In the the far wake, distinct groups comprised of four vortices form, and the separation distance between these groups increases with distance downstream. Overall, however, the wake remains relatively narrow in this case. The only example of a regular staggered arrangement of the vortices at this wave velocity amplitude occurs for the case $\hat{f} = 2.$. In this case, the wake undergoes a sudden transition at a distance of approximately $70D$ from the cylinder, downstream of which the vortex structures are larger and the streamwise inter-vortex spacing increases. At lower non-dimensional frequencies, $1.825 \leq \hat{f} \leq 1.565$, a 'double' wake type structure develops in which there are four rows of vortices. The same patterns are seen in surface flow visualisation experiments carried out by the author.

At still lower non-dimensional frequencies ($1.295 \leq \hat{f} \leq 1.2$), the wake reverts to a double row of regularly spaced vortices, although the transverse inter-vortex spacing is very small, and the rows almost colinear. At $\hat{f} = 1.$, the wake becomes very broad, and there is much evidence of vortex fission, even in the far wake. The near wake is structurally complex, and consists of vortex triplets separated by a single vortex. Again, surface flow visualisation experiments, conducted by the author at this non-dimensional frequency, show a very similar vortex pattern in the near to mid wake.

When the wave frequency is lower than the natural frequency (case $\hat{f} = 0.69$),

vortex shedding becomes synchronised again, but this time at a shedding frequency equal to the wave frequency. The wake in this case consists of a string of tightly coupled, equidistant vortex pairs. The accelerating velocity field of the wave ($\propto u_w f_w$) promotes the formation of a symmetric system of vortices, whilst the steady current results in an antisymmetric configuration at these Reynolds numbers. The wake patterns that are observed are the result of the competition between these two 'systems'. An antisymmetric vortex street is more stable than a symmetric one, and it is usually found that for cases of high $\hat{u}$ or $\hat{f}$ a symmetric configuration is realised in the near wake, but downstream defers to an antisymmetric one; the lengthscales in the far wake in these cases is generally very large. Surface flow visualisation experiments conducted by the author showed that in some realisations of the flow for which $\hat{u} = 1$ a symmetric vortex street forms, and survives quite far downstream, whilst in others, an antisymmetric configuration is already in existence very close to the cylinder. The lack of repeatability in the experiment means that mode selection is sensitive to prevailing conditions.

A three-dimensional numerical method was developed to study steady flow past a tapered cylinder. These data were compared with a parallel flow visualisation experiment conducted by the author, together with the data of Piccirillo and Van Atta (1993). Qualitative agreement with the flow visualisation experiment was found to be good and both sets of data showed the appearance of large scale vortex dislocations which arise through the discontinuity in shedding frequency between the two ends. Agreement between the present results and those of Piccirillo and Van Atta for the non-dimensional cell size and modulation frequency was also found to be good. A test case for the wave problem was carried out, which utilised linear wave theory to represent the velocity field of the wave. Plots of the vortons at different spanwise planes indicate that the correlation in this direction is weak. The planar vortex

patterns which emerge at different spanwise locations bear some resemblance to the two-dimensional calculations for different strength waves. The work presented here shows that these numerical methods offer promise in the modelling of complex vortical structures which wander through the computational domain. Two-dimensional numerical computations agreed well with surface flow visualisation experiments, and other experimental data for in-line oscillations of cylinders in a steady incident flow. The reason for the good agreement between the two-dimensional computations and the flow visualisation experiments is due to the fact that it is the conditions at the free surface which dictate the flow, in the same way that for steady flow past a tapered cylinder, it is the cells nearer the larger end which are established first. Three-dimensional computations proved expensive, but provide valuable insight into the three-dimensionality of the wake.

Appendix A

Fourier Series

The following identities are used in the Linearised Stability Analysis for the doubly infinite series.

Series for $m = \pm 1, \pm 2, \pm 3, \ldots$:

$$\sum_m \frac{\cos m\phi}{m^2} = \frac{\pi^2}{3} - \pi\phi + \frac{\phi^2}{2} \tag{A.1}$$

$$\sum_m \frac{\sin m\phi}{m^3} = \frac{\phi}{6}(\phi - \pi)(\pi - 2\pi) \tag{A.2}$$

Series for $p = \pm\frac{1}{2}, \pm\frac{3}{2}, \pm\frac{5}{2}, \ldots$:

$$\sum_p \frac{\cos p\phi}{p^2 + k^2} = \frac{\pi}{k}\frac{\sinh k(\pi - \phi)}{\cosh k\pi} \tag{A.3}$$

$$\sum_p \frac{p \sin p\phi}{(p^2+k^2)^2} = \frac{\pi^2}{2k} \frac{\sinh k\phi}{\cosh^2 k\pi} + \frac{\pi\phi}{2k} \frac{\sinh k(\pi-\phi)}{\cosh k\pi} \tag{A.4}$$

$$\sum_p \frac{2k^2 \cos p\phi}{(p^2+k^2)^2} = \frac{\pi}{k} \frac{\sinh k(\pi-\phi)}{\cosh k\pi} + \pi\phi \frac{\cosh k(\pi-\phi)}{\cosh k\pi} - pi^2 \frac{\cosh k\phi}{\cosh^2 k\pi} \tag{A.5}$$

$$\begin{aligned} \sum_p \frac{pk^2 \sin p\phi}{(p^2+k^2)^3} &= \frac{\pi^2}{8k} \frac{\sinh k\phi}{\cosh^2 k\pi} + \frac{\pi\phi}{8k} \frac{\sinh k(\pi-\phi)}{\cosh k\pi} - \frac{\pi^2\phi}{4} \frac{\cosh k\phi}{\cosh^2 k\pi} \\ &\quad + \frac{\pi\phi^2}{8} \frac{\cosh k(\pi-\phi)}{\cosh k\pi} + \frac{\pi^3}{4} \frac{\sinh k\phi \sinh k\pi}{\cosh^3 k\pi} \end{aligned} \tag{A.6}$$

$$\begin{aligned} \sum_p \frac{p^2 k \cos p\phi}{(p^2+k^2)^3} &= \frac{\pi}{8k^2} \frac{\sinh k(\pi-\phi)}{\cosh k\pi} + \frac{\pi\phi}{8k} \frac{\cosh k(\pi-\phi)}{\cosh k\pi} - \frac{\pi^2}{8k} \frac{\cosh k\phi}{\cosh^2 k\pi} \\ &\quad - \frac{\pi\phi^2}{8} \frac{\sinh k(\pi-\phi)}{\cosh k\pi} - \frac{\pi^2\phi}{4} \frac{\sinh k\phi}{\cosh^2 k\pi} \\ &\quad + \frac{\pi^3}{4} \frac{\cosh k\phi \sinh k\pi}{\cosh^3 k\pi} \end{aligned} \tag{A.7}$$

$$\begin{aligned} \sum_p \frac{p^3 k \sin p\phi}{(p^2+k^2)^3} &= \frac{3\pi\phi}{8} \frac{\sinh k(\pi-\phi)}{\cosh k\pi} - \frac{\pi\phi^2 k}{8} \frac{\cosh k(\pi-\phi)}{\cosh k\pi} + \frac{3\pi^2}{8} \frac{\sinh k\phi}{\cosh^2 k\pi} \\ &\quad + \frac{\pi^2\phi k}{4} \frac{\cosh k\phi}{\cosh^2 k\pi} - \frac{\pi^3 k}{4} \frac{\sinh k\phi \sinh k\pi}{\cosh^3 k\pi} \end{aligned} \tag{A.8}$$

Appendix B

Conjugate Gradient Algorithm

The Conjugate Gradient method is used to solve matrix systems of the type:

$$[A]\{x\} = \{b\} \tag{B.1}$$

where $[A]$ is a symmetric positive definite matrix. The Conjugate Gradient method is an example of the nonstationary class of iterative solution methods; these differ from stationary methods [1] in that the computations require information that changes at each iteration. The method proceeds by computing: successive approximations $x_k \quad (k = 1, 2, ...)$ to the solution x^* (say), residuals corresponding to the iterates x_k, and search vectors p_k, which are used to update the iterates and residuals. The Conjugate Gradient method requires one matrix-vector product and two inner products per iteration. The algorithm used is shown below. It should be noted that the initial guess for the unknown vector x_0 is the previous time step value. The constants during the iteration are shown as Greek letters, the arrays as Roman. In the present work, the preconditioning matrix M is the main diagonal of the global stiffness matrix A.

[1] e.g. Jacobi,Gauss-Seidel,SOR,SSOR.

Initialise $\underset{\sim}{x}_0$; $\underset{\sim}{r}_0$

For k=1,...,n **do**

solve M $\underset{\sim}{z}_{k-1} = \underset{\sim}{r}_{k-1}$

$\gamma_k = \underset{\sim}{r}^T_{k-1} \underset{\sim}{z}_{k-1}$

if k=1 **then** $\underset{\sim}{p}_1 \longrightarrow \underset{\sim}{r}_0$

else $\beta_{k-1} = \gamma_{k-1} / \gamma_{k-2}$

$\underset{\sim}{p}_k \longrightarrow \underset{\sim}{z}_{k-1} + \beta_{k-1} \underset{\sim}{p}_{k-1}$

$\underset{\sim}{q}_k \longrightarrow A \underset{\sim}{p}_k$

$\alpha_k = \gamma_{k-1} / \underset{\sim}{p}^T_k \underset{\sim}{q}_k$

$\underset{\sim}{x}_k \longrightarrow \underset{\sim}{x}_{k-1} + \alpha_k \underset{\sim}{p}_k$

$\underset{\sim}{r}_k \longrightarrow \underset{\sim}{r}_{k-1} - \alpha_k \underset{\sim}{q}_k$

if converged: output $\underset{\sim}{x}_k$ **and stop**

end k

Preconditioned Conjugate Gradient algorithm.

Appendix C

Pressure calculation

In the three-dimensional computations presented in chapter 5, the forces on the body are evaluated by first computing the entire pressure field via the solution to a Poisson equation for pressure. Normally, this is derived by taking the divergence of the momentum equations, *viz*:

$$\nabla^2 p = -\rho \nabla \cdot \left(\left(\vec{u} \cdot \nabla \right) \vec{u} \right) \ . \tag{C.1}$$

At the body surface, a Neumann type condition is employed. The forces are then calculated by integrating the pressure field around the body; skin friction forces are calculated directly from the vorticity field at the surface. However, equation C.1 requires the evaluation of the integrals of products of velocity gradients. It was decided here to use the working variable $\vec{\omega}$ as far as possible, and to make use of the 'group representation' method (Christie et al (1980)) to achieve a more accurate representation of the source terms in the pressure equation. The momentum equations may be re-written as:

$$\frac{\partial \vec{u}}{\partial t} + \vec{\omega} \wedge \vec{u} = -\nabla \left(\frac{p}{\rho} + \frac{\vec{u} \cdot \vec{u}}{2} \right) + \nu \nabla^2 \vec{u} \ . \tag{C.2}$$

Taking the divergence yields:

$$\nabla^2 p = -\rho \nabla^2 \left(\frac{\vec{u} \cdot \vec{u}}{2} \right) - \rho \nabla \cdot (\vec{\omega} \wedge \vec{u}) \ . \tag{C.3}$$

Thus representing $\frac{\vec{u} \cdot \vec{u}}{2}$ by a scalar e, and $\vec{\omega} \wedge \vec{u}$ by a vector $\vec{a}$ (both of which may be calculated explicitly at a node) gives:

$$\nabla^2 p = -\rho \left(\nabla^2 e + \nabla \cdot \vec{a} \right) \ . \tag{C.4}$$

The integral of the $\nabla^2 e$ term need not be evaluated over the elements since the nodal global stiffness matrix representing the ∇^2 operator is available; this integral is therefore evaluated by looping over the nodes.

Appendix D

Error in continuity of wave velocity field

Check on continuity for the imposed potential wave solution (see equations 5.75, 5.76 and 5.77):

$$\begin{aligned} u &= f_1(x,z).g_1(x,y) \\ v &= f_1(x,z).g_2(x,y) \\ w &= f_2(x,z) \end{aligned} \tag{D.1}$$

$$Wave: \quad \frac{\partial f_1}{\partial x} + \frac{\partial f_2}{\partial z} = 0 \tag{D.2}$$

$$Mean: \quad \frac{\partial g_1}{\partial x} + \frac{\partial g_2}{\partial y} = 0 \tag{D.3}$$

$$\frac{\partial u}{\partial x} + \frac{\partial v}{\partial y} + \frac{\partial w}{\partial z} = g_1.\frac{\partial f_1}{\partial x} + f_1.\frac{\partial g_1}{\partial x} + f_1.\frac{\partial g_2}{\partial y} + \frac{\partial f_2}{\partial z} \qquad \text{(D.4)}$$

$$\frac{\partial u}{\partial x} + \frac{\partial v}{\partial y} + \frac{\partial w}{\partial z} = (g_1 - 1).\frac{\partial f_1}{\partial x} \qquad \text{(D.5)}$$

And, $(g_1 - 1) \sim \frac{1}{x^2}$; $\frac{\partial f_1}{\partial x} \sim \frac{u_w}{\lambda_w}$

i.e. , $\nabla \cdot \vec{u} = O[\frac{u_w}{x^2 \lambda_w}]$.

This error in the divergence does not of course guarantee that the error in the velocity field is of the same order, but it is likely to be of a similar order.

References

[1] F.H. Abernathy and R.E. Kronauer. The formation of vortex streets. *J. Fluid Mech.*, 13:1–20, 1962.

[2] F. Ahlborn. Über den Mechanismus des Hydro-dynamischen Widerstandes. *Abh. Geb. Naturwiss*, 17, 1902.

[3] C.R. Anderson. A method of local corrections for computing the velocity field due to a distribution of vortex blobs. *J. Comp. Phys.*, 62:111–123, 1986.

[4] H. Aref. Integrable, chaotic, and turbulent vortex motion in two-dimensional flows. *Ann. Rev. Fluid Mech.*, 15:345–89, 1983.

[5] G.R. Baker. A test of the method of Fink and Soh for following vortex sheet motion. *J. Fluid Mech.*, 100:209–220, 1980.

[6] R.I. Basu. Aerodynamic forces on structures of circular cross section. Part 1. Model-scale data obtained under two-dimensional conditions in low turbulence streams. *J. Wind Engng. Indust. Aero.*, 21:273–294, 1985.

[7] G. Batchelor. *An introduction to fluid dynamics.* Campridge Univ. Press, 1967.

[8] P.W. Bearman. Investigation of the flow behind a two-dimensional model with blunt trailing edge and fitted with splitter plates. *J. Fluid Mech.*, 21:241–245, 1965.

[9] P.W. Bearman. Vortex shedding from oscillating bluff bodies. *Ann. Rev. Fluid Mech.*, 16:195–222, 1984.

[10] P.W. Bearman. Challenging problems in bluff body wakes. In *Proc. IUTAM Symposium on Bluff Body Wakes, Dynamics and Instabilites*, pages 1–10, Göttingen, Germany, 1992. Springer-Verlag.

[11] P.W. Bearman and J.M.R. Graham. Vortex shedding from bluff bodies in oscillatory flow: A report on Euromech 119. *J. Fluid Mech.*, 99:225–45, 1980.

[12] P.W. Bearman, J.M.R. Graham, and E.D. Obasaju. A model equation for the transverse forces on cylinders in oscillatory flows. *Appl. Ocean Res.*, 6:166–72, 1984.

[13] C. Begue, B. Cardot, and O. Pironneau. Simulation d'écoulements turbulents à moyenne instationnaire. Technical Report 914, INRIA, October 1988.

[14] M.G. Benson et al. A viscous splitting algorithm appllied to low Reynolds number flows around a circular cylinder. *J. Fluids and Struct.*, 1989.

[15] R.E.D. Bishop and A.Y. Hassan. The lift and drag forces on a circular cylinder oscillating in a flowing fluid. *Proc. Roy. Soc. A*, 277:51–75, 1964.

[16] P.A. Blackmore. The effects of aircraft trailing vortices on house roofs. *J. Wind Engng. Indust. Aero.*, 52:155–70, 1994.

[17] M.S. Bloor. The transition to turbulence in the wake of a circular cylinder. *J. Fluid Mech.*, 19:290–304, 1964.

[18] M. Braza, P. Chassaing, and H. Ha Minh. Numerical study and physical analysis of the pressure and velocity fields in the near wake of a circular cylinder. *J. Fluid Mech.*, 165:79–130, 1986.

[19] B. Cantwell and D. Coles. An experimental study of entrainment and transport in the turbulent near-wake of a circular cylinder. *J. Fluid Mech.*, 136:321–74, 1983.

[20] C. Canuto et al. *Spectral methods in fluid dynamics.* Springer-Verlag, New York, 1988.

[21] C. Chang and R.L. Chern. A numerical study of flow around an impulsively started circular cylinder by a deterministic vortex method. *J. Fluid Mech.*, 233:243–63, 1991.

[22] J.R. Chaplin. In *Proc. IUTAM Symposium on Bluff Body Wakes, Dynamics and Instabilites*, page 320, Gőttingen, Germany, 1992. Springer-Verlag.

[23] J.P. Choquin and G.H. Cottet. Sur l'analyse d'une classe de méthodes de vortex tridimensionelles. *C.R. Acad. Sci. Paris, Série I*, 306:739–42, 1988.

[24] A.J. Chorin. Numerical study of slightly viscous flow. *J. Fluid Mech.*, 57:785–796, 1973.

[25] A.J. Chorin. Vortex models and boundary layer instability. *SIAM J. Sci. Stat. Comput.*, 1:1–21, 1980.

[26] A.J. Chorin and P.S. Bernard. Discretization of a vortex sheet with an example of roll-up. *J. Comp. Phys.*, 13:363–379, 1973.

[27] J.P. Christiansen. Numerical simulation of hydrodynamics by the method of point vortices. *J. Comp. Phys.*, 13:363–379, 1973.

[28] J.P. Christiansen and N.J. Zabusky. Instability, coalescence and fission of finite-area vortex structures. *J. Fluid Mech.*, 61:219–43, 1973.

[29] I. Christie et al. Product approximation for non-linear problems in the FE method. Technical Report NA/42, Dept. of Maths, University of Dundee, 1980.

[30] J.M. Cimbala, H.M. Nagib, and A. Roshko. Wake instability leading to new large scale structures downstream of bluff bodies. *Bull. Am. Phys. Soc.*, 27:1256, 1981.

[31] J.M. Cimbala, H.M. Nagib, and A. Roshko. Large structure in the far wakes of two-dimensional bluff bodies. *J. Fluid Mech.*, 190:265–98, 1988.

[32] T. Corke et al. A new technique for introducing controlled sheets of streaklines in wind tunnels. *IEEE Publication 77-CH 1251-8 AES*, 1988.

[33] Y. Couder and C. Basdevant. Experimental and numerical study of vortex couples in two-dimensional flows. *J. Fluid Mech.*, 173:225–51, 1986.

[34] M. Countanceau and J.R. Defaye. Circular cylinder wake configurations: a flow visualisation survey. *Appl. Mech. Rev.*, 44(6):255–305, 1991.

[35] P.D. Cozens. *Numerical modelling of the roll damping of ships due to vortex shedding.* PhD Thesis, Imperial College, London, 1987.

[36] E. Detemple-Laake and H. Eckelmann. Phenomenology of Kármán vortex streets in oscillatory flow. *Exp Fluids*, 7:217–27, 1989.

[37] D.J. Doorly and C.H. Liu. Vortex formulation and vortex particle-in-cell method for 3D flows. In *Proc. 6th ISCFD Conf.*, Lake Tahoe, 1995. Springer-Verlag.

[38] J.W. Eastwood and R.W. Hockney. Shaping the force law in two-dimensional particle mesh models. *J. Comp. Phys.*, 16:342–59, 1974.

[39] L. Euler. *Histoire de l'Académie des Sciences de Berlin.* 1755.

[40] H.E. Fiedler. Coherent structures in turbulent flows. *Prog. Aerospace Sci.*, 25:231–69, 1988.

[41] P.T. Fink and W.K. Soh. Calculation of vortex sheets in unsteady flow and applications in ship hydrodynamics. In *Proc. of the 10th Symp. on Naval Hydro.*, pages 463–88, Cambridge, Massachusetts, 1974.

[42] P.T. Fink and W.K. Soh. A new approach to roll-up calculations of vortex sheets. *Proc. Roy. Soc. A*, 362:195–209, 1978.

[43] D. Fishelov. Vortex methods for slightly viscous three-dimensional flow. *SIAM J. Sci. Stat. Comput.*, 11:485–91, 1990.

[44] R. Franke. Analysis of experimental vortex-shedding data with respect to turbulence modelling. In *Proc. 7th Symp. on Turbulent Shear Flows*, Stanford University, 1989.

[45] R. Franke and W. Rodi. Calculation of vortex shedding past a square cylinder with various turbulence models. In *Proc. 8th Symp. on Turbulent Shear Flows*, Technical University of Munich, 1991.

[46] M. Gaster. Vortex shedding from slender cones at low Reynolds numbers. *J. Fluid Mech.*, 38:565–576, 1969.

[47] J.H. Gerrard. The mechanics of the formation region of vortices behind bluff bodies. *J. Fluid Mech.*, 25:401–13, 1966.

[48] J.H. Gerrard. The three-dimensional structure of the wake of a circular cylinder. *J. Fluid Mech.*, 25:143–64, 1966.

[49] J.H. Gerrard. The wakes of cylindrical bluff bodies at low Reynolds number. *Phil. Trans. Roy. Soc. London*, A288:351, 1978.

[50] G. Giannakidis. *Private Communication*, 1994.

[51] J. Gould and S.P. Fiddes. Computational methods for the performance prediction of HAWTs. *J. Wind Engng. Indust. Aero.*, 39:61–72, 1992.

[52] J.M.R. Graham. Computation of viscous separated flow using a particle method. In *Numerical Methods in Fluid Mechanics*, pages 310–317. Oxford University Press, 1988.

[53] J.M.R. Graham. Report on the session comparing computation of flow past circular cylinders with experimental data. In *Proc. IUTAM Symposium on Bluff Body Wakes, Dynamics and Instabilites*, pages 317–23, Gőttingen, Germany, 1992. Springer-Verlag.

[54] J.M.R Graham and P.D. Cozens. Vortex shedding from edges including viscous effects. *Fluid Dyn. Res.*, 3:111–114, 1988.

[55] H.L. Grant. The large eddies of turbulent motion. *J. Fluid Mech.*, 4:149–98, 1958.

[56] C. Greengard. The core spreading vortex method approximates the wrong equation. *J. Comp. Phys.*, 61:345–48, 1985.

[57] C. Greengard and V. Rokhlin. A fast algorithm for particle simulations. *J. Comp. Phys.*, 73:325–48, 1987.

[58] O.M. Griffin and S.E. Ramberg. The vortex street wakes of vibrating cylinders. *J. Fluid Mech.*, 66:553–576, 1974.

[59] O.M. Griffin and S.E. Ramberg. Vortex shedding from a cylinder vibrating in line with an incident uniform flow. *J. Fluid Mech.*, 75:257–271, 1976.

[60] N.D. Ham. Aerodynamic loading on a two-dimensional airfoil during dynamic stall. *AIAA*, 6:1927–1934, 1968.

[61] F.H. Harlow. The particle-in-cell computing method for fluid dynamics. In B. Adler et al, editor, *Methods in Computational Physics*, volume 3, pages 319–43. New York: Academic Press, 1964.

[62] H. Helmholtz. On integrals of the hydrodynamic equations, which express vortex-motion. *Philosophical Magazine and Journal of Science(4)*, Supplement to 33(226):485–511, 1868.

[63] H. Honji, S. Taneda, and M. Tatsuno. Some practical details of the electrolytic precipitation method of flow visualization. Technical Report 89, Research Institute for Applied Mechanics, Kyushu University, 1980.

[64] P. Huerre and P.A. Monkewitz. Local and global instabilities in spatially developing flows. *Ann. Rev. Fluid Mech.*, 22:473–537, 1990.

[65] M. Y. Hussaini, A. Kumar, and M.D. Salas, editors. *Algorithmic trends in computational fluid dynamics.* Springer-Verlag, New York, 1993.

[66] D. Jespersen and C. Levit. Numerical simulation of flow past a tapered cylinder. *AIAA*, (91-0751), 1991.

[67] Smagorinsky J.S. General circulation experiments with the primitive equations, Part 1, Basic experiments. *Mon. Weather Rev.*, 91:99–164, 1963.

[68] T. von Kármán . Über den Mechanismus des Widerstands, den ein bewegter korper in einer Flüssigkeit erfährt. *Göttinger Nachrichten, Math. Phys. Kl.*, pages 509–17, 1911.

[69] T. Kawamura and K. Kuwahara. Computation of high Reynolds number flow around a circular cylinder with surface roughness. *AIAA*, (84-0340), 1984.

[70] S. Kida. Stabilizing effects of finite core on Kármán vortex street. *J. Fluid Mech.*, 122:487–504, 1982.

[71] B. Kinsman. *Wind waves : their generation and propagation on the ocean surface.* Prentice-Hall, Englewood Cliffs, N.J., 1965.

[72] G.R. Kirchoff. *Vorlesungen über Matematische Physik*, 1:466, 1876.

[73] N.E. Kochin et al. *Theoretical Hydrodynamics.* Willey Interscience, 1982.

[74] A.N. Kolmagorov. Equations of turbulent motion of an incompressible fluid. *Izv. Acad. Sci. USSR Phys.*, 6(1-2):56, 1942.

[75] P. Koumoutsakos, A. Leonard, and F Pepin. Boundary conditions for viscous vortex methods. *J. Comp. Phys.*, 113:52–61, 1994.

[76] K. Kuwahara and K. Ishii. Computation of flow around a circular cylinder in a supercritical regime. In *Proc. Symp. on Numerical Simulations in Aerodynamics*, pages 167–178, Tokyo, 1986.

[77] K. Kuwahara and H. Takami. Numerical studies of two-dimensional vortex motion by a system of point vortices. *J. Phys. Soc. Japan*, 34:247–53, 1984.

[78] H. Lamb. *Hydrodynamics.* Campridge Univ. Press, 1932.

[79] A. Leonard. Vortex methods for flow simulation. *J. Comp. Phys.*, 37:289–335, 1980.

[80] A. Leonard. Computing three dimensional incompressible flows with vortex elements. *Ann. Rev. Fluid Mech.*, 17:523–559, 1985.

[81] C. Lewis and M. Gharib. An experimental exploration of three-dimensionality in the laminar wake of a stepped cylinder. *Phys. Fluids*, A4:104–117, 1992.

[82] M.J. Lighthill. In J. Rosenhead, editor, *Introduction. Boundary Layer Theory.* Oxford University Press. New York, 1963.

[83] M.J. Lighthill. Campridge Univ. Press, 1978.

[84] G. Marchuk. In B. Hubbard, editor, *Numerical solution of PDE's II.* Academic Press: New York, 1971.

[85] S. Mas-Gallic. *Contribution à l'analyse numérique des methodes particulaires.* Thèse d'Etat, Université Paris VI, 1987.

[86] T. Matsui and M. Okude. Formation of the secondary vortex street in the wake of a circular cylinder. In *Proc. IUTAM Symposium on Structure of Complex Turbulent Shear Flow. 1982.*, Marseille, 1983. Springer-Verlag.

[87] E. Meiburg and J.C. Lasheras. Experimental and numerical investigation of the three-dimensional transition in plane wakes. *J. Fluid Mech.*, 190:1–37, 1988.

[88] J. Meneghini. *Numerical Simulation of bluff body flow control using a discrete vortex method.* PhD Thesis, Imperial College, London, 1993.

[89] R.W. Metcalfe et al. Secondary instability of a temporally growing mixing layer. *J. Fluid Mech.*, 184:207–243, 1987.

[90] D.W. Moore. Finite amplitude waves on aircraft trailing vortices. *Aero. Quart.*, 23:307–14, 1972.

[91] D.W. Moore. The spontaneous appearance of a singularity in the shape of an evolving vortex sheet. *Proc. Roy. Soc. A*, 365:105–119, 1979.

[92] D.W. Moore. Numerical and analytical aspects of Helmholtz instability. In F.I. Niordson and N. Olhoff, editors, *Theoretical and applied mechanics, IUTAM*, pages 263–74. Amsterdam: North-Holland, 1984.

[93] D.W. Moore and R. Griffith-Jones. The stability of an expanding circular vortex sheet. *Mathematika*, 21:128–33, 1974.

[94] M.V. Morkovin. Flow around a circular cylinder - kaleidoscope of challenging fluid phenomena. In *Proc. ASME Symp. on Fully Separated Flows*, Philadelphia, 1964.

[95] P.J. Naylor. *A discrete vortex model for bluff bodies in oscillatory flow.* PhD Thesis, Imperial College, London, 1982.

[96] B.R. Noack and H. Eckelmann. A low-dimensional Galerkin method for three-dimensional flow around a circular cylinder. *Phys. Fluids*, 6:124–43, 1994.

[97] C. Norberg. In *Proc. IUTAM Symposium on Bluff Body Wakes, Dynamics and Instabilites*, page 320, Göttingen, Germany, 1992. Springer-Verlag.

[98] E.A. Novikov. Dynamics and statistics of a system of vortices. *Sov. Phys. JETP*, 41(5):937–943, 1975.

[99] Y. Ogami and T. Akamatsu. Viscous flow simulation using the discrete vortex model - the diffusion velocity method. *Computers and Fluids*, 19(3/4):433–41, 1991.

[100] A. Ongoren and D. Rockwell. Flow structure from an oscillating cylinder. Part 2: mode competition in the near wake. *J. Fluid Mech.*, 191:225–45, 1988.

[101] S.A. Orszag and Y.H. Pao. Numerical computation of turbulent shear flows. In F.N. Frenkiel and R.E. Mann, editors, *Proc. Symp. on Turbulent Diffusion in Environmental Pollution.* Academic Press, London, New York, 1974.

[102] N.N. Ostrikov and E.M. Zhmulin. Vortex dynamics of viscous fluid flows. Part 1. Two-dimensional flows. *J. Fluid Mech.*, 276:81–111, 1994.

[103] A. Papangelou. Vortex shedding from slender cones at low Reynolds numbers. *J. Fluid Mech.*, 242:299–321, 1992.

[104] V.C. Patel, W. Rodi, and G. Scheuerer. Turbulence models for near-wall and low Reynolds number flows: a review. *AIAA*, 23:1308–1319, 1984.

[105] J. Peiro, J. Peraire, and K. Morgan. *FELISA System, Reference Manual.* 1994.

[106] N. Peters. Calculation of the instationary turbulent flow past a flat plate using a net-free numerical method. In E.H. Hirschel, editor, *Proc. GAMM-Conference on Numerical Methods in Fluid Mechanics*, pages 134–141. Springer-Verlag, 1975.

[107] R. Peyret and T.D. Taylor. *Computational methods for fluid flow.* New York: Springer-Verlag, 1983.

[108] P.S. Piccirillo and C.W. Van Atta. An experimental study of vortex shedding behind a linearly tapered cylinder at low Reynolds number. *J. Fluid Mech.*, 246:163–195, 1993.

[109] C. Rehbach. Numerical calculation of unsteady three-dimensional flows with vortex sheets. *AIAA*, (78-111), 1978.

[110] P.J. Roach. *Computational fluid dynamics.* Hermosa, Albuquerque, New Mexico, 1972.

[111] W. Rodi. On the simulation of turbulent flow past bluff bodies. In *Proc. 1st Int. Symp. on Comp. Wind Eng.*, Tokyo, 1992.

[112] L. Rosenhead. The formation of vortices from a surface of discontinuity. *Proc. Roy. Soc. A*, 134:170, 1931.

[113] L. Rosenhead. Vortex systems in wakes. *Adv. in Appl. Mech.*, 3:185–95, 1953.

[114] A. Roshko. On the development of turbulent wakes from vortex streets. *NACA Technical report*, (1191), 1954.

[115] A. Roshko. Perspectives on bluff body aerodynamics. In *Proc. 2nd Int. Coll. on Bluff Body Aerod. and Applic.*, pages 7–10, Melbourne, Australia, 1992.

[116] J.-Y. Sa and K.-S. Chang. On far-field stream function condition for two-dimensional incompressible flows. *J. Comp. Phys.*, 91:398–412, 1990.

[117] P.G. Saffman. Dynamics of vorticity. *J. Fluid Mech.*, 106:49–58, 1981.

[118] P.G. Saffman. *Vortex dynamics.* Campridge Univ. Press, 1992.

[119] P.G. Saffman and G.R. Baker. Vortex interactions. *Ann. Rev. Fluid Mech.*, 11:95–122, 1979.

[120] P.G. Saffman and D.I.. Meiron. Difficulties with three-dimensional weak solutions for inviscid incompressible flow. *Phys. Fluids*, 29(8):2373–2376, 1986.

[121] P.G. Saffman and J.C. Schatzmann. Stability of a vortex street of finite vortices. *J. Fluid Mech.*, 117:171–85, 1982.

[122] T. Sarpkaya. Computational methods with vortices - The 1988 Freeman Scholar lecture. *J. Fluids Engng.*, 111:5–52, 1989.

[123] H. Sato. Experimental investigation on the transition of laminar separated layer. *J. Phys. Soc. Japan*, 11:702, 1960.

[124] A. Savvides. *Computational analysis of 2-D uniform viscous flow around a circular cylinder using a Fourier series truncation method.* MPhil/PhD transfer report, Dept. of Aeronautics, Imperial College, London, 1994.

[125] S. Siddiqi. Trailing vortex roll-up computations using the point vortex method. *AIAA*, (87-2479), 1987.

[126] F.J. Simoes. *A steady inviscid flow model for horizontal axis wind turbine rotors under high loading.* PhD thesis, Imperial College, London, 1991.

[127] P.A. Smith and P.K. Stansby. Generalized discrete vortex method for cylinders without sharp edges. *AIAA*, 25(2):199–200, 1987.

[128] P.A. Smith and P.K. Stansby. Impulsively started flow around a circular cylinder by the vortex method. *J. Fluid Mech.*, 194:45–77, 1988.

[129] P.A. Smith and P.K. Stansby. Postcritical flow around a circular cylinder by the vortex method. *J. Fluids and Struct.*, 3(3):275–92, 1989.

[130] T.P. Sommer. *A three-dimensional cloud-in-cell method.* MSc Thesis, Dept. of Aeronautics, Imperial College, London, 1990.

[131] A. Sommerfeld. *Mechanics of deformable bodies.* New York/London: Academic, 1964.

[132] P.R. Spalart. *Numerical simulation of separated flows.* PhD Thesis, University of California, Berkeley, 1982.

[133] P.K. Stansby and A.G. Dixon. Simulation of flows around cylinders by a Lagrangian vortex scheme. *Appl. Ocean Res.*, 5(3):167–178, 1983.

[134] A. Sugavanam and J.C. Wu. Numerical study of separated turbulent flow over airfoils. *AIAA*, 20:464–70, 1982.

[135] S. Szepessy. *On the three-dimensionality of vortex shedding from a circular cylinder.* PhD Thesis, Chalmers University of Technology, Göteborg, Sweden, 1991.

[136] S. Taneda. Downstream development of wakes behind cylinders. *J. Phys. Soc. Japan*, 14:843–48, 1959.

[137] I. Tani. Low-speed flows involving bubble separations. *Prog. Aerospace Sci.*, 5:70–103, 1964.

[138] N. Tombazis. *Effects of three-dimensional disturbances on bluff body near-wakes.* PhD Thesis, Imperial College, London, 1993.

[139] A.A. Townsend. The mechanism of entrainment in free turbulent flows. *J. Fluid Mech.*, 26:689–715, 1966.

[140] A.A. Townsend. Flow patterns of large eddies in a wake and in a boundary layer. *J. Fluid Mech.*, 95:515–37, 1979.

[141] M.F. Unal. In *Proc. IUTAM Symposium on Bluff Body Wakes, Dynamics and Instabilites*, page 320, Gőttingen, Germany, 1992. Springer-Verlag.

[142] C.W Van Atta and P.S. Piccirillo. Topological defects in vortex streets behind tapered cylinders at low Reynolds numbers. In P. Coullet and P Huerre, editors, *New Trends in Nonlinear Dynamics and Patterning Phenomenon: The Geometry of Non Equilibrium*, pages 243–50. Plenum, 1990.

[143] S.E. Widnall, D.B. Bliss, and C.Y. Tsai. The instability of short waves on a vortex ring. *J. Fluid Mech.*, 66:35–48, 1966.

[144] R. Wille. Kármán vortex street. *Adv. in Appl. Mech.*, 6:273–87, 1960.

[145] C.H.K. Williamson. Defining a universal and continuous Strouhal-Reynolds number relationship for the laminar vortex shedding of a circular cylinder. *Phys. Fluids*, 31:2742–2744, 1988.

[146] C.H.K. Williamson. The natural and forced formation of spot-like 'vortex dislocations' in the transition of a wake. *J. Fluid Mech.*, 243:393–441, 1992.

[147] C.H.K. Williamson. 2-D and 3-D aspects of the wake of a cylinder, and their relation to wake computations. In C.R. Anderson and C. Greengard, editors, *Vortex Dynamics and Vortex Methods.* American Mathematical Society, Providence, Rhode Island, 1994.

[148] C.H.K. Williamson. Three-dimensional vortex dynamics in the wake of a cylinder. In S.I. Green, editor, *Fluid vortices*. Dordrecht: Klumer Academic, 1995.

[149] G.S. Winckelmans. *Topics in vortex methods for the simulation of three- and two-dimensional incompressible unsteady flows*. PhD Thesis, California Institute of Technology, Pasadena, 1989.

[150] G.S. Winckelmans and A. Leonard. Weak solutions of the three-dimensional vorticity equation with vortex singularities. *Phys. Fluids*, 31(7):1838–1839, 1988.

[151] J.C. Wu. Numerical boundary conditions for viscous flow problems. *AIAA*, 14:1042, 1976.

[152] J.A. Young. *Viscous flow around vortex shedding flowmeters: a discrete vortex model*. PhD Thesis, Imperial College, London, 1989.

[153] N.J. Zabusky. Coherent structures in fluid dynamics. In *The significance of Nonlinearity in the Natural Sciences*, pages 145–205. New York: Plenum, 1977.

[154] M. M. Zdravkovich. Smoke observations of the formation of a Kármán vortex street. *J. Fluid Mech.*, 37:491–96, 1969.

[155] A. Zervos, S. Huberson, and A. Hemon. Three dimensional free wake calculation of wind turbine wakes. *J. Wind Engng. Indust. Aero.*, 27:65–76, 1988.

[156] C.Y. Zhou. *Effects of combination motions on cylinders in waves and currents*. PhD Thesis, Imperial College, London, 1994.

[157] O.C. Zienkiewicz and K. Morgan. *Finite elements and approximation*. John Wiley and Sons Inc., New York, Chichester, Brisbane, Toronto, Singapore, 1983.

BIBL. LONDIN.